UC Berkeley
UC Berkeley Electronic Theses and Dissertations

Title
Printed Nitrate Sensor Nodes for Precision Agriculture

Permalink
https://escholarship.org/uc/item/2625h73g

Author
Goodrich, Payton James

Publication Date
2022

Peer reviewed|Thesis/dissertation

Printed Nitrate Sensor Nodes for Precision Agriculture

by

Payton James Goodrich

A dissertation submitted in partial satisfaction of the

requirements for the degree of

Doctor of Philosophy

in

Engineering - Mechanical Engineering

in the

Graduate Division

of the

University of California, Berkeley

Committee in charge:

Professor Tarek Zohdi, Chair
Professor Ana Claudia Arias
Professor Lisa Pruitt

Summer 2022

Printed Nitrate Sensor Nodes for Precision Agriculture

For you, the reader. I hope you gain something for your journey.

Contents

List of Figures

List of Tables

Acknowledgments

There are so many people I would like to acknowledge for their part in the completion of this work. The leading position of honor goes without question to Carol Baumbauer, who I have hailed as my 'partner-in-crime' throughout my Ph.D. program. Carol and I joined the Arias Research Group around the same time, and over the years our work converged with one another's. What a blessing. Many of the conclusions found in this dissertation would never have been reached if not for the countless mid-day dissections of each other's results and her tenacious dedication to finding the root of a problem. For that, I am forever grateful.

I would also like to thank my other lab mates and past mentors in the Arias Research Group with whom I worked closely: Dr. Anju Toor, Dr. Margaret Payne, Dr. Alla Zamarayeza, and Maykel Nijenhuis. I would also like to thank my lab mates in the Multiphysics Simulation and Optimization Laboratory: Omar Betancourt, Emre Mengi, Roger Isied, Zachary Yun, Brian Howell, and Avery Rock. A special thank you to the members of the Advanced Manufacturing for Energy Lab. They were the ones to bring me to Berkeley in the first place: Dr. Paul Wright, Dr. Bernard Kim, Dr. Bala Kumaravel, Dr. Zackary Gima, and Dr. Martin Cowell. Thank you all for my roots.

A heartfelt thank you to all of the spectacular researchers that I had the pleasure of mentoring over my graduate career: Vy Luu, Catherine Kim, Dat Nguyen, Alexis Flores-Betancourt, Claire Beckstoffer, Emma Wawryznek, Lucia Landeros, Aashray Machanda, Nithila Poongovan, Galen Penvenne, and Noa Souccar. I wish you all wings.

Thank you to my academic collaborators at other universities, including the folks at the Boulder Experimental Electronics and Manufacturing Laboratory out of CU Boulder's Department of Mechanical Engineering, Raj Khosla's Agronomics Lab out of KSU's Department of Agronomy, and our friends just down the hill in the Silver Lab in the Department of Environmental Science, Policy and Management.

Finally, I would like to thank MY mentors who made this all possible. Dr. Ana Arias adopted me into her research group early on and without hesitation. She has given me lasting life advice and remains my closest mentor and role model. Dr. James (Jim) Evans and I have had many in-depth discussions regarding the material science and electrochemistry involved in the ion-selective electrodes. I thank him for the sense of academic vigor he instilled in me. Dr. Tarek Zohdi gave the first lecture I attended at Berkeley, and, fortunately, I enjoyed his teaching style more than I was intimidated by the maths. It took me three tries to pass the course, and now a good portion of this dissertation is built on his lectures.

Abstract

Printed Nitrate Sensor Nodes for Precision Agriculture

by

Payton James Goodrich

Doctor of Philosophy in Engineering - Mechanical Engineering

University of California, Berkeley

Professor Tarek Zohdi, Chair

Nitrate is a critical nutrient for plant growth and a primary component of commercial fertilizers. Unfortunately, nitrate production is an energy-intensive process and, when applied in excess, generates greenhouse gases and pollutes the water supply. Despite this, tools for monitoring nitrate and other nutrients in the soil are inadequate. Measurements must be made at a high spatial and temporal resolution to optimize agricultural water and fertilizer inputs.

We will present the model-based design, fabrication, and implementation of wireless nitrate sensor nodes in a precision farming system. First, I will discuss the design, fabrication, and characterization of fully printed potentiometric nitrate sensors, describing in detail key performance metrics and benchmarking our sensors against existing sensors in the literature. We will next define and demonstrate the optimized placement of soil sensors in agricultural fields using machine learning optimization approaches to determine the scale of production required to meet the project goals and inform the design space of the wireless sensor nodes. The nitrate sensors were modified, integrated into a WiFi-enabled sensor node, and characterized in varying solution and soil conditions. The sensor node was adapted into a low-cost, naturally-degradable, passive RFID nitrate sensor node, characterized, and modeled into a wireless sensor network sampled by autonomous UAV drones. Finally, I describe the challenges of interference and present preliminary results of a multianalyte nitrogen sensor array.

Introduction

This thesis is divided into two sections. In the first section, a technical primer is given to provide a starting point for readers interested in sensor, printing, and machine learning technologies. In the second section, these three technologies are combined to demonstrate my dissertation work in developing nitrogen sensor nodes for precision farming applications.

Grain growers apply on the order of a hundred to a few hundred pounds of nitrogen per acre, depending on the crop and field conditions[1]. At a cost of tens of cents to a dollar (USD) per pound, with prices rapidly increasing in recent months, it is the second highest cost for many crops, outdone only by seeds[2]. Nitrate fertilizer is conventionally applied uniformly across a field despite studies that have shown existing nitrate concentration in the soil can vary significantly on the order of tens of meters. Precision agriculture practitioners aim to designate site-specific management zones to direct more efficient nitrogen application, but the tools they have to gather data are limited. Optical remote sensing can be used to estimate nitrogen in growing plant material, but to get measurements of nitrate in the soil, a soil sample must be collected and taken back to a laboratory, for analysis via chromatography or spectrographic methods[3;4]. Such measurements are highly accurate, but they are also expensive, labor-intensive, and give data for only one point in time and space. Nitrate is highly mobile, so concentrations change over time. Models can be developed to estimate nitrate fluxes based on measurements at the beginning and end of a season, but these rely on many estimations and assumptions[5].

Environmental quality monitoring and precision agriculture require nitrate sensors that are robust enough to survive field deployment and soil insertion, can be mass-produced, and involve few or no moving parts. Additionally, the data must be simple to read. Printed solid-state potentiometric ion-selective electrode sensors have the potential to meet these criteria.

The use of printing methods for sensor fabrication offers several advantages such as low cost, high throughput, and ease of fabrication. In order to realize the benefits of printing and enable large-scale sensor deployment, both electrodes must be printed.

Previous works have shown printed nitrate ISEs for use in aqueous environments[6–9] and agriculture[6;8;10–13]. Dam et al.[11] demonstrated potentiometric nitrate sensors having a screen-printed nitrate ISE paired with a commercial RE for agriculture applications.[14–16]. Similarly, inkjet-printed nitrate ISEs were reported by Jiang et al.[17] using a commercial Ag/AgCl reference electrode during measurements.

In this work, we demonstrate fully printed, potentiometric nitrate sensors and characterized their sensitivity, selectivity, and stability. We then integrated the sensors into a wireless sensor node and characterized its sensitivity to nitrate concentration and moisture levels in the soil. We then replaced the components of the nitrate sensor node with naturally degradable components and characterized the devices. We propose a model-driven paradigm of measuring these sensors using swarms of UAV drones whose flight paths are optimized using machine learning. Finally, we demonstrate the need for sensor arrays to account for the interference that different analytes could cause, and provide preliminary results for a nitrogen sensor array that measures nitrate, nitrite, and ammonium concentration in aqueous solutions.

Part I

Technical Primer

Chapter 1

Sensors

Best Things dwell out of Sight
The Pearl—the Just—Our Thought...
– Emily Dickinson

For just a moment, silence your mind and be fully aware.

What do you hear? Look around, what do you see? Can you smell anything? Are you hot or cold? Is the fabric on your skin soft or scratchy? Can you taste anything on your breath?

Our senses are the gateways to interacting with the world around us. They ground us in reality.

Each of what we call 'senses' are actually a complex biological network of sensors that were developed over millions of years of evolution. According to Darwinism, biological evolution is a competition that naturally selects for traits that increase survival and reproduction, which means that our sensors (senses) were made with the primary purpose of giving us the information needed to survive.

Fortunately for us, human civilization has developed to a point where day-to-day survival is not a constant concern for most people. Our natural evolution progressed in tandem with our technical innovation, and now the tools we develop allow us to guide our own evolution. Electronic sensors are among these tools. They enhance and expand human perception, broadening our ability to understand the world around us. At the time of this writing, there are about one trillion sensors in the world[18], over 10 billion of which are 'smart' sensor nodes that are connected to the ever-growing internet-of-things (IoT)[19]. As sensors capture more and more of our world, these devices will not only give us a clearer understanding of our world but also help us make sense of how we want to shape it.

A

B
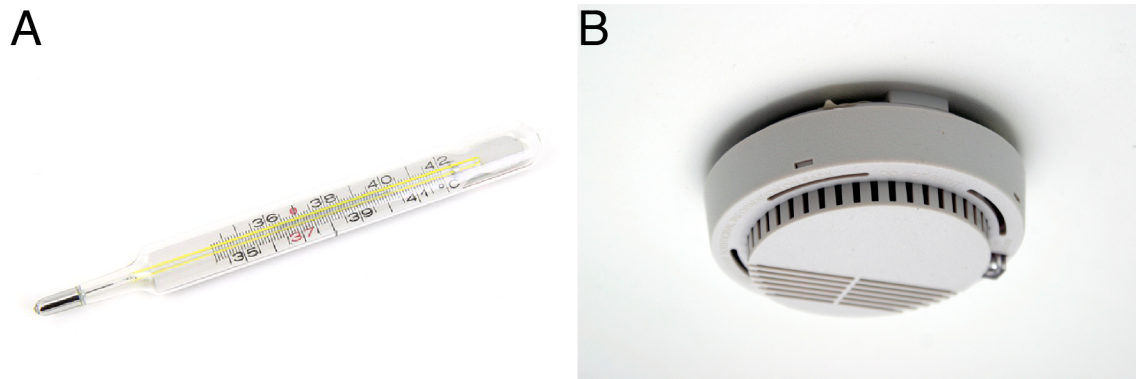
Figure 1.1: Sensors vs. detectors. A) A liquid-in-glass thermometer is one of the simplest and most widely recognized temperature sensors. B) A smoke detector is a detector, which is different from a sensor because it does not measure the amount of smoke.

1.1   What is a Sensor?

A sensor is a device that is able to *detect* and *measure* some physical quantity of interest and *communicate* that information to another device or person[20]. A common example of a sensor that you might recognize is the liquid-in-glass thermometer, shown in Figure 1.1. In this type of thermometer, a thin glass tube is filled with a small volume of liquid mercury that collects in a bulb at the bottom. Then, as temperature changes, the mercury expands or contracts in response, causing the peak of the mercury to move up or down the long stem. The stem, as you may know, is calibrated and marked with numbers corresponding to the temperature in Fahrenheit, Celsius, or both. In this example, the sensor *detects* the change in temperature (our physical quantity of interest) by the liquid expanding or contracting in the glass tube. The temperature is *measured* and *communicated* to a person by the numbered ticks on the thermometer stem.

A sensor should not be mistaken for a detector, which is able to *detect* and *communicate* a physical quantity, but fails to *measure* it. Consider for example a smoke detector, such as the one shown in Figure 1.1B. A smoke detector is able to *detect* whether or not there is smoke, but it doesn't *measure* how much smoke there is. To a smoke detector, there is no distinction between a blazing house fire and overcooked salmon: both cause it to brazenly *communicate* its detection of smoke.

Contrary to the thermometer example above, most modern sensors are electronic devices, which will be the type of sensor that will be discussed in this dissertation. Many electronic sensors work by having some material that is sensitive to the physical quantity that is being measured, causing a property of that material to change with respect to the physical quantity. Other electronic sensors take advantage of natural laws, such as conductive metal wires arranged in a loop to measure the strength of the magnetic field that it's in. Later in Section 1.2, we will go over the various types of sensors and the transduction mechanisms that a sensor might use. However, regardless of the mechanism or the physical property that is being measured, all electronic sensors have a sensing element that converts the signal of the physical quantity to an electric signal.

As a quick aside, the opposite of a sensor is an actuator, which converts an electric signal into a mechanical action[21]. Some common examples of actuators are electrical motors, hydraulic pumps, or pneumatic valves. Sensors and actuators are both transducers, which is a device that converts energy from one form to another. The distinction here is the intended purpose of the device: sensors measure and detect, while actuators perform an action. A more quantitative way of thinking of this is to look at energy conversion efficiency. The efficiency of energy conversion for sensors is immaterial because their purpose is to detect and measure. For example, if one sensor is 10% efficient at energy conversion but is less accurate than a second sensor that is only 2% efficient, then the second sensor is still an objectively better sensor of the two sensors because it is better at detecting and measuring. Contrarily, efficiency is an important metric for actuators because their purpose is to perform an action. An electric motor with a 2W load is objectively better than a motor with a 5W load, assuming they perform the same task equally well.

1.2 Sensor Classification

The organization and classification of sensors vary throughout the academic literature and commercial marketplace. This is because there really is no perfect form of organization, as there are many 'one-off' devices that sense for some unique purpose or by some unique method[21]. Further, there are many ways to categorize sensors: sensor specifications, sensor materials, transduction mechanisms, the quantity being measured, the field of application, whether the sensor is active or passive, direct or complex, and many, many more[22]. It is analogous to classifying humans: humans can be classified by their age, gender, race, nationality, preferred sports team, favorite color, or the size of their ears. Similarly, sensors can be classified in many such ways.

Table 1.1: Classification of sensors by energy forms

Energy Type	Example Measurands
Mechanical	Length, area, volume, velocity, acceleration, mass flow, force, torque, pressure, acoustic wavelength, acoustic intensity
Thermal	Temperature, specific heat, entropy, heat flow
Electrical	Voltage, current, charge, resistance, inductance, capacitance, dielectric constant, polarization, electric field, frequency, dipole moment
Magnetic	Field intensity, flux density, magnetic moment, permeability
Radiant	Intensity, phase, wavelength, polarization, reflectance, transmittance, refractive index
Chemical	Composition, concentration, reaction rate, pH, oxidation/reduction potential

In this section, we will describe a few of the more useful modes of classifying sensors.

Energy Form

One way of classifying sensors is by the energy type of the signal that they are measuring[23]. Table 1.1 lists the six energy forms or signal domains generally encountered, with examples of typical properties that are measured using those energy forms.

Passive & Active

Sensors can also be classified as passive or active types. The distinction is simple: active sensors provide their own energy source to operate, while passive sensors use naturally available energy. An interesting example of both an active and a passive sensor is a camera. In a brightly lit location, natural light will illuminate the photographed subjects and then reflect toward the camera lens, where the camera simply records the radiation provided (passive mode). In a dark room, however, there won't be enough ambient light for the camera to record the subjects adequately. Instead, the camera uses its own energy source - the 'flash' - to illuminate the subjects and record the radiation reflected off them (active mode).

Direct & Complex

Often, one or more transformation is required for the electrical signal to be generated. The steps involved can be either direct or complex. A direct sensor is one that can directly convert the measured quantity into an electrical signal, while a complex sensor requires multiple conversion steps. Take for instance an infrared distance sensor. The sensor sends out an infrared beam which reflects off a target some short distance away, is read by a photodiode, and the time is recorded to calculate the distance to the target. In this example, we see that a sensor such as this involves several transformations: from an electric current to photons, reflection, and conversion back into electric current.

In the following section, we will explore the underlying mechanisms for how these transformations take place.

1.3   Transduction Mechanisms - How do Sensors Make Measurements?

In the marketplace, people generally care more about the sensed quantity and how well the sensor performs for their specific application, while academic researchers and sensor designers are also interested in *how* the sensor measures the quantity. This section is concerned with the latter.

The means by which a sensor makes a measurement is called the transduction mechanism. Transduction is the conversion of one source of energy to another, and *all* sensors utilize some form of energy transformation to make and communicate their measurements.

It should be noted that this is not an exhaustive list of transduction mechanisms. This list only covers a small fraction of the many universal laws describing the conversion of one energy form to another.

Rather, this list focuses on transduction principles that describe converting one energy type to electrical energy. This is because all electrical sensors must take advantage of at least one of these mechanisms, and often more.

What this list does *not* cover is transduction from any energy type to another type other than electrical. For example, the thermal expansion principle that governs the liquid-in-glass thermometer example at the beginning of this chapter is not described, because that (non-electric) sensor operates on the principle of converting thermal energy to gravitational energy. This list also does not include modes of biological or nuclear signal transduction mechanisms for the sake of brevity.

Electrical Mechanisms

Electrical transduction mechanisms are ones that convert one form of electrical energy to another. While these mechanisms can be used to measure electrical quantities directly (such as those listed in Table 1.1), they are also used in complex sensors as one of several steps to transform one signal into another.

Voltage, Current, & Resistance

In any homogeneous material, electrons move about randomly like gas in a closed container. That is, of course, until we submit the material to an electric field. Consider a bar of an arbitrary material, and let's imagine connecting it to a car battery with the large alligator-mouthed jumper cables. As soon as the connection is made, there is now an electric field, E within the bar:

$$E = \frac{V}{l} \tag{1.1}$$

where V is the voltage of the battery, and l is the length of the bar between the two clamps. Now, all of the free-moving electrons are set into uniform motion. The rate that the electrons travel is called the current, and is defined by:

$$i = \frac{V}{R} \tag{1.2}$$

where R is the resistance. With the exception of superconductors, all materials have electrical resistivity, ρ_e, which is a measure of a material's ability to resist current flow. Thus, resistance can be related by:

$$R = \rho_e \frac{l}{A} \tag{1.3}$$

where l is the length of the material and A is the cross-sectional area. Equation 1.3 describes the fundamental relationship between resistance and its parameters.

Voltage, current, and resistance are closely related to one another, and many sensors that utilize one of these mechanisms are very likely to use one of the others. For example, consider a sensor whose sensing element operates on the principle that the resistance changes with respect to the measurand. A sensor designer may choose to put the sensing element in series with a non-variable resistor to form a voltage divider, in which case the voltage across the divider would be the output signal. Or, the designer may put the sensing element in parallel with a non-variable resistor, and measure the current as the output signal.

Capacitance

In a capacitive sensor, the measurand needs to change one of the parameters that define capacitance. Capacitance is defined as:

$$C = \frac{q}{V} \tag{1.4}$$

or, for a parallel plate capacitor:

$$C = \frac{\epsilon_r \epsilon_0 A}{d} \tag{1.5}$$

where C is the capacitance, q is the net capacitor charge, V is the potential difference between the capacitor plates, ϵ_r is the relative permittivity, ϵ_0 is the permittivity of a vacuum, A is the plate area, and d is the distance between the plates. Most often, it is one of the values in Equation 1.5 that is varied in a capacitive sensor. It should be noted that Equation 1.5 only holds for a parallel plate capacitor, and different geometries such as cylindrical or interdigitated capacitors will result in modified formulas. However, the overarching principle of a capacitive sensor applies to all geometries.

When connected to an electric circuit, capacitance can be represented as a complex resistance:

$$\frac{V}{i} = -\frac{1}{j\omega C} \tag{1.6}$$

where $j = \sqrt{-1}$ and i is the sinusoidal current with a frequency of ω, meaning that the complex resistance of a capacitive sensor is frequency dependent. Thus, capacitance can be used as a sensing element to measure properties with frequency-dependent behavior.

Electromechanical Mechanisms

Piezoelectricity

There is a small set of crystalline materials that generate an electric charge when subjected to stress, as shown in Figure 1.2. When a horizontal force is applied across the material, the hexagonal lattice becomes deformed. Figure 1.2B shows a compressing force, shifting the atoms in a way that polarizes the y-axis. In Figure 1.2C, a tensile force is applied such that the charge is opposite of what it was under compression.
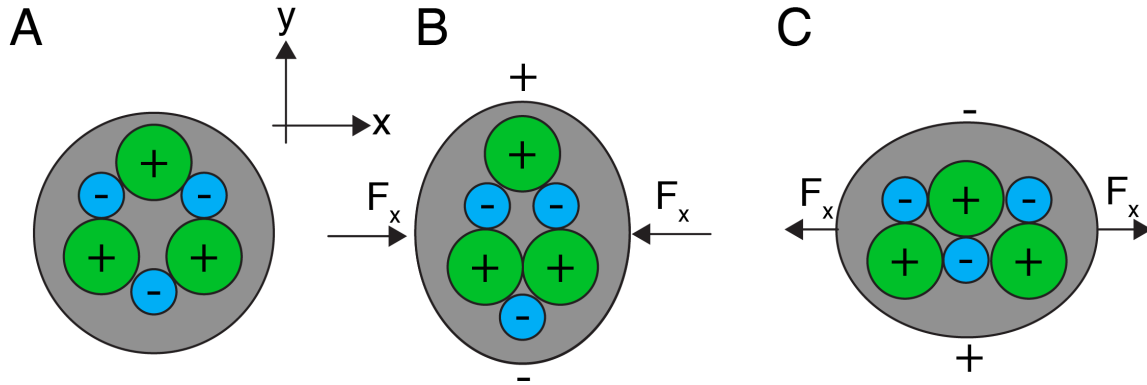
Figure 1.2: The piezoelectric effect. A) A piezoelectric material at rest. B) A piezoelectric material responding to applied stress in the x-direction results in a net potential across the lattice in the y-direction. C) When the opposite stress is applied, the potential is reversed.

Piezoelectric materials can be placed between a pair of electrodes to form all kinds of force-sensitive sensors. In this orientation, the piezoelectric material becomes the dielectric of the capacitor, which will generate an electric voltage across the capacitor in response to stress.

Piezoresistivity

Where the piezo*electric* effect is a change in a material's *electric potential* in response to a mechanical force, the piezo*resistive* effect is a change in a materials *resistance* in response to a mechanical force. So far, we have regarded the specific resistivity and conductivity of materials as being constant. In reality, these values vary with a handful of properties, such as strain temperature, and magnetic field. We will discuss some of these properties later in this section, but for now, let's focus on the relationship between resistance and strain.

Consider the stretching of a wire by applying some force, F. From mass conservation, we know that the volume, V, must remain constant, so as the length l increases, the cross-sectional area, A, must decrease. We can then rewrite Equation 1.3 as:

$$R = \frac{\rho_e}{V} l^2 \tag{1.7}$$

and differentiate it to obtain the piezoresistive effect:

$$\frac{dR}{dl} = 2\frac{\rho}{V}l \tag{1.8}$$

Thermoelectric Mechanisms

Thermoresistance

Similar to magnetoresistance, the specific resistivity and conductivity of materials also rely on the temperature:

$$\rho_e = \rho_{e,0}\left(1 + \alpha\frac{T - T_0}{T_0}\right) \tag{1.9}$$

where $\rho_{e,0}$ is a reference resistance (usually measured at T = 25°C) and α is the temperature coefficient of resistance. Equation 1.9 is a linear-regression model for temperature-dependent behavior of resistive materials, though higher order polynomial equations can also be used for higher accuracy.

Thermoresistive temperature sensors can be made from materials whose temperature coefficient of resistivity is sufficiently high and predictable.

Magnetoelectric Mechanisms

Hall-effect

The hall-effect is a phenomenon where electrons will experience a sideways force when subjected to an external magnetic field. The magnitude and direction of this force are:

$$\boldsymbol{F} = q_e\boldsymbol{v}_e\boldsymbol{B} \tag{1.10}$$

where q_e and $\boldsymbol{v}_e$ are the charge and velocity of an electron, respectively, $\boldsymbol{B}$ is the magnetic field, and boldface font is an indication of vectors. The magnetic field could be those produced by permanent magnets, the earth's rotation, or even from power line current.

Consider electrons moving in a ribbon-like strip of conductive material and placed in a magnetic field, the electrons traversing the strip will be deflected in response to the magnetic field. If one were to put a voltmeter and connect it to the sides of the conductive strip, then a voltage would be measured where:

$$V_H = hi\boldsymbol{B}sin\theta \tag{1.11}$$

where V_H is the hall potential, h is a sensitivity coefficient, and θ is the angle between the magnetic field vector $\boldsymbol{B}$ (of magnitude B) and the current i.

Magnetoresistance

Magnetoresistive sensors also require an external magnetic field, though their operating principle is different. In some materials such as ferromagnetic alloys, the electrical resistance changes in the presence of an external magnetic field, B:

$$\frac{\rho_e}{\rho_{e,0}} = \left(\frac{\rho_e(B) - \rho_{e,0}}{\rho_{e,0}}\right) = \left(\frac{R(B) - R_0}{R_0}\right) \tag{1.12}$$

where $\rho_e(B)$ and $\rho_{e,0}$ are the electrical resistivities in magnetic fields of magnitude B and 0, respectively, and $R(B)$ and R_0 are similar electrical resistances, respectively[24].

Photoelectric Mechanisms

Photoconductive Effect

When light strikes a semiconductor material with pn-junctions, a photon can transfer its energy to an electron. If the energy is sufficiently high, the electron can become mobile, resulting in an electric current. If the light of a proper wavelength hits the semiconductor crystal, then the concentration of charge-carrying electrons and holes will increase, thereby increasing the conductivity of the crystal, as given by:

$$\sigma_p = \frac{1}{R} = e\left(\mu_e n + \mu_h p\right) \tag{1.13}$$

where e is the charge of an electron, μ_e is the electron mobility, μ_h is the hole mobility, and n and p are the concentrations of electrons and holes, respectively. Thus, the conductivity of the material is directly proportional to the amount of light of a high-enough frequency that the semiconductor crystal is exposed to.

Photovoltaic Effect

The photovoltaic effect is the generation of potential across a positive-negative junction of a semiconducting material when exposed to a flux of photons. The generated potential is described by:

$$V = V_0 \ln(E_{irr}) \tag{1.14}$$

and:

$$V_0 = \frac{kT}{q} \ln\left(\frac{N_A N_D}{n_i^2}\right) \tag{1.15}$$

where E_{irr} is the radiative energy of the light striking the semiconductive sensor element in $\frac{W}{m^2}$, k is Boltzmann's constant, T is the absolute temperature, q is the charge of an electron, N_A is the electron doping densities on the p-type side, N_D is the hole doping density on the n-type side, and n_i is the intrinsic carrier density. From Equations 1.14 and 1.15, we see that a photovoltaic sensing element converts light intensity to an electric potential.

Electrochemical Mechanisms

Amperometric

An amperometric sensor measures the current flow between two electrodes in a three-electrode setup. The reference electrode (RE) is designed to maintain a constant potential in varying electrolytic environments. The counter electrode (CE) counters the reactions occurring at the working electrode (WE). In an amperometric sensor, the potential between the RE and WE is held constant while the current between the CE and WE are measured, as shown in Figure 1.3A. The current is generated from the reactions occurring at the surface of the WE, which could be driven by immobilized enzymes, microbes, noble metal catalysts, or other reagents.

Depending on the reaction taking place at the WE, different numbers of electrons are produced as a result of the reaction. Michaelis-enten kinetics are generally used to describe the rate of these reactions, and thus describe the mechanism for how these sensors operate. The current, i, of an amperometric sensor, is given by:

$$i = nFA_{WE}v_a \tag{1.16}$$

where n is the number of electrons transferred in the reaction, F is Faraday's constant, A_{WE} is the area of the WE, and v_a is the reaction rate. From Equation 1.16, we see that Amperometric sensors can be used to measure diffusion coefficients, electrode reaction rates, and adsorption parameters.
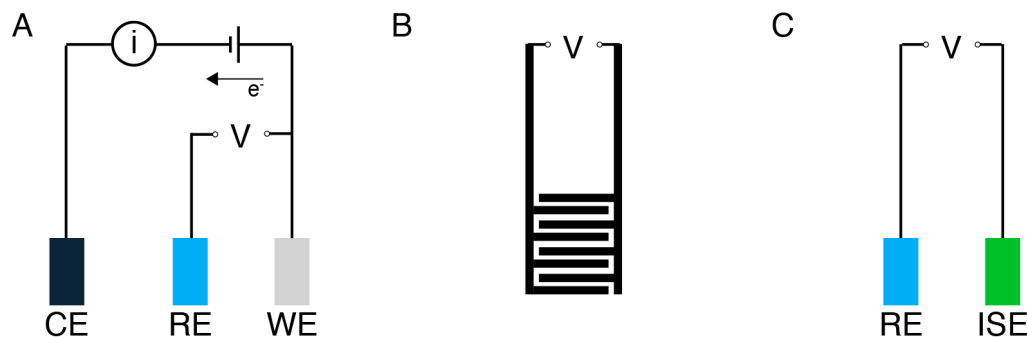
Figure 1.3: A) Schematic of an amperometric sensor. The voltage between the reference electrode and working electrode is held constant while the current between the working electrode and counter electrode is measured. B) Schematic of a conductometric sensor. The conductivity of the electrolytic solution that the sensor electrodes are exposed to is measured directly by the voltage drop across the electrodes. C) A schematic of a potentiometric sensor. The potential of the ion-selective electrode is measured with respect to the reference electrode.

Impedimetric

Impedimetric sensors are essentially electrochemical conductivity sensors that measure the impedance of an electrolyte in the electrochemical cell. Here, we consider the impedimetric and conductometric sensors together, as the output of one is the inverse of the other and otherwise operates in entirely the same way. In a homogeneous electrolytic solution, the conductance is given by:

$$G = \frac{1}{R} = \frac{A}{\rho_e L} = G_0 \beta \sqrt{c} \tag{1.17}$$

where ρ_e is the electrolyte's resistivity, L is the segment of solution within the electric field, A is the cross-sectional area of the electric field, G_0 is the conductance of the electrolyte at infinite dilution, β is a characteristic of the electrolyte that's found empirically, and c is the concentration of the solution. According to Equation 1.17, ρ_e is related to the concentration and charge of the analytes in the solution.

As eluded to earlier, impedimetric sensors operate similarly to the resistive sensors, except the resistor is replaced with the electrolytic solution. Changes in properties of the electrolytic solution - such as the concentration of an analyte, or the

addition of another analyte - will cause a measured change in the electrolytic conductance, G. A schematic of an impedimetric sensor is shown in Figure 1.3B.

Potentiometric

A potentiometric sensor measures the open-circuit potential across a two-electrode device, such as the one shown in Figure 1.3C. Similar to amperometric sensors, the reference electrode (RE) provides 'electrochemical ground'. The second electrode is the ion-selective electrode (ISE), which is sensitive to the analyte-of-interest. The ISE is connected to a voltage sensor alongside the RE. The voltage sensor must be very sensitive and have a high input impedance, allowing only a very small current to pass.

There are four possible mechanisms by which ionophores can interact with ions: dissociated ion exchange, charged carrier exchange, neutral carrier exchange, and reactive carrier exchange[25]. Dissociated ion-exchange ionophores operate by classical ion-exchange over a phase boundary, in which hydrophilic counter-ions are completely dissociated from the ionophore's lipophilic sites, preserving electroneutrality while allowing sites for the ions in solution to bind to. Charged-carrier ionophores bond with opposite-charged ions to make a neutrally charged molecule, and the ions with which they bond are determined by thermodynamics and the Hofmeister principle[26]. Neutral carrier ionophores are typically macrocyclic, where many organic molecules are chained together to form a large ring-like shape whose gap is close to the molecular radius of the primary ion[27]. Finally, reactive carrier ionophores are mechanistically similar to neutral carrier ISEs, with the only difference being that reactive carriers are based on ion-ionophore covalent bond formation while neutral carriers are based on reversible ion-ionophore electrostatic interaction. Neutral carrier and reactive carrier ion exchange both are dependent on the mobility, partition coefficients, and equilibrium constants of the ions and carriers in the membrane phase[25]. Some examples of the chemical structures of ionophores are shown in Figure 1.4.

The potential from the interaction of the ISE and RE with the analyte-of-interest in the solution is given by:

$$E_{cell} = E_{ISE} - E_{RE} + E_j \tag{1.18}$$

where E_{cell} is the potential difference measured in the cell, E_{ISE} is the potential of the ISE, E_{RE} is the potential of the RE, and E_j is the liquid-junction potential. As described earlier, the RE is used as a constant-potential reference element, while the liquid-junction potential can be found by calibrating a potentiometric sensor in a
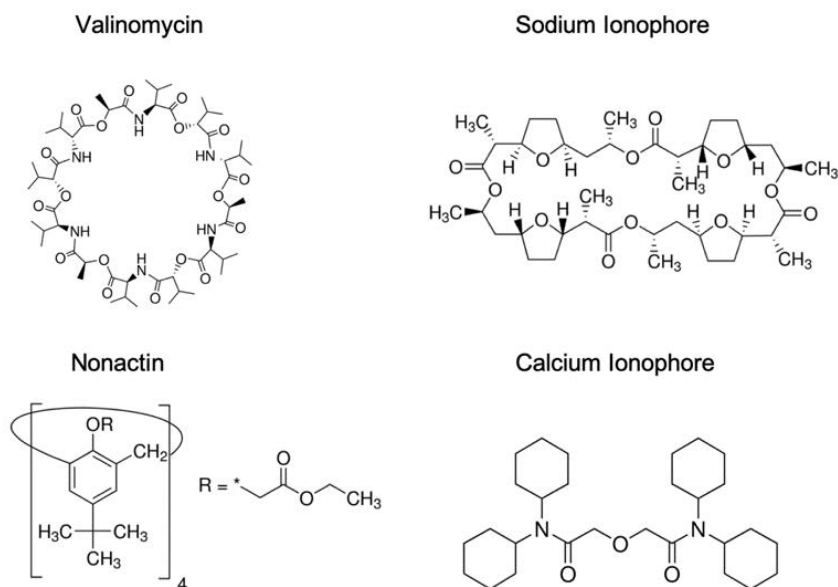
Figure 1.4: Examples of four different ionophores used in potentiometric sensors.

solution of a known concentration. This allows a correlation to be made between the measured potential difference, E_{cell}, and the logarithm of the activity of the primary analyte, as described in the Nernst Equation:

$$E = E_0 + \frac{RT}{z_i F} \ln a_i \qquad (1.19)$$

where E is the measured potential, E_0 is the measured potential of a 1M solution of the primary analyte i at 25°C , R is the ideal gas constant, T is the temperature, z_i is the valency charge of the primary analyte i, F is Faraday's constant, and a_i is the activity of the primary analyte i.

Nernstian behavior is frequently associated with an electrochemical reaction, but for solid-state ionophore-doped polymeric ISEs, no electrochemical reactions (in the usual sense) need to be invoked to explain the Nernstian behavior [28]. The ISE consists of an organic phase membrane doped with an ionophore, L, that has a strong affinity to the primary ion. If the ionophore is a neutral carrier, then a hydrophobic counter ion to the primary ion (sometimes called an ion-excluder or ionic site in literature) is necessary for selectivity [28]. The potential then is given by thermodynamics:

$$E_{ISE} = E^0_{ISE,i} + \frac{RT}{z_i F} \ln a_{i,solution} + \frac{RT}{z_i F} \ln \frac{1}{a_{i,membrane}} \qquad (1.20)$$

The ionophore in the membrane phase effectively holds the activity of the ion in the membrane constant, making Equation 4.1 become:

$$E_{ISE} = E^0_{ISE,i} + \frac{RT}{z_i F} \ln a_{i,solution} \qquad (1.21)$$

which is the Nernst equation.

If the temperature is known (either by approximation or by measurement with a temperature sensor), then from Equation 1.19 we see that the measured potential is logarithmically proportional to the activity of the primary analyte (the chemical being sensed). The activity of an analyte denotes the 'active' concentration of a species in solution and is given by:

$$a_i = f_i c_i \qquad (1.22)$$

where f_i and c_i are the activity coefficient and the concentration of analyte i, respectively. For sufficiently dilute solutions of approximately 0.1 M or less, then f_i can be calculated according to Debye-Huckel theory. Thus, for a calibrated potentiometric sensor, the concentration of the primary analyte can be determined from the measured cell potential, E_{cell}.

Potentiometric sensing is the primary focus of this dissertation. Chapter 4 discusses potentiometric sensing in greater detail.

1.4   Measurands - What do Sensors Measure?

The list of properties that sensors can measure is perpetually growing. In this section, we will give some examples of the types of measurands that sensors measure, and indicate some of the transduction mechanisms that those sensors might use[29].

Just as Section 1.3 was not an exhaustive list of transduction mechanisms, this too is not an exhaustive list of sensor types. Acoustic, enzymatic, microbial, and radiation sensors, to name a few, have been omitted for the sake of brevity. Other types of sensors (such as light and temperature sensors) have been omitted because sensors of those types were discussed when describing their corresponding transduction mechanisms.

Chemical Sensors

Chemical sensors are sensors that measure a particular chemical species in an aqueous solution, such as NO_3^-, PO_4^{3-}, K^+, or Cl^-. Of interesting note is that almost all chemical sensors can be designed to operate by any of the electrochemical transduction mechanisms presented in the previous section. Many chemical sensors utilize electrochemical transduction mechanisms, though it is possible to also make chemical sensors that operate with photoelectric mechanisms, for example, ion-gas chromatography.

Flow Sensors

A fundamental principle of physics is that mass cannot be created nor destroyed. In the absence of mass sinks, the mass flux (flow) summation in any boundary volume must be zero. For a fluid flowing through a plane, the flow is equal to:

$$Q = \frac{V}{\Delta t} = \frac{M}{\rho \Delta t} = \int v dA \tag{1.23}$$

where Q is the flow rate, V is the volume, t is time, M is mass, ρ is the fluid density, v is the fluid velocity, and A is the cross-sectional area. A conventional flow sensor usually measures the fluid's velocity, v. So, if the cross-sectional area of the tube is not known or if the velocity is not uniform through the cross-section (hint: it rarely is), then the measurement alone is relatively pointless. A better technique to measure flow is to use a differential pressure sensor that is exposed to the flow stream at two points along the flow vector, and apply Bernoulli's equation to calculate the flow rate:

$$Q = \xi A \sqrt{\Delta p} \tag{1.24}$$

where ξ is a term found through empirical calibration.

Moisture & Humidity Sensors

The term 'moisture' generally refers to the water content of solids, while the term 'humidity' is reserved for the water vapor content in gases. Generally, moisture and humidity sensors are capacitive, resistive, or optical. For capacitive sensors, the transduction is based on the fact that water has a different electrical permittivity than dry air (in the case of humidity) or most solids (in the case of moisture). Thus, the capacitance will also change as the amount of humidity or moisture increases.

$$C = \frac{\epsilon_0 \epsilon_r A}{g} = C_0 + C_{H_2O} \tag{1.25}$$

In a resistive sensor configuration, the sensor operates on the premise that the resistivity of most non-metal conductors is dependent on their water content. These sensors are typically designed such that the sensing element is a highly resistive conductor. As the moisture or humidity increases, water penetrates the conductor and increases the conductivity, so the measured resistance across the sensing element changes proportional to the water content.

Positional Sensors

Positional sensors are some of the most common in the world, and there are likely several within reach of you as you read this. Smartphones and wearable health devices utilize various sensors to track how many steps you take in a day, the intensity of your workouts, and what route to take home from work.

Displacement, velocity, and acceleration can sometimes all be found with a single device, as each quantity is the time-derivative of the prior. In practice, however, it is common to use separate devices for any of these three measurements because the cost of these sensors is relatively cheap, and it is easy to build systematic errors if the timing mechanism is off.

The measurements for displacement, velocity, and acceleration must be made with respect to some frame of reference. For example, consider a group of people playing a game of billiards in a moving train car. Observers on the train platform would assign different velocity vectors to the balls during play than observers on the train.

Displacement & Angular Displacement Sensors

Displacement and angle sensors commonly use potentiometers when the value is expected to be suitably small. A potentiometer transduces linear or angular displacement to a change in electrical resistance.

For a displacement sensor, a conductive wire is wrapped around a non-conductive rod, and a sliding contact is attached to the object whose displacement is being measured. A known voltage is supplied across the wound wire, and as the object moves, the sliding contact will make contact with the wound wire, shorting that part of the circuit. Then, the output voltage across the wire is measured, which will be proportional to the amount of the wire shorted by the sliding contact, which

is proportional to the object's displacement. The same principles are applied to measure the angle for a potentiometer operating in angular displacement mode.

There are other methods for measuring displacement, but these methods can also be used to measure velocity, as described in the following section.

Velocity & Angular Velocity Sensors

Velocity measurements utilize a variety of approaches ranging from radar, laser, and sonic sensor systems. These types of sensors use one of these modulating signals to send a sound or light wave in a direction and measure the time it takes to bounce off of a surface, return to the sensor, and activate a sensing element that is sensitive to that modulating signal. Using this, the device can calculate the distance between the sensor and the reflecting object by dividing lag time by the wave speed. Then, because these devices often operate at a high frequency, the measurement can be made again, and the change in distance divided by the change in the time between measurements yields a linear velocity.

Angular sensors can also be used in some cases to measure linear velocity. In a car, for example, the speedometer is a linear velocity sensor, but it makes its measurement using an angular velocity sensor on the drive shaft and calculates the linear velocity from the assumed tire size.

Acceleration & Angular Acceleration Sensors

Acceleration measurements are most commonly made with accelerometers. Accelerometers are most commonly MEMS devices that are extraordinarily cheap, have a low-power requirement, and utilize the capacitance transduction mechanism. The charged electrode of an interdigitated parallel-plate capacitor structure is vibrated at a high mechanical frequency. Then, when acceleration occurs, if it is perpendicular to the gap between the two capacitor plates, the force from the acceleration will cause the moving electrode of the parallel-plate capacitor to deflect towards the other plate, changing the space of the gap between the two, thereby changing the measured capacitance.

Pressure Sensors

The operating principle of most pressure sensors is based on the conversion of a pressure exertion on a pressure-sensitive element with a defined surface area. In response, the element is displaced or deformed. Thus, a pressure measurement may be

reduced to a measurement of a displacement or a force that results from a displacement. Because of this, many pressure sensors are designed using either the capacitive or the piezoresistive transduction mechanisms. In each, a deformable membrane is suspended over an opening, such that the pressure on one side of the membrane is controlled while the pressure on the other side is the subject of the measurement. As the pressure on the measurement side changes, the membrane will deform proportionally to the difference in pressure. For a piezoresistive transducer, the membrane is designed to maximize stress at the edges, which modulates the resistance proportional to the deformation. For a capacitive transducer, the membrane is made of or modified with a conductive material, while a surface on the pressure-controlled side of the membrane is also conductive, and the pair act as a parallel-plate capacitor. Then, the membrane is designed to maximize deflection at the center of the membrane, thereby changing the electrode gap and capacitance.

1.5 Sensor Circuits - How do Sensors Communicate?

Practically speaking, a sensing element does not function by itself. It is always a part of a larger 'sensor circuit': a circuit with other electronics, such as signal conditioning devices, microcontrollers, antennas, power electronics, displays, data storage, and more. Sensor circuits fit within the broader subject of systems engineering, which is a vast field in its own right. Figure 1.5 shows one possible sensor circuit configuration.

Depending on the design of the circuit and which components are included in it, the signal that is output by the sensing element might be conditioned to the specifications of a connected microcontroller, saved onto a flash drive, shown on a display, and sent to a phone, saved on a remote server, or many other possibilities. Rather than discuss all possible sensor systems and circuit designs, we have selected the most common - and arguably most essential - components in any given sensor system and summarized them in this section.

Microcontrollers

Since the invention of microprocessors in the late 1960s, new types of *intelligent* or *smart* sensors have been developed[30]. Smart sensors are those that are integrated with a programmed microcontroller. A microcontroller is a small computer that operates as the 'brains' of a circuit. Microcontrollers contain one or more central
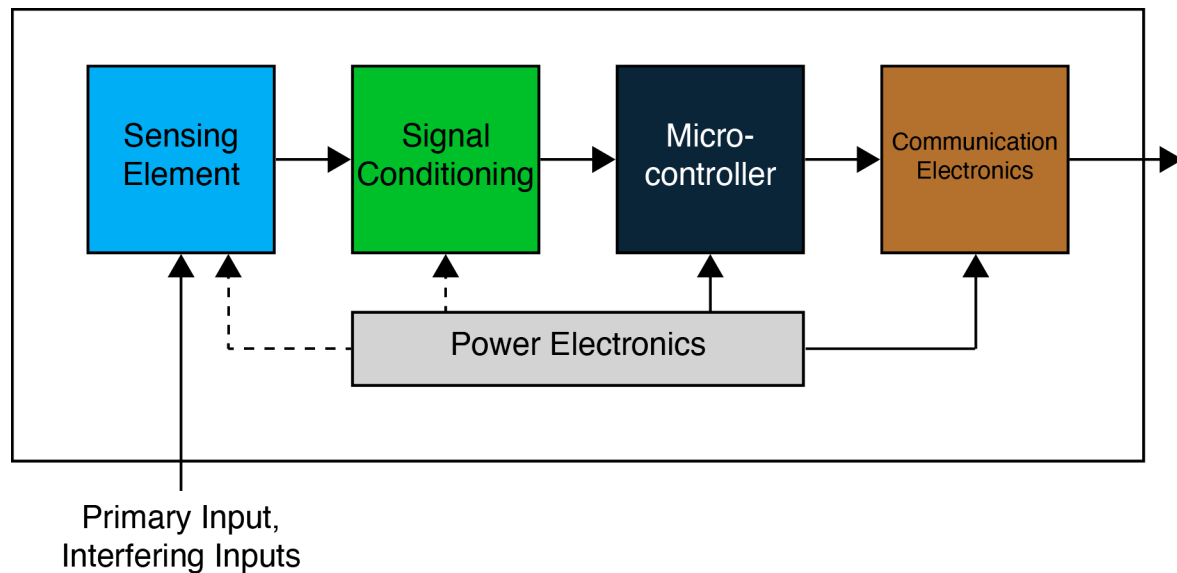
Figure 1.5: Schematic of a basic sensor circuit. The sensing element generates an electric signal proportional to the input signal, which is conditioned and received by a microcontroller. The programmable microcontroller determines how often to sample the conditioned signal, performs functions on the received data, whether or not to store the data, and pushes data to the communication electronics. The power electronics supply an excitation signal to the sensing element if it is an active sensor.

processing units (CPUs), a small amount of programmable memory, and input/output (I/O) peripherals. In a sensor circuit, these I/Os are connected to the power electronics, communications electronics, and the sensing element through the signal conditioning electronics.

Signal Conditioning

Microcontrollers operate in the digital domain and require a digital input signal to understand. However, very few sensing elements provide a digital output directly. Furthermore, even if digitized, some sensor output signals do not scale to the digital I/O values determined by the microcontroller. Signal conditioning electronics act as 'buffers' that condition a signal to be compatible with a microcontroller[31].

Amplifiers are the most common signal conditioning electronics. Amplifiers can be used to increase the gain of a signal, invert a signal, or filter out certain fre-

quencies[32]. Also commonly used are analog-to-digital converters, which convert a continuous analog signal to a finite number of digital values that can be read by a microcontroller[31].

Power Electronics

In some form or another, all sensor circuits require power to operate. The components of a sensor circuit that generate, attenuate, or store energy to power the other circuit components are called power electronics. This may include batteries, energy harvesters, and various power conditioning devices.

A sensor circuit can be made passive, where there is no energy storage within the circuit. The concept is similar to passive sensing elements described in section 1.2: passive sensor circuits use the naturally available energy to operate. This can be done if the quantity that is being measured can also be harnessed to power the device, such as light powering a photovoltaic sensing element.

If there is no passive power generation, power electronics are vital for a sensing circuit's function. This could be as simple as a coin-cell battery connected to the microcontroller's power I/O pins or as complex as a circuit with multiple energy harvesting and energy storage modalities.

Communications

A sensor is not a sensor if it does not communicate its measured signal to another person or device. Communication electronics are what fulfill this function. Communication electronics can be wired or wireless. When communicating data to a person, wired communications electronics could be displays or speakers that communicate the data through images or audio. When communicating data to another computer, wired communication electronics come in the form of a 'bus', a catch-all term for all the hardware, wires, software, and communication protocols used between devices. At the time of this writing, wireless communications *must* be between the sensor circuit and another electronic device, though perhaps in future years, technology will develop a way for people to directly interface with wireless data transfer. In the meantime, wireless communications generally incorporate an antenna that attenuates an electrical signal into a directional RF frequency following one of many wireless communication protocols such as WiFi, Bluetooth, or RFID.
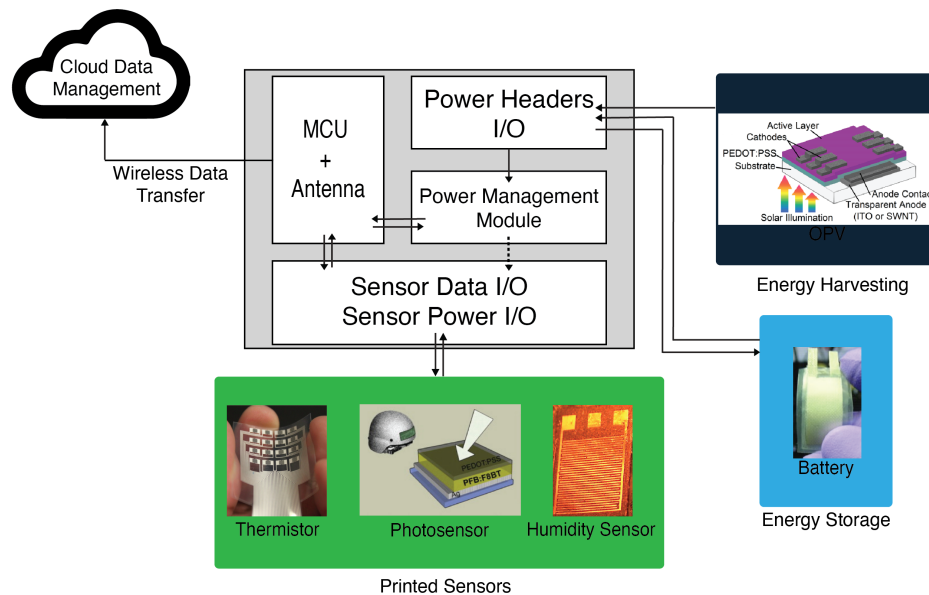
Figure 1.6: Schematic of a wireless sensor node circuit with example devices from the Arias Research Group.

Sensor Nodes

When integrated in a way such that the output of a sensor circuit is communicated to one or more other discrete electronic systems using radio-frequency (RF) communication instead of or in addition to a person or group of people, the circuit is called a 'sensor node'. Depending on the sensor's purpose and how it is designed to communicate its information, the sensor node could have one of innumerable configurations, such as the one shown in Figure 1.6.

1.6   Important Sensor Metrics

A handful of common metrics are used to describe the performance regardless of their transduction mechanism or what they measure. Meanwhile, some metrics are specific to certain types of sensors. For example, the most important metric for strain gauges is the gauge factor, which measures the ratio between the relative change in the strain gauge's resistance and the strain gauge's state of strain. The gauge factor is a completely irrational metric to compare two light intensity sensors.

In this section, we discuss metrics commonly used to discuss any kind of sensor or sensor system. An expansive list of metrics and other technical terms and abbreviations is available in Appendix A.

Sensitivity, Selectivity, and Stability

Sensitivity

There is an ideal or theoretical input-output relationship for every sensor[22]. This relationship can be plotted with the input signal of the measurand on the x-axis, and the output signal on the y-axis. When this is done, the best-fit mathematical model that fits this data is called the transfer function. The simplest transfer function is linear and has the form:

$$y = Sx + B \tag{1.26}$$

where S is the slope of the transfer function and B is the offset. Alternatively, the transfer function could be exponential:

$$y = B + S \ln x \tag{1.27}$$

logarithmic:

$$y = Be^{Sx} \tag{1.28}$$

power:

$$y = Sx^k + B \tag{1.29}$$

or polynomial:

$$y = \sum_{i=1}^{N} B_i \frac{S_i^i}{i!} x^i \tag{1.30}$$

where k is a power factor. For Equations 1.26 - 1.30, the larger that the term for S is, the larger the output signal will be for a given input signal. S is the sensitivity, a ratio between the output signal and the measured property. It is beneficial for this value to be large and constant because it measures to what degree the primary measurand influences the sensor's output.

Selectivity

The selectivity (sometimes called the specificity) measures the degree to which a sensor measures the target quantity alone. This is important because sensing elements can be exposed to many different signals - not just the signal that they are measuring. Consider a photovoltaic light intensity sensor set outside to monitor day-night cycles. The sensing element will not only be exposed to the sunlight, but also diurnal changes in temperature, fluctuating humidity, occasional moisture in the form of rain, and slight pressure fluctuations from a breeze. If this light sensor has cross-sensitivity to any of these other measurands, it could mistake a change in one of those signals for a change in the light intensity.

A selectivity coefficient can quantify selectivity, k_{ij}, where for a sensor with a linear transfer function:

$$k_{ij} = \frac{S_j}{S_i} \tag{1.31}$$

where S is the sensitivity of the sensor to a primary measurand, i, and an interfering measurand, j. k_{ij} must be found empirically, and should ideally be very small. If it is not, then the influence of the interfering signal must either be considered when calculating error terms or accounted for by a second sensor. Selectivity will be explored briefly in Section 4.4 and in-depth in Chapter **??**.

Stability

Stability is related to the lifetime of a sensor. It is the tendency for a sensor to behave in a predictable, unchanging, and expected manner. Naturally, all built things will gradually break down under entropy, but the degree to which a sensor resists these changes and maintains function is called stability.

Stability can be quantified in several ways, and how it is quantified often depends on the sensor type. The most obvious method is to continuously test a sensor under unchanging conditions, but this isn't always reasonable because some sensors may take months, years, or even decades to break down. Another more attractive method is to simulate sensor breakdown at an accelerated rate by cycling it through different temperature and humidity levels in an environmental chamber. In either case, perhaps the most popular quantification of stability is characterizing 'drift', which is the change in either a sensor's sensitivity, offset, or absolute output value over a specified time period:

$$\bar{\dot{\psi}} = \frac{\Delta \psi}{\Delta t} \tag{1.32}$$
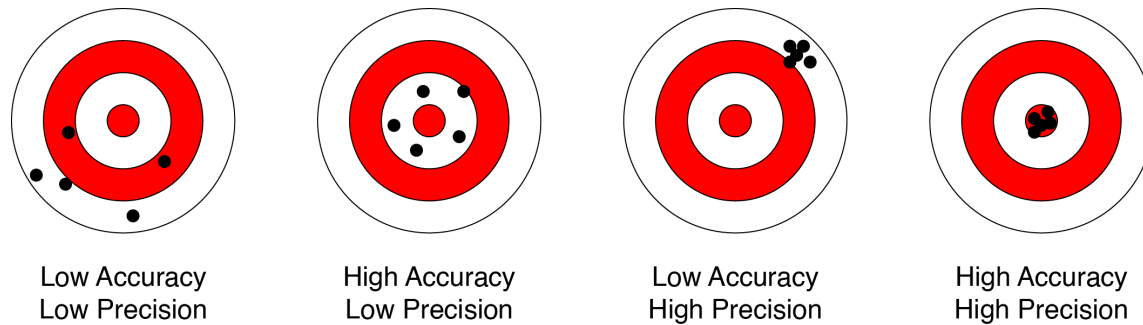
Figure 1.7: Schematic depicting the difference between precision and accuracy using a dart board analogy. In this analogy, the bullseye represents the ground-truth value of the quantity being measured, the black dots represent measurements made, and the size of the black dots represents the measurement resolution.

where ψ is the property that is changing over time.

Accuracy, Precision, & Resolution

Accuracy, precision, and resolution are all commonly used as performance indicators in sensors and are often used to rank different sensors against one another. 'Good' sensors should have high accuracy and precision with fine measurement resolution. Figure 1.7 gives a quick description of these values with the classic dartboard analogy.

Accuracy

Accuracy is a measure of how close a measurement or an average of measurements is to the ground-truth value, and is reported as a percentage. Reporting accuracy can sometimes be confusing because, in some fields, it has become common practice to report the error rate as accuracy when traditionally, the error rate is inversely related to accuracy. In the traditional sense, accuracy is defined as the difference in the error rate from 100%:

$$Accuracy = \left(1 - \frac{|x_{measured} - x_{actual}|}{x_{actual}}\right) \cdot 100\% \tag{1.33}$$

Precision

Precision measures the degree to which a sensor produces repeated measurements under unchanged conditions. This is closely related to the variance of a set of measurements, and is one way that precision is sometimes reported:

$$\sigma_x^2 = \frac{1}{N-1} \sum_{n=1}^{N} (x_i - \bar{x})^2 \tag{1.34}$$

The lower the variance, the higher the precision.

Resolution

The sensor's resolution is the smallest change a sensor can detect in the measured quantity. For example, the resolution of an analog watch would be one second, because that is the distance between one marking and another. Suppose one used a digital thermometer to read the temperature of kettle water heating up for tea, and on the display, it reads "67.8°C ". The resolution of this measurement would be 0.1°C because it would take a change of at least 0.1°C to change its output.

Error

In science and engineering, 'error' does not mean a mistake or blunder. Rather, it is a quantitative measurement of the inevitable uncertainty that comes with all measurements[33]. This means errors are not mistakes; they cannot be eliminated merely by being careful. All sensors have some inherent error (or uncertainty) in their measurement. The best that one can hope for is to ensure that the errors are minimized where possible and to have a reasonable estimate of the magnitude of the error.

One of the best ways to assess the reliability of a measurement is to perform it several times and consider the different values obtained. Experience has shown that no measurement - no matter how carefully it is made - will obtain the same values. Error analysis is the study and evaluation of uncertainty in a measurement.

Uncertainties can be classified into two groups: *random* errors and *systematic* errors. Figure 1.8 highlights these two types of error using a dartboard example. Systematic errors always push the measured results in a single direction, while random errors are equally likely to push the results in any direction. Consider trying to time an event with a stopwatch: one source of error will be the reaction time of the
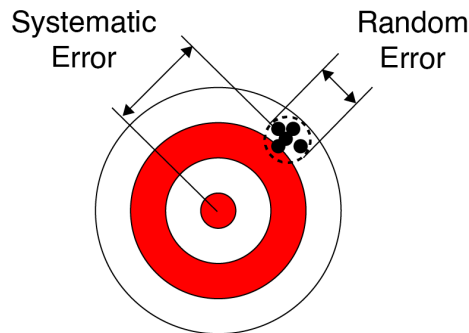
Figure 1.8: Schematic depicting systematic versus random errors. Systematic errors result from various factors and can be corrected with compensation methods. The random error follows a Gaussian distribution and is caused by the repeatability of the measurand and the summation of all random noise sources.

user starting and stopping the watch. The user may delay more in starting the stopwatch, thereby underestimating the duration of the event, but they are equally likely to delay more in stopping the stopwatch, resulting in an overestimate of the event. This is an example of random uncertainty. Consider if the stopwatch consistently runs slow - in this case, all events will be underestimated. This is an example of systematic uncertainty. Systematic errors are hard to evaluate and sometimes even difficult to detect. However, the use of statistics gives a reliable estimate of random error.

Mean

Suppose we want to measure some quantity, x. Assume we have identified and reduced all systematic uncertainties to a negligible level. Because all remaining sources of uncertainty are random, we should be able to identify them by repeating the measurement several times. After we have taken the measurements, we will see that the values differ. In statistics, the best representation of the measured value would be the average or the *mean* of the measured values:

$$\bar{x} = \frac{x_1 + x_2 + ... + x_N}{N} = \frac{1}{N} \sum_{n=1}^{N} x_i \tag{1.35}$$

where x_i is an individual measurement and N is the total number of measurements made.

Standard Deviation

The standard deviation is an estimate of the average uncertainty of the measurements. Consider any single measurement, x_i, to the mean, $\bar{x}$. The measurement deviates from the best estimate by $x_i - \bar{x}$. If our measurements are precise, the value of any deviation is likely small. If some of the deviations are large then the measurements are not precise. To estimate the average reliability, we square the value of each deviation and take the square root of the result to evaluate the deviation's magnitude, then calculate the mean of these values. The result is the standard deviation, σ_x:

$$\sigma_x = \sqrt{\frac{1}{N-1} \sum_{n=1}^{N} (x_i - \bar{x})^2} \qquad (1.36)$$

Standard Error

We have seen how the best estimate for a quantity x is $\bar{x}$ and that the average uncertainty of the separate measurements is σ_x. However, $\bar{x}$ represents a combination of all N measurements, and we have reason to believe it is better than any single measurement taken alone. In fact, the uncertainty of $\bar{x}$ is given by the standard error, $\sigma_{\bar{x}}$:

$$\sigma_{\bar{x}} = \frac{\sigma_x}{\sqrt{N}} \qquad (1.37)$$

An important feature of the standard error is that as we increase the number of measurements we make, the value of the standard error will decrease. This makes sense: as we increase the number of measurements we make, we are less and less uncertain of the average result of the measurements.

1.7 Concluding Remarks

When originally setting out to write this chapter, I envisioned writing a collection of various sensors and their applications. It quickly became clear that an entire book - let alone a chapter! - could embrace this massive scope. Instead, what I have written here has the less ambitious goal of serving as a 'Sensors 101' reference text for students, researchers, engineers, and the tangentially curious.

The field of sensor technology is broad and spans the scope of nearly every scientific and technical discipline. Sensors are the eyes, nose, and ears of modern

electronics, and they will continue to get smaller, better, and more prevalent. The diaspora of sensors and how they will affect the future of humanity is difficult to understate.

Chapter 2

Printed Electronics

2.1 Conventional, Printed, & Hybrid Electronics

Electronics fabrication and manufacturing can be subdivided into conventional, printed, and hybrid electronics. Conventional electronics include all those made in foundries, using complementary metal-oxide semiconductors (CMOS), microelectromechanical systems (MEMS), or similar technologies. They also include through-hole electronics used in breadboarding, which are not discussed here. Printed electronics, on the other hand, encapsulates all electronics that utilize solution-based processing of electroactive materials. Finally, hybrid electronics include all electronics that use a combination of both conventional and printed electronics.

Conventional Electronics

In the kingdom of electronics, silicon reigns. Since the first integrated circuits (ICs) were fabricated at Texas Instruments and Fairchild Semiconductor in the early 1960s,

the number of ICs that can fit on a chip has doubled approximately every two years following the well-known Moore's law. This has been made possible by reducing the minimum feature size. As of 2022, through advancements primarily related to the development of new processing techniques, the smallest transistors today are 2 nm - small enough to fit 50 billion on a chip the size of a fingernail[34].

While ICs were first built using germanium, they were soon replaced by silicon for two key advantages. First, silicon is abundant in nature, providing the possibility of manufacturing electronics with a low-cost starting material[35]. Second, the processing advantages of silicon raised it above other semiconducting materials.

CMOS is the technology used to make most conventional electronics. The MOS and bipolar structures are fabricated through repeated application of several processing steps, such as Photolithography, Etching, Diffusion, Oxidation, Evaporation, Sputtering, Chemical Vapor Deposition (CVD), Ion Implantation, Epitaxial Growth, and Annealing[32]. The strength of this manufacturing strategy lies in the standardization of these processes; It is possible to reliably and repeatably make micro- and even nano-scale features by carefully following a process recipe.

Despite the benefits, there are some limitations to conventional electronic manufacturing technologies. For one, the processing temperatures to obtain critical components in these devices are hundreds to thousands of degrees Celsius, which limits material selection drastically. Of these limited materials, they are nearly all rigid at room temperature. Rigid materials are inherently difficult to integrate with biological applications; Nature is full of organic curves and fractal patterns, while conventional electronics are Cartesian and rectilinear. There are also practical limitations to the size of silicon-based electronics, leading to the largest commercially-available silicon wafer being only 450 mm in diameter[36]. These primary limitations motivate printing technologies, which circumvent these problems and offer additional benefits.

Printed Electronics

Where conventional electronics are forged in a foundry and submitted to various standard processes, printed electronics are made at low temperatures using different solution processing techniques[37]. Printing technologies are revolutionizing the field of flexible and high surface area sensors and electronics and offer cost-effective routes for processing a wider variety of materials than conventional electronics[38]. Reducing material waste, low fabrication cost, and simplified patterning techniques make printing an attractive manufacturing strategy[39–41]. In particular, printed electronics:

1. Enable integration of non-conventional materials

2. Utilize Additive Manufacturing principles

3. Produce large volumes with high throughput

4. Facilitate low-costs

5. Can be flexible, stretchable, or rigid

Because the processing temperatures are much less than those required for rigid silicon electronics, there are many more materials compatible with printing that would otherwise melt or incinerate at foundry temperatures. These materials can be solution-processed, i.e., the discrete material particles can be suspended or dissolved in a liquid-phase solvent and deposited onto a substrate - or 'printed'. Printing is an additive process, meaning material is only deposited where it is used, and there are no steps that require removing material as in conventional lithographic processes. Many of these printing processes can easily be scaled to roll-to-roll processing, making it possible to produce large volumes of printed electronics at minimal cost with the ability to change the design of the printed device quickly. Finally, the low temperatures of printed technologies also allow for using plastic, paper, or other flexible materials as the base substrate.

Despite the benefits, there are very few fully-printed electronic systems in practice. It is challenging to build analogs to the transistor using printed technologies. While there has been a lot of research on developing printed transistors[42;43], more work needs to be done for wider adoption[15]. Thus, most self-proclaimed printed electronic systems are hybrid electronic systems in disguise.

Hybrid Electronics

Hybrid electronics leverage the advantages of both conventional and printed electronics while avoiding many shortcomings of each[44]. They consist primarily of printed, electronic devices and interconnects, with necessary conventional components attached by various soldered or conductively adhered joints. A schematic of the fabrication of a hybrid electronic system is shown in Figure 2.1.

In wearable electronic applications, skin-like flexible electronic sensors can conform and interface to the skin better than conventional electronic devices to improve comfort and SNR[45? −48] while connecting to rigid silicon-based ICs for data processing and communications[49–51]. A similar approach can be used for environmental and remote sensing applications, where sensors and organic solar cells can scale to larger areas by being printed[52].
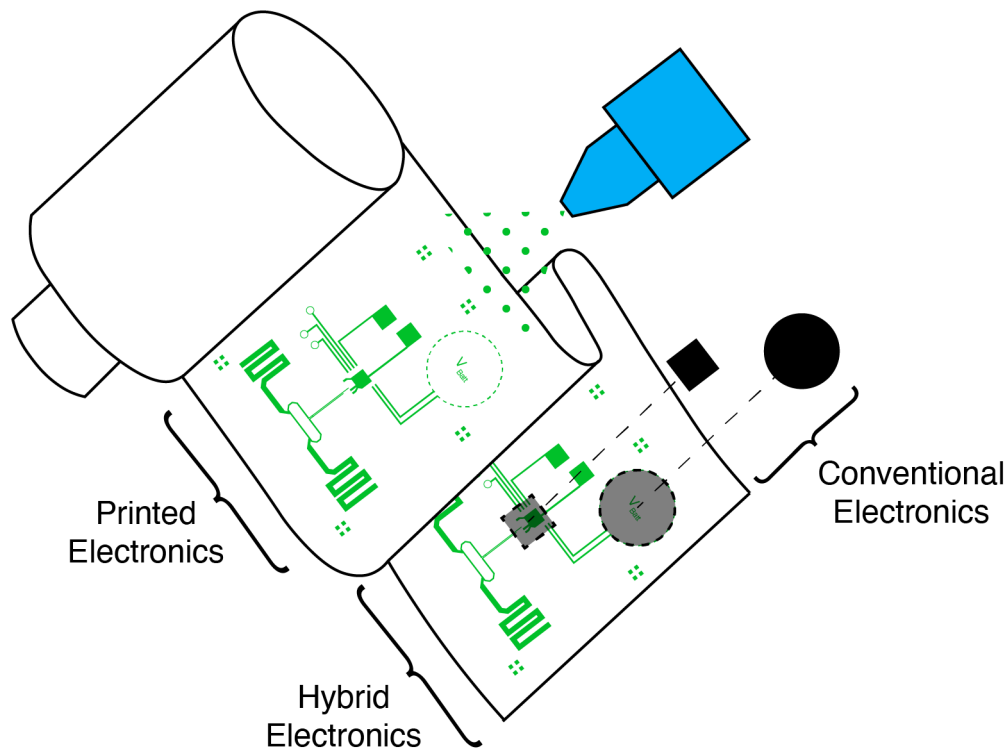
Figure 2.1: Hybrid electronics incorporate printed electronics with conventional electronics. Devices that require a large surface area, non-conventional materials, or flexibility are printed, and conventional electronic devices are attached to flexible electronic substrates for data processing and communications.

The remainder of this chapter will discuss printing in the context of printed and hybrid electronics. First, we will investigate the materials used in printed electronics and how they are used to make printed electronic devices. We will review the different printing methods used to fabricate or manufacture printed electronic device layers. Post-processing steps will be briefly explained. Finally, we present a step-by-step guide for designing a printed electronic device.

2.2   Printing Materials

.

Substrates

A substrate is the material that is being printed onto. Substrates determine the bulk mechanical properties of the device, which is a large part of why flexible films are most commonly chosen. Polymer films, for example, can be flexible and/or conformal, which can be leveraged in the design of manufacturing processes and used in various application spaces where physical flexibility is essential. In other areas where flexibility is not necessary or specific substrate material is required for additional features in a device, it is still possible to print onto rigid substrates.

Substrates play a prominent role in the quality of a printed feature. When a surface's surface energy is high, the printed ink will try to spread. When the surface energy is low, the ink will form islands or beads of ink. The material properties primarily determine the surface energy of a surface, though processing of the material can modify its surface energy[42;53;54].

Inks

The key ingredients of printed electronic devices are colloidal solutions called inks. Inks consist of at least a solvent and a particulate matter, often also include a binder, and sometimes include many other tuning components, such as lubricants, resins, surfactants, dyes, stabilizers, and other materials. These individual components modify the physical parameters of the ink to make it easier to print and/or to improve the performance of the printed component.

Conductors

Conductors are the base structural block of all electronic devices - printed or otherwise. They carry the power that powers the device, form the interconnections between device layers, and transmit data in an electric signal. In printed electronics, the conductor is either made from nanocomposite ink or organic polymers.

Nanocomposite inks are common conductors in printed electronics and are made up of conductive particles, polymer binders, a solvent, and sometimes other tuning components. The suspended conductive particles, when printed, form a percolated network within the non-conductive polymer binder, while the solvent evaporates away. Silver, carbon, and copper inks are the most popular choices of conductive particles for conductors, though other metals are sometimes used as well[55–58]. The selection of conductor and the particle:binder ratio can be altered to tune the conductivity of the printed feature. However, these changes affect other material properties of the composite as well.

Crystalline organic conducting materials - such as doped polyacetylene films - can be altered chemically to get desired electric and mechanical properties[59], and many have interesting optical properties as well. PEDOT:PSS (3, 4-polyethylene dioxythiopene-polystyrene sulfonic acid) has become a popular and well-researched conductive polymer because of its relatively-high conductivity (3 x 10^4 S/m) and transparency. This is far from the conductivity of other options (for example, silver has a conductivity of 6 x 10^7 S/m), though the ancillary benefits are worth the trade-off in many applications.

Semi-conductors

Semiconductor materials are vital components for active electronics and sensors. While inorganic semiconductors are used primarily in conventional electronics, organic semiconductors steal the spotlight in printed technologies. Compared to inorganic semiconductors such as silicon, organic semiconductors are attractive in printing because they are solution processable at ambient temperatures. Commonly used organic semiconductors such as regioregular poly(3-hexylthiophene) (P3HT), poly(triarylamine), poly(3,3-didodecyl quaterthiophene) (PQT), poly(2,5-bis(3-tetra-decyllthiophen-2-yl) and thieno[3,2-b]thiophene) (PBTTT) are chosen because of their desirable charge transport properties and mobility[60].

Dielectrics

Dielectrics are used in printed electronics to separate the layers of multilayered printed structures, act as the sensing element for some capacitive sensors, and/or encapsulate finished devices. Inorganic dielectrics used in conventional electronics (such as silica or alumina) are not easily printable, but other organic dielectrics can be printed easily. Poly(4-vinylphenol) (PVP), poly (methyl methacrylate) (PMMA), Polyethylene Terephthalate (PET), Polyimide (PI), Polyvinyl alcohol (PVA), and Polystyrene (PS) are common selections of dielectrics[61;62].

2.3 Printing Methods

.

There are many different methods of printing, each with its benefits and detriments. Figure 2.2 presents a selection of methods. Each of these printing methods will be discussed briefly here, and are the primary fabrication method of the devices discussed later in this dissertation work.
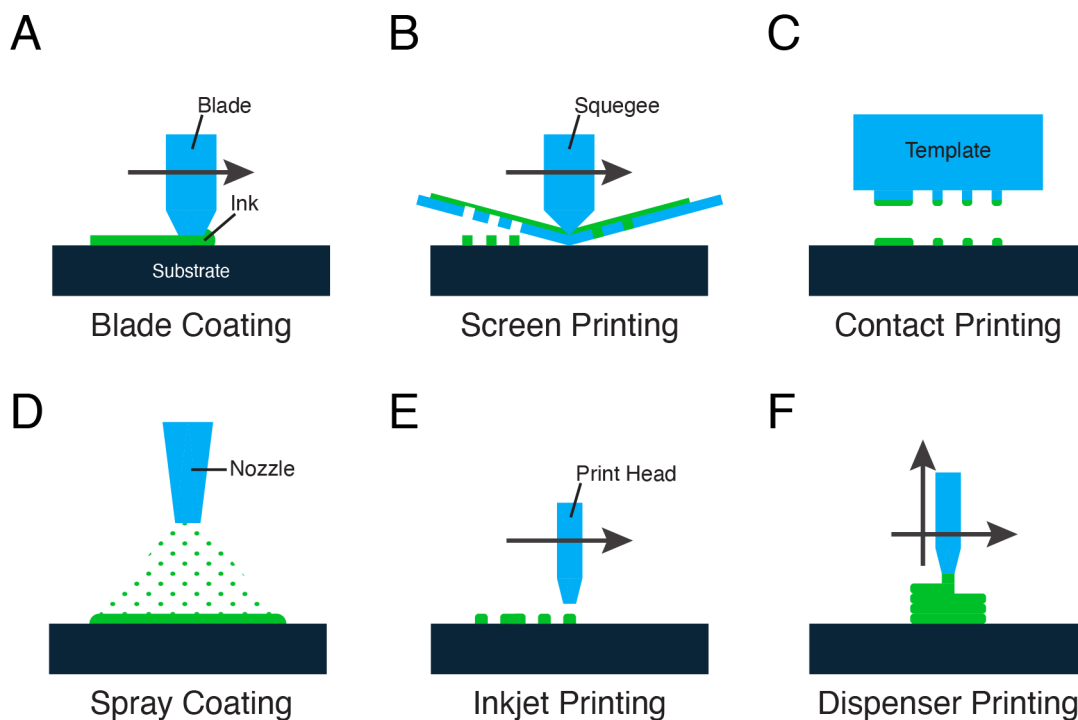
Figure 2.2: Schematic of several printing methods. A) Blade coating is a blanket deposition process where an angled blade sweeps ink across a substrate at a controlled thickness by tuning the print rate and the gap between the blade and the substrate. Using a stencil and/or surface treatment can be used to make patterned features. B) Screen printing is a patterned deposition process where ink is flooded across a patterned, emulsified mesh screen, and then pushed through the openings in the screen by a rubber-like squeegee. C) Contact printing is a patterned deposition process, and encompasses all methods where the solutions are deposited directly from one substrate to another, such as from a patterned roller or stamp. D) Spray coating is a blanket deposition process where a low-viscosity ink is aerosolized and ejected from a nozzle using controlled pressures. E) Inkjet printing is a patterned deposition process where an electrohydrodynamic jet delivers picoliter-volume drops-on-demand corresponding to pulses of a piezoelectric actuator. F) Dispenser printing is a patterned deposition process that pumps viscous inks or composite filaments through a tube attached to a multiaxis movable chassis.

Blade Coating

Blade coating (called 'doctor blade coating' by some) is a method that blanket deposits of a coat of ink with a well-controlled thickness. A schematic of this method is shown in Figure 2.2A. While blade coating is formally a blanket coating process, it is possible to obtain a patterned layer by incorporating a stencil. 'Stencil printing', as it is generally called, uses a stencil as a shadow mask, allowing it to pattern features with low resolution. If low viscosity inks are being used, it is also possible to improve the quality of a print by modification of the surface energy of the substrate[42].

Screen Printing

Screen printing is the most widely used printing method in the printed electronics industry[63], and a schematic of the process is shown in Figure 2.2B. An emulsified mesh screen with patterned and non-patterned areas is used as a template. Highly viscous inks (often called 'pastes' in this application because of their similar consistency to adhesive pastes) are spread across the screen, which is then lowered onto the substrate, and the ink is forcibly pushed through the openings in the mesh by a rubber-like squeegee. Because of the thixotropic properties of the highly viscous ink, the printed features very closely replicate the pattern of the screen.

Contact Printing

There are various forms of contact printing, and each utilizes some form of a template that's engraved with a pattern. The extruded parts of the pattern are dipped or coated with ink, which is then transferred to the substrate surface by the printing process. Figure 2.2C shows a schematic of the process using a pad or stamp as the printing template. The different contact printing methods (such as gravure, pad, flexographic, etc.) differ in their scalability, preferred ink viscosity, feature size, and scalability.

Spray Coating

Where blade coating is good for depositing viscous thick films, spray coating is a great choice for printing low viscosity solutions in a thin, blanketed layer. Figure 2.2D shows a schematic of spray coating. The ink is first turned into an aerosol of micron-scale droplets pneumatically or ultrasonically[63]. Then, an air stream is introduced, capturing some of these particles in its flow and flying through a nozzle

where a ring-shaped air sheath aerodynamically focuses them. The strength of the primary and sheathing flow allows the user to tune the deposition rate and area, down to a diameter of 5 μm.

Inkjet Printing

Inkjet printers are already widely used in offices, homes, and factories. However, in the field of printed electronics, instead of printing pigmented inks, inkjet printers print electroactive inks. Figure 2.2E shows the general process.

Inkjet printers usually utilize computer-aided design (CAD) software that allows a user to generate digital designs of the pattern that they want to print. The design is then processed by the computer and converted into a program that controls the motion of the print head, as well as delivers small electrical pulses when the print head passes over the patterned areas. These pulses actuate a small piezoelectric diaphragm in the print head, causing it to deliver picoliter-volume drops at the desired locations.

Dispenser Printing

Dispenser printing encompasses all printing techniques that employ a semi-continuous flow of ink through a nozzle or print head. A schematic of the process is shown in 2.2F. The composition of inks in dispenser printers can vary widely, from solvent-less fused deposition modeling (FDM) printers to binder-less direct ink writers (DIW), and everything in between. In any case, dispenser printing utilizes a nozzle mounted on a 2D- or 3D- chassis. Similar to inkjet printers, CAD is used to generate digital designs of the printed pattern, and the computer generates a program that controls the print head and the flow rate through the nozzle to create the desired pattern.

An exciting application of dispenser printing is the incorporation of electroactive particles in the polymer filaments used in FDM-type 3D printers[64–66]. In this method, the 'ink' is a solventless blend of 3D printing polymer and electroactive particles such as carbon black[64]. The polymer pellets are heated beyond their melting point and mixed with the particles before being extruded into a wire-shaped filament that is coiled and later used in the FDM 3D printer. The 3D printing process then remelts the wire by Joule heating of the nozzle and mechanical pushing the filament through the nozzle at a controlled rate while the chassis moves the nozzle to the desired location of the pattern.

DIW is a similar process to FDM printing with three distinct features. First, the ink of a DIW always includes a solvent to control the viscosity of the ink, though

sometimes the solvent is a gel-phase material such as PVDF[67]. Second, the material is physically pumped through the nozzle like squeezing ketchup through a bottle. Finally, the ink does not need to be heated in DIW, whereas the filament in FDM printing will only flow when brought past its glass transition temperature, and is generally brought close to or beyond the melting temperature of the polymer. These differences give some advantages to DIW. Because DIW can be performed at lower temperatures and the rheology can be tuned by changing the volume of solvent, a wider range of materials can be used[68;69].

2.4   Post-processing printed materials

After printing, there are several heat-treatment steps that may be required to complete the printed component layer. The most common of these are annealing, curing, and sintering.

Annealing is a heat-treatment process that is used to relieve the internal stresses of a material. Annealing is more commonly used for the heat-treatments of macro-scale metals, ceramic glasses, and high-performance polymers, though it is also applied to printed electronic components as well. A macro-scale example would be a cold-rolled steel billet annealed so that it can be worked further into final products. In printed electronics, annealing is more commonly used to reduce the internal stresses of the polymer binder or to reshape the crystallinity, such as PLA[70].

Curing is a process that accelerates a chemical reaction, and in the case of printed electronics, it almost always refers to the crosslinking of a thermoset polymer binder. Thermoset polymers that do not set in a reasonable time at room temperature are cured at higher temperatures (and sometimes lower pressure) in an oven or vacuum oven. The monomers react much more rapidly at the curing temperature, hardening it beyond what would otherwise be possible.

Sintering is a process for causing nano- or micro-scale particles to become a monolithic bulk material by diffusion. Sintering may occur in either or both of the solid and liquid states. Consider the extreme case of a composite of perfectly sphere-shaped particles in a polymer matrix. Regardless of the particle:polymer ratio, two perfect spheres can only contact one another at a single point. If these were the conductive particles in a printed conductor composite, then the resistance would be very high despite the inherent conductivity of the particles because the cross-sectional area would be infinitesimal. In sintering, the composite would be heated above the melting temperature of the conductive particles so that they diffuse into one another, increasing the cross-sectional surface area and improving particle-to-particle contact.

Because of the nature of nano- and micro-scale particles, the sintering temperature is often much less than the melting point of the macro-scale material.

2.5 Author's Guide to Designing a Printed Electronic Device

It can be very easy to get 'lost in the weeds' when first learning about different printing strategies. Here, we present a guide in an effort to make the selection less complicated. After deciding you want to leverage the many advantages of printing electronics discussed in Section 2.1, then it is recommended that one chooses the type of printing by considering the following list of steps and questions. Record the responses to each:

1. What is being made?
The obvious starting point to making anything is to know - at least vaguely - what it is that you want to make. The components of a transistor are different than those of a heating element. It may be helpful to first consider the conventional electronic analog of whatever it is that you want to make and list out the minimum-required components of that device.

2. What are the specifications of the device?
What are the outputs of the device, and how will you benchmark the device performance? For example, if you are making a sensor, you may specify a range of values that the sensor will be within 95% accuracy bounds. Or if you are making an antenna, you may determine the desired frequency band and operational amplitude.

3. What layers *must* be present for the device to work?
At a minimum, every printed electronic device must have a conductor layer. What other layers need to be present? For example, for printed displays, several layers of semiconductors and dielectrics need to be present. Draw a top and a side view of a simple version of your envisioned device to better record and visualize the target result, and label each layer in the stack.

4. Build a model.
From the recorded responses to steps 2 and 3, work backward to build a theoretical model for determining the parameters of each component in the device. This is the most difficult step and requires a good understanding of physical laws. The

complexity of the model can be simple or in-depth, but it is important to have something to work from.

For the remaining questions in this list, consider and record an answer *for each layer* in the printed device. The answers will be informed by the model.

5. What planar resolution is needed?

How crisp do the edges of your printed features need to be? Does the printed layer need to interface with conventional electronics, and if so, how do you plan on doing so? Do you need to be able to print features smaller than 100 μm?

6. What vertical resolution is needed?

With the horizontal resolution known, how thick of a printed layer is needed? For a printed conductor, for instance, the width, length, and thickness is related to the resistance of the conductor by:

$$R = \rho_e \frac{l}{wt} = R_s \frac{l}{w} \tag{2.1}$$

where ρ_e is the resistivity of the printed conductor composite, R_s is the sheet resistance, and the l, w, and t are the length, width, and thickness of the conductor, respectively. How might the vertical resolution affect the performance of other printed layers in the device?

7. How many devices are required?

Some printing methods are more easily scaled to produce higher volumes of devices with high repeatability, while others are better suited for prototyping small batches of printed electronic devices quickly and with minimal hassle.

8. Will you design the ink, or will you use a commercially-available ink?

The main reason for considering this question is to know whether or not the mechanical and electrical properties of the ink are variable or not.

If using a commercially-available ink, there is very little that can be done to tune the properties (safely). This is because the ingredients of these are trade-secret, and so unless given direct instruction from the ink manufacturer, it is not recommended to modify the ink in any way, as the addition of ancillary ingredients could cause unexpected or undesired results.

If, on the other hand, you are planning to design your own ink, then there are many more dials that can be tuned in the printing process. By designing your own ink, you can adjust the material ratios to change the rheological properties and improve the printability, or adjust the volume fraction of active material to adjust the

electrical performance. However, this requires a lot more work, so if the goal of the project is to make a device rather than to develop a new ink, then it is the author's recommendation to use commercially-available inks where possible.

9. Select a printing method.

After considering the above questions, you should have a good idea of what will be needed for each component in the printed device. With the recorded answers, refer to Table 2.1, which is a summary of the characteristics of the different printing methods discussed in this chapter, to determine what printing option is best for that component. Often, the fabrication of a printed device requires the application of multiple methods.

10. Plan fabrication and characterization steps.

Record a detailed list of each step in the fabrication process with printing and post-processing parameters. You may want to try a range of values at first or employ statistical strategies to investigate the effect of how different parameters affect different measurable properties of the printed device. Along that line of thinking, it is recommended that you plan characterization steps between each layer in the printed device, particularly for anything that influences the specifications laid out in Step 2.

11. Execute & Iterate.

Now that you have considered everything, you are ready to print. Execute the plan, and record your results. Characterize the device to test against the specifications laid out in Step 2. It is okay if some things don't work as planned! Design is an iterative process, and it is ultimately faster to fail early and often. Iterate through the steps in this list until the device that you make is within the specifications.

Table 2.1: Characteristics of select printing methods. Ink viscosity is reported as the range of dynamic viscosity within the range of the method's shear rate. The minimum feature resolution is of the planar dimension.

Method	Deposition Type	Shear Rate (s^{-1})	Ink Viscosity (cP)	Min. Resolution (μm)	Thickness	Scales?
Blade Coating	Blanket	1-20,000[42]	100-10,000[71]	N/A	μm	✓
Stencil Printing	Patterned	1-20,000[42]	1-10,000[42;53;71]	≈ 100[71]	μm	
Screen Printing	Patterned	≈ 100[72]	500-50,000[73]	20	μm	✓
Contact Printing	Patterned	Varies	1-5,000[38]	1-200[38]	nm-μm	✓
Spray Coating	Blanket	$\geq 10^4$[74]	1-150[75]	N/A	nm	✓
Inkjet Printing	Patterned	10^4-10^6	1-100[38]	15-100[38]	nm	
Dispenser Printing	Patterned	0.01-2000[76]	$1 - 10^6$[68;77]	10-200[68]	μm-cm	

2.6 Concluding Remarks

Printing is a disruptive technology that is a complete change in how electronics are made. However, considerable advances in printed and hybrid electronics are still needed to deliver on its market promises. Part of the problem is that printed electronics are always benchmarked against conventional silicon microelectronics in areas that favor silicon. This is erred thinking; Printed electronics should not compete against conventional electronics in areas such as charge mobility for printed semiconductors, the conversion efficiency of printed solar cells, or minimum feature dimension size. While researchers should strive to improve these areas, the future of printed electronics lies in its advantages over conventional electronics: large area, flexible, and low-cost manufacturing of electronics with high volumes and a wider variety of viable materials. These advantages open a new world of possibilities that would be unpractical to achieve with silicon alone.

Chapter 3

Artificial Intelligence & Machine Learning

Or maybe going through the wave equation.
An ancient engine offers no momentum,
About the power from an old vibration,
And nothing but a little bit of venom.

Surrounded by a sin Omega T,
On the other side of you and me.

– Hafez, an AI

3.1   What is Artificial Intelligence & Machine Learning?

Artificial Intelligence (AI) is the capability of a computer system to mimic human cognitive functions. Computer scientists commonly develop AIs to mimic how humans learn and solve problems. They do this by programming the computer system to use math and logic to simulate people's reasoning to learn and make decisions.

Machine Learning (ML) is a subcategory of AI. Specifically, it is the application of mathematical models to help a computer system improve - or 'learn'- without direct instruction. This enables a computer system to continue improving on its own based on its previous results or experiences.

AI is what an 'intelligent' computer system uses to behave and perform tasks like humans. ML is how a computer system builds its intelligence.

There are three primary strategies for building an ML program. These are supervised learning, unsupervised learning, and reinforcement learning.

Supervised learning has the defining characteristic of access to annotated training data[78]. Supervised learning algorithms induce models from the training data, which can then be applied to classify other unlabelled test data. A common analogy for supervised learning is that of a teacher teaching a student: the teacher trains a student with lots of practice problems, and then the student takes a test without the teacher's help.

If supervised learning is analogous to a classroom learning environment, then unsupervised learning is like throwing a child into the deep end of the pool to teach them how to swim. Unsupervised learning modes do *not* have access to labeled training data. Instead, unsupervised learning algorithms learn by clustering the data together in different ways, and trying to find patterns[78;79]. The child in the pool will learn that behavior where they tread their legs and wave their arms brings them closer to the surface.

Finally, reinforcement learning is akin to training a dog with treats. A dog will act however it wants, but they will learn that certain desired behaviors will result in a treat, such as returning to their handler when they shout 'come' or reclining onto their haunches when they call 'sit'. In a reinforcement learning program, the 'treat' is a numerical output[80]. In practice, a reinforcement learning program will perform a task by trial-and-error, the task result will be scored, and then the program will attempt the same task again with behavior similar to its highest-scored behavior in previous trials.

Regardless of the learning strategy, all machine learning algorithms (MLAs) follow a process flow similar to the one shown in Figure 3.1. A computer model is built and executed, the simulation results are scored by calculating an error term, and the error drives adjustment of the computer model parameters.

Why does all of this matter? First, computers can do simple input-output processes *much* faster than a human - about 10 million times faster[81]. The 'brain' of a computer does not get tired or distracted as a human's brain does, emotional influences don't cloud their findings, and they can be reprogrammed for different tasks practically instantaneously. For problems requiring many simple, repetitive calculations and objective tasks, computers have a clear advantage. Second, ML offers methods to optimize problems that were previously infeasible. With ML, one can model a problem based on simulation or experimental data, and then an MLA can solve the problem and be used as the basis for optimal design and/or control.

This chapter will focus on using ML to optimize models of physical systems. First,
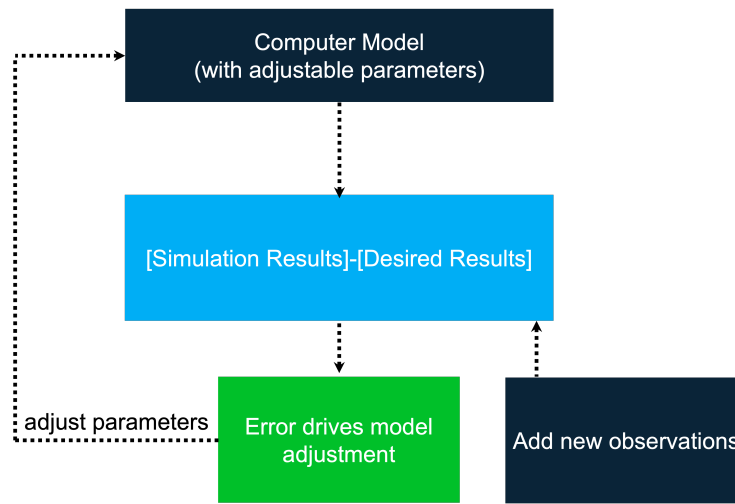
Figure 3.1: Schematic of the machine learning process for optimizing simulated systems.

we will discuss the principles of optimization. Next, we will explain how different MLA types minimize objective functions to reduce error and optimize these systems.

3.2 Principles of Optimization

Optimization is the process by which the best or most desirable outcome is reached. In the application of ML, optimization is done by changing the inputs of an objective function - a function that describes whatever it is that you are trying to optimize - to minimize or maximize it. The difference between the actual output and the desired output is the error, the magnitude of which may be used to manipulate the inputs of the function.

Objective Functions

Objective functions - also referred to here as 'cost functions' - are functions that return a scalar value used to determine the ranking or 'fitness' of whatever it is that you are trying to optimize. By convention, the fittest solution to a problem is the one that has the smallest objective function output, though some choose to set up objective functions such that maximizing the output yields the best results. In this

chapter, we will maintain the convention that minimization of the objective function optimizes a system to prevent confusion.

It is perhaps easiest to learn what objective functions are through examples. In the following sections, we will define the components of objective functions through real-world examples.

Consider if one were trying to minimize the cost of fencing materials to enclose a 400-acre rectangle for cattle ranching. Because fencing is priced per linear foot, one might want to minimize the total length of the perimeter. In this scenario, the 'objective' is to build a fence whose enclosed area is 400 acres at the lowest possible expense. In this specific case, the objective can be described mathematically as an objective function:

$$\Pi(L) = w_1 L \tag{3.1}$$

where Π is the objective we want to minimize (dollar-cost of building the fence), w_1 is a weighting factor (dollar-cost per linear foot of fence), and L is the length of the fence. As you may know, one way to find the minimum of a function is to take the function's derivative, set it equal to zero, and solve for the variables algebraically. Then, the solution to the objective function can be solved analytically. For simplicity, in this example, we assume that the 400-acre enclosed area is rectangular, with side lengths x and y.

$$L = 2(x + y)$$
$$A = x \cdot y$$
$$y = \frac{A}{x}$$
$$\Pi = w_1 L = 2w_1(x + \frac{A}{x})$$
$$\Pi_{Min} = \nabla\Pi \to 0$$
$$\nabla\Pi = \frac{\partial}{\partial x} 2w_1(x + \frac{A}{x}) = 0$$
$$2w_1(1 + \frac{A}{x^2}) = 0 \to x = \sqrt{(A)}$$
$$y = \frac{A}{x} = \sqrt{(A)}$$
$$L = 2(x + y) = 2 \cdot A$$
$$\Pi = 2w_1 A$$
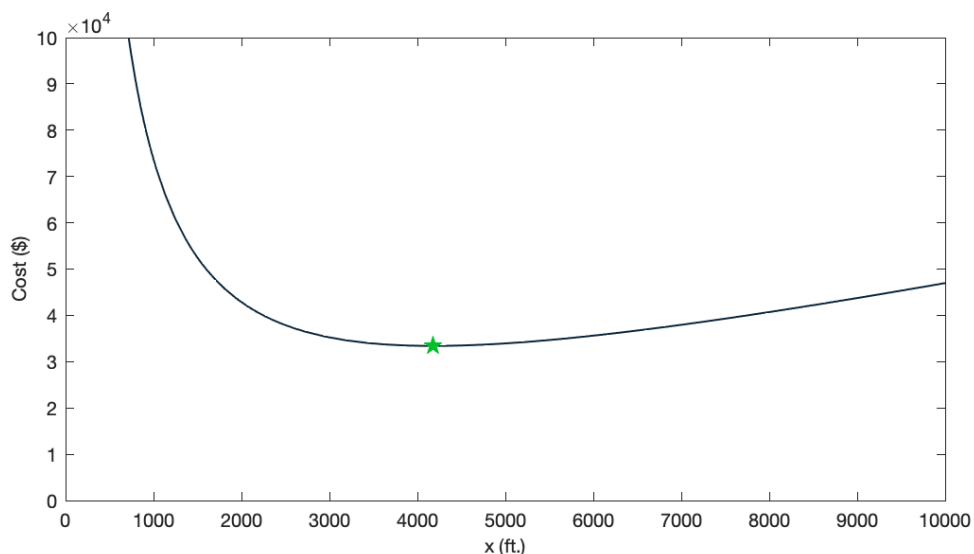
Figure 3.2: The cost of fencing material to enclose a 400-foot area as a function of the side-length, x. A minimum value of \$33,390 is reached at $x = 4173.73$ ft.

Assuming a cost of \$2 per linear foot of fencing, $w_1 = 2$, the cost function Π is plotted as a function of the length of one of the sides of the rectangular area, x, in Figure 3.2.

While a single-variable cost function like this example is relatively easy to solve, it can quickly become more complex as more variables and conditions are introduced. Let's consider again trying to minimize the cost of fencing materials to enclose a 400-acre ranch. However, one of the sides of the rectangle is next to a road and requires special fencing material valued at \$5 per foot. Now the cost function would become:

$$\Pi = 2w_1x + w_1y + w_2y$$
$$= w_1\left(2x + \frac{A_d}{x}\right) + w_2\frac{A_d}{x}$$

This cost function can still be solved analytically, though it will be more diffi-cult. What if, however, we were to find that because of a limitation in the fencing equipment, it will cost an extra \$0.01 every 100 feet that fencing material is placed

away from the road? Or, what if we were to find a pond in the way of our fencing path that will require the fencing to make a path around it?

In the fencing example, the cost function minimized a single design variable - the dollar cost of fencing. However, it should not be confused that cost functions necessarily minimize a dollar cost, nor should it be confused that all cost functions have a single objective of the cost function. Many cost functions will maximize, minimize, and tune multiple design variables simultaneously, and the weighting term, w adjusts the degree of importance of each design variable. The larger the value of a weighting term is compared to the other weighting terms, the greater the influence that design variable will have on the cost function.

Consider now a scientist is trying to optimize the traits of a new apple species. This cost function may include several related and unrelated factors to optimize for. They may want to maximize the size of the apple, sweetness, yield, climate resilience, and disease resistance. Conversely, it would be beneficial to minimize the fertilizer use, number of seeds, etc. These different goals or targets are called design variables. We then define $\mathbf{\Lambda}$, a vector of N design variables such that:

$$\Pi(\mathbf{\Lambda}) = \Pi\{\Lambda_1, ..., \Lambda_N\} \tag{3.2}$$

Each of these design variables Λ_i may be written such that its contribution to the overall cost function is minimized when the design variable is maximized, minimized, approaches the desired value, or fits within a zone of acceptable values. Consider our apple genetics example from before. Using the yield of apples as a design variable, to minimize the value of the cost function as the yield increases, we can define the design variable as so:

$$\Lambda_{yield} = \frac{w_{yield}}{N_{Apples}} \tag{3.3}$$

Thus, as the number of apples increases, the value of Λ_{yield} would decrease, thereby minimizing $\Pi(\mathbf{\Lambda})$. Consider a design variable we would want to minimize, such as the average volume of fertilizer needed to keep an apple tree healthy. A viable design variable term for this would be:

$$\Lambda_{fertilizer} = w_{fertilizer}V_{fertilizer} \tag{3.4}$$

In this case, $\Lambda_{fertilizer}$ decreases as the volume decreases, thereby minimizing $\Pi(\mathbf{\Lambda})$. Another design variable term we can use in an objective function is to tune a variable to a predetermined value. Continuing with our apple genetics example, one might want to tune the size of an apple to be large, but not so large as to not fit into an average person's hand. In this case, let's assume that after some market research

and user studies, the team in charge of designing this new breed of apple has decided that the perfect apple has a radius of 10 cm. We can then write the design variable Λ_{size} as:

$$\Lambda_{size} = w_{size} \frac{||r_{actual} - r_{desired}||}{||r_{desired}||} \tag{3.5}$$

In this example, we are normalizing the magnitude of the difference between the actual and the desired size values to ensure a positive value.

A final consideration is the inclusion of step-wise, active-inactive constraints that 'turn on' when the design variable is above and/or below threshold values. These design variables constrain the solution to a zone of interest by having a variable weighting term. For example, it would be desirable to have the apples fully ripen sometime in October because of the availability of fruit pickers and to take advantage of the autumn orchard tourists. In this case, we can write a term for the design variable as:

$$\Lambda_{harvest} = \hat{w}_{harvest} \frac{||t_{harvest} - TOL_{harvest}||}{||TOL_{harvest}||} \tag{3.6}$$

where:

$$\hat{w}_{harvest} = \begin{cases} 0 & \text{for } -TOL_{harvest} \leq t_{harvest} \leq TOL_{harvest} \\ w_{harvest} & \text{otherwise} \end{cases} \tag{3.7}$$

and $TOL_{harvest}$ is the 'tolerance', i.e. the acceptable range of the zone. In this case, as soon as $t_{harvest}$ falls outside of the acceptable range, $\Lambda_{harvest}$ will have a step-wise increase from 0 to the weighted value of the term.

Finding the Minimum of Objective Functions

Now that we have a defined objective function - which could be the summation of several competing objectives, as shown above - how does one find the minimum of this function? For the fence building example in Figure 3.2, we are only solving for the solution to a single univariate problem, so the derivative search method is viable. But what if the problem we were trying to solve was multivariate? Or, what if our source data is prone to error? What if the problem is nonlinear? What if there *aren't* and clear solutions to the problem? What if there are *multiple* clear answers? In many real-world physical systems, any of these scenarios may be the case.

The following sections will discuss different MLAs to optimize such systems.

3.3 Brute Force Methods

Before discussing the different MLAs that may be used to optimize a problem, we wanted to quickly discuss the alternative: Brute Force Methods (BFMs).

Theory

Where MLAs find trends to inform their learning, BFMs don't attempt to learn a system. Instead, BFMs look at every possible solution to a problem and pick the best one. Considering 3.1, it would be as though the 'add new observations' and 'error drives model adjustment' blocks were removed, with the computer model parameters being adjusted incrementally rather than informed by the results of previous iterations.

Still, BFMs can be useful for problems of limited scale or complexity, so we will discuss the theory here.

Given a number of adjustable parameters, $\Lambda \overset{\text{def}}{=} \{\Lambda_1, \Lambda_2, \Lambda_3, \ldots, \Lambda_N\}$, bound each parameter with a maximum and minimum possible value:

$$\Lambda_1^{(-)} \leq \Lambda_1 \leq \Lambda_1^{(+)},$$
$$\Lambda_2^{(-)} \leq \Lambda_2 \leq \Lambda_2^{(+)},$$
$$\Lambda_3^{(-)} \leq \Lambda_3 \leq \Lambda_3^{(+)},$$
$$\ldots$$
$$\Lambda_N^{(-)} \leq \Lambda_N \leq \Lambda_N^{(+)}$$

These upper and lower limits should generally be dictated by what is physically feasible. Next, define an increment that each parameter will 'step' through to test for an optimal solution, $\Delta\Lambda_i = constant$. Then, the solution for every possible permutation of parameters must be computed and scored:

$$\Pi(\Lambda) = \begin{pmatrix} \Lambda_1^{(-)} : \Delta\Lambda_1 : \Lambda_1^{(+)} \\ \Lambda_2^{(-)} : \Delta\Lambda_2 : \Lambda_2^{(+)} \\ \Lambda_3^{(-)} : \Delta\Lambda_3 : \Lambda_3^{(+)} \\ \vdots \\ \Lambda_N^{(-)} : \Delta\Lambda_N : \Lambda_N^{(+)} \end{pmatrix} \tag{3.8}$$

Limitations of Brute Force Methods

The reason that BFMs aren't used for all problems is related to their computational expense. For many real-world problems, the time complexity of BFMs is often greater than $O(N!)$. This is *much* slower than MLAs in most cases. Finally, BFMs rely on the computing power of the devices they are executed on rather than smart algorithm design.

3.4 Gradient-based Methods

For many optimization problems, gradient-based methods are a simple and efficient way to quickly obtain a local minimum of an objective function.

Theory

This approach generally starts by postulating initial guesses for values of the function constants. The method includes a means for altering the constants to get a better fit. The process is repeated until the fit has acceptable accuracy. In such procedures, to obtain a new directional step for $\mathbf{\Lambda}$, one must solve the following system:

$$[\mathbf{I\!H}]\{\Delta\mathbf{\Lambda}\} = -\{\boldsymbol{g}\}, \tag{3.9}$$

where $[\mathbf{I\!H}]$ is the Hessian matrix $(N \times N)$, $\{\Delta\mathbf{\Lambda}\}$ is the parameter increment $(N \times 1)$, and $\{\boldsymbol{g}\}$ is the gradient $(N \times 1)$. This is determined by forcing the gradient of $\nabla_{\mathbf{\Lambda}}\Pi(\mathbf{\Lambda}) = \mathbf{0}$. Expanding (linearizing) around a first guess $\mathbf{\Lambda}^i$ yields:

$$\nabla_{\mathbf{\Lambda}}\Pi(\mathbf{\Lambda}^{i+1}) \approx \nabla_{\mathbf{\Lambda}}\Pi(\mathbf{\Lambda}^i) + \nabla\left(\nabla_{\mathbf{\Lambda}}\Pi(\mathbf{\Lambda}^i)\right) \cdot (\mathbf{\Lambda}^{i+1} - \mathbf{\Lambda}^i) + higher\ order\ terms \approx \mathbf{0} \tag{3.10}$$

or, in more streamlined matrix notation, defining the Hessian, $[\mathbf{I\!H}] = \nabla\left(\nabla_{\mathbf{\Lambda}}\Pi(\mathbf{\Lambda})\right)$ and $\{\boldsymbol{g}\} = \nabla_{\mathbf{\Lambda}}\Pi(\mathbf{\Lambda})$, then

$$[\mathbf{I\!H}]\{\Delta\mathbf{\Lambda}\} + \{\boldsymbol{g}\} = \mathbf{0}. \tag{3.11}$$

Following a standard Newton-type multivariate search, a new design increment is computed,

$$\Delta = (\Delta\Lambda_1, \Delta\Lambda_2, ...\Delta\Lambda_N), \tag{3.12}$$

for a design vector, $\mathbf{\Lambda}$, by solving the following system, $[\mathbf{H}]\{\Delta\mathbf{\Lambda}\} = -\{\mathbf{g}\}$, where $[\mathbf{H}]$ is the $(N \times N)$ Hessian matrix, with components:

$$H_{ij} = \frac{\partial^2 \Pi(\mathbf{\Lambda})}{\partial \Lambda_i \partial \Lambda_j}, \tag{3.13}$$

$\{\mathbf{g}\}$ is the $(N \times 1)$ gradient, with components:

$$g_i = \frac{\partial \Pi(\mathbf{\Lambda})}{\partial \Lambda_i} \tag{3.14}$$

and where $\{\Delta\mathbf{\Lambda}\}$ is the $(N \times 1)$ design increment with components $\Delta\Lambda_i$.

After the design increment has been solved for, one then forms an updated design vector, $\mathbf{\Lambda}^{new} = \mathbf{\Lambda}^{old} + \Delta\mathbf{\Lambda}$, and the process is repeated until $||\Pi|| \leq TOL$, where TOL is the tolerance.

Explicitly, the incremental system is:

$$
\begin{bmatrix}
\frac{\partial^2 \Pi(\Lambda)}{\partial \Lambda_1 \partial \Lambda_1} & \frac{\partial^2 \Pi(\Lambda)}{\partial \Lambda_1 \partial \Lambda_2} & \frac{\partial^2 \Pi(\Lambda)}{\partial \Lambda_1 \partial \Lambda_3} & \frac{\partial^2 \Pi(\Lambda)}{\partial \Lambda_1 \partial \Lambda_4} & \cdots \\
\frac{\partial^2 \Pi(\Lambda)}{\partial \Lambda_2 \partial \Lambda_1} & \frac{\partial^2 \Pi(\Lambda)}{\partial \Lambda_2 \partial \Lambda_2} & \frac{\partial^2 \Pi(\Lambda)}{\partial \Lambda_2 \partial \Lambda_3} & \frac{\partial^2 \Pi(\Lambda)}{\partial \Lambda_2 \partial \Lambda_4} & \cdots \\
\frac{\partial^2 \Pi(\Lambda)}{\partial \Lambda_3 \partial \Lambda_1} & \frac{\partial^2 \Pi(\Lambda)}{\partial \Lambda_3 \partial \Lambda_2} & \frac{\partial^2 \Pi(\Lambda)}{\partial \Lambda_3 \partial \Lambda_3} & \frac{\partial^2 \Pi(\Lambda)}{\partial \Lambda_3 \partial \Lambda_4} & \cdots \\
\frac{\partial^2 \Pi(\Lambda)}{\partial \Lambda_4 \partial \Lambda_1} & \frac{\partial^2 \Pi(\Lambda)}{\partial \Lambda_4 \partial \Lambda_2} & \frac{\partial^2 \Pi(\Lambda)}{\partial \Lambda_4 \partial \Lambda_3} & \frac{\partial^2 \Pi(\Lambda)}{\partial \Lambda_4 \partial \Lambda_4} & \cdots \\
\cdots & \cdots & \cdots & \cdots & \cdots \\
\cdots & \cdots & \cdots & \cdots & \cdots \\
\frac{\partial^2 \Pi(\Lambda)}{\partial \Lambda_N \partial \Lambda_1} & \frac{\partial^2 \Pi(\Lambda)}{\partial \Lambda_N \partial \Lambda_2} & \frac{\partial^2 \Pi(\Lambda)}{\partial \Lambda_N \partial \Lambda_3} & \frac{\partial^2 \Pi(\Lambda)}{\partial \Lambda_N \partial \Lambda_4} & \cdots
\end{bmatrix}
\begin{Bmatrix}
\Delta\Lambda_1 \\ \Delta\Lambda_2 \\ \Delta\Lambda_3 \\ \Delta\Lambda_4 \\ \cdots \\ \cdots \\ \Delta\Lambda_N
\end{Bmatrix}
= -
\begin{Bmatrix}
\frac{\partial \Pi(\Lambda)}{\partial \Lambda_1} \\ \frac{\partial \Pi(\Lambda)}{\partial \Lambda_2} \\ \frac{\partial \Pi(\Lambda)}{\partial \Lambda_3} \\ \frac{\partial \Pi(\Lambda)}{\partial \Lambda_4} \\ \cdots \\ \cdots \\ \frac{\partial \Pi(\Lambda)}{\partial \Lambda_N}
\end{Bmatrix}. \tag{3.15}
$$

The derivatives must often be computed numerically:

- For the first derivative of Π at $(\Lambda_1, \Lambda_2, \Lambda_3)$:

$$\frac{\partial \Pi}{\partial \Lambda_1} \approx \frac{\Pi(\Lambda_1 + \Delta\Lambda_1, \Lambda_2, \Lambda_3) - \Pi(\Lambda_1 - \Delta\Lambda_1, \Lambda_2, \Lambda_3)}{2\Delta\Lambda_1} \tag{3.16}$$

- For the second derivative at $(\Lambda_1, \Lambda_2, \Lambda_3)$:

$$
\begin{aligned}
\frac{\partial}{\partial \Lambda_1}\left(\frac{\partial \Pi}{\partial \Lambda_1}\right) &\approx \frac{\left(\frac{\partial \Pi}{\partial \Lambda_1}\right)\big|_{\Lambda_1 + \frac{\Delta\Lambda_1}{2}, \Lambda_2, \Lambda_3} - \left(\frac{\partial \Pi}{\partial \Lambda_1}\right)\big|_{\Lambda_1 - \frac{\Delta\Lambda_1}{2}, \Lambda_2, \Lambda_3}}{\Delta\Lambda_1} \\
&= \frac{1}{\Delta\Lambda_1}\left(\left(\frac{\Pi(\Lambda_1 + \Delta\Lambda_1), \Lambda_2, \Lambda_3 - \Pi(\Lambda_1, \Lambda_2, \Lambda_3)}{\Delta\Lambda_1}\right)\right. \\
&\quad - \left.\left(\frac{\Pi(\Lambda_1, \Lambda_2, \Lambda_3) - \Pi(\Lambda_1 - \Delta\Lambda_1, \Lambda_2, \Lambda_3)}{\Delta\Lambda_1}\right)\right).
\end{aligned} \tag{3.17}
$$

- For the cross-derivative at (Λ_1, Λ_2):

$$
\begin{aligned}
\frac{\partial}{\partial \Lambda_2}\left(\frac{\partial \Pi}{\partial \Lambda_1}\right) \quad &\approx \quad \frac{\partial}{\partial \Lambda_2}\left(\frac{\Pi(\Lambda_1 + \Delta\Lambda_1, \Lambda_2, \Lambda_3) - \Pi(\Lambda_1 - \Delta\Lambda_1, \Lambda_2, \Lambda_3)}{2\Delta\Lambda_1}\right) \\
&\approx \quad \frac{1}{4\Delta\Lambda_1 \Delta\Lambda_2}\left(\Pi(\Lambda_1 + \Delta\Lambda_1, \Lambda_2 + \Delta\Lambda_2, \Lambda_3) - \Pi(\Lambda_1 - \Delta\Lambda_1, \Lambda_2 + \Delta\Lambda_2, \Lambda_3)\right) \\
&- \quad \left(\Pi(\Lambda_1 + \Delta\Lambda_1, \Lambda_2 - \Delta\Lambda_2, \Lambda_3) - \Pi(\Lambda_1 - \Delta\Lambda_1, \Lambda_2 - \Delta\Lambda_2, \Lambda_3)\right). \quad (3.18)
\end{aligned}
$$

Limitations of Gradient-based Methods

One can apply a gradient-based method if the objective function is sufficiently smooth in that region of the parameter space. Unfortunately, objective functions are often nonconvex in design parameter space and nonsmooth due to the variety of design variables. For example, if there are active-inactive constraints in the cost function, it is likely that the function is non-differentiable (non-continuous) across the domain. Finally, sample size effects can induce stochastic behavior in the objective function.

Furthermore, gradient-based methods can converge on incorrect answers if there are several local minimums and the initial guess is poor. In these, cases, the algorithm may converge on a local minimum instead of a global minimum. Consider for example the two following equations, which are plotted in Figure 3.3 in the range $-20 \le x \le 20$:

$$\Pi_A = x^2 \tag{3.19}$$

$$\Pi_B = x + \frac{\pi}{2}sin(x) \tag{3.20}$$

In both cases, the global minimum of the equation is at $x = 0$. In Figure 3.4, we apply a gradient-based method to both equations and plot the solution that the algorithm converges on for $x_0 = 0.2$, 2, and 20. For Π_A, the algorithm will converge on the global minimum regardless of the initial guess for $x = x_0$, as shown in Figure 3.4A-C. However, for Π_B, the algorithm will converge to the nearest local minima, meaning it obtains different solutions depending on the initial guess for $x = x_0$. Only when the initial guess is sufficiently close to the global minimum will the algorithm yield the desired solution, such as in Figure 3.4D.

As you can see, there are plenty of cases where minimizing a cost function is difficult with the direct application of gradient methods. This motivates non-derivative search methods found in other types of MLAs.
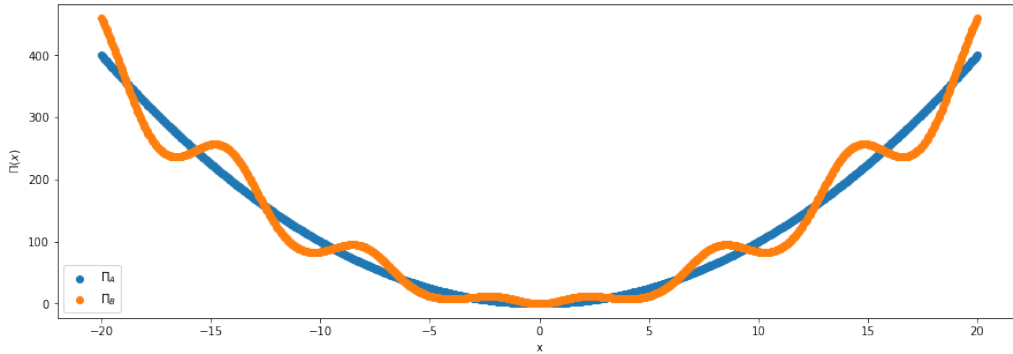
Figure 3.3: Plot of Equations 3.19 and 3.20. Each is a univariate equation with a global minimum at $x = 0$, while Equation 3.20 has multiple local minima.
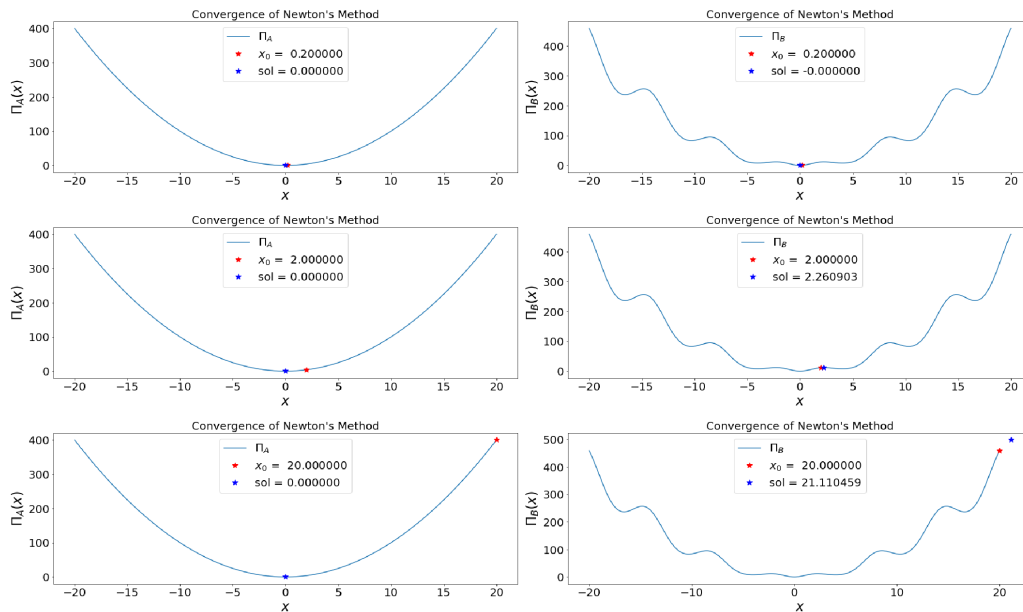
Figure 3.4: Examples of using Newton's Method to find local minima. The plots on the left show the solution to the equation $\Pi_A = x^2$, while the plots on the right show the solution to the equation $\Pi_B = x + \frac{\pi}{2}sin(x)$. In all plots, the red marker indicates the initial guess, and the blue marker indicates the solution. For Pi_A, Newton's method consistently found the global minimum. For the plots on the right, the initial guess can result in different solutions.

3.5   Genetic Algorithms

Theory

One of the most basic subset of MLA's are Genetic Algorithms (GAs)[82–85]. Genetic algorithms are extremely useful for multivariate system optimization where gradient methods are not preferred due to the nonconvex, nonsmooth nature of the system[86–88]. The rapid rate at which the simulations can be completed enables the ability to explore inverse problems seeking to determine what parameter combinations can deliver the desired result[89–92].

GAs earn their name because they mimic the process by which evolution causes different lifeforms to develop traits; They reflect the aspects of natural selection where the fittest individuals are selected to procreate. Individuals with the best traits are more likely to survive long enough to reach sexual maturity. Upon mating with another individual whose traits have allowed them to survive to sexual maturity, the two parents create a child whose traits are somewhere between those of the parents. In the case of a GA, the 'individuals' are replaced with 'design strings'. A design string is a possible combination of parameters (which replace the 'genetic traits' in this analogy). Just as only the fittest of individuals can pass on their genetic traits, only the fittest design strings (whose fitness is determined by the objective function) are 'mated' with other high-ranking design strings to generate 'child strings', which are design strings whose parameters are somewhere between those of the 'parent strings'.

While each GA is tailored to its use case, broadly speaking, they involve the following essential concepts:

1. **Population Generation:** Generate a population of genetic strings: $\mathbf{\Lambda}^i$

2. **Performance Evaluation:** Compute performance of each genetic string: $\Pi\left(\mathbf{\Lambda}^i\right)$

3. **Rank Genetic Strings:** Rank the strings: $\mathbf{\Lambda}^i, i = 1, \ldots, N$

4. **Mate and/or mutate strings:** Mate pairs to produce offspring. Optionally, include the possibility of randomly 'mutating' a gene.

5. **Gene Elimination:** Remove poorly performing genetic strings from the gene pool

6. **Population Regeneration:** Repeat steps 2-5 with the updated gene pool and new random genetic strings until $\Pi(\Lambda_{min} < TOL)$

7. **Solution Post-Processing:** Optionally, apply a gradient-based method after reaching a small enough tolerance to find the true, global minimum within the local solution valley - *if the objective function is smooth enough*

Per convention, we define the objective function as a multivariate problem to be minimized:

$$\Pi(\mathbf{\Lambda}) = \Pi\{\Lambda_1, \Lambda_2, \Lambda_3, \dots, \Lambda_N\} \tag{3.21}$$

In a GA, we systematically minimize Equation 3.21, $\min_\Lambda \Pi$, by varying the design parameters: $\Lambda^i \stackrel{\text{def}}{=} \{\Lambda_1^i, \Lambda_2^i, \Lambda_3^i, \dots, \Lambda_N^i\}$. Similar to a BFM, the system parameter search is conducted within constrained ranges of each parameter:

$$\Lambda_1^{(-)} \leq \Lambda_1 \leq \Lambda_1^{(+)},$$
$$\Lambda_2^{(-)} \leq \Lambda_2 \leq \Lambda_2^{(+)},$$
$$\Lambda_3^{(-)} \leq \Lambda_3 \leq \Lambda_3^{(+)},$$
$$\dots$$
$$\Lambda_N^{(-)} \leq \Lambda_N \leq \Lambda_N^{(+)}$$

Just like the BFM, these upper and lower limits should generally be dictated by what is physically feasible. However, where a BFM steps through the parameter space with a defined increment for each parameter, $\Delta\Lambda_i$, GAs tackle the problem with a considerable amount more finesse; GAs sweep the domain of possible design values rather than selecting discrete increments to test for solutions. This also has an advantage over gradient-based methods, which begin with an initial guess for the parameters, making this strategy susceptible to becoming 'trapped' in local minima. These two advantages make GAs well-suited for nonconvex, nonsmooth, multivariate, and/or multistage systems.

To generate a population of S starting genetic strings, the design string parameters are first generated randomly within the range of permitted values:

$$\mathbf{\Lambda}^i, (i = 1, 2, 3, \dots, S)$$
$$\mathbf{\Lambda}^i \stackrel{\text{def}}{=} \left\{\Lambda_1^i, \Lambda_2^i, \Lambda_3^i, \Lambda_4^i, \dots, \Lambda_N^i\right\}$$

where:

$$\underline{\Lambda}^{(i)} = \begin{pmatrix} \Lambda_1^- \leq \Lambda_1^{(i)} \leq \Lambda_1^+ \\ \Lambda_2^- \leq \Lambda_2^{(i)} \leq \Lambda_2^+ \\ \Lambda_3^- \leq \Lambda_3^{(i)} \leq \Lambda_3^+ \\ \Lambda_4^- \leq \Lambda_4^{(i)} \leq \Lambda_4^+ \\ \ldots \\ \Lambda_N^- \leq \Lambda_N^{(i)} \leq \Lambda_N^+ \end{pmatrix}$$

After all design strings have been generated, their performance is calculated by calculating the output of the cost function when the parameters of the design string are the inputs: $\Pi\left(\boldsymbol{\Lambda}^i\right), (i = 1, \ldots, S)$. The strings then need to be ranked in increasing order: $\boldsymbol{\Lambda}^i, (i = 1, \ldots, S)$, such that $\Pi(\Lambda^1) \leq \Pi(\Lambda^2) \leq \ldots \leq \Pi(\Lambda^S)$

Then, beginning with the best-performing pairs, mate the nearest pairs and produce two offspring:

$$\boldsymbol{\lambda}^i \stackrel{\text{def}}{=} \phi_i \cdot \boldsymbol{\Lambda}^i + (1 - \phi_i) \cdot \boldsymbol{\Lambda}^{i+1}$$
$$\boldsymbol{\lambda}^{i+1} \stackrel{\text{def}}{=} \hat{\phi}_i \cdot \boldsymbol{\Lambda}^i + \left(1 - \hat{\phi}_i\right) \cdot \boldsymbol{\Lambda}^{i+1},$$

where ϕ_i and $\hat{\phi}_i$ are random numbers such that $0 \leq \phi_i \leq 1$ and $0 \leq \hat{\phi}_i \leq 1$, and $\phi_i, \hat{\phi}_i$ are different for each component of each genetic string. Thus, each child string can be defined as:

$$\boldsymbol{\lambda}^i = \begin{pmatrix} \Lambda_1^{pi}\phi_1 + \Lambda_1^{p(i+1)}(1 - \phi_1) \\ \Lambda_2^{pi}\phi_2 + \Lambda_2^{p(i+1)}(1 - \phi_2) \\ \ldots \\ \ldots \\ \ldots \\ \ldots \\ \ldots \\ \ldots \\ \ldots \\ \Lambda_N^{pi}\phi_N + \Lambda_N^{p(i+1)}(1 - \phi_N) \end{pmatrix} \tag{3.22}$$

where $\phi_i \in \text{rand}[0,1]$.

After the children have been generated, the worst performing strings need to be eliminated. Eliminate the bottom $M < S$ strings, and keep the top $K < N$ parents and top K offspring (K offspring $+K$ parents $+M = S$)

Figure 3.5: Cost function evolution for a genetic algorithm where the parents are retained each generation. The value of the best-performing design string is monotonically decreasing, and the average cost of the parent design strings is close to the best-performing string, while the average cost of all design strings is several orders of magnitude higher and not monotonically decreasing.

If one does not retain the parents in the algorithm above, inferior performing offspring may replace superior parents. Thus, top parents should be kept for the next generation. This guarantees a monotone reduction in the cost function. Furthermore, retained parents need not be re-evaluated, making the algorithm less computationally less expensive since these parameter sets do not have to be reevaluated (or ranked) in the subsequent generations. Numerous studies have shown that the advantages of parent retention outweigh inbreeding for sufficiently large population sizes [86–92]. Figure 3.5 shows the evolution of the cost function result of an arbitrary genetic algorithm.

The process is repeated with top gene pool (K offspring and K parents), plus M new, randomly generated strings. Optionally, one could set the GA to rescale the range of parameters to restart the search around the best performing parameter set every few generations, which could speed up the solution time, but risks missing the global minimum if the algorithm if this update occurs too early in the execution.

As the GA iterates through time, the best-performing string will get closer and closer to the global minimum. The basic action of a GA is shown schematically in
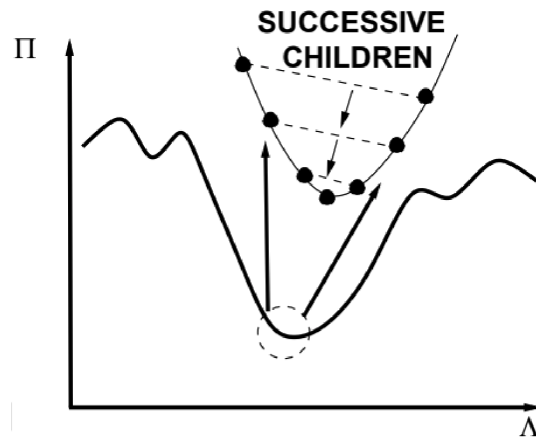
Figure 3.6: The basic action of a genetic algorithm. Throughout multiple generations, high-performing strings are matched with other high-performing strings to make a children string whose parameters are between those of their parents.

Figure 3.6.

Limitations of Genetic Algorithms

While GAs excel at quickly scanning the design space to isolate multiple local minima, they are comparatively slow in converging to find the absolute minima for the location by the nature of resource allocation in generating new random strings. As the computation time increases, the likelihood that a random string outperforms all other strings in the population is increasingly unlikely. Using a GA for an initial search before refining the search using Newton's method is a 'best-of-both-worlds' approach to highly multivariate problems.

3.6 Artificial Neural Networks

Artificial Neural Networks (ANNs) are input-output type models like the other MLAs. However, there are some fundamental differences between ANNs and other MLAs.

Theory

ANNs are essentially adaptive nonlinear regressions of the form:

$$Output = \mathcal{F}\left(Input, w_1, w_2, ..., w_n, b_1, b_2, ..., b_m\right) \tag{3.23}$$

where $\mathcal{F}$ is the ANN. ANNs are named such because, when drawn schematically, are biomimetic of the complex, bioelectrochemical neural networks that make up the brains of creatures in the animal kingdom. As such, the structures in a neural network are likewise named after the parts of an animal brain. These are:

- **Synapses**: Multiply inputs by weights representing the input's relevance to the desired output.

- **Neurons**: Add the outputs of all connected synapses and apply an activation function.

It is difficult to describe the purpose of an activation function without first understanding the architecture of neural networks and how they work. Figure 3.7 is a schematic of a neural network. Figure 3.7A shows the overall architecture of an arbitrarily-shaped neural network, while Figure 3.7B shows the architecture of a single neuron and its connected synapses.

From Figure 3.7A, we see that a neural network comprises multiple layers, each of which comprises multiple neurons. Synapses connect neurons to all other neurons of the layers immediately to the left and to the right of their layer, but there are no connections between neurons of the same layer or of neurons to other neurons several layers away. At the input layer, no computation is performed; neurons simply pass on the information to the first hidden layer. Any layer that is not the input layer or the output layer is called a hidden layer, and it's within these layers that the bulk of the processing is done. They are called hidden layers because they are not 'exposed', i.e. once the ANN program is written, they are an abstraction and perform all of the computations, transforming inputs step-by-step from the input layer to the output layer. There can be multiple hidden layers depending on the architecture of the neural network, and the overall design of neural network architectures is one of great research and will not be discussed here. Finally, the output layer brings all the information 'learned' through the hidden layers and outputs the final result.

At the neuron level, shown in Figure 3.7B, we can explain what happens at each neuron. All neurons from the previous layer in the ANN output their result, which becomes the inputs of this neuron. The inputs are carried to the neuron on the synapse (the connection between the two neurons) and are multiplied by a weighting
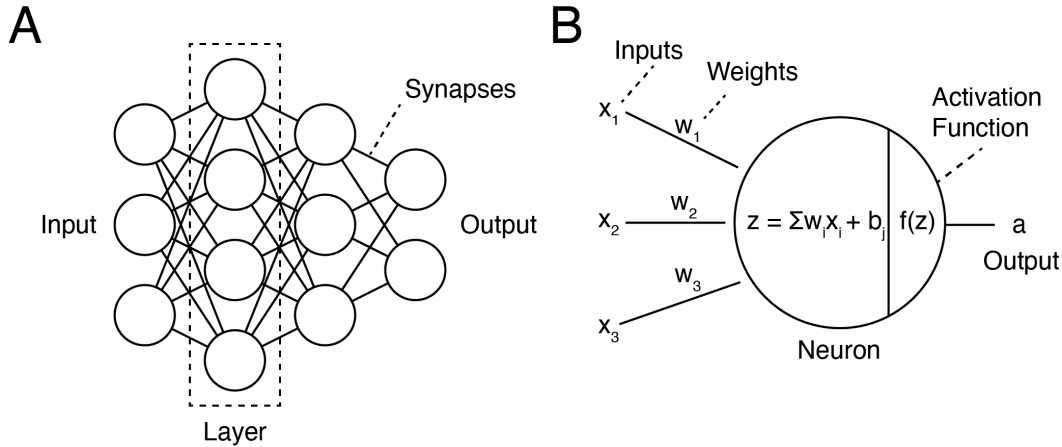
Figure 3.7: A) Schematic of an artificial neural network comprised of: (1) four layers (one input layer, two hidden layers, and one output layer), (2) 12 neurons (3+4+3+2), and (3) 30 synapses. B) Schematic of a neuron in an artificial neural network. Each neuron sums the weighted inputs and adds a bias term. The result is input into an activation function, which determines whether or not the neuron should 'fire'.

term, w^i, which, similar to objective function definitions, is a scalar term indicative of how important that particular synapse is in the scope of the entire network. The neuron sums all of the weighted terms and adds a bias, b^j, which, similar to the weights, represents how important that particular neuron is in the scope of the entire network. This result of this equation, z, is then fed into an activation function, $f(z)$. Different ANNs will use different activation functions, such as those shown in Figure 3.8, but the activation function is the same for all neurons in the network. The exception to this is the output layer, which sometimes has a unique activation function. Activation functions are named because they determine whether or not z is worthy of influencing subsequent layers. They are mathematical gates between the input feeding the current neuron and its output going to the next layer. In other words, activation functions decide whether or not the neuron's output is important in the prediction process using simpler mathematical operations. The result of the activation function $a = f(z)$ is output from the neuron and used as the input for the subsequent layer in the ANN.

The weights must be 'trained' to achieve the desired output. Training is a calibration process analogous to the design string ranking, mating, and elimination

Activation Functions

Sigmoid
$\sigma(x) = \frac{1}{1+e^{-x}}$
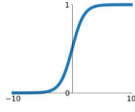
tanh
$\tanh(x)$
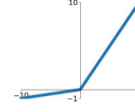
ReLU
$\max(0, x)$

Leaky ReLU
$\max(0.1x, x)$
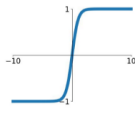
Maxout
$\max(w_1^T x + b_1, w_2^T x + b_2)$
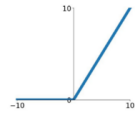
ELU
$\begin{cases} x & x \geq 0 \\ \alpha(e^x - 1) & x < 0 \end{cases}$
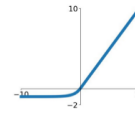
Figure 3.8: A list of activation functions commonly used in artificial neural networks[93].

discussed in Section 3.5. From Section 3.1, ANNs are a subset of the supervised learning approach, and they require a set of training data where both the inputs *and* the outputs are known. There are several strategies used for training ANNs, but regardless of method, all follow the same generalized steps:

1. Guess a set of trial weights and biases given by the vectors $\mathbf{w}^{i=1}$ and $\mathbf{b}^{i=1}$, insert into the ANN, and calculate the output:

$$\mathcal{O}^i = \mathcal{F}\left(\mathcal{I}, \mathbf{w}^i, \mathbf{b}^i\right)$$

2. Simulate the system and compute the error:

$$\mathcal{E}^i = \left(\mathcal{O}^{desired} - \mathcal{O}^i\right)^2$$

3. Adjust the weights and biases corresponding to the error:

$$\mathbf{w}^{i+1} = \mathbf{w}^i + \Delta\mathbf{w}^{i+1}$$

4. Iterate steps 1-3 until there are no more sets of training data, or $\bar{\mathcal{E}}_{rms} < TOL$

First, one guesses the values of the weights of the N synapses and the biases of the M neurons. These are generally written in vector format for fast processing:

$$\mathbf{w}^{i=1} = \begin{pmatrix} w_1 \\ w_2 \\ w_3 \\ \dots \\ w_N \end{pmatrix}^{i=1}, \qquad \mathbf{b}^{i=1} = \begin{pmatrix} b_1 \\ b_2 \\ b_3 \\ \dots \\ b_M \end{pmatrix}^{i=1} \tag{3.24}$$

The training data inputs are then fed into the system. Each neuron of the input layer is assigned one of the input parameters, which are then fed forward through the hidden layers of the ANN, where their values are multiplied by the weighted terms, transformed through the activation function, and fed forward through subsequent layers. After each set of training data, the ANN outputs, $\mathbf{a}^i$, are compared to the outputs of the training data, $\mathcal{O}^i$, and an error term is calculated:

$$\mathcal{E} = (\mathbf{a}^i - \mathcal{O}^i)^2 \tag{3.25}$$

We want to correct all the weights and bias values to minimize the squared error. When the error is close to zero for many training data sets, the ANN has been trained to model the system.

Consider one of the weights w_2 in Figure 3.7B. Using a truncated Taylor series, a finite difference approximation for the derivative of $\partial\mathcal{E}/\partial w_2$ can be written as:

$$\frac{\partial\mathcal{E}}{\partial w_2} = \frac{0 - \mathcal{E}}{w_{2,n} - w_2} \tag{3.26}$$

where $w_{2,n}$ is the value of w_2 corresponding to an error $\mathcal{E}$ equal to zero. Rearranging yields a prediction of a new value of $w_{2,n}$ that would make the error go to zero:

$$w_{2,n} = w_2 + \frac{0 - \mathcal{E}}{\frac{\partial\mathcal{E}}{\partial w_2}} \tag{3.27}$$

However, we have more weights and biases, so we only want to correct a fraction of the error. Specifically, we modify the equation to:

$$w_{2,n} = w_2 + \gamma\frac{0 - \mathcal{E}}{\frac{\partial\mathcal{E}}{\partial w_2}} \tag{3.28}$$

where γ is the learning rate parameter and is inversely proportional to the number of weights and biases in the ANN:

$$\gamma \approx \frac{1}{m + n} \tag{3.29}$$

where m is the number of bias terms, and n is the number of weight terms. This logic is applied to all the network weights and biases. To do this, one must be able to evaluate all of the derivatives. This is accomplished by the successful application of the chain rule. This correction approach is called backpropagation and is how the ANN learns over time. These steps are then repeated until there are no more training data sets or until the root-mean-square error falls below some threshold value.

Limitations of Artificial Neural Networks

There are a few things to watch out for when designing and executing an ANN, though the main concern is the activation function. Selection of activation functions is a crucial step: choosing the wrong activation function can lead to either vanishing or exploding gradients that will either dramatically increase or eliminate the outputs of neurons, or update the weights and biases of each iteration by so much that they 'slingshot' back and forth from iteration-to-iteration, never approaching some steady-state value. Furthermore, when selecting an activation function for the output layer, one must consider the range of values one expects. One can use the linear or ReLU activation functions if the output can be any numeric value.

3.7 Concluding Remarks

In this chapter, we laid the groundwork for understanding and writing MLAs to model and optimize physical systems. In all optimization problems, the 'optimal' result is reached by either maximizing or minimizing an objective function, depending on the convention. Different types of MLAs utilize different approaches to obtaining solutions to these objective functions, several of which were described.

Several other ML approaches were not addressed here. This was for no reason other than because they are outside my expertise. Deep learning, for example, is a similar strategy to ANNs, that executes with an unsupervised approach. Although they have been theorized about since the 1940's[94], they've only caught traction since the introduction of activation functions in 2012, where Ng and Dean demonstrated the labeling of cats in unlabelled youtube videos[93;95]. Natural language processing (NLP) is a subcategory of MLAs that are not only responsible for predictive texts[96], but are also being used to predict dementia and Alzheimer's from people's writings with 92% accuracy[97].

Part II

Dissertation Work

Chapter 4

Printed Nitrate Sensors

Milkweeds and murky brakes, quaint pipes and sun-dew,
And rare and virtuous roots, which in these woods
Draw untold juices from the common earth,
Untold, unknown, and I could surely spell
Their fragrance, and their chemistry apply
By sweet affinities to human flesh
– Ralph Waldo Emerson

4.1   Why Care About Nitrate?

Unless you are already a researcher in a related field, you probably are wondering why anyone would care about nitrate. "Nitrate..." you might think to yourself, "Isn't that the stuff you're supposed to avoid in processed foods? Ugh, I really should commit to that new diet everyone is talking about..." If your thought process sounded even remotely like this when reading the chapter title, then although you may be correct in your consumptional aspirations, the scope of your understanding of nitrate is incomplete. This is a forgivable offense, because if this were not the case, then I would have far less to write about in this chapter. Beyond food preservatives[98], nitrates are also used in heart medicines[99], explosives[100], and most notably, agricultural crop production.

Nitrate - or NO_3^- - is a critical nutrient for plant growth[101]. Plants use nitrates to make various nucleotides, amino acids, and proteins[102] - the fundamental building blocks of life. Unfortunately, nitrate is also a harmful pollutant of drinking water[103]

and excess nitrate is known to cause adverse outcomes to human health[104;105]. Nitrates can also run off and accumulate in still bodies of water, which leads to harmful algal blooms and eutrophication[106]. All of this is to say that there is competing interest in using nitrates in agriculture: we want to use enough nitrate to produce vibrant crops, but not so much that we poison our own environment and drinking supply.

Despite this, tools for monitoring nitrate over time and space are inadequate at the time of this writing. To better quantify the nitrate problem and tailor nitrate fertilizer inputs in agriculture, measurements of nitrate concentrations in soil need to be made more frequently, at higher spatial resolutions, and over larger areas. The remainder of this dissertation work is poised to address this. In this chapter, we will discuss the development and characterization of nitrate sensing elements. In Chapter 5, we will then discuss the adoption of these sensors into a wireless sensor network for precision agriculture. Finally, in Chapter **??**, we will discuss implementing a potentiometric sensor array that measures the concentration of several other agricultural nitrogen sources ancillary to nitrate.

4.2   Nitrate Sensing Modalities

Spectrophotometric Analysis

Spectrophotometric analysis is a lab-scale process predicated on the fact that different electrolytic solutions absorb different wavelengths of light. A nitrate solution absorbs UV-wavelight at 220 and 275 nm[107]. Thus it is possible to sense concentrations of nitrate by measuring how much light is absorbed in this spectrum.

Unfortunately, this method only really works when the sample being measured is only composed of nitrate and water, which is not representative of practically any use-case scenario. Other organics absorb light in the same band as nitrate, so any contamination would suffer from selectivity issues.

Ion-exchange Chromatography

Ion-exchange chromatography is a lab-scale process requiring large, expensive equipment. In this measurement technique, a sample is taken from whatever it is whose chemical concentrations you would like to measure, and is rinsed with high-purity water. The water is then passed through a pressurized column where ions are absorbed by ion-exchangers: resins that are selective to different ions. The column of

ion exchangers is then flushed with an ion-extraction liquid, such as potassium chloride, while the conductivity of the liquid is measured. The retention time is measured to determine the contents of the sample[107;108], with different ions having different retention times for different ion extraction liquids. The peak of the conductivity measurement corresponds to the concentration of each ion.

Ion-selective Amperometry

Ion-selective amperometry is a three-electrode electrochemical technique that measures the magnitude of a DC current between a working electrode (WE) and a counter electrode (CE) when a constant potential is held between the WE and a reference electrode (RE). The WE is generally doped with a microbe or enzyme that reacts with the primary measurand within a certain range of electrochemical potentials. Thus, when the potential between the WE and RE is set to a value within this range, the current between the WE and the CE corresponds to the concentration of the primary measurand. While this method can be made highly selective, enzymes and microbes behave differently in different soil types[109].

Impedance Spectroscopy

Impedance spectroscopy sensors are impedimetric-type sensors and work by applying small AC voltages at various frequencies between two electrodes in order to drive the diffusion of electrochemical species onto or off of the electrode while measuring impedance change. As discussed in Section 1.3, impedimetric sensors demonstrate poor selectivity, and the high-frequency excitation signals and complicated onboard calculations require more sophisticated onboard computing compared to ion-selective amperometric or potentiometric sensors[110;111].

Ion-selective Potentiometry

A potentiometric sensor measures the open-circuit potential between an ISE and a RE. The RE serves the purpose of providing 'electrochemical ground', while the ISE is sensitive to the primary analyte (whatever chemical the sensor is supposed to sense). A high input impedance voltage sensor is placed between the ISE and the RE to measure the difference in electrical potential between the two electrodes, and this electrical potential corresponds to the concentration of the primary analyte.

Table 4.1: Qualitative comparison of different nitrate sensing modalities.

Sensing Modality	Soil Compatible?	Selective?	Low Cost?
Spectrophotometric Analysis			
Ion-exchange Chromatography		✓	
Ion-selective Amperometry		✓	✓
Impedance Spectroscopy	✓		
Ion-selective Potentiometry	✓	✓	✓

Picking a Modality

There are several things to consider when we decided what type of sensing modality should be used to measure nitrate concentrations in agriculture. The feasibility of the different sensing modalities discussed here to reach or surpass these considerations are shown in Table 4.1.

First, the sensor must be *soil compatible*, meaning the sensor has to work in a soil environment. Soil is a three-phase (solid, liquid, and gas) complex medium[112] consisting of (in no particular order) various organic matter, minerals, metals, ceramics, air, water, microbial colonies, fungi, and (if the conspiracy theorists are to be believed) mole people[113]. Plants uptake aqueous-phase nitrates from their roots, so the measurement itself should be made on nitrate in the aqueous phase.

Second, it has to be *selective*. Soil contains many different chemicals, many of which may contribute to a false nitrate signal if the sensor is not selective enough. In this case, the sensor would be ineffective at measuring nitrate, rendering it pointless.

Third, the sensor should be *low cost*. The goal of this work is to increase the number of sensors used in agriculture, but realistically, the sensors won't be adopted if it doesn't make sense financially. In other words, the cost of sensors has to be less than or equal to the sum of the cost of the fertilizers it offsets, the cost of healthcare associated with nitrate leaching into the water supply, and the cost of the environmental damage caused by eutrophication.

Finally, the sensor must be able to sense nitrate at the concentrations that are commonly found in agricultural soils. Figure 4.1 shows the approximate linear range of concentrations that these sensing modalities have, though some outliers exist.

Combining both the qualitative and quantitative metrics discussed here, potentiometric-type sensors were determined to be the most appropriate for the application of measuring nitrate levels in the soil. They are soil compatible, selective to nitrate, and can be made using low cost print-based fabrication methods.
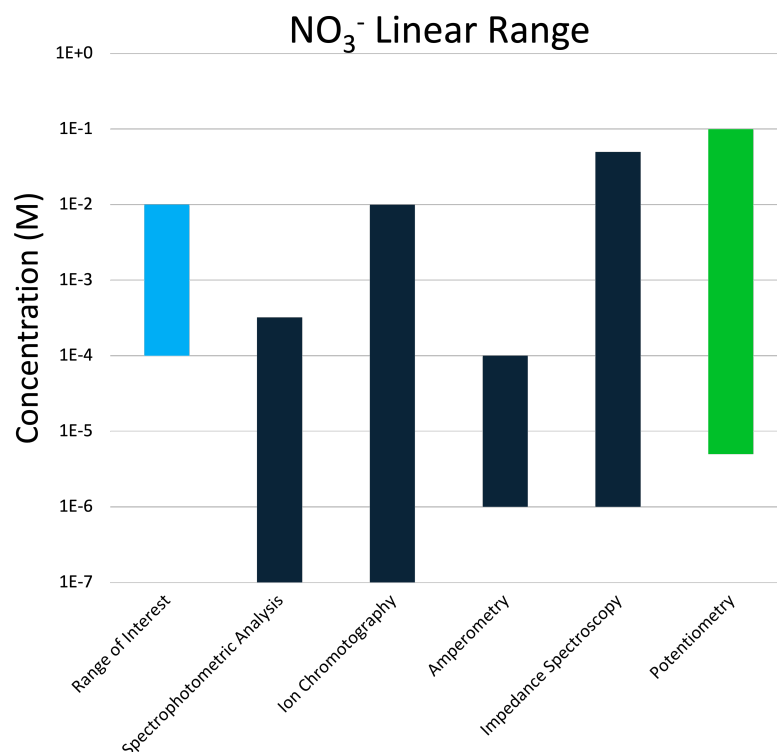
Figure 4.1: Comparison of the linear range of various nitrate sensor types. The 'range of interest' shown in blue corresponds to the range of nitrate concentration in agricultural soil.

4.3 Potentiometric Ion-Selective Electrode Sensors

A potentiometric sensor measures the open-circuit potential between an ISE and a RE. An accurate and practical method to measure an electrode's potential in isolation (absolute electrode potential) has yet to be developed, so instead a RE is used as an 'electrochemical ground' or reference potential for the ISE to be compared against. The ISE, on the other hand, has a dynamic potential that changes corresponding to changes in the concentration of the primary analyte. A high input impedance voltage sensor is placed between the ISE and the RE to measure the difference in electrical potential between the two electrodes, and because the RE potential is unchanging,

the measured potential difference corresponds to the concentration of the primary analyte.

The ISE consists of an organic phase membrane that is doped with an ionophore, L, that has a strong affinity to the primary ion. The potential then is given by thermodynamics:

$$E_{ISE} = E^0_{ISE,i} + \frac{RT}{z_i F} \ln a_{i,solution} + \frac{RT}{z_i F} \ln \frac{1}{a_{i,membrane}} \tag{4.1}$$

The ionophore in the membrane phase effectively holds the activity of the ion in the membrane constant, so we can account for the $\frac{RT}{z_i F} \ln \frac{1}{a_{i,membrane}}$ term in the standard potential term which is also constant:

$$E^{0*}_{ISE,i} = E^0_{ISE,i} + \frac{RT}{z_i F} \ln \frac{1}{a_{i,membrane}} \tag{4.2}$$

making Equation 4.1 become:

$$E_{ISE} = E^{0*}_{ISE,i} + \frac{RT}{z_i F} \ln a_{i,solution} \tag{4.3}$$

which is the Nernst equation. If the temperature is known (either by approximation or by measurement with a temperature sensor), then from Equation 1.19 we see that the measured potential is logarithmically proportional to the activity of the primary analyte. The activity of an analyte denotes the 'active' concentration of a species in solution and is given by:

$$a_i = f_i c_i \tag{4.4}$$

where f_i and c_i are the activity coefficient and the concentration of analyte i, respectively. Thus, for a calibrated potentiometric sensor, the concentration of the primary analyte can be determined from the measured cell potential, E_{cell}.

Key Components

Ion-selective Electrode

The ISE consists of an ion-selective membrane, an ion-to-electron transducer layer, a conductor, packaging, and encapsulation.

Ion-selective Membrane

The ion-selective membrane (ISM) is the sensing element of an ISE sensor. It is made up of a hydrophobic polymer, a plasticizer, an ionophore, and in many cases, an ion-excluder.

The primary ingredient of an ISM is a hydrophobic polymer (most commonly poly(vinyl chloride) (PVC)) which forms the backbone matrix of the ISM. A plasticizer is added to solvate the polymer into a gel-like membrane-phase material. The plasticizer solvent fills and spreads the gaps between the polymer chain, thereby increasing the flexibility and softening the polymer matrix[114].

An ionophore is a chemical designed to selectively interacts with an ion-of-interest[6;115–122]. For example, a magnesium-selective ISM would include an ionophore that selectively and reversibly binds to magnesium ions. In Section 1.3, we discussed the four possible mechanisms by which ionophores can interact with ions (dissociated ion exchange, charged carrier exchange, neutral carrier exchange, and reactive carrier exchange)[25]. Of these, neutral carrier ionophores are most widely used in ISE sensors based on polymer membranes. Neutral carrier ionophores are typically macrocyclic, where many organic molecules are chained together to form a large ring-like shape whose gap is close to the molecular radius of the primary ion[27]. For example, the potassium ion-selective membrane uses valinomycin as the ionophore. Valinomycin in the membrane can selectively form a complex with potassium ion (K^+) from the solution. The cavity within the interior of the valinomycin fits potassium ions, and the ions are held there due to their interactions with the ester carbonyl oxygen atoms of the valinomycin molecule. This is what provides selectivity of valinomycin to potassium and allows the reversible exchange of potassium ions with the analyte solution via complexation between potassium and valinomycin.

If the ionophore is, in fact, a neutral-carrier ionophore, then it is necessary to also include a hydrophobic counter ion to the primary ion (sometimes called an ion-excluder or ionic site in literature) for selectivity[28].

Ion-to-Electron Transducer Layer

Ion-to-electron transducer layers, hereafter shortened to 'transducer layer', is the component in an ISE that is responsible for arbitrating the build-up of electrical charge or potential from a concentration of ions. There are two broad types of transducer layers. The first is transducer layers that operate on redox activity, and the second is transducer layers that operate on a capacitor-like electric double-layer potential.

Transducer layers that operate on redox activity have a liquid or solid electrolyte that separates the ISM from the conductor. Conventional ISEs have a liquid separa-

Table 4.2: Commercially-available ionophores for ions relevant to biological systems. Descriptors such as "Magnesium Ionophore IV" originates from the catalogs of major commercial suppliers. Consult the cited literature for further detail.

Ion Name	Symbol	Ionophore Descriptor	Reference
Ammonium	NH_4^+	Ammonium Ionophore I	[123]
Calcium	Ca^{2+}	Calcium Ionophore I	[124]
Calcium	Ca^{2+}	Calcium Ionophore II	[125]
Calcium	Ca^{2+}	Calcium Ionophore III	[126]
Calcium	Ca^{2+}	Calcium Ionophore IV	[127]
Calcium	Ca^{2+}	Calcium Ionophore V	[128]
Chloride	Cl^-	Chloride Ionophore I	[129]
Chloride	Cl^-	Chloride Ionophore II	[130]
Chloride	Cl^-	Chloride Ionophore III	[130]
Chloride	Cl^-	Chloride Ionophore IV	[131]
Copper	Cu^2+	Copper Ionophore I	[132]
Copper	Cu^2+	Copper Ionophore IV	[133]
Copper	Cu^2+	Copper Ionophore V	[134]
Hydrogen	H^+	Hydrogen Ionophore I	[135]
Hydrogen	H^+	Hydrogen Ionophore II	[136]
Hydrogen	H^+	Hydrogen Ionophore V	[137]
Lead	Pb^2+	Lead Ionophore I	[138]
Lead	Pb^2+	Lead Ionophore IV	[139]
Magnesium	Mg^+	Magnesium Ionophore I	[140]
Magnesium	Mg^+	Magnesium Ionophore II	[141]
Magnesium	Mg^+	Magnesium Ionophore IV	[142]
Magnesium	Mg^+	Magnesium Ionophore VI	[143]
Mercury	Hg^2+	Mercury Ionophore I	[144]
Nitrate	NO_3^-	Nitrate Ionophore VI	[145]
Nitrite	NO_2^-	Nitrite Ionophore I	[146]
Potassium	K^+	Potassium Ionophore I	[147]
Potassium	K^+	Potassium Ionophore II	[148]
Potassium	K^+	Potassium Ionophore III	[149]
Sodium	Na^+	Sodium Ionophore I	[150]
Sodium	Na^+	Sodium Ionophore II	[151]
Sodium	Na^+	Sodium Ionophore III	[151]
Sodium	Na^+	Sodium Ionophore IV	[152]
Sodium	Na^+	Sodium Ionophore VI	[153]
Sodium	Na^+	Sodium Ionophore X	[154]
Zinc	Zn^{2+}	Zinc Ionophore I	[155]
Zinc	Zn^{2+}	Zinc Ionophore IV	[156]
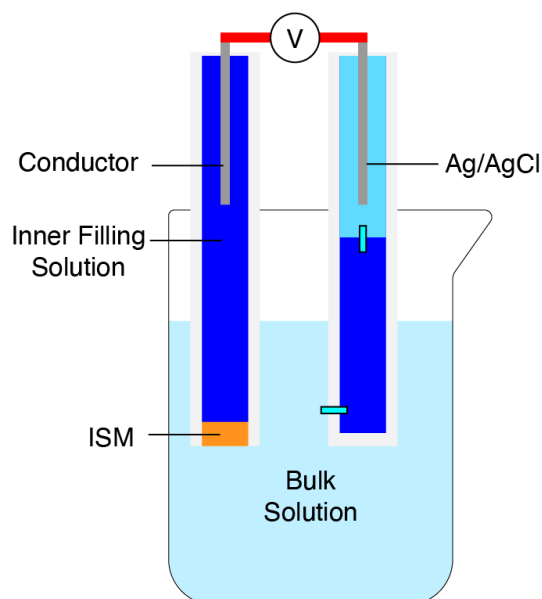
Figure 4.2: Schematic of a conventional potentiometric ion-selective electrode sensor. The ion-selective electrode (left) is connected electrically to the reference electrode (right) by a voltage sensor, and ionically through the bulk solution.

tor (commonly called an 'inner-filling solution') that performs ion-to-electron transduction by means of an electrochemical reaction. For example, the 'conventional' ISE architecture is an Ag/AgCl wire in a glass tube filled with a fixed concentration of Cl$^-$inner-filling solution that is in contact with the ISM. A schematic of a conventional potentiometric ISE sensor is shown in Figure 4.2.

For all-solid-state ISEs without redox properties, ion-to-electron transduction is the result of the electrical double layer forming at the ISM/transducer interface. This interface can be schematically described as an asymmetrical electrical capacitor, in which one side carries a charge in the form of ions, i.e., cations and anions from the ion-selective membrane, and the other side is formed by an electrical charge, i.e., electrons or holes in the solid contact[157].

It is possible to make an ion-selective electrode without including a transducer electrode[158]. When a transducer layer is not used and the ISM is coated directly onto the conductor, ion-to-electron transduction behaves similar to a redox-free transducer layer where the charge is dependent on the quantity of charge in the electric double layer. However, sensor drift and erratic responses are more prevalent in ISEs without a transducer layer because a deleterious water layer can form more easily between

the ISM and conductor, which will be discussed in greater detail later in Section 4.4. Also, generally, there is a smaller contact area between an ISM/conductor interface compared to a transducer/conductor interface because of the nature of the materials used in each. As we discussed earlier, the surface area of this interface is critical for ion-to-electron transduction. Finally, the ISE can become polarized by the small (pA or less) currents associated with potentiometric measurements.

Conductor

The conductor is in contact with the transducer layer. It carries data as an electric potential from the electrode to the voltage sensor. It is often a metal, though any conductive material - such as allotropes of carbon or silicon - can also be used.

Packaging & Encapsulation

Finally, the ISE must be held together with physical packaging and encapsulation. These components are tied to the ease of handling, impact resistance, and physical durability of the sensor. It also aids in preventing oxidation, corrosion, and other undesirable processes.

Reference Electrode

As described earlier in Section 4.2, the RE act's as an 'electrochemical ground', providing a stable, well-known reference potential that is unchanging in varying ionic environments[159]. The stable potential is generated by an electrochemical reaction that also provides the namesake of the electrode. For example, the standard hydrogen electrode (SHE) is named after the redox half cell reaction: $2\,H^+_{(aq)} + 2\,e^- \longrightarrow 2\,H_{2(g)}$. When an abundance of reactants are made available, the reaction will occur spontaneously, and always at the same potential (given all other factors also remain constant).

There are REs based on a handful of different chemical reactions, each offering different drawbacks and advantages over the others. However, the Ag/AgCl RE is by and far the most commonly used because of its distinct advantages. As it's named suggests, it is based on the silver-silver chloride reaction, $AgCl_{(s)} + Ag_{(s)} + e^- \rightleftharpoons Ag^+ + Cl^- + Ag_{(s)} + e^-$, which occurs at +0.222V vs. the SHE.

In this work, we use the Ag/AgCl electrode exclusively as the RE, and will therefore only be concerned with this RE chemistry hereafter. In conventional ISE sensors, such as the one shown in Figure 4.2, the metal conductor (Ag) is in contact with a sparingly soluble solid salt of the corresponding metal cation (AgCl) which

is suspended in a reference solution of the anion that forms that salt (KCl, NaCl, etc.)[160]. The reference solution is separated from the bulk solution by a salt bridge.

Salt Bridge

The salt bridge separates the transducer and the bulk solution that is being sampled. In practice, the salt bridge is often contained in nanoporous glass (glass frit), polymer membrane, hydrophilic gel, or capillary[160]. In conventional REs, a glass frit is most commonly used as the salt bridge. The salt bridge must allow electrical contact between the bulk solution and the Ag/AgCl by ionic conductivity with relatively low resistance[161].

In the case of many solid-state REs, the salt bridge is a salt-loaded polymer membrane, hereafter simply called the salt membrane. The salt membrane of a RE behaves like the salt bridge of an electrochemical cell. It is therefore of utmost importance to load the salt membrane with a surplus of salt so that the RE reaction occurs spontaneously. In the case of the Ag/AgCl electrode, the solvated polymer membrane is doped with KCl, NaCl, or another chloride salt such that a surplus of Cl^- anions are available for the reaction at the Ag/AgCl electrode. Because of the solubility of these salts, there is a slow diffusion of the membrane-phase salt into the bulk aqueous solution, meaning that over time, Cl^- ions will slowly leech into the sample that is being measured[160].

Transducer

Several configurations that an Ag/AgCl RE might take[160], primarily differentiated by the phase and material choice of the transducer layer. In conventional REs, the transduction layer is a concentrated salt solution that functions on classical ion exchange, as discussed earlier. However, there are also polymeric solid-state transducers, many of which are similar if not identical to the transducer layer materials used in ISEs.

Ag/AgCl Electrode

The Ag/AgCl electrode is the reference electrode's most important component. This electrode is often a layer of AgCl chemically grown or printed on top of a pristine silver layer, or sometimes a composite of Ag and AgCl particles. In both cases, the Ag/AgCl electrode is the site for the electrochemical reactions to occur.

Ideally, the two half-cell reactions occurring at the reference electrode are:

$$AgCl_s + e^- \rightleftharpoons Ag_s + Cl^- \tag{4.5}$$

and:

$$Ag_s \rightleftharpoons Ag^+ + e^- \tag{4.6}$$

for a full cell reaction of:

$$AgCl_{(s)} + Ag_{(s)} + e^- \rightleftharpoons Ag^+ + Cl^- + Ag_{(s)} + e^- \tag{4.7}$$
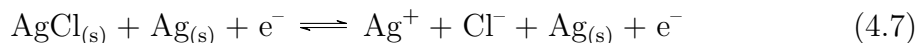
Unfortunately, it is possible for secondary, unwanted reactions to occur, creating complexes such as $AgCl_2$ or $AgCl_3$ which can lead to the dissolution of AgCl, resulting in signal drift and sensitivity problems.

Conductor, Packaging, & Encapsulation

The conductor, packaging, and encapsulation components of a reference electrode have identical roles and design considerations as their corresponding ISE components, and so are not repeated here.

Voltage Sensor

Finally, a potentiometric sensor requires a voltage sensor connected to the conductor of the ISE and the conductor of the RE to measure the electrical potential difference between the two. Whether it is a voltmeter or a potentiostat, the voltage sensor should have a sufficiently high input impedance to minimize the flow of current in the system, which as we have discussed, could cause polarization of the ISM or other drift-enabling effects.

4.4   Printed Potentiometric Nitrate Sensors

In Section 4.2, we identified ion-selective potentiometry as a sensing method that can be executed in soil, and that ISE sensors can be made at low cost. This is because it is possible for the ISE and RE components of the sensor to be made by print-based fabrication methods, the benefits of which were discussed in Chapter 2. In this section, we will discuss the fabrication and characterization of printed potentiometric nitrate sensors.
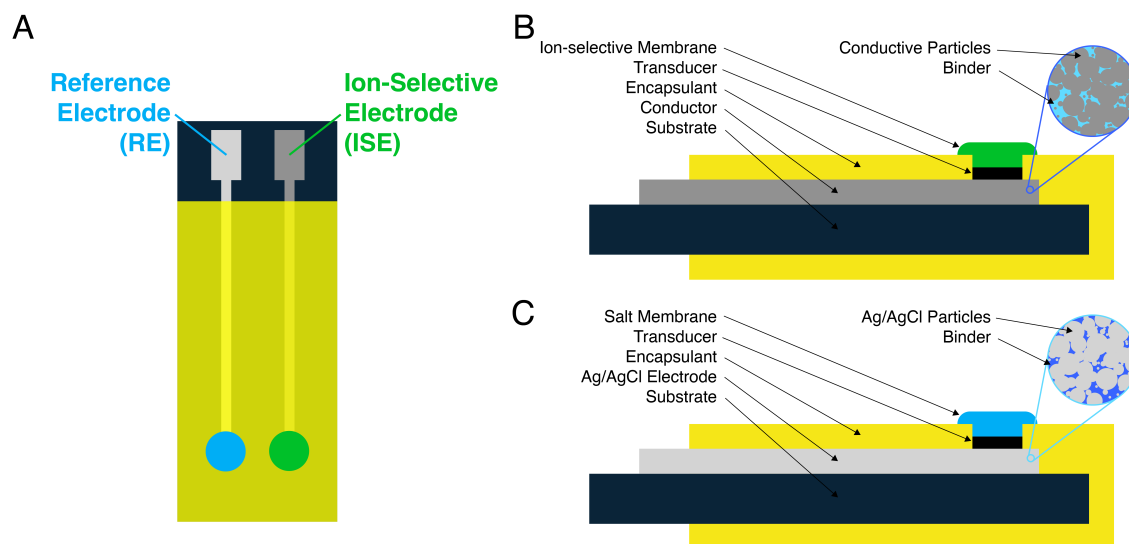
Figure 4.3: A) Schematic of a printed nitrate-selective sensor. B) Printed ISE layers. C) Printed RE layers.

Sensor Fabrication

Printed potentiometric nitrate sensors have all of the same components as a conventional potentiometric ion-selective sensor such as the one shown in Figure 4.2, but in the interest of printability and miniaturization, the inner-filling solutions of the RE was replaced with a solid-state transducer layer, while the ISE does not incorporate a formal transducer layer at all, and rather relies on capacitive transduction without a transducer layer described previously. The glass tube packaging was likewise removed. Instead, the conductor wires were printed onto a thin substrate and encapsulated. A schematic of a fully-printed potentiometric nitrate sensor is shown in Figure 4.3.

Ion-selective Electrode Fabrication

ISEs were fabricated according to the process illustrated in Figure 4.4A. Gold electrodes, which are 3.5 mm diameter circles connected to a 1 mm wide trace, were printed on 25 μm thick PQA2 PEN using Harima Nanopaste(Au) NPG-J gold ink in a Dimatix inkjet printer at ambient conditions. Printed gold electrodes were sintered at 250 °C for 50 minutes and then encapsulated with 75 μm thick laser cut Teflon
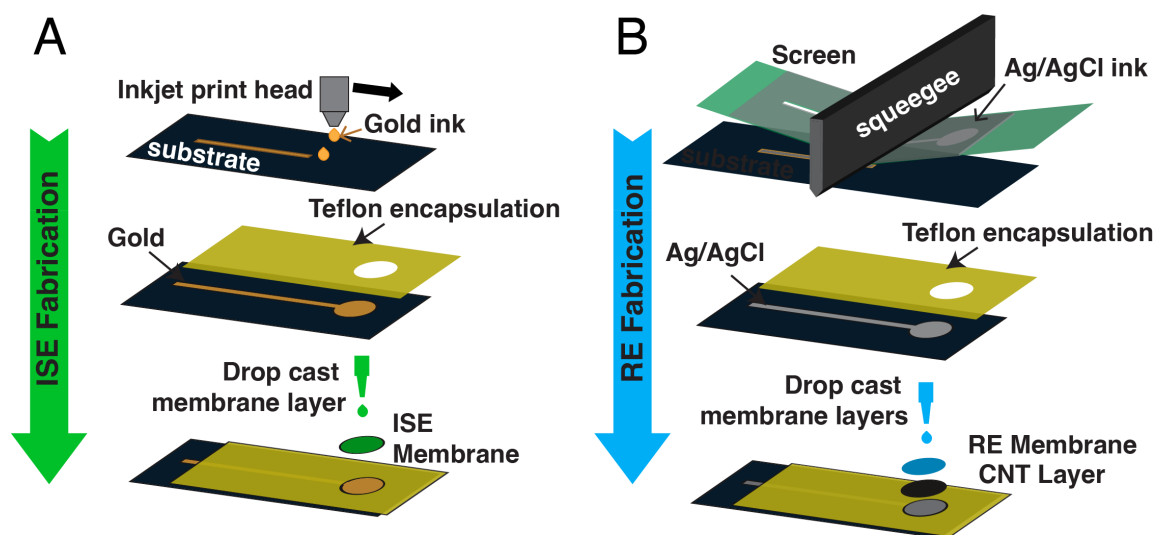
Figure 4.4: Nitrate sensor fabrication. A) Nitrate ion-selective electrode fabrication steps. A gold conductor was inkjet printed onto a PQA2 substrate, sintered, and encapsulated with a Teflon tape with a window for the electrode area. A nitrate-selective membrane cocktail was then drop cast on the exposed area of the electrode and allowed to dry in a fumehood. B) Nitrate reference electrode fabrication steps. Ag/AgCl paste was screen printed onto PET and cured. Then, a patterned Teflon tape encapsulant with a window for the electrode area was adhered to the substrate. A carbon nanotube transducer layer was drop cast onto the exposed Ag/AgCl electrode and allowed to dry in a fumehood for 15 minutes. Finally, a salt membrane cocktail was drop cast on top of the dried transducer layer and allowed to dry in a fumehood for 15 minutes.

tape with 5 mm diameter circular windows for the active area. The window in the encapsulant was larger than the electrode to allow space for the membrane to seal to the substrate, preventing bubbles or delamination of the membrane. ISE membranes were fabricated by mixing 5.2 wt% Nitrate Ionophore VI , 47.1 wt% dibutyl phthalate, 0.6 wt% tetaroctylammonium chloride, and 47.1 wt% PVC. A total of 0.2 g of this mixture was dissolved in 1.3 mL of THF. 16 μL of the membrane solution was drop-cast on the printed gold electrode surface. The resulting ISE dried in a fume hood for 15 minutes.

Reference Electrode Fabrication

Printed RE fabrication is outlined in Figure 4.4B. Ag/AgCl electrodes with the same geometry as the gold electrodes were screen printed on 25 μm thick PQA2 PEN using Engineered Materials Systems, Inc. CI-4001 ink. Three layers of ink were printed; each layer was dried before the next was printed. Printed Ag/AgCl electrodes were then annealed at 120 °C in a vacuum oven for 2 hours and encapsulated with 75 μm thick laser-cut Teflon tape.

The REs employed a CNT transducer layer between the Ag/AgCl electrode and the membrane. This transducer was composed of 0.01 g of CNT (iP-Single Walled Carbon Nanotubes from Carbon Solutions, Inc) and 0.05 g of F127 (poly(ethylene glycol)-block-poly(propylene glycol)-block-poly(ethylene glycol) diacrylate) dissolved in 10 mL of THF, which were sonified for 1 hour in an ice bath using a Branson Digital Sonifier probe. The resulting transducer cocktail was deposited in two separate 2 μL aliquots onto the printed REs surface.

The salt membrane was made by dissolving 1.58 g of Butvar B-98 (poly(vinyl butyral) (PVB), 1.00 g of NaCl, and 1.00 g of $NaNO_3$ in 20 mL of methanol. The mixture was sonified for 30 minutes in an ice bath, and the resulting salt membrane cocktail was deposited on top of the CNT transducer in three separate 2 μL aliquots. Unless otherwise noted, all chemicals used in both ISE and salt membranes were obtained from Millipore Sigma.

Sensor Assembly

Fully printed sensors were attached to an acrylic block for mechanical stability. 8331D silver conductive epoxy (MG Chemicals) was used to connect wires, and the joint was encapsulated by Gorilla two-part epoxy. Figure 4.5 shows a photograph of a fully-assembled sensor.

Sensor Characterization

In an ideal ISE sensor, the ISE demonstrates a Nernstian response to changes in primary analyte concentration, while the RE maintains a constant potential in all concentrations of solution. The ISE and RE should also be perfectly selective to the primary analyte, meaning that changing the concentration of interfering analytes would not change the potential of either electrode. Both electrodes should also be stable, meaning that the reported potentials of either electrode should be time-independent and consistent over minutes, hours, days, and even weeks of measurements. Unfortunately, all real-world devices contain some number of non-idealities,

Figure 4.5: Picture of the assembled nitrate sensor. The nitrate sensor electrodes were adhered to an acrylic stake for mechanical support and ease of handling in experiments.

resulting in systematic errors. While these flaws can be minimized by careful design and fabrication practices, it is impossible to remove all flaws. This necessitates the characterization of the ISE sensors to determine how well the sensors that were fabricated perform in their use case and to benchmark those performances against other existing sensor technologies.

In the following section, we characterized the printed nitrate ISE sensors in terms of their sensitivity, selectivity, and stability. When characterizing properties that apply to both ISEs or REs, we characterized the ISE and RE individually first, and then as a fully-printed pair (i.e., as a fully-printed ISE sensor).

Sensitivity Characterization

Perhaps the most important figure-of-merit in any ISE sensor is the sensitivity of the sensor to the primary analyte. Sensitivity is the ratio between the output signal and the measured property, so in the case of ISE sensors, sensitivity is reported in units of volts per decade change in concentration. This property is of particular importance in ISE sensors for several reasons, but the main reason is that sensitivity is the measure of 'to what degree does our sensor respond to what it is trying to measure?'. Another reason is that the larger the sensitivity, the larger the signal-to-noise ratio (SNR) and the smaller the sources of random error.

For a nitrate sensor, we can calculate the theoretical sensitivity at room temperature as the slope in the Nernst Equation, shown in Equation 4.3, by replacing z_i with the valency charge of -1 for the NO_3^- ion. Doing so yields an ideal sensitivity of -59.1 mV/decade(NO_3^-), or a -59.1 mV change per 10x increase in NO_3^- concentration.

Ion-Selective Electrode Sensitivity

To characterize the sensitivity of the printed nitrate ISE, its potential was measured against a commercially-available conventional Ag/AgCl electrode in varying concentrations of NaNO$_3$, shown in Figure 4.6A. Figure 4.6B shows the potential over time for one ISE measured against glass commercial reference electrode in nitrate solutions between 20 mM and 0.05 mM. This ISE reported a stable value after about 30 seconds after a change in concentration. The data from 4.6B can alternatively be plotted versus nitrate concentration on a log scale, as shown by the blue circles in figure 4.6C. The other lines in 4.6C represent the sensitivity for six other ISEs in three batches. The average sensitivity for all seven sensors is -54.1 ± 2.1 mV/decade.

The linear range of these sensors was found to be between 0.05 mM and 100 mM. This range is equivalent to 3.1 to 6,200 ppm NO$_3^-$ or 0.7 to 1,400 ppm (NO$_3^-$-N). This is in good agreement with other nitrate ISEs in literature, which typically exhibit a range of 10^-6 M - 10^-1 M. Concentrations of nitrate in agricultural fertilizer vary widely depending on crop and soil type as well as fertigation technique, but a few 100's of ppm would be a high nitrate concentration in fertilizer[162]. In the United States, the Environmental Protection Agency's drinking water quality standards specify a maximum of 10 ppm NO$_3^-$, and some studies have shown an increased risk of certain health conditions for water with 5 ppm NO$_3^-$ or greater. The sensors presented here cover concentrations from drinking water to concentrated fertilizer.

In Figure 4.6C, the sensitivity curves for different sensors are offset one from another. This offset is the result in different values for $E_{ISE,i}^{0*}$, which is the sum of standard potentials for all boundaries in the ISE. This variation in $E_{ISE,i}^{0*}$ is common in ISEs (particularly in ISEs that utilize a capacitive transducer rather than a redox transducer[163]) and means that each sensor must be individually calibrated before use. E^0 variation has a variety of causes, many of which are summarized in Hu *et al.*[158]. Properly, E^0 is the potential at ion activity of 1, which is outside of the linear range of the sensors. E^0 values presented here are calculated using the potential at 1 mM NO$_3^-$ concentration. Within one batch of ISEs, the E^0 variation was found to be 12.5 mV. The measurements for one batch were done with each ISE paired with one of five different commercial REs. While nominally identical, the standard potential of these five commercial REs was compared in 1 M KCl solution and was found to vary by up to 11 mV different from each other. This difference in commercial RE performance is consistent with E^0 values obtained within a batch of ISEs. The batch-to-batch variation is 83 mV over six batches. This significant variation may be due to variation in the membrane drying conditions, sections of crystallized PVC in the membranes, or other minor effects[163].

Another reason for mismatched standard potential is when different materials
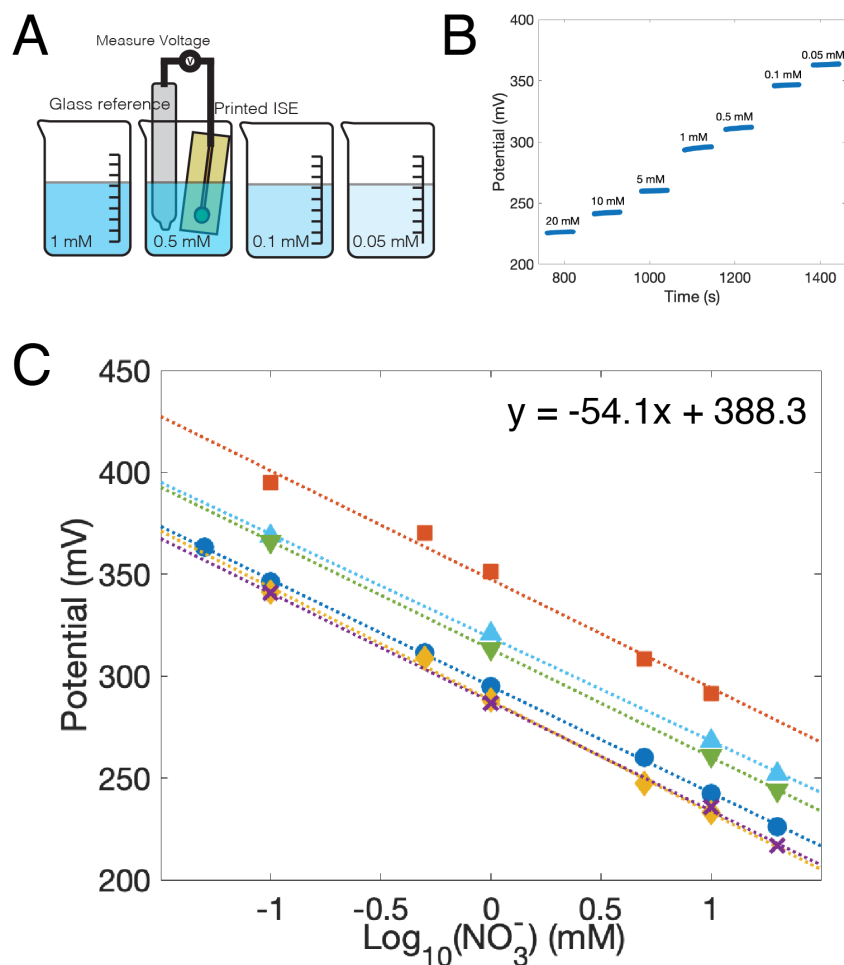
Figure 4.6: (**a**) Characterization of a printed nitrate-selective electrode against a commercial reference electrode in $NaNO_3$ solutions of varying concentrations. (**b**) Potential over time response of a printed nitrate-selective electrode in changing concentrations of nitrate.(**c**) Sensitivity plot of six nitrate-selective electrodes overlaid, showing high repeatability and near-Nernstian response of -54.1 mV/dec $\pm$ 2.1 mV/dec.
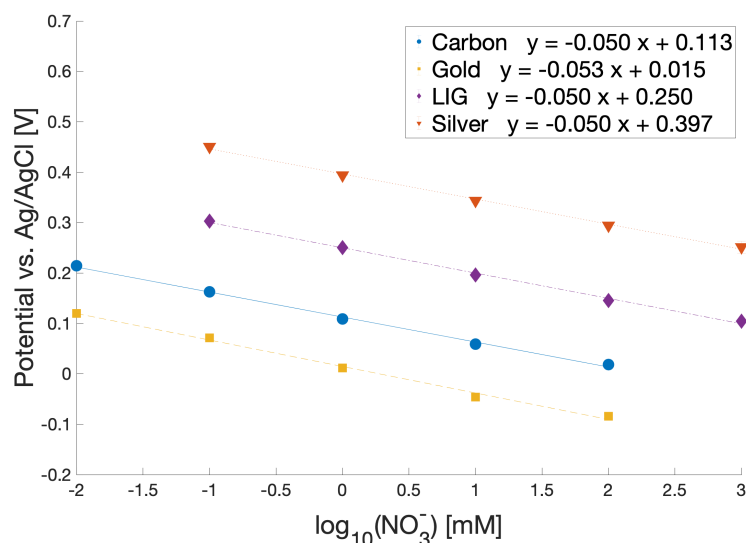
Figure 4.7: Sensitivity of nitrate ion-selective electrodes using different materials for the conductor.

are used as a conductor. Because the standard potential is calculated as the sum of all standard boundary potentials between the ISE and RE, changing the conductor layer material causes an offset in boundary layer potential between the transducer layer and the conductor. Figure 4.7 shows the impact that changing the conductor material has on the overall sensitivity and standard potential of the nitrate ISE. All nitrate ISE conductors were made using the same pattern described in the fabrication section. LIG conductors were prepared according to literature[164–167]. Carbon conductors were screen printed with Creative Materials 114-34A/B187 solvent-resistant carbon ink. The silver conductors were screen printed with Creative Materials 127-07 extremely conductive ink.

Fertilizers often include nitrate in salts other than $NaNO_3$, so the ISEs were also characterized in the presence of two other common nitrate salts: KNO_3 and NH_4NO_3 commercial fertilizers. The resulting sensitivity to all three nitrate salts is shown in Figure 4.8. For four sensors, the sensitivity in NH_4NO_3 was -51.2 ± 4.0 mV/decade, and for KNO_3 sensitivity was -52.6 ± 5.0 mV/decade. This shows that ISE sensitivity depends only on the NO_3^- anion and not the associated cation. However, the standard potential does vary from one salt to another, which motivates the need to characterize the selectivity of the ISEs.
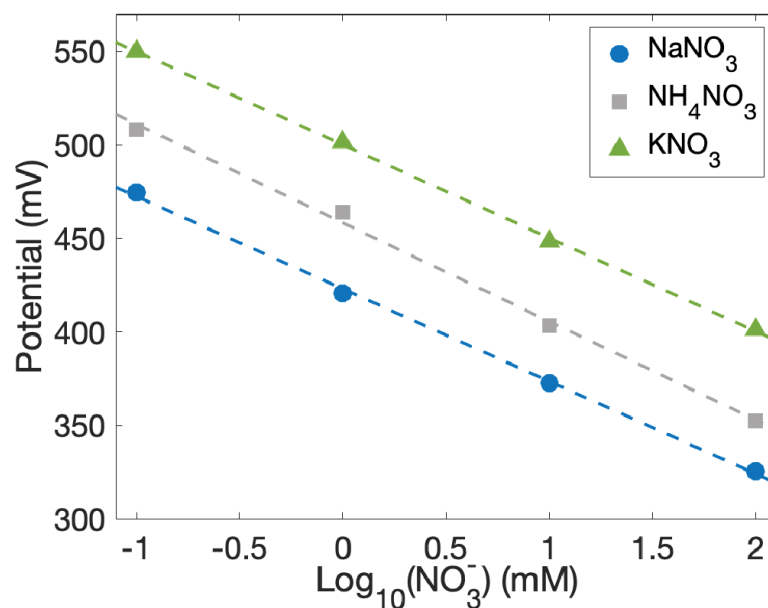
Figure 4.8: Sensitivity of nitrate ion-selective electrodes in different nitrate salts.

Reference Electrode Sensitivity

REs act as an electrochemical ground, therefore their potential must remain unchanged in varying ionic environments. The precise composition of the printed RE will impact E^0 in the Nernst equation. However, because E^0 is constant, the offset is easily accounted for in calibration.

The performance of printed REs was determined by measuring them versus a commercial Ag/AgCl double junction RE, as in Zamarayeva *et. al*[168], and illustrated in Figure 4.9A. First, pristine printed Ag/AgCl electrodes were measured, and the resulting data is shown in Figure 4.9B. The output voltage is unstable since these printed REs lacks a source of chloride ions, which are needed for the Ag/AgCl reversible reaction that keeps the reference potential stable.

The surface area and composition of the printed RE were modified by adding a CNT layer and a PVB-NaCl membrane. The characterization is shown in Figure 4.9C. These electrodes used the formulation developed in Zamarayeva[168] for use in chloride-rich environments. REs with a NaCl membrane showed a -18 mV/decade sensitivity to nitrate.

The optimized RE composition was achieved with the addition of $NaNO_3$ to

the PVB-NaCl membrane. Cattrall and Zamarayeva *et al.*[168;169] have shown that including the ion of interest in the membrane of a RE reduces its sensitivity to that ion. To reduce sensitivity to nitrate, $NaNO_3$ was needed in the membrane; sensitivity data for this electrode is shown in Figure 4.9D. This formulation has a sensitivity of -3 mV/decade, which is a marked improvement over the NaCl membrane alone.

The effect of adding the ion of interest to the reference electrode membrane is highlighted in Figure 4.9E, where the NaCl membrane and $NaCl+NaNO_3$ membranes are directly compared. In this figure, potentials are normalized by subtracting the average potential in 1 mM nitrate from the average potential at each concentration, and the potential offsets are plotted versus concentration. The RE whose membrane includes $NaCl+NaNO_3$, represented by red triangles, has a flatter slope which reflects its insensitivity to nitrate concentration.

Repeatability across different reference electrodes is shown in Figure 4.9F where voltage vs concentration for five printed REs with the $NaCl + NaNO_3 + PVB$ membranes is displayed. All the printed REs showed stable potential response over three orders of magnitude change in the nitrate concentration.

Fully Printed Nitrate Sensor Sensitivity

Pairing the printed ISE with a printed RE results in a fully printed sensor that realizes the full benefits of printing: low cost, high-throughput manufacturing, no glass or liquid components, and production in form factors that are suitable for use in field deployments. Figure 4.10A shows the potential over time for a printed ISE measured against a commercial reference in blue and that same ISE paired with a printed reference in green. The E_0 value changed, which was expected because the interfaces present in a printed RE are different from those of a commercial RE. For this sample, the fully printed senor's potential was about 87 mV below the printed ISE-commercial RE pair. Both versions have high sensitivity greater over the range 0.1 mM to 100 mM, response times less than 10 seconds, and hysteresis less than 5%.

The sensitivity of these ISEs, when measured against glass REs, were -54.3 $\pm$ 2.6 mV/dec, which is near Nernstian and comparable to other nitrate ISEs in literature, as shown in Table 4.4. Printed pairs have a sensitivity of 48.0 $\pm$ 3.3 mV/decade for n=4 sensors. The sensitivity of the four sensors, from two batches, is shown in figure Figure 4.10B. The sensitivity of fully printed pairs was about 4 mV/decade less than the sensitivity of ISEs measured against glass references, owing to the slight sensitivity of the printed references themselves to nitrate. Again, E_0 variation is considerable, particularly from batch to batch. This is expected given the batch-to-batch variability of the ISEs and the sample-to-sample variation of printed REs.
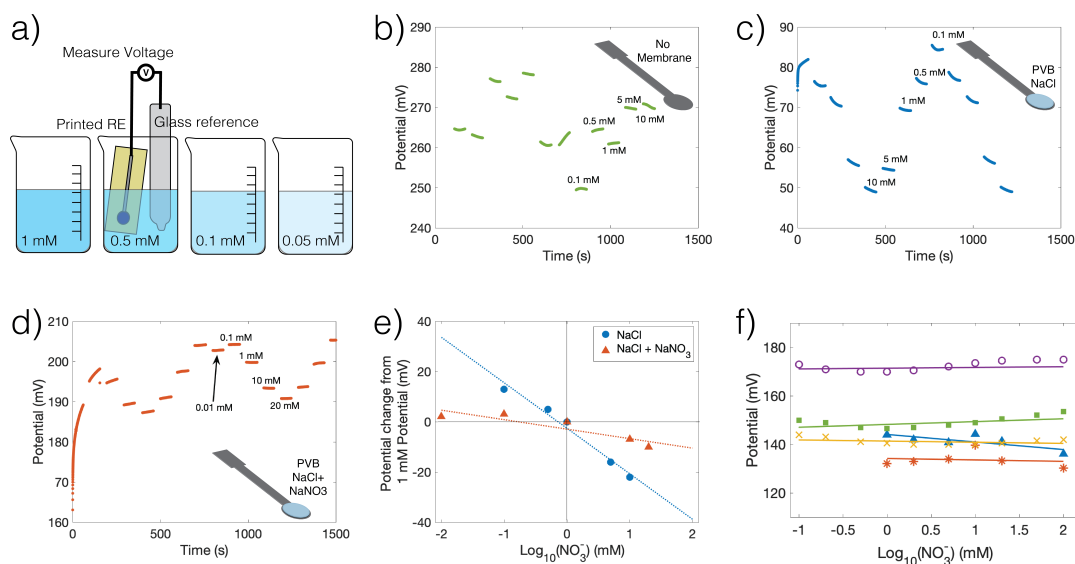
Figure 4.9: Printed nitrate-selective reference electrode membrane optimization. A) Measuring a printed reference electrode against a commercial reference electrode in NaNO$_3$ solutions of varying concentrations. Potential over time in changing concentrations of nitrate of a printed Ag/AgCl reference electrode with B) no added membrane, C) PVB membrane with NaCl added, and D) PVB membrane with NaCl and NaNO$_3$ added. Measurements in B-D were done against a commercial Ag/AgCl reference electrode. E) Sensitivity of printed reference electrodes with NaCl in PVB membrane (blue) NaNO$_3$ and NaCl in PVB membrane (red). The absolute value of the voltage measured at 1 mM NaNO$_3$ has been set to 0 mV to facilitate the comparison of slopes. F) Sensitivity of five printed reference electrodes to NO$_3$ is 2.96 ± 1.9 mV/decade.
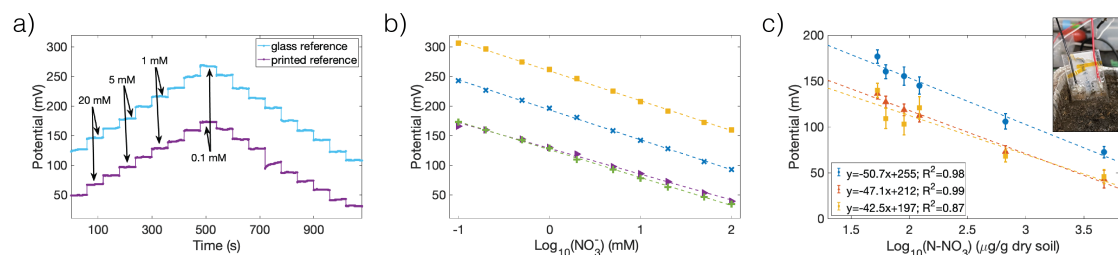
Figure 4.10: Printed nitrate sensor sensitivity characterization. A) Potential over time for one ISE was measured against a commercial glass reference electrode and against a printed reference electrode. The change of reference electrode changed the E_0 of the pair by 87 mV. B) Sensitivity curves for two batches of two printed pairs. The average sensitivity for these four electrodes is 48.0 ± 3.3 mV/decade. C) Potential versus nitrate concentration for three sensors in a high organic matter soil.

Fully printed sensors were measured in high organic matter soil from a field site in California. Six small pots of soil were prepared, and each was watered to saturation with a different concentration of KNO_3 solution. The printed sensors were inserted into each pot in turn, and the potential was recorded. Actual NO_3 concentration–including background NO_3^- already present in the soil prior to watering and was measured using standard techniques.

The relationship between the sensors' potential and the log of the concentration of nitrate is linear with R^2 values of 0.98, 0.99, and 0.87. The average sensitivity is -47 mV/decade, which is remarkably close to their sensitivity in an aqueous solution. These results are promising for the future application of printed ISEs in soil media and will be explored further in Chapter 5.

Selectivity Characterization

Soil is a complex environment containing a host of ions other than NO_3^-. Ideally, nitrate ISEs should be insensitive to all ions other than NO_3^-, and REs should be stable regardless of the concentration of any ion. Selectivity studies quantify the degree to which these behaviors are true and identify elements that could cause measurement errors.

The Nicolsky-Eisenman equation describes the potential, E generated by a potentiometric sensor in the presence of interfering species[170].

$$E = E_0 + 2.3026 \frac{RT}{zF} log_{10}(a_A + \sum_B K_{A,B}^{POT}(a_B)^{\frac{z_A}{z_B}}) \tag{4.8}$$

It assumes Nernstian behavior for all ions, and interfering species' responses are weighted by their respective Nicolsky-Eisenman coefficient, $K_{A,B}^{POT}$, where A is the primary ion (nitrate, in this case) and B is the interfering species. $K_{A,B}^{POT}$ should be less than 1, and the nearer to zero, the less sensitive the ISE is to that interfering species.

Based on a soil chemistry report from A & L Western Agricultural Laboratories, we selected eight possibly interfering species to test for: sulphate (SO_4^{2-}), chloride (Cl^-), phosphate (PO_4^{3-}), nitrite (NO_2^-), ammonium (NH_4^+), calcium (Ca^{2+}), potassium (K^+) and magnesium (Mg^+). Higher concentrations of SO_4^{2-} and Cl^- were also tested because they rank above NO_3^- in the Hoffmeister series, so are of particular concern as interfering species. The concentrations of these chemicals and the complete salt used as the source of the ions are listed in table 4.3.

Ion-Selective Electrode Selectivity
The two-solution method, which is a mixed solution method described in[170] was used to determine the $K_{A,B}^{POT}$ values for the eight ions listed previously. In all cases, baseline E values were measured in 1 mM $NaNO_3$ and the interfering solutions contained both the interfering salt and 1 mM $NaNO_3$.

Reference Electrode Selectivity
Because REs should not have Nernstian responses to ions, equation 4.8 is not a good model for RE behavior. Instead, simple ΔE values are reported in table 4.3, where ΔE is the difference between the potential measured in 1 mM $NaNO_3$ and the potential measured in 1 mM $NaNO_3$ and the interfering salt.

As shown in Table 4.3 the $K_{A,B}^{POT}$ values for the ISEs and ΔE values for REs are quite small for most ions except Ca^{2+} at concentrations that are expected in soil. Ca^{2+}, however, had a significant impact on both the ISE and the RE, indicating that in soils with high concentrations of these elements, the sensor might be unreliable, or at least require site-specific calibration.

Table 4.3: Nickolsy-Eisenman coefficients for ions found in soil

Chemical	Concentration (ppm)	Concentration and salt used	$K_{A,B}^{POT}$ for ISE	ΔE for RE (mV)
Sulphate	20 ppm	0.2 mM Na_2SO_4	-0.087	-0.67
Sulphate	96 ppm	1 mM Na_2SO_4	-0.019	-4.33
Chloride	35.5 ppm	1 mM NaCl	0.064	0.33
Nitrite	30 ppm	0.65 mM $NaNO_2$	0.086	-0.67
Ammonium	10 ppm	0.55 mM NH_4Cl	0.012	-0.67
Potassium	600 ppm	15.3 mM KCl	0.317	-2.33
Magnesium	400 ppm	16.5 mM MgCl	0.004	3.67
Phosphate	20 ppm	0.2 mM Na_3PO_4	0.074	2.00
Chloride	5300 ppm	150 mM NaCl	0.002	2.67
Calcium	3000 ppm	75 mM $CaCl_2$	1.377	12.67

Table 4.4: Comparison of sensitivity, selectivity, and reference electrodes for nitrate-selective potentiometric sensors.

Fabrication Technique	ISE Materials	Sensitivity	Selectivity Ions	Reference Electrode Materials	Reference Electrode Characterization	Application	Reference
Screen printing, drop casting	AgCl, gel	−54	$H_2PO_4^-$, SO_4^{2-}, NO_2^-, CO_2	Commercial		Soil extraction	[11]
Screen printing	PTFE membrane	−57.2	$H_2PO_4^-$, SO_4^{2-}, Cl^-	Not specified		Wastewater	[171]
Drawing, drop casting	Pencil Graphite	−49.4	SO_4^{2-}, Cl^-, NO_2^-, OH^-	Commercial		Soil extraction	[6]
Stencil printing	Silver	−57	$H_2PO_4^-$, SO_4^{2-}, Cl^-	Ag/AgCl Paste		Soil slurry, pulses in soil	[17]
Laser Direct Writing & Drop Casting	LIG	−54.8		Ag/AgCl paint		Soil slurry, pulses in soil	[172]
Evaporation & dispenser printing	Gold & POT-MOS$_2$	−64	PO_4^{3-}, SO_4^{2-}, Cl^-, NO_2^-, HCO_3^-	Screen printed Ag/AgCl with Nafion	versus Cl^-	Soil slurry, pulses in soil	[13]
	Glassy carbon, graphene	−57.9	SO_4^{2-}, Cl^-	Commercial		Drinking water	[173]
Electrodeposition	Au-NP and PPy on glassy carbon	−50.4	PO_4^{3-}, SO_4^{2-}, Cl^-, Br^-	Commercial			[174]
Electrodeposition	Au-NP, PPy, & graphene oxide	−50	$H_2PO_4^-$, SO_4^{2-}, CH_3COO, HCO_3	Commercial		Soil Percolate	[175]
Drop casting	Graphene/TTF on glassy carbon	−59.1		Commercial			[176]
	CNT/ionic liquid on glassy carbon	−52.3 to −57.1	$H_2PO_4^-$, SO_4^{2-}, Cl^-, NO_2^-, CO_3^-, CH_3COO, F^-, Br^-	Commercial			[177]
Electrodeposition	PPy on wire	−54.1		Commercial		Pulses in soil	[178]
Inkjet printing & screen printing	Gold	−54.1	PO_4^{3-}, SO_4^{2-}, Cl^-, NO_2^-, NH_4^+, Ca^{2+}, K^+, Mg^{2+}	Screen printed Ag/AgCl with CNT & NaCl/NaNO$_3$	vs. NO_3^-, other ion interference	Field soil	This Work

Fully Printed Nitrate Sensor Selectivity
In addition to being insensitive to interfering ions, their presence should not lower the sensitivity of the ISEs to NO_3^-. The sensitivity of four sensors was measured between 0.1 and 100 mM concentrations of KNO_3 and NH_4NO_3 fertilizers, and 0.05 to 50 mM $Ca(NO_3)_2$. The sensitivities in KNO_3 and NH_4NO_3 fertilizers were -52.6±5 mV/decade and -51.1± 4 mV/decade, respectively, but -29.3±10.6 mV/decade in $Ca(NO_3)_2$. The impact of Ca^{2+} on sensor behavior is important because Ca^{2+} can be present at high concentrations in soil, and is used in fertilizers as well.

In a soil environment, any ions commonly found in soil (such as the eight listed here) can vary by several orders of magnitude, meaning even ions with small interference coefficients can cause inaccurate readings from a potentiometric ISE sensor. In Chapter **??**, we further investigate "the interference problem".

Stability Characterization

The final figure-of-merit for nitrate ISE sensors that we will discuss is stability. Stability is related to the lifetime of a sensor; It is the tendency for a sensor to behave in a predictable, unchanging, and expected manner. Naturally, all built things will gradually break down under the weight of entropy, but the degree to which a sensor resists these changes and persists in its intended function is called stability.

Measuring a sensor's potential drift and/or reproducibility is the most direct method for understanding a sensor's stability. However, in the case of potentiometric ISE sensors, several other techniques for diagnosing possible causes of sensor drift, including water layer tests, chronopotentiometry, and electrochemical impedance spectroscopy (EIS).

Drift
The simplest and most common way of describing a sensor's stability is to characterize the sensor's drift. To characterize the drift of a potentiometric ISE sensor, all one has to do is place the sensor in a known concentration of primary analyte solution for a period of time while intermittently sampling the output signal. When the polarizable ISE reaches steady-state equilibrium in the solution, it exhibits the same potential as a galvanostatically charged capacitor:

$$E = E^0 + i\left(R + \frac{t}{C}\right) \tag{4.9}$$

where i is current, R is the bulk resistance of the electrode, t is time, and C is the capacitance. The calculation for drift, then, is:

$$\bar{\dot{E}} = \frac{\Delta E}{\Delta t} = \frac{i}{C} \tag{4.10}$$

Where $\bar{\dot{E}}$ is the potential drift. When the measurement is done in 1 M of the primary analyte, then this is the 'standard potential drift'. According to Equation 4.10, to minimize drift, it is beneficial to have a large electrode capacitance and a small resistance to reduce the current[158]. We measured the potential of several nitrate ISEs over a 24h period and plotted them in Figure 4.11. By performing a linear regression of the potential over time, the drift then is the slope of the fit line. The nitrate sensors exhibited drift on tens of microvolts to several millivolts per hour. Considering a nitrate sensor with a near-nernstian response of -50 mV per decade and a drift of 1 mV per hour, then one would expect the sensor could be off by an entire order of magnitude after two days of continuous measurements. To stay within a 5% error bound over a 30-day period, the drift needs to be about 4 μV per hour or less.

Some researchers have been able to minimize potential drift to a few μV per hour[179;180]. However, not many demonstrate good stability over the course of weeks to months, which is desirable for the use-case of sensing chemicals in soil[13]. Figure 4.12 shows the drift of several ISEs from other research groups in recent years[163], with the green stars indicating the drift of the nitrate ISEs in Figure 4.11.

It should be noted that Figures 4.11 and 4.12 showcase the drift that is attributable to the ISE alone - but of key importance is the fact that it is impossible to measure ISE drift directly due to variations in other potential differences in other parts of the measuring system, such as the liquid junction potential of the reference electrode, or oxidation and corrosion at dissimilar metal interfaces.

Reproducability
For potentiometric ISEs, the effect of potential drift can also be seen if a set of ionic solutions are measured repeatedly over a period of time. When this is done, one will see that the difference between the measured potentials in the different solutions (i.e. the sensitivity) will remain about the same, but the absolute value generally drifts by several millivolts. The degree to which the sensitivity or the standard potential changes after a period of disuse is called the reproducibility of a sensor. Figure 4.13, for example, shows the response of the same printed nitrate sensor measured twice with an eleven-day gap between measurements.

Water Layer Formation
Perhaps the most common cause of drift in ISEs is the formation of an undesired
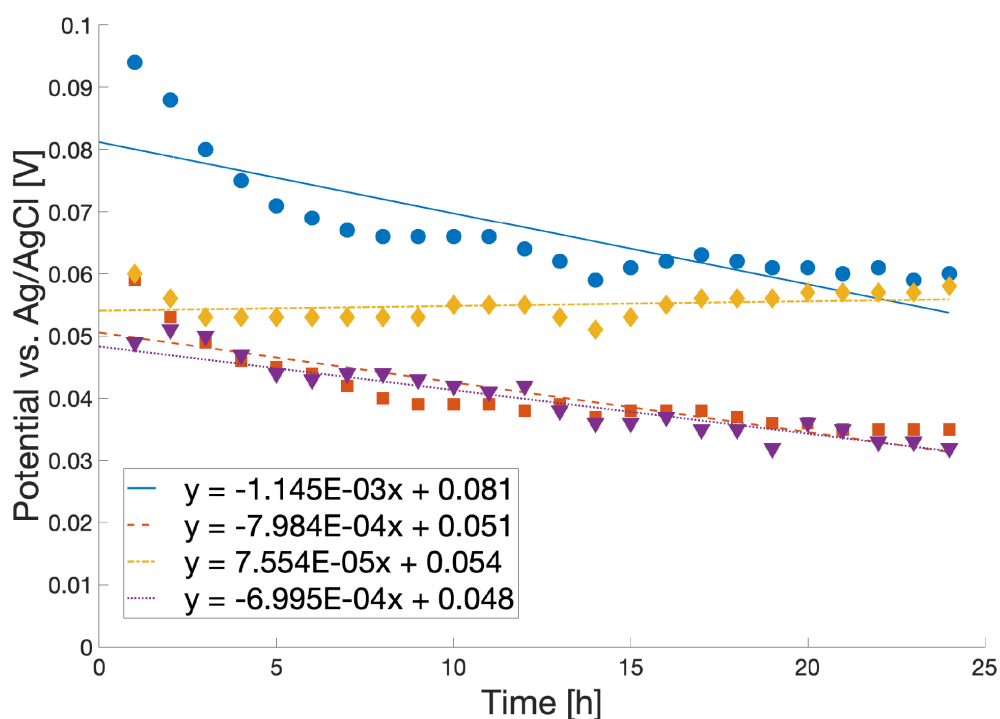
Figure 4.11: Potential drift of nitrate ion-selective electrodes. Four nitrate ion-selective electrodes were immersed in 100 mM NaNO₃ for 24 hours and their potential was recorded. The entries in the legend are equations of the linear fit with the slope in units of volts per hour.

water layer[181;182]. A 'water layer' in the field of ISE research refers to a small water layer (sometimes nanometer thickness or less) that can form between the conductor and transducer[181;183]. This water layer then acts as an unintentional electrolyte reservoir that re-equilibrates with any change in the bulk sample composition[183].

Several mechanisms can cause the formation of a water layer. If the ISM and transducer layer do not have good contact with the subsequent layers and do not form a hydrophobic seal, then it is possible for the bulk solution to 'fill in' the space by capillary force, not unlike water soaking into a napkin or paper towel. However, if there *is* a good seal in different layers, it is still possible for a water layer to form. For example, if the microstructure of the ISM contains 'pinholes' (tube-like voided discontinuities in the polymeric matrix), water can likewise transport through
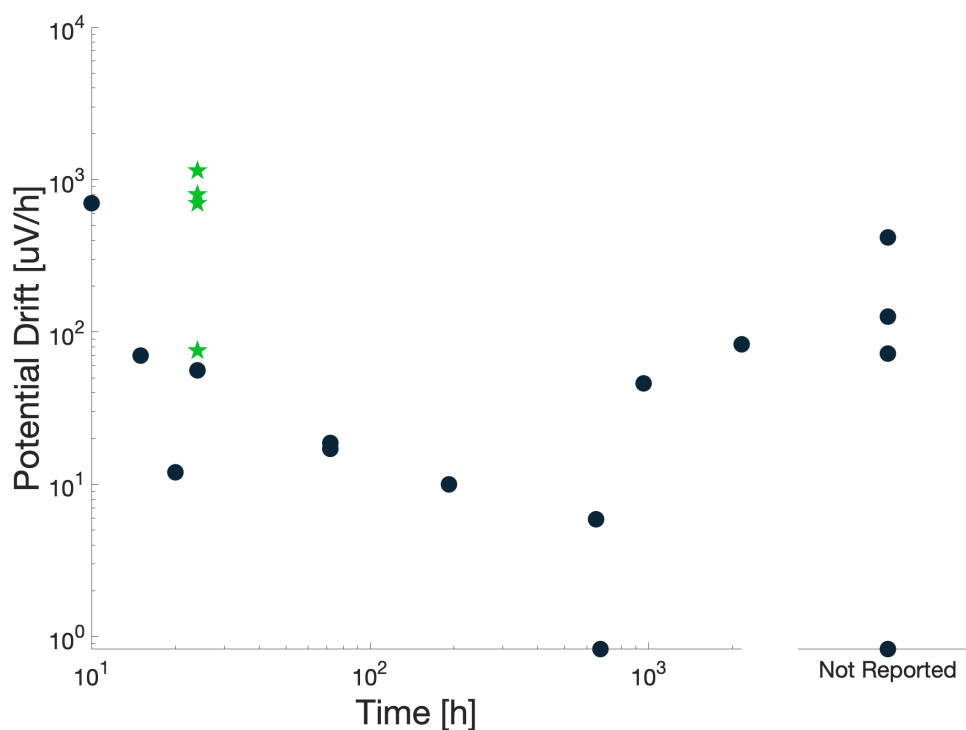
Figure 4.12: Recorded drift rate of several ion-selective electrodes in literature, reported in Rousseau *et. al.*[163]. The x-axis shows the time period over which the drift was calculated. The green stars indicate the drift of the nitrate ISEs from Figure 4.11

these channels to the layers below. Pinholes can be avoided by careful deposition techniques or by making thicker ISM layers. For the latter, the likelihood of forming a pinhole penetrating through the entire membrane is inversely proportional to the membrane thickness. Finally, even if there is a hydrophobic seal and there are no pinholes, water will still diffuse through the membrane to some degree, as the diffusion coefficient of a typical PVC membrane is on the order of 10^-8 cm^2/s[184]. This is why PVC and other hydrophobic polymers are frequently chosen as the polymer matrix - their high level of hydrophobicity and small diffusion coefficients make it so the water diffusion rate through the ISM is negligible.

A simple test to determine if a water layer is forming within an ISE was designed by Fibbioli *et al.*[181] and is now widely used within the field of polymeric ISE research.
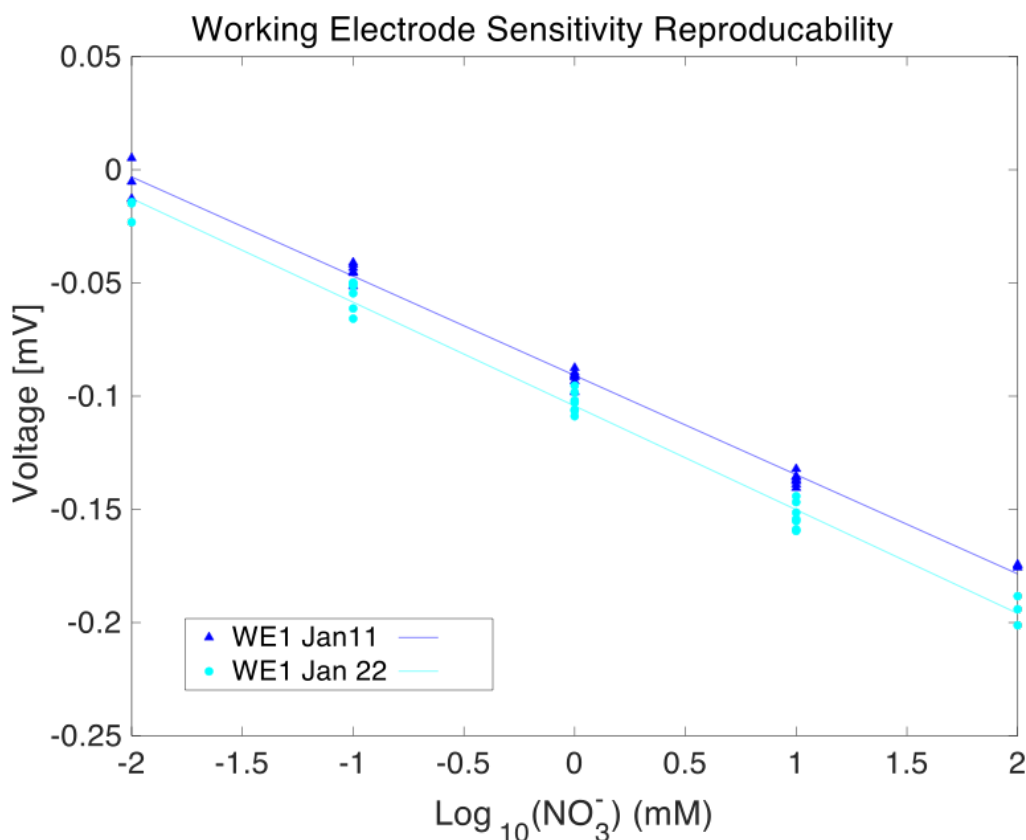
Figure 4.13: Reproducability of nitrate ion-selective electrodes sensitivity.

As it has come to be known, the' water layer test' is a relatively simple three-part potentiometric measurement[185]. First, the ISE is conditioned in a concentrated (say, 100 mM) solution of its primary analyte. Then, the electrodes are moved to a concentrated solution of a known interfering analyte. Finally, the electrodes are placed back in the concentrated solution of the primary analyte. The electrode potential is continuously recorded against a commercial Ag/AgCl RE following each exposure to the different solutions. The duration that the electrodes need to be soaked in each solution depends on the thickness of the membranes and the ISE response. Each exposure lasts several hours, and some experiments lasting up to 45 hours have been reported[186;187]. A schematic describing the water layer test for a nitrate ISE is shown in Figure 4.14.

Figure 4.15 shows the water layer test performed on the nitrate ISE. In this
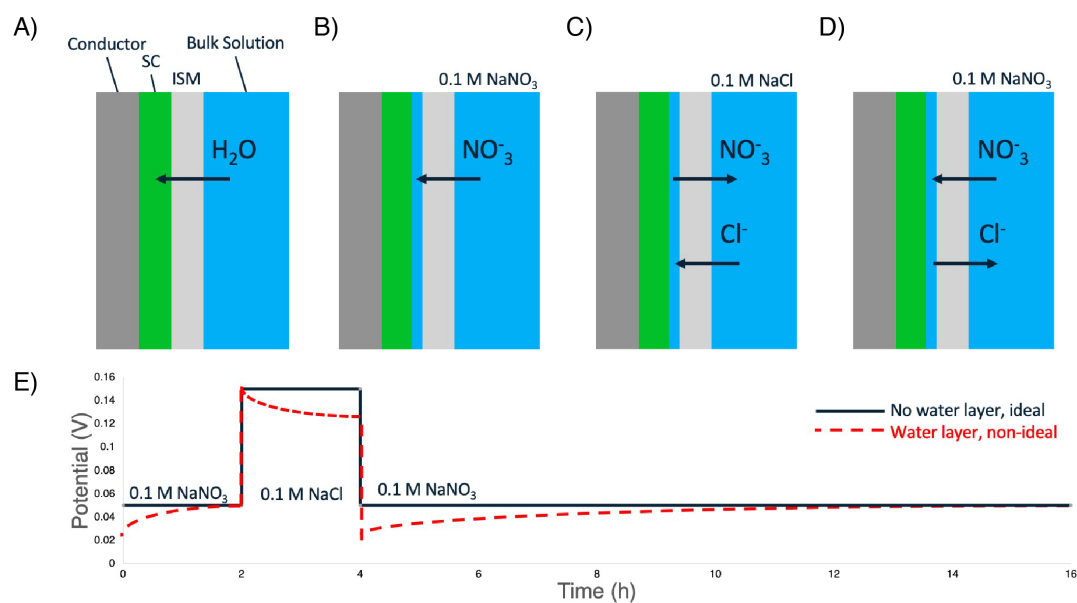
Figure 4.14: Schematic illustration of fluxes and recorded potential transients in the aqueous water layer test with a solid-contact nitrate-selective electrode. A) Formation of an aqueous water layer due to water transport B) NO_3^- ion concentration in the aqueous layer increases during conditioning in a primary (NO_3^-) ion solution, causing a negative potential drift. C) Replacing the NO_3^- ion solution to an interfering (Cl^-) ion solution reverses the flux of NO_3^- ions and the potential drift as NO_3^- ion concentration decreases and Cl^- ion concentration increases in the aqueous water layer. D) Returning the electrode into the primary NO_3^- ion solution causes a readjustment of NO_3^- concentration in the aqueous layer, resulting in a potential drift in the positive direction.
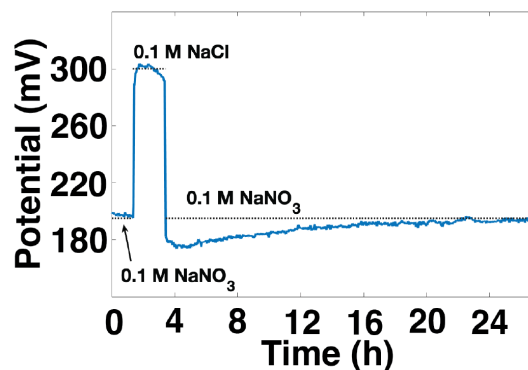
Figure 4.15: Water layer test of nitrate ion-selective electrodes. The nitrate ion-selective electrode was placed in 100 mM NaNO$_3$ for two hours, then 100 mM NaCl for two hours, followed by 100 mM NaNO$_3$ for 24 hours.

water layer test, 100 mM NaNO3 was used as the primary solution, and 100 mM NaCl was the interfering solution. First, the ISE was conditioned in 100 mM NaNO$_3$ until it was stable. The final hour of stable output in NaNO$_3$ is shown, followed by two hours in the interfering solution, and returning to NaNO$_3$ for 24 hours. The potential shows some drift during both the NaCl step and the NaNO$_3$ return, which could indicate the presence of a water layer on the electrode's surface, which is not unexpected for this type of coated-wire electrode. However, the electrode's stability is on par with values reported in the literature, which involved specific modifications for stability. The difference between the potential immediately before and the potential immediately after the NaCl step is 15 mV, the same as found by Chen *et. al.* for electrodes using gold nanoparticles and Polypyrrole (PPy) to improve stability[188].

Chronopotentiometry
Another technique for investigating the stability of an ISE is current-reversal chronopo-tentiometry. Recall that in Equation 4.10, potential drift is inversely proportional to the capacitance of the ISE. Current-reversal chronopotentiometry is a technique that allows one to find the capacitance of an ISE[189]. Current-reversal chronopotentiom-etry is a three-electrode electrode technique with the ISE as the working electrode (WE), a commercial Ag/AgCl electrode as the RE, and a glassy carbon electrode as the counter electrode (CE). The WE is polarized with a few nanoamps of current (usually 1 nA) while the electrode potential is recorded[189]. Rearranging Equation
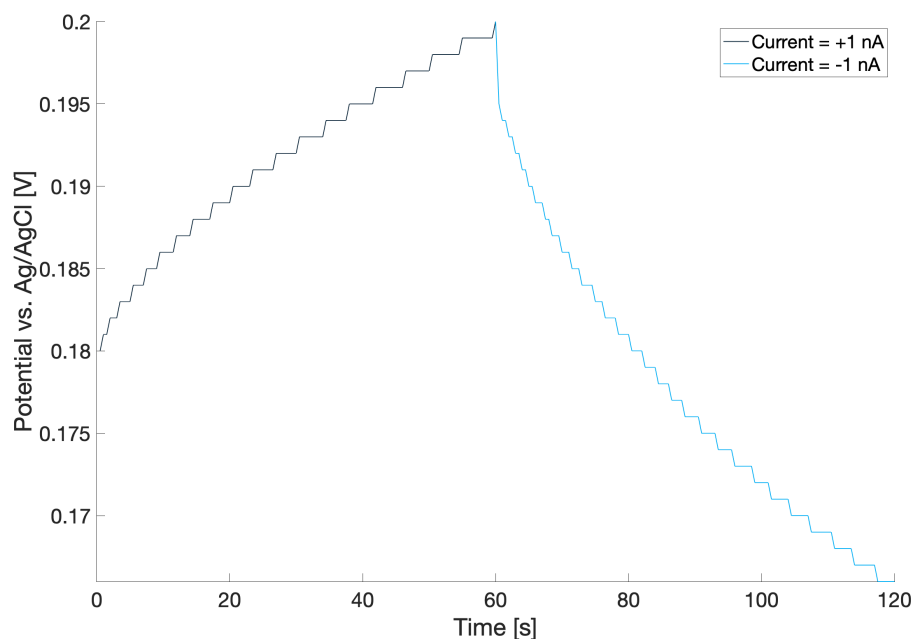
Figure 4.16: Reverse-current chronopotentiogram of the nitrate ion-selective electrode recorded in 100 mM NaNO$_3$.

4.10 allows one to solve for the capacitance from the rate of potential change and the current input. After a short period of time, the current flow is reversed, and the bulk resistance of the electrode can be calculated from the ohmic drop when the current is reversed by rearrangement of Equation 4.9.

A nitrate ISEs was configured into the three-electrode system described above and submerged in 100 mM NaNO$_3$. A +1 nA current was applied for 60s, at which point the current was reversed to -1 nA for another 60s. The potential is plotted over time in Figure 4.16.

The differences in the electrical parameters of the electrodes reflect the differences in their potentiometric response[177]. The total resistance of the electrode is calculated using the expression $R_{tot} = \frac{E}{2i}$, where i is 1 nA[177]. The drift, $\frac{\Delta E}{\Delta t}$, is calculated by fitting a linear regression to the slope of the charge cycle, where the slope is the drift rate. Finally, the capacitance is calculated as $C = i/\frac{\Delta E}{\Delta t}$. We found that the electrode has a total resistance of 2.5 MΩ, a drift of 0.3 mV/s, and a capacitance of 3.4 μF. These numbers are in good agreement with other works[177;189], though the
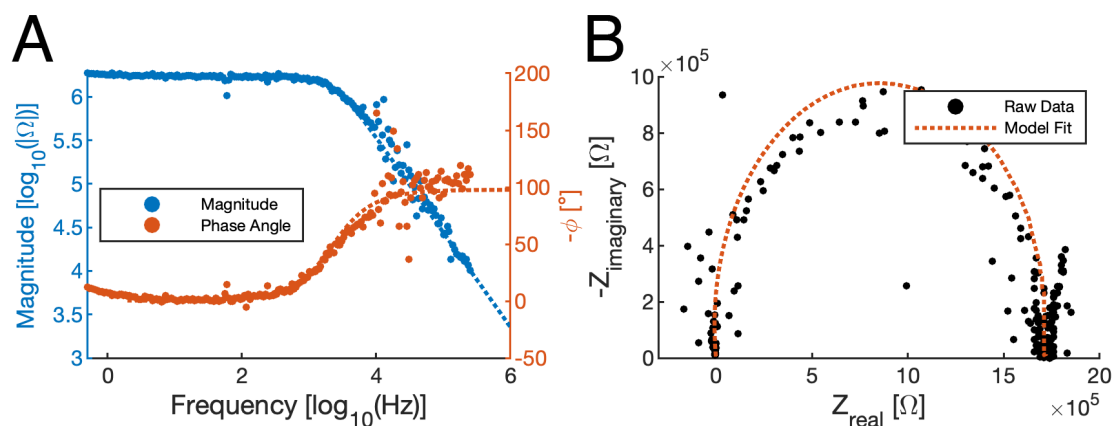
Figure 4.17: Impedance spectra of the nitrate ion-selective electrodes. A) Bode plot. B) Nyquist plot.

electrode's capacitance is smaller by one or two orders of magnitude. This makes sense due to the lack of a transducer layer on these electrodes, which motivates the inclusion of a transducer layer to increase the electrode capacitance to decrease the drift.

Electrochemical Impedance Spectroscopy

EIS is an electrochemical technique that provides in-depth information about the dielectric properties of solid-state ISE sensors [177;183]. EIS can also identify water layers, pockets of water in membrane pores, and pinholes. Finally, EIS characterizes the contact resistance of the boundaries between layers, which should be minimized to ensure a hydrophobic seal and reduce the ISE impedance.

The nitrate ISEs were configured in a three-electrode system, with the ISE as the WE, a commercial Ag/AgCl electrode as the RE, and a glassy carbon electrode as the CE. The three electrodes were immersed in 100 mM $NaNO_3$ solution and the impedance spectra were recorded in the frequency range of 0.5 Hz - 200 kHz. The Bode plot is shown in Figure 4.17A, and the Nyquist plot is shown in Figure 4.17B.

The electrode demonstrated a bulk impedance of 1.72 MΩ. Higher bulk resistance of ISEs with PVC and DBF-based membranes has been previously reported, which could be accounted for by membrane thickness and the lack of a transducer layer in our device.

4.5 Concluding Remarks

In this chapter, we have demonstrated nitrate sensing elements for measuring nitrate in soil - the primary component of fertilizers and the most important ingredient for plant growth. We designed and fabricated fully printed potentiometric nitrate sensors comprised of a printed nitrate ISE and printed RE. The printed nitrate ISEs showed a near-Nernstian sensitivity of -54.1 mV/dec $\pm$ 2.1 mV/dec when paired with a glass RE. A printed RE with low sensitivity to nitrate was developed using a membrane composed of PVB, NaCl, and $NaNO_3$. Fully printed nitrate sensors demonstrated a sensitivity of -48.0$\pm$ 3.3 mv/dec in solution and -47 mV/decade in soil. The printed sensors were selective to nitrate and did not have significant sensitivity to sulfate, chloride, phosphate, nitrite, ammonium, potassium, or magnesium at concentrations found in soil, though calcium does interfere with the sensors' behavior. The sensors are as stable as many other potentiometric ISE sensors in the literature but are not yet stable enough for long-term use in agricultural settings. Implementation of a transduction layer, and increasing the membrane thickness would likely increase the sensor stability.

The nitrate ISE sensors discussed in this chapter are not really *sensors* by the definition we outlined in Chapter 1. Rather, they are only the *sensing element*, and they need to be incorporated into a sensor circuit in order to properly communicate their measurements, as discussed in Section 1.5. In Chapter 5, we will explore what it would take to implement nitrate ISE sensors into a sensor circuit, and more importantly, how to integrate these sensors into a precision agriculture system.

Chapter 5

Implementation of Nitrate Sensors for Agricultural Applications

How love burns through the Putting in the Seed
On through the watching for that early birth
When, just as the soil tarnishes with weed,
The sturdy seedling with arched body comes
Shouldering its way and shedding the earth crumbs.
– Robert Frost

5.1   The Argument for High-Density Soil Sensing in Agriculture

Precision agriculture offers a pathway to increase crop yield while reducing water consumption, carbon footprint, and chemicals leaching into groundwater. Precision agriculture is the practice of collecting spatial and temporal data in an agricultural field to match the inputs to the site-specific conditions[190]. While industrial agriculture seeks to maximize crop yield, there is also the consideration of maintaining a healthy ecosystem. Fortunately, these are not competing interests; Numerous case studies have demonstrated that adopting precision agriculture techniques increases crop yield while lessening detrimental environmental effects[190–194].

Consider first the use of irrigation in agriculture, which accounts for approximately 36.7% of the freshwater consumption in the U.S.[195], 65% in China[196], and

77% in New Zealand[197]. Part of why so much water is used in agriculture is, quite simply, because crops need a lot of water to grow. For example, high-production maize crops require 600,000 gallons of water per acre per season - that's an Olympic swimming pool's worth of fresh water per acre[198]! Adopting precision agriculture practices - such as variable-rate irrigation - have proven to reduce water consumption by 26.3%[197;199].

Meanwhile, fixing nitrogen from the air to produce fertilizers is an extraordinarily energy-intensive process[200–202] and accounts for nearly 2% of the U.S.'s annual CO_2 emissions[203]. Crops recover only 30-50% of nitrogen in fertilizers[204], which means that over half of the nitrogen becomes a potential source of environmental pollution, such as groundwater contamination, eutrophication, acid rain, ammonia redeposition, and greenhouse gases[205]. Fortunately, precision agriculture practices have demonstrated an increase in nitrogen use efficiency[192;206;207], thereby reducing both the production volume of fertilizer as well as the amount that is polluted into the environment.

We began this exploration from the (no pun intended) ground-up. First, we investigated how many sensors are needed to inform a precision agriculture system. The results of that work informed the design of nitrate sensor nodes to fulfill those specifications, and lab-scale versions of those nodes were fabricated and tested in greenhouse experiments. After these WiFi-enabled nitrate sensor nodes were validated, we replaced the components of the nitrate sensor node with naturally-degradable alternatives to realize a no-maintenance version of the sensor node. The fabrication methods were scalable and low cost, while the sensors were comparable to their non-degradable twins. Such sensors could be widely distributed throughout a landscape to map nitrate movement through the watershed, inform the efficient application of fertilizer, or alert residents to elevated nitrate levels in drinking water.

5.2 Optimized Placement of Agricultural Soil Sensors

Background

Accurate soil data is crucial information for precision agriculture[208]. In particular, the moisture content[209–211] and the concentration of various chemical analytes[212–215] in soil have a significant influence on crop health and yield. These properties vary considerably over short distances, which begs the question: What spatial density does soil need to be sampled to capture soil variability? Half of the

5.2 - Optimized Placement
of Agricultural Soil Sensors

5.3 - Nitrate Sensor
Nodes

5.4 - Naturally-degradable
Nitrate Sensor Nodes

5.5 - An Agricultural Wireless Sensor Network
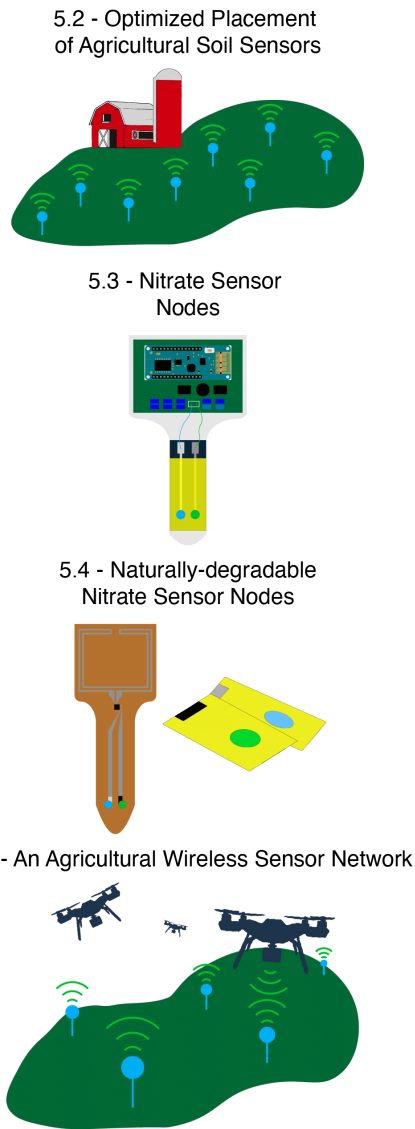
Figure 5.1: Visual outline of Chapter 5. In Section 5.2 we will investigate the demand
for soil sensors in precision farming. Section 5.3 will explore the implementation of
nitrate sensors into a soil sensor node. Section 5.4 will describe the design, fabrica-
tion, and testing of naturally-degradable nitrate sensor nodes. Finally, Section 5.5
will propose a paradigm for sampling data from the distributed sensor nodes using
UAV drones.

spatial range, referred to hereafter as the 'half-variogram range'[216], can be used as a "rule-of-thumb" to account for the spatial dependency of agricultural measurements[217]. The variance of a measurand, z, as a function of distance is empirically given by:

$$\hat{\gamma}(\vec{h}) = \frac{1}{2} \cdot \frac{1}{N(\vec{h})} \sum_{i=1}^{N(\vec{h})} \left[z\left(\vec{x}_i + \vec{h}\right) - z\left(\vec{x}_i\right) \right]^2 \tag{5.1}$$

where $\hat{\gamma}$ is the variance, $z\left(\vec{x}_i\right)$ and $z\left(\vec{x}_i + \vec{h}\right)$ are the measured values of the measurand z at $N(\vec{h})$ pairs of comparisons separated by the vector $\vec{h}$. Numerous studies have determined the spatial range of various soil properties in various soil conditions[213–215;217–222], which demonstrates the fact that the half-variogram range itself varies depending on the geographic location and sampling method[217]. Recently, Longchamps & Khosla analyzed and tabulated the spatial ranges of numerous soil properties reported in literature[223], which can be used as informed estimates for spacing sensors when no other information about the soil is known.

Geostatistically representative soil data can be collected with agricultural sensors spaced at the half-variogram range[217]. The data gathered from these sensors can be used to inform management techniques such as variable-rate technologies, which adapt to the heterogeneities of an agricultural field and thus enable site-specific management[224–230]. For example, farmers could tailor their nitrogen and water management to site-specific conditions[231], which would, in turn, reduce nitric oxide emissions, increase yields, and reduce fertilizer use[192]. Other researchers have investigated the use of machine-learning algorithms as tools for decision-making in precision agriculture[232–235] however, to the best of our knowledge, no authors have optimized agricultural soil sensor placement using the half-variogram range to inform the placement of sensors.

In this work, we developed a sequential gap reduction (SGR) algorithm that determines an optimal distribution of soil sensors across several types of agricultural fields. We use the half-variogram range of nitrate as the basis for sensor distribution in four agricultural field shapes: a circular field, a rectangular field, a field with both circular and rectangular features, and a field shape determined from an image.

Theory

Digital expression of an agricultural field

Similar to how an agricultural field can be defined in the real world as a geographic
area at a location, a digital representation - or 'simulation' - of an agricultural field
can be defined as many discrete pixels, where each pixel's position corresponds to a
geographic coordinate and its size to an area. Here, we briefly discuss three methods
of expressing an agricultural field in a digital format.

For agricultural fields that a simple geometric shape can approximate - such as
a rectangular farm or a central-pivot farm - expressing the farm digitally is trivial.
For a rectangular-shaped field, we discretize the space into a grid of uniform pixels
with dimensions proportional to the length and width of the physical domain. For a
central-pivot field, we bound the field in a square grid of uniform pixels, loop through
each pixel in the grid, and add the pixel to a list if that pixel's coordinates are equal
to or less than the field's radius. This technique is demonstrated in Figure 5.2A for
a rectangular-shaped field and in Figure 5.2B for a central-pivot field.

When the boundaries of the agricultural field are not regularly shaped, we define
the field by a list of consecutive coordinate points that, when piecewise connected
by polynomial curves, form an enclosed shape. Here, we adopt a simple ray tracing
algorithm to determine whether or not a pixel is inside or outside of this bound-
ary[236;237]. Given an enclosed boundary and a point in space, if one were to draw
an infinite vector in any direction originating from that point, it will intersect the
boundary an odd-numbered amount of times if-and-only-if the point is within the
enclosed space, which is shown in Figure 5.2C. This holds for all points in space
except for points on the boundary, which must be determined explicitly. In this way,
we use the coordinates of each pixel as a point to determine if a pixel is inside the
boundary and append it to a list.

Finally, satellite or drone visible-spectra images of agricultural land are already
stored in a digital, pixelized format. Such images and datasets are widely available
from Google Earth, NASA Earth Observatory, or the USDA cropland data layer.
Computer vision techniques can differentiate the arable land on a field from ob-
structions (such as roads, buildings, trees, and ponds) and store those pixels in a
list[238–240]. This process is visualized in Figure 5.2D.

In all cases, it is essential to note the physical dimensions that a single pixel
represents. It should also be noted that because each method requires discretization
of the field, the results are approximations whose accuracy increases proportionally
to the number of pixels used.
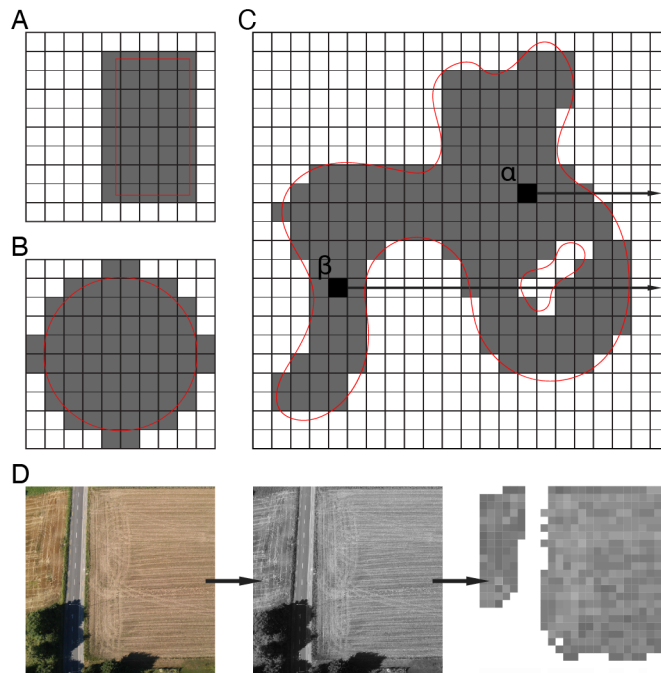
Figure 5.2: Methods of defining agricultural fields in a digital domain. A) Rectangular fields were defined by discretizing the field into a grid of uniform pixels proportional to the length and width of the physical field. B) Central-pivot fields were defined by superimposing a uniform grid of pixels over the field and appending all pixels whose coordinates are within the radius of the pivot arm to a list of field pixels. C) Irregularly shaped fields were defined by superimposing a uniform grid over the field and appending all pixels whose rays pass through an odd number of boundary lines. In this case, pixel α has a ray that passes through a single boundary line, while pixel β has a ray that passes through five boundary lines. D) Digital images of agricultural fields are in a digital domain by definition but require computer vision techniques to determine which pixels in the image correspond to arable land.

Optimized Sensor Placement

The optimal layout of sensors in an agricultural field is achieved when, using the fewest number of sensors possible, all points in the field are statistically represented by the data collected by sensors in that field. For a given sensor, the data collected from that sensor is statistically significant for all points within a radial distance equal to the half-variogram range of that sensor[217]. Thus, if we consider an agricultural field a two-dimensional collection of pixels, we can model sensors as circles with a radius equal to the half-variogram range. Using this definition for placement, our problem is similar to the circle packing problem. Circle packing (or more broadly "object packing") is a well-researched area in mathematics that has many practical applications[241]. Object packing aims to fit as many of some objects within a domain as possible without any overlap. There are several algorithms that aim to optimize object packing, such as random sequential addition[242], the Metropolis algorithm[243], and various particle growth schemes[244? –246]. The limit of packing efficiency for equal-size circles in two dimensions is about 91% for a hexagonal grid[247]. While circle-packing nearly describes our model problem, there is one major caveat: no physical justification prevents the circles (sensors) from overlapping one another. This 'soft boundary' makes it possible to achieve 100% coverage of the domain by allowing overlap. If the only objective was to maximize the effective areal coverage of the field, then one could distribute sensors next to one another without discretion. However, the monetary cost of sensors, sensor operation, and sensor maintenance makes this approach unreasonable, which motivates our stated objective of maximizing field coverage with the fewest number of sensors possible.

We developed and applied the SGR algorithm to place sensors within the field to minimize the overlap of each sensor's coverage radius. The general process is as follows:

1. **INITIALIZE:** Select a random pixel in the field and place a sensor there

2. **GENERATE:** Select a random pixel in the field

3. **TEST:** Check to see if a sensor placed at that pixel would overlap with any other sensor already set in the field. If not, append that pixel to the list of placed sensors within the field.

4. **SCORE:** Compute the score of the design.

5. **ITERATE:** If the score is below the threshold, iterate through the algorithm.

The outcome of this algorithm is that sensors are placed throughout the field such that sensors are placed in the largest gaps between sensors. This is done by incrementing the acceptable distance between sensors by a small amount and then making many attempts at placing a sensor before repeating the process. We score the fitness of each placement design by the ratio of the number of field pixels that are within the half-variogram range of a sensor to the total number of pixels in the field. In other words, what percentage of the field area is within the half-variogram range of one or more sensors? This process is repeated until it is impossible to place a sensor outside of the range of all other sensors in the design, or until the field is completely covered. The flowchart for this algorithm is shown in Figure 5.3A, and a schematic depicting the evolution of sensor placement in an arbitrary field shape is shown in Figure 5.3B.

Computational Methods

We encoded the two-dimensional problem for an agricultural field in a geographic coordinate system.

Digital expression of an agricultural field

We generated digital expressions of four types of agricultural fields to show the flexibility and range of the SGR sensor placement method. First, we generated a 50-hectare circular field with a $\frac{1}{2}$-mile (400m) radius. Second, we generated a rectangular-shaped 93-hectare field. Third, we generated a 22-hectare field with straight and curved boundaries. Finally, we generated a field from an image of pixels.

For each of the four fields described above, we defined the agricultural field with two Nx2 matrices of pixels. First, the domain of the problem was expressed as D, a N_{dp}x2 vector of values where N_{dp} was the number of pixels within the scope of consideration, and the two columns were the longitudinal and latitudinal coordinates, respectively. Similarly, the agricultural field is expressed as Ω, a N_{fp}x2 vector of values such that $\Omega \subseteq D$, where N_{fp} was the number of pixels within the bounds of field and the two columns were the longitudinal and latitudinal coordinates, respectively.

Optimized sensor placement

We optimized the distribution of sensors throughout the field using the SGR algorithm. The algorithm was as follows:
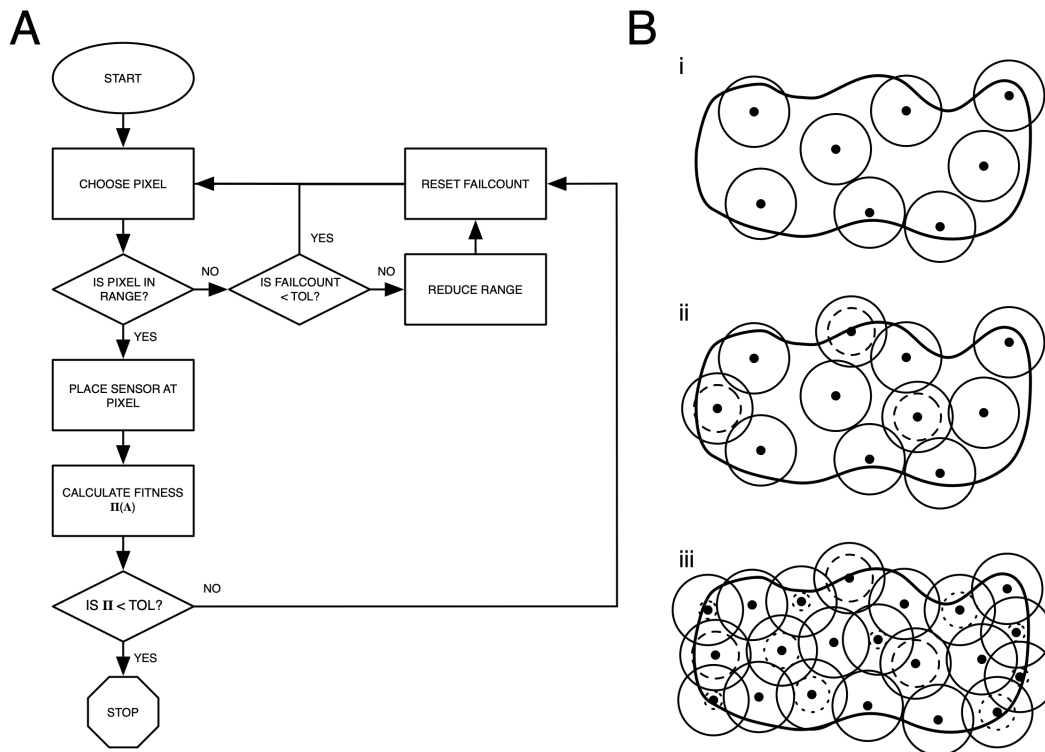
Figure 5.3: A) Flowchart of the Sequential Gap Reduction algorithm used to place sensors in a digitized agricultural field. B) Schematic depicting the action of the Sequential Gap Reduction algorithm. i) First, sensors are added to the field at randomly selected pixels within the field boundary so there is no overlap between the sensors' effective coverage radius. The sensors are depicted as small black circles, and the sensor's effective coverage area is depicted as a solid line encircling the sensor. ii) Once it is no longer possible to add more sensors this way, the minimum allowable distance between sensors is decreased - represented by a dashed circle - while the effective coverage area of the sensors remains the same. iii) This process is repeated until all gaps have been filled and all pixels within the boundary are within the effective coverage radius of at least one sensor.

1. **INITIALIZE:** For a given matrix of field pixels within the domain, $\Omega \subseteq D$, select a random pixel within the field Ω: $P = (p_x, p_y) \in \Omega$ and append it to $\bar{\Lambda}$, a N_sx2 vector of sensor coordinates, where $\Lambda_i = (\lambda_x, \lambda_y)$.

2. **GENERATE:** Select a random pixel within the field:
   $P = (p_x, p_y) \in \Omega$

3. **TEST:** For all Λ_i, if $||P - \Lambda_i|| \geq R$, $\Lambda \cup \{P\}$ where R is the half-variogram range

4. **SCORE:** Calculate fitness, $\Pi(\Lambda) = \frac{n(\Gamma)}{n(\Omega)}$, where $\Gamma \subseteq \Omega \mid TOL \geq ||\Gamma_i - \Lambda_i||$

5. **ITERATE:** If $\Pi \leq TOL$, loop to Step 2.

Results

The placement of sensors determined by the SGR algorithm is shown in Figure 5.4A-D. We used 40 meters as the half-variogram range, which is a conservative value for soil nitrate[223;248]. In Figure 5.4A, we determined the placement of sensors in a circular field with a 400-m radius, which is a standard length for a central-pivot irrigation arm[228]. Figure 5.4B shows the optimal placement of sensors for a rectangular farm field with dimensions corresponding to the average small-family U.S. farm[249]. As of 2017, small family farms make up 89% of farms in the U.S.[250]. Figure 5.4C demonstrates that the SGR algorithm could adapt and generate sensor placement for an arbitrary field shape defined by several boundary points. In Figure 5.4D, the SGR algorithm distributed sensors in a field generated from a digital image. The sensors were efficiently placed such that they cover all of the pixels of the image while ignoring the islands of non-field pixels, such as those in the 'a' and 'l'. In real-world applications, this image could be captured from satellite imagery, such as those available on Google Earth, ArcGIS, or other publicly available data sets.

A hexagonal-grid sensor distribution scheme is shown in Figure 5.4E-H. Hexagonal packing is the most efficient packing method known to date, and circles can be packed in two dimensions to completely cover an area when staggered by a distance of $R\sqrt{3}$ in the x-direction and $\frac{3R}{2}$ in the y-direction.

The field coverage for varying numbers of sensors for the SGR and hexagonal-packing schemes are shown in Figure 5.4I-L. The SGR algorithm outperformed the efficient hexagonal-grid distribution scheme when less than $\approx$95% of the field is covered for the circular and rectangular field types. Still, the hexagonal-packing method could cover the entire field with fewer sensors. This is because the SGR algorithm
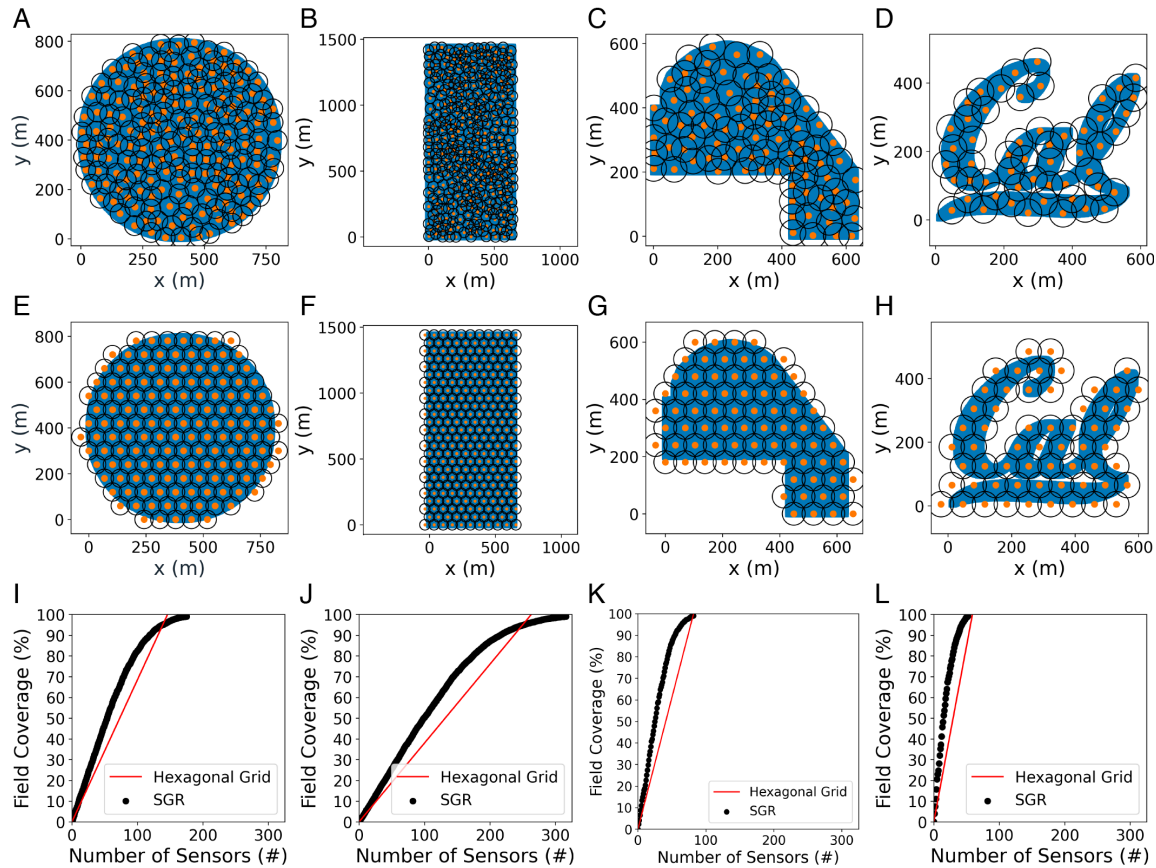
Figure 5.4: Sensor placement using the A-D) SGR algorithm and E-H) hexagonal grid distributions using a 40m half-variogram range as the effective sensing radius for various field types. The orange circular markers indicate the sensor coordinates, and the black ring around the sensor indicates the half-variogram range that the sensor covers. A-D) Sensor placement for the circular, rectangular, user-defined boundary, and fields generated from an image using the SGR algorithm. E-H) Sensor placement for the circular, rectangular, user-defined boundary, and fields generated from an image using a hexagonal grid spacing. I-L) Plots of the effective field coverage for a given number of sensors. The black curve is the field coverage for a distribution using the SGR algorithm, while the red line is for the hexagonal distribution.

prioritizes maximizing field coverage at each step, making it superior to other distribution schemes when the domain is sufficiently spacious. However, suppose the field shape is relatively simple, and the objective is to cover the entire field with sensors. In that case, the uniform distribution approach outperforms SGR because the field as the whole area can be covered with fewer sensors. As the complexity of the field becomes high, however, the SGR algorithm becomes preferential. The number of sensors required to cover the user-defined boundary type field shown in Figures 5.4C and 5.4G was the same. For the field generated from an image in Figures 5.4D and 5.4H, the SGR algorithm outperformed the hexagonal packing scheme for any number of sensors, as shown in Figure 5.4L, and required only 52 sensors to completely cover the field compared to 59 for the hexagonal packing method.

Conclusion

The proposed SGR algorithm maximizes the coverage of any arbitrarily-shaped agricultural field with fewer sensors than a grid-based distribution in most cases. These findings can be adopted for variable-rate irrigation applications and provide farmers with valuable data to decide how many sensors they wish to deploy for their particular agricultural field.

5.3   Nitrate Sensor Nodes

The work in the previous section indicates that hundreds or more sensors are required for the precision management of nitrate in agricultural fields. As a first step, we've developed convenient nitrate sensor nodes using a combination of printed nitrate sensors and conventional electronics.

Fabrication

The nitrate sensor nodes are hybrid electronic systems, consisting of a printed nitrate sensor interfacing with a conventional PCB containing signal conditioning electronics, a microcontroller, and communication electronics. The printed nitrate sensors were designed similar to those in Section 4.4, except that the gold electrode was replaced with a carbon electrode. The carbon electrode functions as a hybrid conductor and transducer layer owing to its high specific surface area and conductivity. First, fully-printed nitrate ion-selective electrodes (ISEs) and Ag/AgCl reference electrodes

(REs) were made on separate substrates. Afterward, the electrodes were cold-sintered to wires and connected to a custom WiFi-enabled circuit mounted on a support stake.

Ion-selective Electrode Fabrication

Carbon electrodes with 3.5 mm diameter circles connected to a 1 mm wide trace were screen printed on 100 μm thick polyethylene terephthalate (PET) using Creative Material's 114-34A/B-187 carbon ink (Creative Materials, Ayer, MA). The printed carbon electrodes were allowed to dry overnight and then encapsulated with 75 μm thick laser-cut Teflon tape with circular windows of 5 mm diameter for the active area. The window in the encapsulant was larger than the electrode to allow space for the membrane to seal to the substrate, preventing bubbles or delamination of the membrane. The nitrate selective ISMs were fabricated by mixing 5.2 wt% Nitrate Ionophore VI, 47.1 wt% dibutyl phthalate, 0.6 wt% tetaroctylammonium chloride, and 47.1 wt% PVC. A total of 0.2 g of this mixture was dissolved in 1.3 mL of THF, and 16 μL of the membrane solution was drop-cast on the printed carbon electrode surface and dried in a fume hood for 15 minutes.

Reference Electrode Fabrication

Ag/AgCl electrodes with the same geometry as the carbon electrodes were screen printed on 100 μm thick PET using Engineered Materials Systems, Inc. CI-4001 ink. After printing, the ink was dried with a hot air gun before printing the same pattern atop the previous layer, repeating this process until three layers were printed. The Printed Ag/AgCl electrodes were then annealed at 120 °C in an oven for two hours and encapsulated with 75 μm thick laser-cut Teflon tape.

The REs employed a CNT transducer layer between the Ag/AgCl electrode and the membrane. This transducer was composed of 0.01 g of CNT (iP-Single Walled Carbon Nanotubes from Carbon Solutions, Inc) and 0.05 g of F127 (poly(ethylene glycol)-block-poly(propylene glycol)-block-poly(ethylene glycol) diacrylate) dissolved in 10 mL of THF, which were sonified for 1 hour in an ice bath using a Branson Digital Sonifier probe. 11 μL of the resulting transducer cocktail was deposited onto the printed REs surface.

The salt membrane was made by dissolving 1.58 g of Butvar B-98 (poly(vinyl butyral) (PVB), 1.00 g of NaCl, and 1.00 g of $NaNO_3$ in 20 mL of methanol. The mixture was sonified for 30 minutes in an ice bath, and 16 μL of the resulting salt membrane cocktail was deposited on top of the CNT transducer. Unless otherwise noted, all chemicals used in ISE and salt membranes were obtained from Millipore Sigma.

Figure 5.5: Picture of a completed nitrate sensor node mounted on an acrylic stake.

Nitrate Sensor Node Assembly

After each electrode was made, they were cold-sintered to 22 AWG wire using 8331D
silver conductive epoxy (MG Chemicals, Burlington, ON, Canada) and encapsulated
with Gorilla 2-part Epoxy (Gorilla Glue Co, Cincinnati, OH). Then, the electrodes
were adhered to a laser-cut acrylic stake with Kapton tape. The wires were connected
to a custom printed circuit board (PCB) containing signal conditioning electronics
and a WiFi-enabled Arduino MKR1010 board. A completed stake is shown in Figure
5.5.

Characterization

The nitrate sensors were first measured directly using an IVIUM-n-stat. Afterward,
the nitrate sensor node circuit was calibrated by placing the device in aqueous so-

lutions of 0.1 mM - 1 M NaNO$_3$ while recording the output and transmitting the
timestamped data over WiFi. The nitrate sensor nodes were then characterized in
various soil experiments to demonstrate their potential for wireless readout in an
agricultural system.

Sensor-Only Measurements in Solution

After cold-sintering wires to the ISE and RE, but before connecting the wires to the
signal conditioning and PCB, the sensors were first characterized directly by connect-
ing the wires to an IVIUM-n-stat. The sensitivity of all sensors was recorded, while
water layer tests and electrochemical impedance spectroscopy (EIS) were performed
on a subset of the sensors following the same procedures outlined in Section 4.4.

Sensitivity
To characterize the sensitivity of the printed nitrate sensor, the ISE potential was
measured against the printed RE in varying concentrations of NaNO$_3$, shown in
Figure 5.6A. For this characterization, the sensors were cycled between 100 mM
and 0.01 mM in one-minute intervals while the potential was recorded, as shown
in Figure 5.6B . The 0.01 mM measurement showed a substantially smaller change
in potential compared to the other steps, indicating that 0.01 mM is less than the
linear range of the sensor. This is in agreement with other nitrate-selective sensors
in the literature, and so for the remaining analyses throughout this section, the 0.01
mM measurements are neglected when calculating the sensitivity. The sensitivity
of the carbon electrode nitrate sensors was -55.6 $\pm$ 3.5 mV/dec, which is about 8
mV/dec higher magnitude than the gold-electrode nitrate sensors in Section 4.4. The
sensitivity of the eight sensors is plotted together in Figure 5.6C.

Water Layer Test
As discussed in Section 4.3, one benefit of including a transducer layer is that it resists
the formation of a harmful water layer. This is highlighted in Figure 5.7, where we
compare the results of identical water layer tests between two gold electrode ISEs
from Section 4.4 against two carbon electrode ISEs used in the nitrate sensor nodes.
In this water layer test, 100 mM NaNO3 was used as the primary solution, and 100
mM NaCl was the interfering solution. First, the ISE was conditioned in 100 mM
NaNO$_3$ until it was stable. The final hour of stable output in NaNO$_3$ is shown,
followed by two hours in the interfering solution, and returning to NaNO$_3$ for 24
hours. In both plots, horizontal lines were superimposed on the figure equal to the
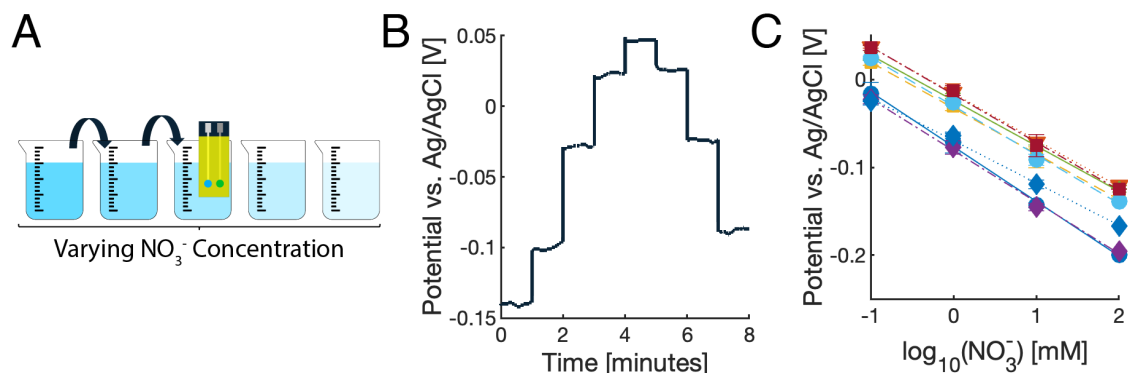
Figure 5.6: A) Characterization of the nitrate sensor in $NaNO_3$ solutions of varying concentrations. B) Potential over time for one printed nitrate sensor measured between 0.01 mM and 100 mM. C) Sensitivity curves plotted from 100 mM - 0.1 mM for seven nitrate sensors, showing high repeatability and near-Nernstian response of -55.6 $\pm$ 3.5 mV/dec.

potential at the two-hour mark when the sensors were transferred from the primary analyte solution to the interfering solution.

Electrochemical Impedance Spectroscopy

The nitrate ISEs were configured in a three-electrode system, with the ISE as the WE, a commercial Ag/AgCl electrode as the RE, and a glassy carbon electrode as the CE. The three electrodes were immersed in 100 mM $NaNO_3$ solution, and the impedance spectra were recorded in the frequency range of 0.5 Hz - 200 kHz. The Bode plot is shown in Figure 5.8A, and the Nyquist plot is shown in Figure 5.8B.

The electrode demonstrated a bulk impedance of 1.86 MΩ, which is larger than that of the gold electrodes. Higher impedance means less current flows through the device when operating, which improves the sensor's stability and lifetime. The small semi-circle from approximately 1.6 to 1.8 MΩ can be attributed to the impedance of the membrane:transducer interface, indicating that there is not a water layer being formed.

Sensor Node Calibration in Solution

After the sensors were characterized on the IVIUM-n-stat, the ISE and RE electrode wires were connected to the inputs of the signal conditioning circuit, which is func-
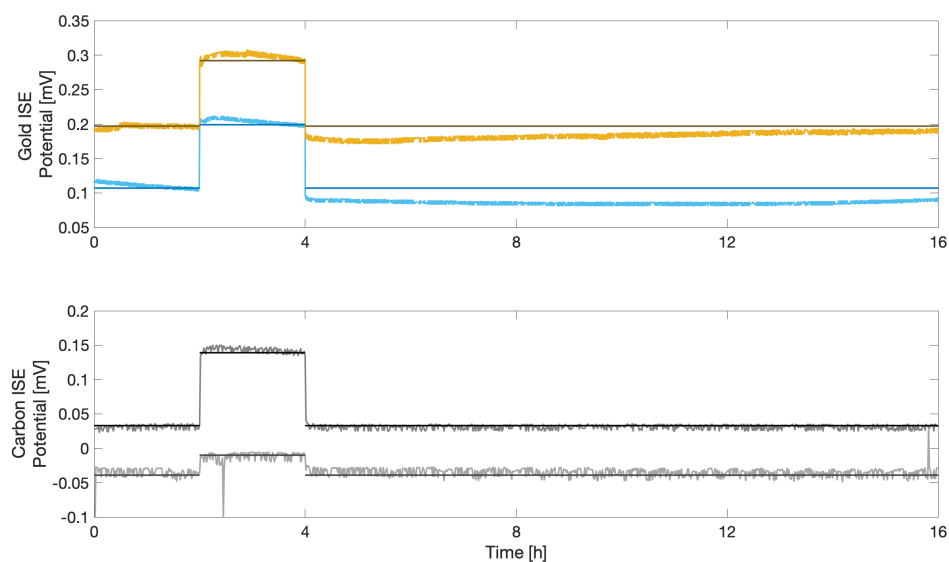
Figure 5.7: Comparison of the water layer test between gold and carbon conductor
ion-selective electrodes. Horizontal lines were superimposed in both plots equal to the
potential at the two-hour mark when the sensors were transferred from the primary
analyte solution to the interfering solution.
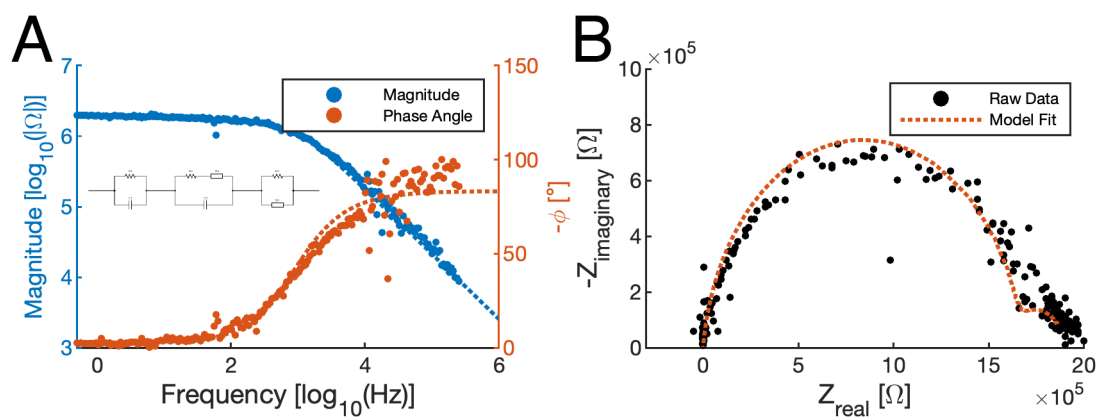
Figure 5.8: Impedance spectra of the nitrate ion-selective electrodes. A) Bode plot
with the equivalent circuit in the inset. B) Nyquist plot.

tionally a differential amplifier with buffered inputs. Each electrode is connected
to a buffer amplifier, and the outputs are passed to a differential amplifier. This
circuit is needed because, as discussed in Section 4.3, the input impedance needs to
be sufficiently high to minimize current flow through the device, which could oth-
erwise polarize the membranes and accelerate signal drift. Lab scale potentiostats
(such as the IVIUM-n-stat used for all previous measurements) are typically on the
order of 10^{12} Ω. In contrast, most commercial microcontrollers (such as the Arduino
MKR1010) only have an input impedance on the order of 10^8 Ω. From the EIS per-
formed on the carbon ISEs, shown in Figure 5.8B, we measured a bulk impedance
of 1.86 x 10^6 Ω, meaning an input impedance of at least 1.86 x 10^8Ω is needed to
reduce systematic error to less than 1%[163]. Table 5.1 shows the input impedances of
several voltmeters and potentiostats. Further, assuming that the ISE is outputting,
say, 200 mV, then the current flowing between the ISE and RE would be on the order
of 100 pA, while for long-term stability, sub pA currents are needed[163]. The circuit
we've implemented effectively increases the input impedance while not affecting the
amplitude of the differential output signal. In this case, the circuit we use increased
the input impedance from 10^8 Ω to 10^{10} Ω.

Table 5.1: Input impedances of several measuring devices

Instrument	Input Impedance
Fluke Multimeter	10^6Ω
DAQ970a	10^6Ω
Raspberry Pi ADC pin	10^6Ω
ESP8266 ADC pin	10^7Ω
Arduino ADC pin	10^8Ω
Keithley Potentiostat	10^{10}Ω
EmStat Pico	10^{12}Ω
IVIUM Potentiostat	10^{12}Ω

The microcontroller program was written in C using the Arduino IDE and up-
loaded to the MKR1010. On startup, the program initializes by connecting to the
local WiFi, updating to the local date and time, and assigning internal variables. It
then enters an infinite loop that averages the potential difference across the inputs
and uploads the result to a spreadsheet over WiFi at a user-specified sampling fre-
quency. The pseudo-code of the program is as follows:

Input : Two potentials corresponding to the ISE and the RE
Output: Time-stamped, time-averaged potentials uploaded to a cloud
spreadsheet
System Initialization;
while *running* **do**
> read ISE_Potential;
> read RE_Potential;
> sensorPotential = ISE_Potential - RE_Potential;
> sum = sum + sensorPotential;
> delay(readRate);
> **if** *time % uploadRate == 1* **then**
>> averagePotential = sum $\cdot \frac{uploadRate}{readRate}$;
>> cloudWrite(sensorID,averagePotential,time)
>
> **end**

end

Algorithm 1: Nitrate Sensor Node Pseudocode

The nitrate sensor nodes were calibrated in 0.1 mM - 10 mM $NaNO_3$ solutions, which encompasses the normal levels of nitrate found in agricultural soil[251]. A schematic of the process is shown in Figure 5.9A. The sensor nodes were initially placed in a 10 mM solution while the program ran on the microcontroller, uploading the recorded potential over WiFi to an online spreadsheet once per minute. Once the potential of the sensor stabilized, it was then moved to a 1 mM solution, followed by a 0.1 mM solution. The data plotted over time for a single sensor node is plotted in Figure 5.9B, corresponding to the same sensor from Figure 5.6B. Comparing the two figures, it is noted that the E_0 values do not overlap. There are two primary reasons for this. First, the sensor measurement is the sum of the boundary potentials, and because the interfaces of the metal contacts within a potentiostat are different than those in the PCB circuit, a different constant offset potential, E_0, is obtained from Equation 1.19. The second reason is associated with microcontroller design and how microcontrollers 'read' voltages from their input pins[252], which causes a positive potential bias in the reported measurements. These factors explain the large variation in E_0 shown in Figure 5.9C, which shows the calibration plot for seven nitrate sensor nodes. Despite the variation in offset potential, the slopes of the calibration curves are comparable to those obtained when the sensors are measured directly. The seven nitrate sensor nodes demonstrated a near-nernstian response of -64.5 ± 16 mV/dec.
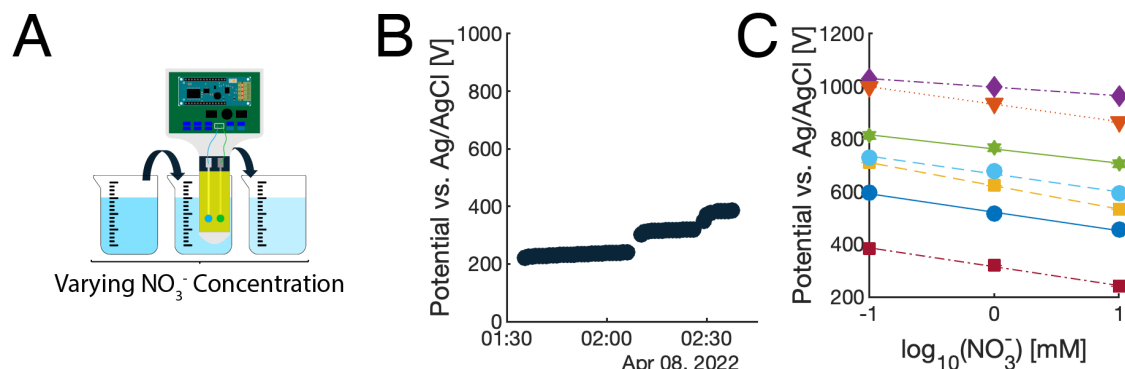
Figure 5.9: Nitrate sensor node calibration. A) Calibration of the nitrate sensor node in NaNO3 solutions of varying concentrations. B) Potential over time for one printed nitrate sensor measured between 0.1 mM and 1 mM. C) Calibration curves plotted from 0.1 mM - 1 mM for seven nitrate sensor nodes, showing a near-nernstian response of -64.5 ± 16 mV/dec.

Sensor Node Measurements in Soil

Soil is a complex environment. It is a three-phase medium containing organic matter, minerals, metals, ceramics, gases, water, and a host of biological life. This is all to say that many things could complicate potentiometric nitrate sensor readings. Although the nitrate sensor nodes are sensitive to nitrate and are largely insensitive to most other ions (see Table 4.3) - soil is more complicated than aqueous solutions. Ideally, nitrate sensors should not be sensitive to soil properties (such as texture, water content, pH, etc.), but calibration or direct measurement of the interfering property could help return accurate nitrate measurement values.

To characterize the performance of the nitrate sensor nodes in soil, the potential of the nodes was recorded over time in varying nitrate concentrations and moisture levels in three types of agricultural soils. After calibrating the nitrate sensor nodes in aqueous solutions, they were immediately cycled through several containers of soil saturated with aqueous solutions of varying nitrate concentrations. Finally, they were measured in several containers of dry soil with varying volumes of 10 mM nitrate solution.

The nitrate sensor nodes were tested in sand, peat, and clay soils. Sand tests were performed with commercially available desert sand (Mosser Lee, Milston, WI), consisting of only sand-sized soil particles and no initial nitrate concentration. Clay tests were performed with an agricultural clay soil utilized for perennial alfalfa (Medicago

sativa) and from Bouldin Island in the Sacramento–San Joaquin Delta, California
(Bouldin Alfalfa). Peat tests were performed in Miracle-Gro Nature's Care organic
potting mix.

To circumvent the possibility of hysteresis attributed to the exposure of one soil
type before measuring the sensor node in another soil type, the sensors were only
measured in a single kind of soil on a given day, and the stakes were gently but
thoroughly cleaned with deionized water and dried between measurements. In other
words, in a single day, the nitrate sensor nodes were:

1. Calibrated in aqueous nitrate solution

2. Measured in soil containers of a single soil type saturated with varying concentrations of aqueous nitrate solution

3. Measured in soil containers of the same soil type with varying moisture levels

A sample of the raw data collected from a single nitrate sensor node over an
experiment day is plotted in Figure 5.10

Measuring Nitrate Concentration in Soil

In the nitrate concentration experiment, aqueous solutions of 0.1 mM - 1 M
$NaNO_3$ were used to saturate an array of containers containing sand, clay, or peat
soils, depending on which soil type the sensors were being tested in that day. After
saturating the soil with a surplus of nitrate solution, the sensor nodes were placed
in the 0.1 mM container by displacing the soil with a spoon, inserting the stake,
and then gently redistributing the soil over the electrode surfaces. After the nitrate
sensor node was inserted into the container, the program ran on the microcontroller,
uploading the recorded potential over WiFi to an online spreadsheet once per minute.
Once the potential of the sensor stabilized, it was then moved to the 1 mM container,
and so on. Figure 5.11 shows the nitrate sensor nodes being measured in the sand.

After the measurements were made, the nitrate concentration of the soils was
determined by taking KCl extractions and then measuring the extractions with ion-
exchange chromatography. The nitrate sensor nodes' responses to the calibrated
nitrate concentrations are plotted in Figure 5.12.

We expect similar results in measuring the sensor nodes in saturated sand as we
would in aqueous solutions. This is because sand has a low cation exchange capacity,
so few other ionic species are present. Furthermore, uncharged solids in the soil are
unlikely to interfere with the potentiometric measurement.
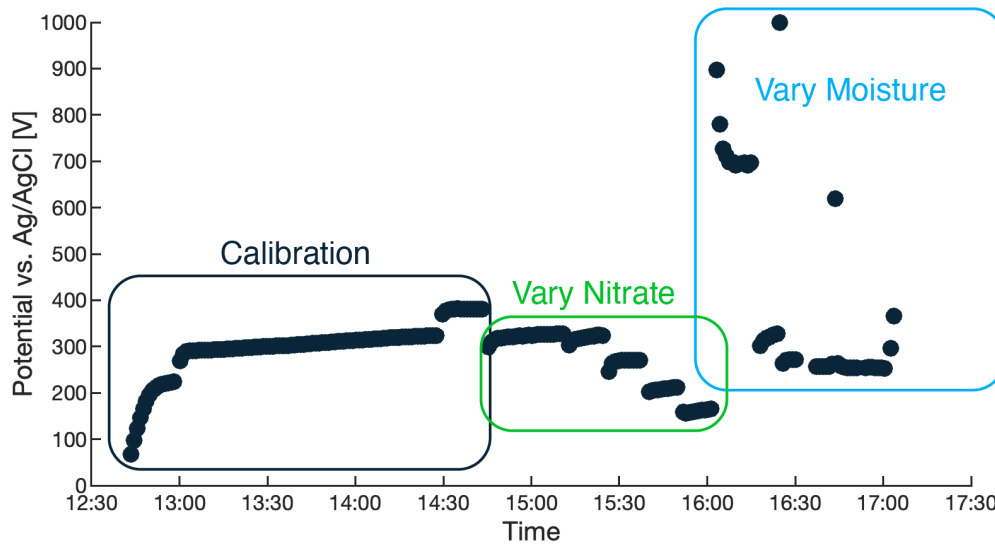
Figure 5.10: Sample of the continuous data stream from the nitrate sensor nodes
during soil characterization. The nitrate sensor nodes were first calibrated in 10 mM,
1 mM, and 0.1 mM NaNO$_3$ solution. Then, they were measured in five containers of
a single soil type saturated with varying concentrations of NaNO$_3$ solution. Finally,
the sensors were measured through six containers of the same soil type as before with
varying moisture content.
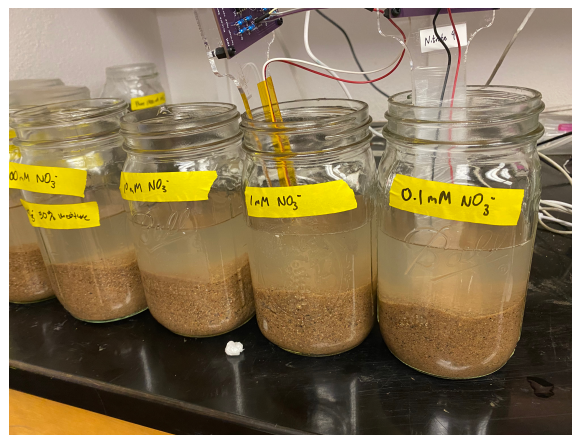
Figure 5.11: Image of nitrate sensor nodes in saturated sand of varying concentra-
tions.
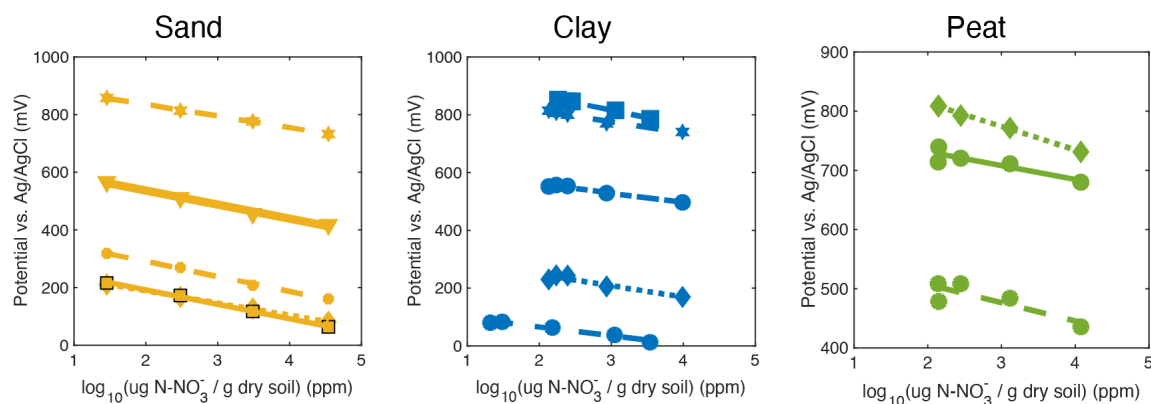
Figure 5.12: Response of nitrate sensor nodes in saturated sand, clay, and peat soils
containing varying nitrate concentrations.

The nitrate sensor nodes in the sand showed strong linear relationships between
nitrate concentration and recorded potential, with about half of the 17 sensor nodes
included in this trial showing R^2 values above 0.99. Eight sensor nodes with $R^2 >$
0.99 were used for the remaining analysis. The average sensitivity for these sensors
was -42 $\pm$ 8 mV/dec. Figure 5.12A shows the linear relationship between nitrate con-
centration and output potential for five of the sensors in the sand, with sensitivities
ranging from -40 to -42 mV/dec.

In clay, five of 14 sensors had R^2 values > 0.9, and the sensitivity of the sensor
nodes was -39 $\pm$ 8 mV/dec mV/dec, shown in Figure 5.12C. Clay has a much finer
grain size and higher cation exchange capacity than sand. This likely explains the loss
in sensitivity when measuring in clay compared to an aqueous solution or saturated
sand. This suggests that soil texture alone is not a primary interfering factor in soil
nitrate measurements, though other soil characteristics (such as pH or ionic exchange
capability) may be. If this is the case, calibration of the sensor in different soil types
would be necessary to deploy such devices in agricultural applications.

Figure 5.12B shows the output potential of three nitrate sensor nodes in peat soil
at varying nitrate levels. The nitrate sensor nodes demonstrated sensitivities of -31
$\pm$ 8 mV/dec, with R^2 values for each sensor's best fit line of 0.8, 0.71, and 0.99. The
low sensitivities and relatively low R^2 values are less than those found in sand or
clay soils. We suspect this is because the sensors had become damaged by the time
of these measurements. The sensors were measured in sand and clay soils before the
measurements in peat, so by the time of these measurements, the sensors had been
inserted, removed, and rinsed from soil media many times, and it is possible that

despite our best efforts, the sensing element may have become damaged. Compared to Figure 4.10, which plots 'fresh' gold electrode nitrate sensors in the same soil type measured with a Campbell Scientific data logger, the sensitivity was -47 mV/dec, R^2=0.95, and E_0 variation 30 mV (n=3). The different results depending on the age of the sensor and the electronics used to measure it highlights the importance of improved stability for real-world use cases.

Impact of Moisture Content

To find the impact of moisture content on the sensor nodes, 10 mM nitrate solution was used to water an array of containers containing sand, clay, or peat soils, depending on which soil type the sensors were being tested in that day. The containers were watered to 0 - 50% volumetric water content (VWC) in 10% increments. The sensor nodes were initially placed in 0% VWC soil while the program ran on the microcontroller, uploading the recorded potential over WiFi to an online spreadsheet once per minute. Once the potential of the sensor node stabilized, it was then moved to the 10% VWC container, and so on.

Ideally, the sensors' output signal should not depend on soil moisture content. However, potentiometric sensors require ionic contact between the two electrodes to function: ions must be able to move freely between the ISE and RE, proportional to the finite current associated with potentiometric measurements. If soil does not hold enough water to support the flow of ions, the sensor becomes an open circuit, and there would be no signal.

The results are shown in Figure 5.13. The potential abruptly increases at low moisture content because the microcontroller is programmed to report high signal output at open-circuit inputs. However, above a certain moisture threshold, sand and clay soils follow the expected pattern: relatively constant potential with respect to moisture content. For sand, the threshold is between 10 and 20% volumetric water content VWC, while for clay, it is between 20 and 30%. This makes sense because clay's matrix potential is higher than sand's, meaning water is bound more tightly to the surfaces of solid particles in clay, lowering the likelihood of an ionic pathway forming between the ISE and the RE of the nitrate sensor. The relationship between water content and sensor signal output in peat soil is less clear. The minimum water threshold seems to be between 10-20%, but the output potential is not as stable between 30-50% VWC. This could be attributed to the possibility of damage build-up in the nitrate sensors, or it could indicate that different sensors have different minimum thresholds. It could also be explained by the variations of water retention in high-organic matter soil. Further investigation is warranted.
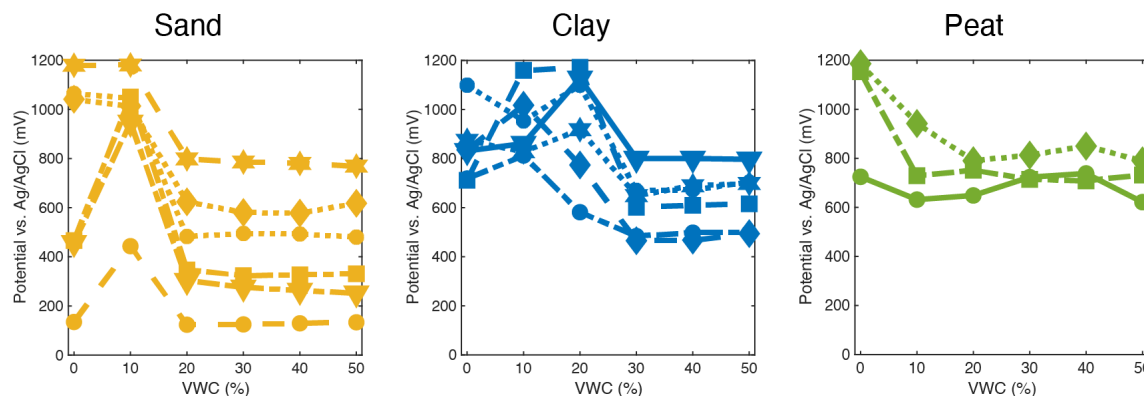
Figure 5.13: Response of nitrate sensor nodes in the sand, peat, and clay soils with
varying levels of 10 mM nitrate solution.

Individual Sensor Node Characteristics

As noted earlier, there is significant E_0 variability from one sensor node to an-
other. Up until now, the behavior of the nitrate sensor nodes has been plotted
altogether. However, when we look at individual sensors, E_0 is relatively consistent,
indicating that the variability has to do mainly with the sensor nodes rather than
the properties of the soil.

Individual sensor nodes have relatively consistent E_0 values across the different
trials. Subsets of the same 20 sensors were used in the six plots shown in Figures
5.12 and 5.13. The sensors with low R^2 in the sand also had low R^2 in clay, while
most sensors with high R^2 in the sand also had high R^2 in clay (70%). Similarly,
sensors with relatively high potential outputs had this characteristic across soil types
and nitrate/moisture measurements. Figure 5.14 shows the response of two sensor
nodes measured in sand and clay soils. Sensor A has a much lower potential than
Sensor B in all cases.

Conclusions

We fabricated 20 nitrate sensor nodes consisting of a printed nitrate sensor, signal
conditioning electronics, and a microcontroller mounted on an acrylic stake. The
nitrate sensor nodes were characterized using lab-scale equipment, calibrated in so-
lution, and measured in varying soil conditions. The nitrate sensors were most
sensitive to sand, with depreciating sensitivity for clay and peat soils. Depending on
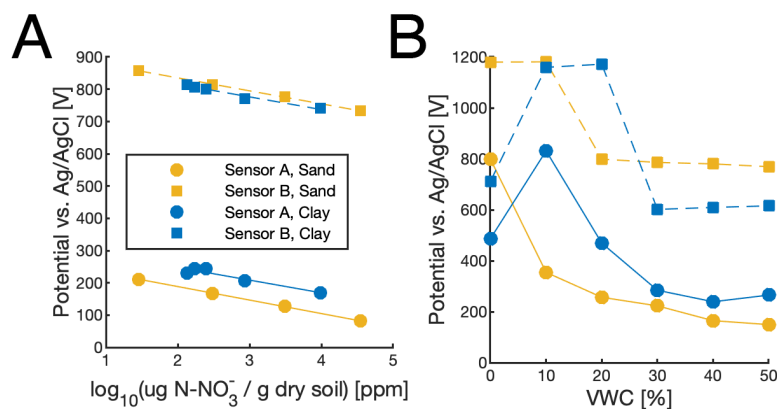
Figure 5.14: Behavior of individual sensor nodes. The responses of two individual sensor nodes are consistent when compared against themselves for different soil types. A) Responses to varying nitrate concentrations in soil. B) Responses to varying moisture content in soil.

the soil type, the sensors require a minimum of 10-30% VWC to measure soil nitrate accurately. This means measurements of nitrate concentration should only be made if the soil is sufficiently moist, which should not be a problem because farmers rarely allow their soils to drop below these values.

While each sensor is consistent throughout the different soil types, sensor-to-sensor variation is a problem that needs to be solved to avoid the calibration of each sensor node. The variation stems mainly from the readout electronics themselves and not from the soil types. The nitrate sensor nodes were relatively stable from measurement to measurement, which took place over a few days to a week for most sensors.

While this hybrid electronic sensor node is helpful for lab-scale characterization and testing nitrate sensor nodes, implementing such a system would be impractical. For instance, WiFi is a relatively short-range protocol that may require several routers to be distributed throughout a field. Furthermore, these nitrate sensor nodes need an external power source such as a battery, which would warrant maintenance throughout a crop rotation. These nodes are also made of long-lasting plastics, meaning every node must be collected at the end of a crop rotation to prevent polluting the field.

These issues above and the need for many sensors to capture the spatial variability of soil motivate the development of naturally-degradable nitrate sensor nodes.

Table 5.2: Definitions and standards relating to the degradation of materials.

Standard	Description	References
Recyclable	Material is able to be reprocessed without significant loss of quality	ISO[253]
Biodegradable	Material will break down to its basic components. Undefined time scale, conditions, or ecotoxicity. No widely-accepted standard.	N/A
Compostable	Material that will break down 90% of mass to basic components within 90 days in an industrial composting site with no measurable ecotoxicity	ASTM[254] & EN[255]
Naturally Degradable	Material will break down to environmentally benign subunits under normal environmental forces.	USCS[256]

5.4 Naturally-degradable Nitrate Sensor Nodes

Background

What is Degradation?

A common misconception surrounding 'green materials' is that if something will decompose or degrade into a naturally-occurring material (i.e., something you can find in nature), it is safe to deploy into the environment. This is an incomplete way of thinking because, by that definition, every material on the planet is 'green.' Stop reading for a moment and take a look around you. Everything you see would eventually break down into naturally-occurring materials on a long enough time scale devoid of human intervention. It was made of materials sourced from our planet, after all. The *time* it takes for something to degrade is also essential and is the basis of many different standards surrounding biodegradation.

Different organizations worldwide have developed standards that benchmark different degrees of how things degrade. Table 5.2 highlights some of the more widely-known standards. Interestingly, these standards vary widely in the description, and only the compostability standards explicitly state the timescale at which those materials degrade.

The standards in Table 5.2 also lack to describe of how these materials might degrade. To design devices that degrade in a controlled manner, one must first

understand the different ways a material might degrade.

Degradation Mechanisms in Soil

There are three ways in which materials degrade. These are compositional or microstructural changes, time-dependent deformation and associated damage accumulation, and environmental attack[257]. Generally, materials degrade by some combination of several mechanisms. There are few opportunities for time-dependent deformation in soil, though several mechanisms catalyze compositional changes or attack material bonds. These primary mechanisms by which materials degrade in soil are discussed here.

Microbial & Enzymatic Digestion

For most materials, microbial activity is the primary contributor to the degradation rate. Microbial and enzymatic digestion describes the degradation carried out by microorganisms and naturally-occurring enzymes. Microbes can degrade most - if not all - naturally occurring organic chemicals and convert them to inorganic end products to supply the microbes with nutrients and energy[258]. As with other life forms, the material's molecular bonds are broken to release energy, transformed into a less thermodynamically energetic material, and excreted from the microbe's system.

Intuitively, different materials degrade at different rates. Generally, more complex molecular structures degrade on longer time scales than simpler ones. Also, different microbes and enzymes are preferential to different molecular compounds. Healthy soil is rich with microbial life[112], and over time, the microbial communities will adapt and digest what is more likely to be available to them.

As an important note for polymers - when a polymer is described formally as a 'biodegradable polymer,' it contains hydrolyzable bonds - meaning they are affected by hydrolysis (which we will describe next). Therefore, their most crucial degradation mechanisms are chemical degradation by hydrolysis or microbial/enzymatic digestion. The latter effect is often referred to as biodegradation, meaning that the degradation is mediated at least partially by a biological system[259].

Hydrolysis

Hydrolysis is the splitting of chemical functional groups by reactions with water. It is most relevant to condensation polymers such as polyesters, polyamides, and polyurethanes but applies to any material whose bonds can be broken in a chemical reaction with water molecules.

Hydrolysis can occur as a bulk degradation process or as a surface-eroding process in polymers depending on the diffusion rate and the degradation rate of the polymer backbone[260]. Suppose water diffuses into the polymer faster than the degradation of polymer bonds. In that case, the polymer will undergo bulk erosion because the degradation will not be limited to the material surface. If the alternative is true, then it will degrade by surface erosion.

Oxidation

Oxidation is a process that transforms metals into metal-oxides, which significantly impacts the electrical and mechanical properties of metallic conductors. Oxidation is a chemical process where metals donate electrons to oxidants. Electron transfer reactions are abundant in soil, such as metal oxidation state changes, organic compound degradation/formation, free radical chemistry, wetland delineation, soil remediation, and more[261].

Dissolution

For many materials, dissolution will also play a role in the bulk degradation of a material. Dissolution is the rate at which a material dissolves in water. Materials with covalent bonds are particularly susceptible to dissolution, as polar water molecules are highly effective at solvating these bonds. Dissolution is also the mechanism that removes oxidized metals from the bulk. This means that whenever water is in contact with metals in the soil, not only will they oxidize it, but some of the metal will be solvated into the aqueous phase and flushed away with the natural groundwater flow. The four primary factors determining dissolution rate are the material type, the material's surface area to volume ratio, the temperature, and the solute concentration already in the aqueous phase.

Designing for Degradation

Since everything degrades naturally, 'Designing for Degradation' means 'designing a means to control or account for the degradation of a device', but that doesn't make for a catchy section title.

Degradation can be controlled by either passive or active means. For passive control, an engineer can change the time to device failure through the selection of materials or by modifying a device's micro- or macrostructural geometry. Alternatively, for active control, the engineer can design a device to be resilient against most degradation mechanisms but be 'triggered' to fail by mechanical or chemical manipulation of the environment.
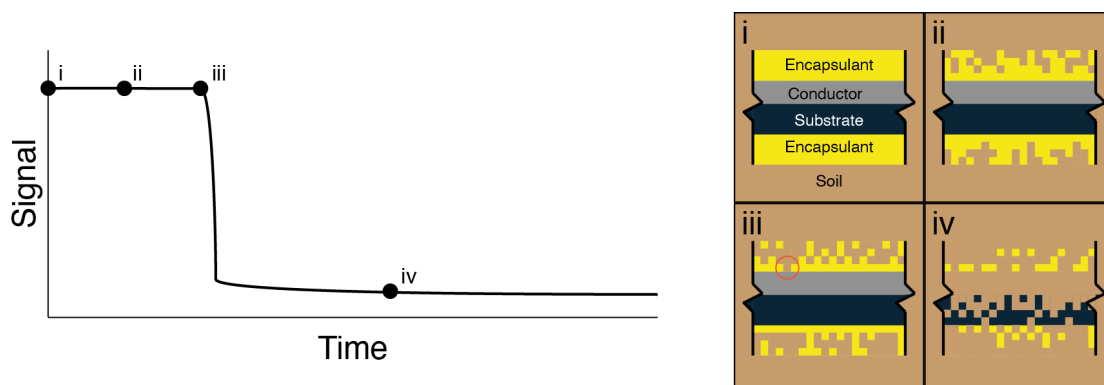
Figure 5.15: Tunable sensor lifetime by using a surface-eroding encapsulant and a water-soluble conductor. Points i-iv on the graph correspond to insets i-iv, which show the degradation of the data-carrying conductor over time. i) The device is planted in soil. ii) Over time, the encapsulant undergoes surface erosion while the conductor and substrate remain unperturbed. iii) End of functional lifetime. At this critical point, the encapsulant has eroded such that the conductor is exposed directly to the soil. The hydrogen bonds of the water-soluble polymer binder are split as soon as they are exposed to moisture. The conductor materials are solvated and mixed into the groundwater at this point. iv) As time proceeds, the remaining encapsulant and substrate materials degrade.

Our strategy for controlling the degradation rate of our device is to apply both principles of passive geometry and material selection. We make devices out of 'shells' of materials that degrade at different rates. More specifically, we paired fast-degrading printed conductors with slow-degrading, wax-based encapsulation that degrades uniformly by surface erosion. Figure 5.15 describes the performance of such a device over time, with cross-sections at critical intervals in the degradation process.

Material selection was determined by literature review and experimentation. Lee *et al.* have investigated the use of electrochemically-sintered zinc in a water-soluble polyvinyl propylene (PVP) binder as a naturally-degradable printed conductor material[262]. Meanwhile, natural waxes have an exciting opportunity as naturally-degradable encapsulation material. They have been able to retain the operation of underlying degradable electronic systems for weeks[263] to months[264]. Figure 5.16 shows the accelerated degradation of wax blends held at elevated temperatures in an incubation chamber over 28 days.
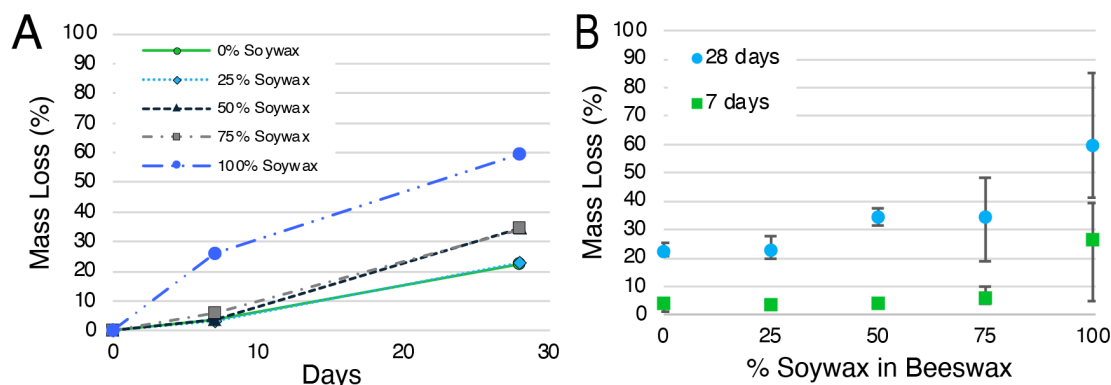
Figure 5.16: Degradation of wax blends in potting soil at 40°C A) Mass loss plotted against time for soy wax/beeswax blends. B) Mass loss plotted against volume fraction of soy wax/beeswax blends after 7 and 28 days.

Unfortunately, it is impractical to make a nitrate sensor node 100% degradable. For example, the ISM, which provides the operating mechanism for the nitrate sensor, necessitates a hydrophobic polymer backbone to function. Because of this, it is impossible to make this component naturally degradable by the current mode of operation. Fortunately, the mass of this component is minimal - only about 0.5 mg. To put that into perspective, it would take 10,000 ion-selective membranes to produce as much plastic pollution as a single credit card. Table 5.3 shows all of the components in a wireless nitrate sensor node and what naturally degradable materials they can be substituted with.

Table 5.3: Common components of a printed hybrid electronic system and their biodegradable counterparts

Component	Function	Conventional Material	Biodegradable Material	Mass
Stake	Enables easy handling and implementation into the ground	ABS Plastic, Acrylic	Wood	16 g
Adhesive	Bonds the substrate to the stake	Acrylates, resins, rubbers	Resins, waxes	100 mg
Substrate	Provides mechanical structure and surface properties	Thermoset & thermoplastic polymer sheets, silicon	Paper	100 mg
Conductor	Carries data as an electric current or potential	High conductivity metals	Printed zinc ink	70 mg
ISE Transducer	Ion-to-electron transduction	PEDOT:PSS, carbon allotropes	Carbon allotropes	0.5 mg
ISM	Binds to the primary ion	PVC + plasticizer + ionophore + ion-excluder		0.5 mg
Ag/AgCl RE	Reversibly reacts with Cl^- to provide a stable reference potential in varying electrolytic environments	Ag/AgCl	Ag/AgCl	7 mg
RE Transducer	Catalyzes the Ag/AgCl reaction	CNT + surfactant		0.1 mg
Salt Membrane	Provides a surplus of Cl^- for the Ag/AgCl reaction and provides an ionically conductive bridge to close the electrochemical circuit	PVB + NaCl		0.5 mg
Encapsulant	Shields electronic components from impact, corrosion, and other environmental factors. Determines the time to device failure.	Thermoplastics, polyurethanes, epoxies	Waxes, biopolymers	200 mg
Microcontroller	Programmable CPU and memory. The 'brains' of the device.	Silicon, etc.		1 g
Energy Storage	Coin cell batteries, lithium batteries, etc.	Various battery chemistries: lithium, zinc, copper, mercury, etc.		3 g
Energy Harvesting	Solar cells, micro-wind turbines, etc.	Varies		100 mg
Antenna	Transmits and receives wireless communications to and from the communications IC	High conductivity metals	Printed zinc ink	7 mg
Communications IC	Conditions and transmits signals between the antenna and the microcontroller	Silicon, etc.		1 mg

Wireless Sensing Strategy

Some components of a conventional wireless sensor node are difficult or even impossible to replace with naturally-degradable materials, as shown in Table 5.3. For example, degradable batteries or other energy storage devices exist in literature[265], but none are resilient or low-cost enough for our application. Similarly, using onboard energy storage and harvesting necessitates a higher complexity microcontroller, which corresponds to larger and more costly microcontrollers.

One method of circumnavigating these components is using passive sensor nodes, such as passive RFID sensors. Passive RFID sensors comprise an antenna, an RFID IC, and a sensor. Of note, there is no onboard energy storage, meaning an external power signal must be sent to the node to take a measurement. In the case of RFID, an RF signal is transmitted by an external RFID reader. The antenna receives the wave and transduces it into an electric signal which 'wakes up' and powers the RFID IC. The RFID IC acts as the microcontroller, communications IC, and power management. When it receives the wake-up signal, it uses the power in that signal to read the sensor and modulate a return signal through the antenna to the reader corresponding to the sensor measurement.

By designing a sensor node using this passive RFID scheme, we estimated that we can make the naturally-degradable nitrate sensor nodes 99.99% degradable by mass.

Fabrication

At this stage in the project, we note that we have not extracted sensor data using RFID readout. Both the naturally-degradable antenna and the naturally-degradable nitrate sensors have functioned as standalone devices. Still, attempts at connecting them together with an RFID IC have been fruitless thus far. We will present the fabrication of the standalone and integrated naturally-degradable nitrate sensors, though the characterization will be limited to the standalone nitrate sensors and antennas.

Naturally-degradable Nitrate Sensors

Conductive carbon strips were blade coated onto a 300 μm thick Strathmore 500 series Bristol paper substrate. Creative Materials 114-34A/B187 was used for the carbon ink. The print was executed using a Zehntner ZUA 2000 Universal Applicator on a ZAA 2300 Automatic Film Applicator with a gate height of 75 μm and print rate of 10 mm/s. A 100 μm thick laser cut polyimide mask was used to define the

75 x 25 mm active area. After the print was completed, the mask was carefully removed, and the strips were cured at room temperature for 24h. An image of the strips is shown in Figure 5.17A.

Ag/AgCl strips were fabricated using the same parameters with Engineered Materials Systems, Inc. CI-4001 ink. Afterward, they were cured in an oven at 120°C for two hours.

After curing, the carbon and Ag/AgCl strips were cut into six equal-sized electrodes. Each electrode was then sandwiched between two patterned wax sheets and heated in an oven at 55°C for thirty minutes. The wax sheets were made by soaking untreated plywood sheets in water before dipping them in molten wax and removing the waxy film that forms on the surface. The thin water layer on the surface of the saturated plywood sheet acts as a barrier to the hydrophobic wax, allowing for easy removal. The thickness of the wax sheets was controlled by dipping the saturated plywood sheets multiple times in quick succession, obtaining wax sheet thicknesses of 350 μm, 700 μm, and 1.25 mm for one, two, and three dip cycles, respectively. The wax sheets used for encapsulating the bottom of the sensors were used as-is, while the sheets used for encapsulating the top of the sensors had 12.5 μm windows for the membranes removed using a laser cutter. An image of an ISE immediately after the encapsulation step is shown in Figure 5.17B.

ISE membranes were fabricated by mixing 5.2 wt% Nitrate Ionophore VI, 47.1 wt% dibutyl phthalate, 0.6 wt% tetaroctylammonium chloride, and 47.1 wt% PVC. A total of 0.2 g of this mixture was dissolved in 1.3 mL of THF. 180 μL of the membrane solution was drop-cast on the ISE surface and dried in a fume hood for 15 minutes.

The REs employed a CNT transducer layer between the Ag/AgCl electrode and the membrane. This transducer was composed of 0.01 g of CNT (iP-Single Walled Carbon Nanotubes from Carbon Solutions, Inc) and 0.05 g of F127 (poly(ethylene glycol)-block-poly(propylene glycol)-block-poly(ethylene glycol) diacrylate) dissolved in 10 mL of THF, which were sonified for 1 hour in an ice bath using a Branson Digital Sonifier probe. 120 μL of the resulting transducer cocktail was deposited onto the RE surface.

The salt membrane was made by dissolving 1.58 g of Butvar B-98 (poly(vinyl butyral) (PVB), 1.00 g of NaCl, and 1.00 g of NaNO$_3$ in 20 mL of methanol. The mixture was sonified for 30 minutes in an ice bath, and 180 μL of the resulting salt membrane cocktail was deposited on top of the CNT transducer. Unless otherwise noted, all chemicals used in ISE and salt membranes were obtained from Millipore Sigma.

After each electrode was made, they were cold-sintered to 22 AWG wire using 8331D silver conductive epoxy (MG Chemicals, Burlington, ON, Canada) and en-
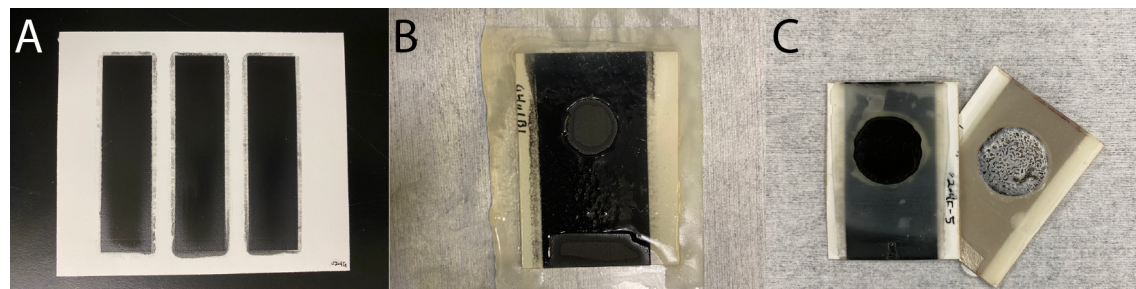
Figure 5.17: Naturally-degradable nitrate sensor fabrication. A) Conductive ink is blade coated onto bristol paper, cured, and cut into six individual electrodes. Carbon ink is used for the ion-selective electrodes, while Ag/AgCl ink is used for the reference electrodes. B) The electrode is sandwiched between two sheets of wax and heated in an oven until semi-molten. The top sheet of wax is patterned with an opening for the sensor membranes and electrical connection. C) Picture of the fabricated devices with the membranes cast.

capsulated with multiple layers of Gorilla 2-part Epoxy (Gorilla Glue Co, Cincinnati, OH). Figure 5.17 shows an image of the fabricated naturally-degradable nitrate sensors.

Naturally-degradable Nitrate Sensor Nodes

Naturally-degradable nitrate sensor nodes consist of a printed nitrate sensor, a printed RFID antenna, and a conventional RFID integrated circuit (IC). First, fully printed nitrate ISEs and Ag/AgCl REs were printed on the same substrate with the antenna and leads for the RFID IC. The RFID IC was then mounted with a pick-and-place machine, and the sensor, antenna, and IC were encapsulated in multiple layers of wax by combining hot lamination and dip-coating steps. The substrate was then adhered to a waxy wood stake for mechanical support by heating the wax to a semi-molten state and compressing the sensor node to the stake. The overall process is shown in Figure 5.18, and each process step will be described in more detail below.

Stake

Stakes were laser cut out of 3 mm thick untreated basswood sheets and soaked in a vat of molten Sky Organics triple filtered beeswax pellets at 75°C for one hour. The stakes were then removed, and the surface of the wax was smoothed to 100 μm
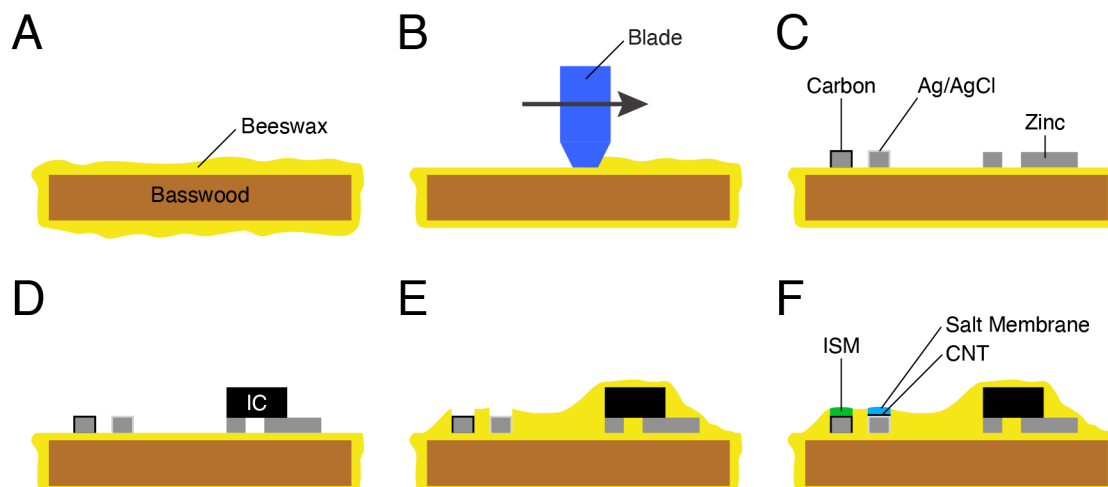
Figure 5.18: Naturally-degradable nitrate sensor node fabrication A) A basswood stake was soaked in molten beeswax and cooled. B) The wax surface was smoothed on each side with a heated doctor blade. C) The antenna and conductors were screen printed with a zinc composite ink and electrochemically sintered. A carbon ion-selective electrode transducer layer and Ag/AgCl reference electrode were blade coated on top of the conductor using a patterned mask. D) An RFID integrated circuit was bonded to the nitrate sensor and the antenna using a pick-and-place machine. E) The nitrate sensor node was encapsulated with a wax-soaked paper scaffold. F) The CNT transducer, salt membrane, and ion-selective membrane were drop cast onto the reference and ion-selective electrodes.

thick by heating a Zehntner ZUA 2000 Universal Applicator on a hot plate set to 300°C and passing over the wax-coated basswood stake on a ZAA 2300 Automatic Film Applicator at a rate of 3 mm/s, repeating until no excess wax was removed.

Antenna & Nitrate Sensor Electrodes

The antenna and conductors of the nitrate sensor were screen printed with a custom zinc ink formula in the same step onto a wax/wood substrate. The conductive zinc ink was prepared by mixing 7.5 μm zinc particles with polycaprolactone (PCL) and anisole in a 30:1:8 ratio by weight. After drying, the zinc was electrochemically sintered by dispenser printing a 50% acetic acid solution over the printed composite ink[262;266]. The acetic acid reacts with the zinc-oxide shells, exposing the underlying

zinc metal and allowing the microparticles to form a metallic zinc percolated network. The acetic acid solution sat for 13 minutes, at which point it was rinsed off with deionized water and dried in an oven at 50°C for 15 minutes. The resulting printed conductor has a conductivity of 3 x 10^5 S/m and a thickness of 35 μm.

The ISE transducer layer and RE were blade coated simultaneously on top of the zinc conductor. A 75μm thick laser cut polyimide mask was used to pattern the 3.5 mm circular features, which were then aligned and printed using a Zehntner ZUA 2000 Universal Applicator on a ZAA 2300 Automatic Film Applicator at a rate of 10 mm/s and a gate height of 75 μm. Creative Material's 114-34A/B-187 carbon ink was used for the ISE transducer, and Engineered Materials Systems' CI-4001 ink was used for the RE. The mask was then carefully removed, and the features were cured at room temperature overnight.

Nitrate Sensor Membranes

ISE membranes were fabricated by mixing 5.2 wt% Nitrate Ionophore VI, 47.1 wt% dibutyl phthalate, 0.6 wt% tetaroctylammonium chloride, and 47.1 wt% PVC. A total of 0.2 g of this mixture was dissolved in 1.3 mL of THF. 16 μL of the membrane solution was drop-cast on the ISE transducer surface and dried in a fume hood for 15 minutes.

The REs employed a CNT transducer layer between the Ag/AgCl electrode and the membrane. This transducer was composed of 0.01 g of CNT (iP-Single Walled Carbon Nanotubes from Carbon Solutions, Inc) and 0.05 g of F127 (poly(ethylene glycol)-block-poly(propylene glycol)-block-poly(ethylene glycol) diacrylate) dissolved in 10 mL of THF, which were sonified for 1 hour in an ice bath using a Branson Digital Sonifier probe. 11 μL of the resulting transducer cocktail was deposited onto the printed REs surface.

The salt membrane was made by dissolving 1.58 g of Butvar B-98 (poly(vinyl butyral) (PVB), 1.00 g of NaCl, and 1.00 g of NaNO₃ in 20 mL of methanol. The mixture was sonified for 30 minutes in an ice bath, and 16 μL of the resulting salt membrane cocktail was deposited on top of the CNT transducer. Unless otherwise noted, all chemicals used in ISE and salt membranes were obtained from Millipore Sigma.

RFID IC Attachment

Figure 5.19 shows the RFID IC attachment process. First, the area where the RFID IC is placed is cleaned of any debris using a gentle stream of clean, dry air.
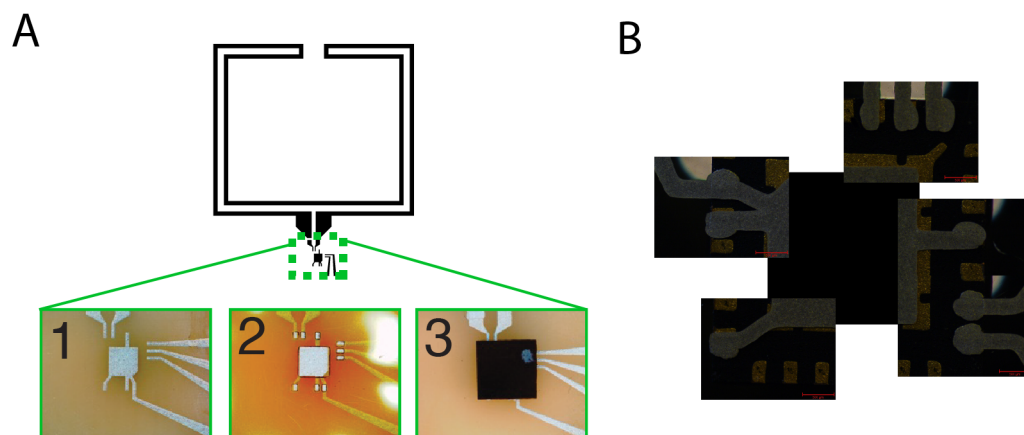
Figure 5.19: RFID IC attachment. A1) The printed conductor pads were cleaned of debris. A2) Conductive ink was stencil printed onto the pads that require electrical contact with the RFID IC. A3) While the pads were still wet, the RFID IC was aligned onto the pads using a pick-and-place machine. B) Composite image including several microscope images of the reverse side of the RFID IC attachment. A transparent PET substrate was used to see the reverse side of the attachment. The gold-colored areas are the metal pads of the IC, while the silver areas are the printed conductor.

Then, a mask of the landing pad pattern is aligned over the substrate, and conductive ink is stencil printed onto the existing landing pads. The substrate is then quickly brought to a pick-and-place machine, and the RFID IC is gently pressed onto the wet pads and held in place while they cure at room temperature. After approximately 15 minutes, the pressure is gently released, and the conductive ink is allowed to cure overnight.

Encapsulation

While most of the node can be encapsulated, the ISE and RE must remain exposed to the environment to function. To do this, Whatman 602H filter paper was used as a scaffold to minimize the spreading of the wax encapsulant. The filter paper was patterned in a laser cutter with 5 mm circular windows for the electrodes and soaked in molten beeswax. They were then removed, cooled, and aligned on top of the nitrate sensors such that the filter paper windows were concentric with the active electrode area. The nitrate sensor nodes were then heated in an oven at 55°C for 30
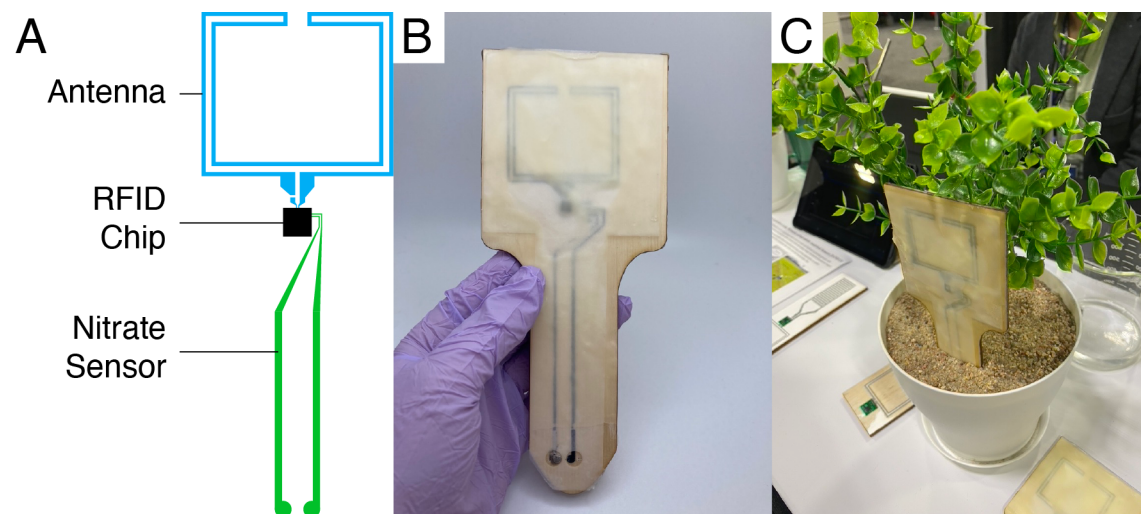
Figure 5.20: Naturally-degradable nitrate sensor node. A) Schematic of the key components of the nitrate sensor node, including an antenna, RFID chip, and a nitrate sensor. B) Photo of a fabricated naturally-degradable nitrate sensor node mounted onto a wax-soaked wooden stake. C) Photo of a naturally-degradable nitrate sensor node in a potted plant.

minutes to bring the wax to a semi-molten state and then gently pressed against the underlying wax layer to form a continuous seal.

The resulting naturally-degradable nitrate sensor node is shown in Figure 5.20.

Characterization

Nitrate Sensor Sensitivity

The sensitivity of the biodegradable nitrate sensors in solution and soil is shown in Figure 5.21. For the measurements in solution, the sensors were conditioned first in 1 mM $NaNO_3$ solution and then measured continuously in the range of 100 mM - 0.01 mM, shown in Figure 5.21A. The sensitivity was -41 mV/dec, as shown in Figure 5.21B. This is a decrease in sensitivity compared to the sensors in Section 4.4 or 5.3, which we attribute to the decrease in performance from the naturally-degradable materials. Still, the results are consistent across multiple sensors, as shown in Figure 5.21C. The sensors were then measured in various soils saturated with varying nitrate concentrations following the same procedure as described in Section 5.3. The sensors
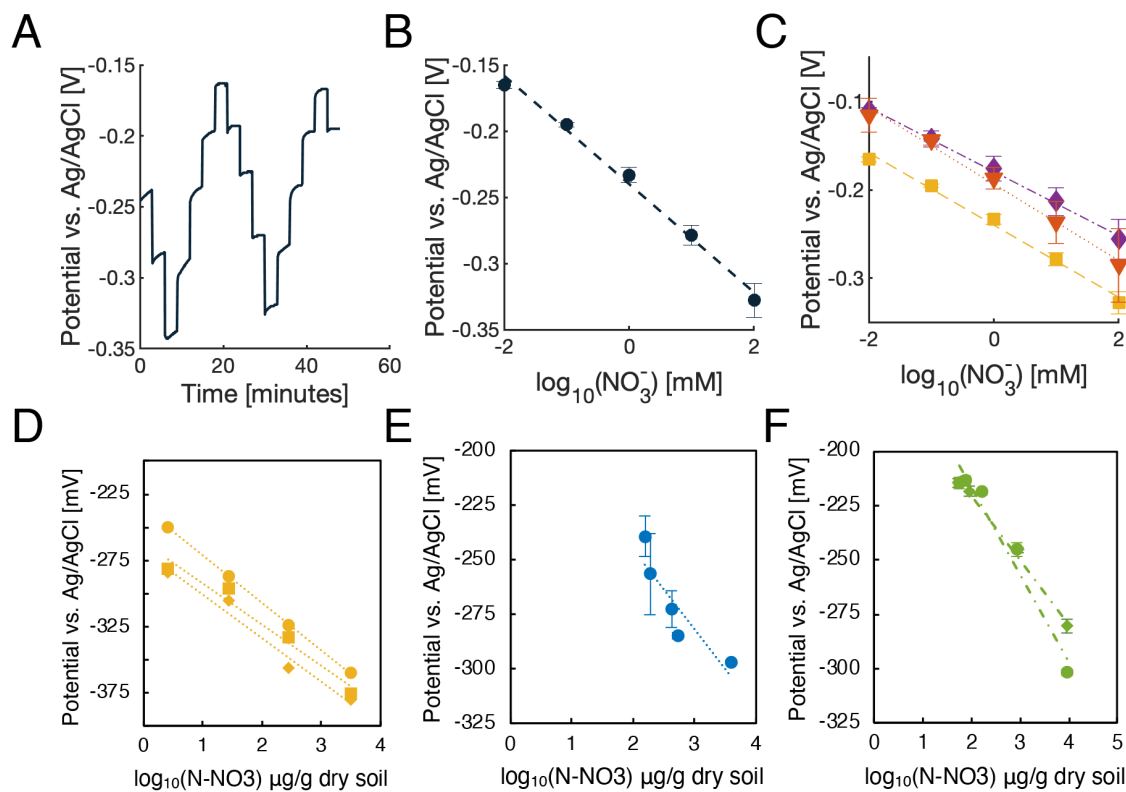
Figure 5.21: Naturally-degradable nitrate sensor sensitivity in solution and soil. A) Potential over time for one printed nitrate sensor measured between 0.1 mM and 100 mM. B) Sensitivity curves plotted from 100 mM - 0.1 mM with a near-Nernstian response of -41 mV/dec. C) Sensitivity of several sensors measured between 0.1 mM and 100 mM, with an average sensitivity of -40.2 $\pm$ 2.91 mV/dec. D) Sensitivity of the naturally-degradable nitrate sensor in the sand, E) clay, and F) peat soil.

demonstrated sensitivities of -33.21 $\pm$ 1.91 mV/dec, -36.54 mV/dec, and -34.75 $\pm$ 5.3 mV/dec for sand, clay, and peat soils, as shown in Figures 5.21D-F, respectively.

Antenna Characterization

The resistance of the zinc conductor was measured over time by a DAQ970a multimeter and is shown in Figure 5.22A. The conductivity increases slowly over time, but the increase is small and within the specifications of this application.
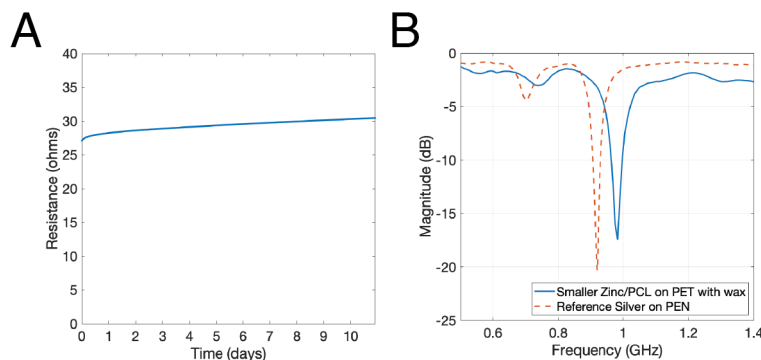
Figure 5.22: Naturally-degradable antenna conductivity and S11 plot. A) The conductivity of the zinc antenna over time. B) S11 plot of the zinc antenna printed on PET and encapsulated in wax compared to a silver antenna printed on PEN.

The S11 plot of the zinc antenna is shown in Figure 5.22B. S11 is a measure of how much power is reflected from the antenna, and if the magnitude of S11 = 0, then all of the energy put into the antenna is reflected, and there is no radiation. The frequency at which an antenna peaks is the natural frequency and ideally lies within the bandwidth of the communications protocol. The magnitude of the S11 measurement indicates the strength of the output RF signal. RFID communications are on the 902-928 MHz frequency band, meaning that this specific antenna is slightly frequency shifted, though this can be adjusted by adjusting the antenna's geometry. We invite the reader to see Carol Baumbauer's dissertation for more details on antenna design.

Degradability & Ecotoxicity

Our collaborators investigated the quantification of degradability and ecotoxicity in Gregory Whiting's group at the University of Colorado, Boulder, and Raj Khosla's group at Kansas State University[266–268].

In Dahal *et. al.*, the degradation rate and ecotoxicity of the sensor components were explored[267]. We found that the wax blends showed no significant degradation after 60 days under greenhouse soil conditions for sand, farm soil, or potting media. Furthermore, none of the materials significantly impacted the growth of maize in this period, including the unpublished results for the ion-selective electrode and reference electrode materials.

Conclusions

We developed naturally-degradable nitrate sensors with a tunable working lifetime.
These sensors performed similar to their non-degradable counterparts and were able
to measure changes in nitrate concentrations for sand, clay, and peat soils with a
high level of repeatability. The sensors are non-ecotoxic, meaning they can be safely
distributed throughout agricultural fields for real-time monitoring of soil nitrate.

5.5   An Agricultural Wireless Sensor Network

Many sensors must be distributed within a field to make accurate precision farming
decisions. The naturally degradable nitrate sensor nodes presented in Section 5.4 are
capable of fitting this task. Still, a system must be put in place to sample the data
used in the precision farming models.

Background

Wireless sensor networks (WSNs) are becoming more and more relevant in agricul-
ture. Researchers have made agricultural WSNs to monitor weeds[269], evapotranspi-
ration[270], crop disease[271], and water use[272]. However, there are limited examples
of agricultural WSNs for monitoring nitrate[273].

The design of a wireless sensor network (WSN) in agriculture has a host of unique
challenges[274;275]. Issues like energy consumption for autonomous operation of sen-
sor nodes dictate design and development issues, including communication protocols
and deployment. Furthermore, the placement of sensor nodes in open, uncontrolled
environments presents another host of unique challenges, such as damage accumu-
lation from weather or wildlife. Finally, the scale it takes to implement WSNs in
agricultural settings is much larger than in commercial or industrial environments.
Cropland accounts for about 11% of the habitable land globally[276;277], and in the
United States, the average crop farm is 445 acres[278]. This dictates the placement
and quantity of sensors needed, as discussed in Section 5.2, and shows that large
numbers of sensor nodes are required.

Different researchers have adopted different strategies for circumventing these
challenges. Ding and Chandra investigated using Wi-Fi for measuring soil moisture
and electrical conductivity[279]. Syrovy *et. al.* utilized Long Range, Wide Area Net-
work (LoRaWAN) communications to transmit data from paper-based soil moisture

sensors[280]. Yu *et al.* deployed a system where the sensors connect directly to a person's phone over Bluetooth Low Energy (BLE)[281].

Here, we propose an agricultural WSN explicitly designed for the precision management of soil moisture and soil nitrate. The naturally-degradable nitrate sensor nodes demonstrated in Section 5.4 can be deployed at minimal cost and without the need for maintenance throughout any agricultural field using the techniques outlined in Section 5.2. Passive RFID sensors have a relatively short range compared to other communication protocols. Hence, a reader needs to be brought to within a few meters of the sensor to sample data from the sensors. Because many sensors need to be distributed across an agricultural field to acquire granular enough data to capture soil variability, drones offer a unique advantage over other existing methods to sample data from the sensors[282]. With drones and drone accessories becoming less expensive, using multiple drones to simultaneously map sensors has become an attractive route to efficiently gather data[283]. Machine-learning algorithms are a promising approach for generating flight path maps due to their ability to solve highly non-convex problems quickly, and even operate in real-time as a digital twin[90–92]. We developed an agent-based dynamics model to generate flight paths for the drones to scan each sensor in the field while circumventing obstacles and avoiding crashes.

Theory

The coordinated effort of multiple drones working towards a common objective has similarities to swarms found in nature, such as bees and ants, where the accumulation of each agent's actions and reactions can give rise to phenomena and emergent behavior where the system becomes more than the sum of its parts. Unlike bees and ants, it is atypical for a drone swarm to contain a 'leader.' In the context of field mapping, the drone swarm adapts to changes within the system, such as the disablement of a few drones due to collisions or other unforeseen causes.

We developed a robust agent-based model capable of optimizing the flight paths of each drone within a swarm to scan all sensors within a simulated agriculture field. The simulations determine each drone's aerial route for optimal flight path planning[88;284]. Each drone within the simulated framework - an 'agent' - has its own characteristics that determine how it interacts with its surroundings, such as its environment and other drones. These characteristic parameters take inspiration from the physics of molecular dynamics, where each agent is modeled as a point-mass particle that is attracted and repelled by other objects within the system[91]. A genetic algorithm determines the direction of propulsion. The framework inputs are the field's shape, the number of agents, and the positions of sensors (targets). This

framework can be used for various sizes and shapes of agriculture fields. Depending
on the field geometry and the locations of sensors within that field, the framework
will output several suggestions of each drone's flight path trajectory. Agents follow
the simplified assumptions:

- The effects of buoyancy, lift, drag, and gravity are of secondary importance
  and may be neglected.

- The agents may propel themselves in any direction in 3D space.

- The agents may be idealized as point masses.

- The agents know the locations of all targets, obstacles, and other agents.

This framework is modeled in a fixed Cartesian basis in $\boldsymbol{e}_1$, $\boldsymbol{e}_2$, and $\boldsymbol{e}_3$ where the
position $\boldsymbol{r}$, velocity $\boldsymbol{v}$ and acceleration $\boldsymbol{a}$ of a drone are described as:

$$\boldsymbol{r} = r_1\boldsymbol{e}_1 + r_2\boldsymbol{e}_2 + r_3\boldsymbol{e}_3,$$
$$\boldsymbol{v} = \dot{\boldsymbol{r}} = \dot{r}_1\boldsymbol{e}_1 + \dot{r}_2\boldsymbol{e}_2 + \dot{r}_3\boldsymbol{e}_3, \tag{5.2}$$
$$\boldsymbol{a} = \ddot{\boldsymbol{r}} = \ddot{r}_1\boldsymbol{e}_1 + \ddot{r}_2\boldsymbol{e}_2 + \ddot{r}_3\boldsymbol{e}_3$$

respectfully. A schematic of this framework is shown in Figure 5.23A.

The only force, F, imposed on each agent, i, is the agent's propulsion, which
is assumed to be of constant magnitude. Hence each agent's equation of motion is
described using Newton's second law:

$$m_i\boldsymbol{a}_i = \boldsymbol{F}_{p,i} = F\boldsymbol{n}_i. \tag{5.3}$$

The distance between an agent with other agents and obstacles is imperative to
calculate the direction $\boldsymbol{n}_i$ of propulsion. At each time step, the model calculates the
Euclidean distance between objects, defined between agent i with position $\boldsymbol{r}_i$ and
another object j in the system at $\boldsymbol{A}_j$ as:

$$d_{ij}^{\{o,a,s\}} \overset{def}{=} \|\boldsymbol{r}_i - \boldsymbol{A}_j\| = \sqrt{(r_{i1} - A_{j1})^2 + (r_{i2} - A_{j2})^2 + (r_{i3} - A_{j3})^2} \tag{5.4}$$

Other objects can be obstacles, other agents, or sensors within the domain, and
are denoted as o, a, and s, respectively. The distance determines the magnitude of
the attraction or repulsion force an agent has towards that particular object; Distant
objects should have a weaker influence than near objects. Therefore, an exponentially

decaying function is used to calculate the interaction vector between an agent and an object:

$$\hat{\boldsymbol{n}}_{i\rightarrow j}^{\{o,a,s\}} = (\underbrace{w_{att}e^{-c_{att}d_{ij}}}_{attraction} - \underbrace{w_{rep}e^{-c_{rep}d_{ij}}}_{repulsion})\boldsymbol{n}_{i\rightarrow j}^{\{o,a,s\}} \tag{5.5}$$

where w_{att} and c_{att} are the weight and exponential decay coefficients of the attraction term, and w_{rep} and c_{rep} are the weight and exponential decay coefficients of the repulsion term, respectively. The direction $\boldsymbol{n}_{i\rightarrow j}$ is the unit normal vector in the direction of the object j relative to agent i and is given by:

$$\boldsymbol{n}_{i\rightarrow j}^{\{o,a,s\}} = \frac{\boldsymbol{A}_j - \boldsymbol{r}_i}{\|\boldsymbol{A}_j - \boldsymbol{r}_i\|} \tag{5.6}$$

Equation 5.5 is calculated for each type of object (agent, sensor, and obstacle) in the system. Generally, a larger attraction term relative to its repulsion term causes a net positive propulsion direction towards sensor objects. The opposite is observed towards obstacles that could leave an agent immobile if too close. The total interaction vector between agent i and all objects of a particular type is the sum of all their interaction vectors, such as those shown in Figure 5.23B. For instance, the total interaction vector given by all sensors on agent i is:

$$\boldsymbol{N}_i^s = \sum_{j=1}^{N_s} \hat{\boldsymbol{n}}_{i\rightarrow j}^s \tag{5.7}$$

where N_s is the total number of sensors in the system. A weighted sum of the total interaction forces of obstacles, sensors, and agents is taken and then normalized to give the final direction of propulsion $\boldsymbol{n}_i$.

Using this framework, the following algorithm determines the flight paths:

1. **INITIALIZE:** Load in the sensor location data within the simulated domain and position agents along one edge of the domain. Assign weight and exponential decay coefficients for each object's attraction and repulsion terms in Equation 5.5.

2. **OBSERVE:** Each agent observes it's surroundings to calculate the attraction and repulsion terms and the optimal direction of propulsion as described in Equations 5.3 - 5.7.

3. **STEP:** Each agent will apply its thrust and accelerate towards the optimal direction given optimal design parameters such as what genetic algorithm outputs. All agents have a maximum velocity of 10 m/s.
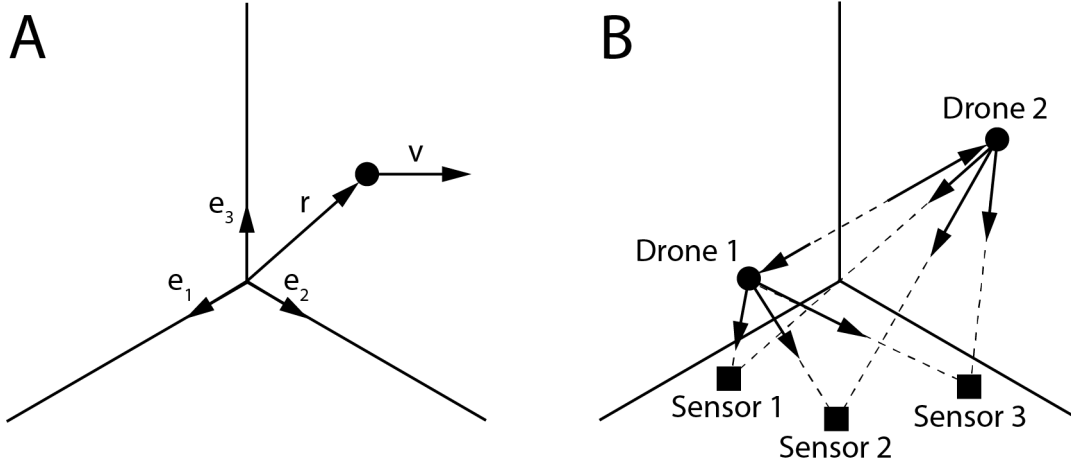
Figure 5.23: A) Schematic of a single-agent model in a Cartesian coordinate system. B) Schematic of the interaction vectors in a two-agent, three-objective system. The instantaneous direction of drone acceleration will be in the net direction of the attraction and repulsion vectors acting on the drone, which changes in magnitude and direction as the drones move within the domain.

4. **TEST:** If an agent is within 2 meters of a sensor, the sensor is considered 'mapped' and removed from the domain. If an agent is within 2 meters of another agent, both will be considered immobile and removed from the domain.

5. **ITERATE:** If there remain sensors that are not scanned, loop to Step 2.

To optimize the flight path mapping, we vary the magnitude and range of the interactive vectors between the agents and the targets are shown in Figure 5.23B and simulate the result. In this simulation, we want to maximize the number of mapped sensors while minimizing the flight time and the number of collisions. Written as a cost function, we have:

$$\Pi = W_1 \frac{S_{total} - S_{mapped}}{S_{total}} + W_2 \frac{t_{actual}}{t_{maximum}} + W_3 \frac{D_{total} - D_{crashed}}{D_{total}} \tag{5.8}$$

where S, t, and D are for sensors, flight time, and drones, respectively, and W_1, W_2, and W_3 are the weights given to each cost term and are determined by the user.

We employ a genetic algorithm to minimize the cost function, using the magnitude and range of the interaction vectors as the design strings.

Computational Method

We adapted the algorithm following Zohdi[87;89;285] to minimize the cost function presented in Equation 5.8. The algorithm for optimizing the system parameters for flight paths for each drone is as follows:

1. **P**OPULATION GENERATION: For a given number of drones, N_s, randomly generate a population of S genetic strings, Λ^i, (i=1,2, 3,..., S):

   $\Lambda^i \stackrel{def}{=} \{\lambda_1^i, \lambda_2^i, \lambda_3^i, \lambda_4^i, ..., \lambda_S^i\} \stackrel{def}{=} \{\lambda_1, \lambda_2, \lambda_3, ..., \lambda_S\}^i$

   $\Lambda^i \stackrel{def}{=} \{w_{att}^{\{o,a,s\}}, w_{rep}^{\{o,a,s\}}, c_{att}^{\{o,a,s\}}, c_{rep}^{\{o,a,s\}}\}^i$

2. **P**ERFORMANCE EVALUATION: Compute fitness of each string, $\Pi(\Lambda^i)$, (i=1, ..., S):

   $\Pi(\Lambda^i) \stackrel{def}{=} W_1 \frac{S_{total} - S_{mapped}}{S_{total}} + W_2 \frac{t_{actual}}{t_{maximum}} + W_3 \frac{D_{total} - D_{crashed}}{D_{total}}$

3. **R**ANK: Rank each string based on their cost output Π, where Rank 1 is the best performing design string that produced the lowest cost and Rank S the worst performing string:

   $\Pi(\Lambda^i, i = 1, ..., S)$

   $\Pi(\Lambda^1) \leq \Pi(\Lambda^2) \leq ... \leq \Pi(\Lambda^S)$

4. **M**ATE: Mate design strings to produce offspring:

   $\Lambda^i \stackrel{def}{=} \Phi^{(1)}\Lambda^i + (1 - \Phi^{(1)})\Lambda^{i+1}$

   where $0 \leq \Phi \leq 1$ and j is a random integer between 1 and N

5. **G**ENE ELIMINATION: Eliminate poorly performing genetic strings, keep top parents and generated offspring

6. **P**OPULATION REGENERATION: Repeat the process with the new gene pool and new *random* genetic strings

This process was repeated until the performance of a genetic string, $\Pi(\Lambda^i)$, fell below the tolerance limit, indicating that the cost function had been minimized. The minimization of the cost function Π is guaranteed to be monotone with increasing generations if the parent strings are retained, i.e., $\Pi(\Lambda^{opt,I}) \geq \Pi(\Lambda^{opt,I+1})$, where $\Lambda^{opt,I+1}$ and $\Lambda^{opt,I}$ are the best genetic strings from generations $I + 1$ and I, respectively. If one does not retain the parents in the algorithm above, inferior performing offspring may replace superior parents. Thus, top parents were kept for the subsequent generation.
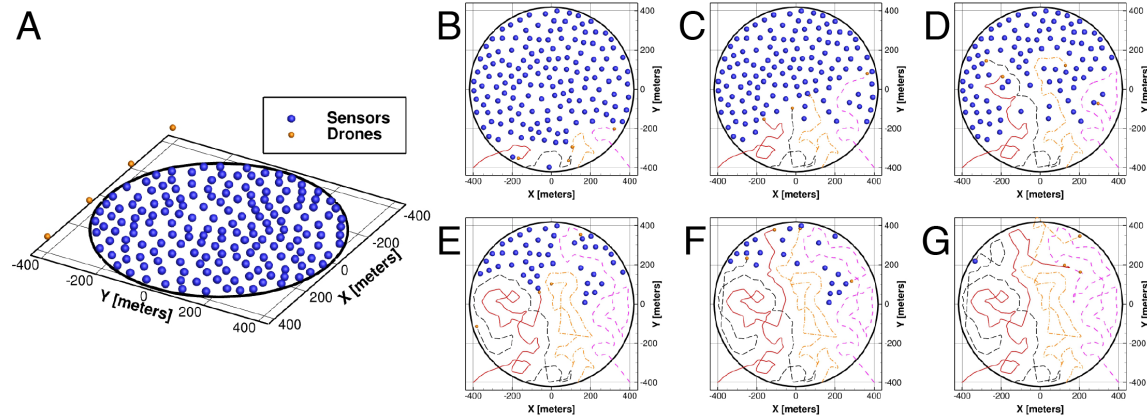
Figure 5.24: Sequences of flight paths for a swarm of four agents (blue = sensor, orange = agents) with an initial configuration in A) and from left to right and top to bottom B-G) there are varying line styles and colors created by each agent's path throughout simulated time.

Results

The optimized location of soil sensors from Figure 5.4A was inserted into the agent-based model to determine flight paths for UAV drone swarms. The flight paths for a four-agent drone swarm in a circular central-pivot irrigation field are shown in Figure 5.24. Starting from the edge of the simulated domain, the simulated drone agents traversed through the central pivot field. They sampled the distributed sensors, as seen in Figures 5.24A and B. Initially, the drones seek out the nearest sensors because they have the strongest interaction force. However, as the flight paths continued to develop (as in Figure 5.24C-F), the number of unscanned sensors dwindled, and the relative attraction strength of more remote sensors grew. This continued until the last sensor was scanned, as shown in Figure 5.24G, and the drones returned to their initial positions. The flight paths do not have a uniform pattern, which is perhaps an unexpected outcome for someone familiar with the 'sweeping' pattern attributed to drone LiDAR mapping. The sweeping motion is unnecessary in this use case as the drones seek their objectives.

Flight paths for swarms of n = 1-8 drones are shown in Figure 5.25. As the number of drones in the swarm increases, each flight path length decreases. In Figures 5.25B and 5.25C, the agents frequently crossed each others paths. However, in Fig. 5.25D, the agents crossed paths less, subdivided the field into their own
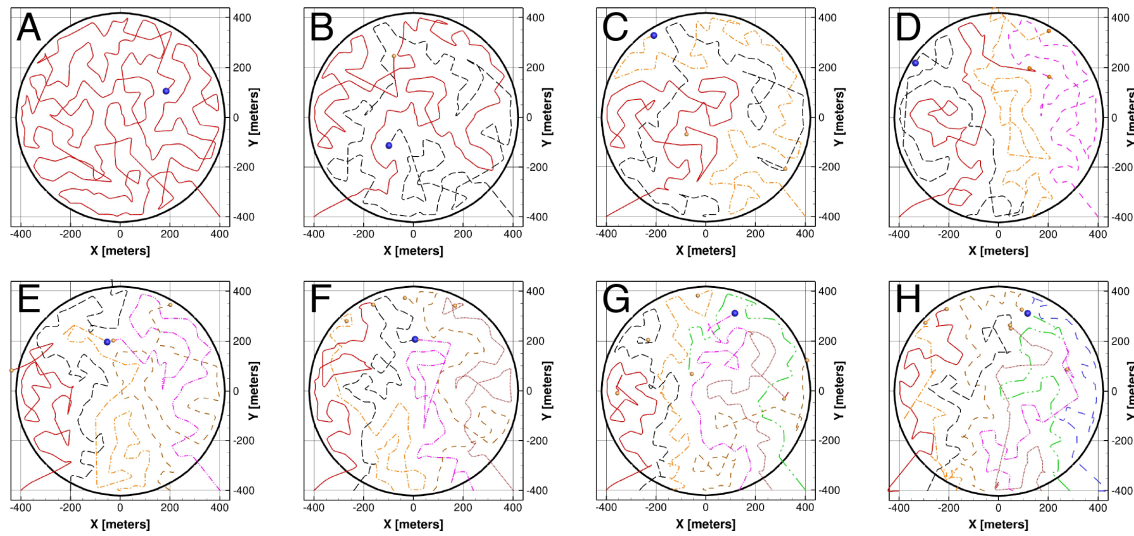
Figure 5.25: Flight paths for drone swarms with A) 1, B) 2, C) 3, D) 4, E) 5, F) 6, G) 7, and H) 8 agents, respectively.

sections, and scanned the sensors within it. For swarms with five or more sensors, as shown in Figures 5.25E - H, more overlapping occurred as agents began to compete over the same sensors. These results may also depend on each drone's initial starting position. The agents in this example were placed at the edge and linearly spaced along the width of the domain. However, one may choose to have the agents start along the circumference of the field, somewhere within the field, or from a single point. A staggered start time would also vary the flight path recommendations.

The benefits of employing a multi-agent swarm of drones are highlighted in Figure 5.26 where a different color indicates each agent's path length on the stacked bar chart. As the number of agents increased, the time required to map all the sensors decreased. Meanwhile, the cumulative total distance traveled to sample all the sensors in the field was relatively consistent for all swarm sizes ranging from one to eight. The distance traveled can be correlated with the amount of fuel or battery power a drone consumes, meaning that a swarm of drones uses a comparable amount of energy as a single drone. Interestingly, the distance traveled was similar between all agents in the swarm regardless of swarm size, as indicated by the similar bar sizes in the stacked bar chart.

To further analyze the trade-offs in swarm size, we examined how many sensors each agent scanned for all swarm sizes. As the number of agents were increased, the
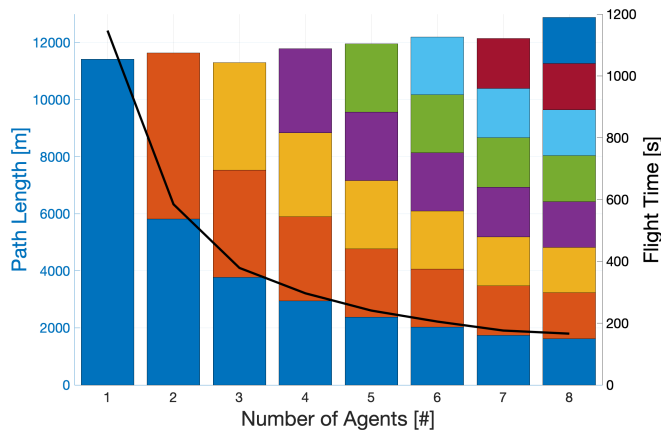
Figure 5.26: Split-axis plot showing the total distance traveled (left) and the flight time to read all sensors in the field (right) for swarms of n = 1-8 agents. Each bar in the stacked bar plot shows the distance traveled for each agent.

variance of the number of sensors each agent scanned per path length also increased, as shown in Figure 5.27. We found that an increase in this variance indicates a case where several agents would 'race' to scan the same sensor. Then, once that sensor was scanned and removed from the domain, the agents would often compete with each other for subsequent sensors. This behavior is wasteful as the agents consume energy, thus creating more conflict between agents instead of collaboration.

Conclusion

The proposed multi-agent flight path mapping can effectively and efficiently generate flight paths for variable numbers of drones to scan all sensors in a field. These findings can be adopted for variable-rate irrigation applications and provide farmers with valuable data to decide how many sensors they wish to deploy for their particular agricultural field. In the case of a 400 m radius central pivot field, it is recommended to have three or four drones because each drone would have a similar number of sensors scanned per unit of energy expenditure. Using multiple drones also significantly decreases the amount of the total time it takes to complete the sensor scanning task within the field compared to a single drone.

A genetic algorithm is employed here because genetic algorithms are easily par-
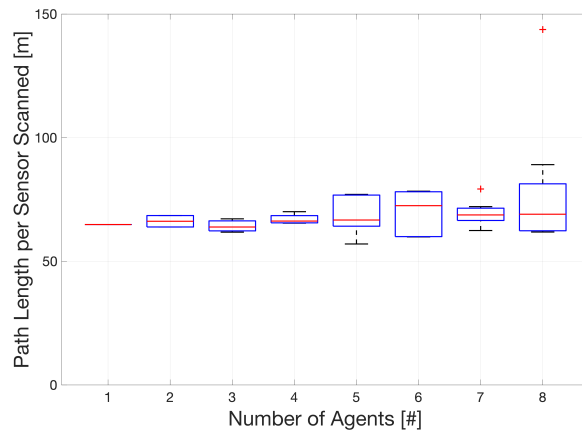
Figure 5.27: Box-whisker plot showing the variance of agents' path lengths normalized by the number of sensors the agent has scanned. Low variance indicates the amount of energy spent per target is evenly distributed across all agents. Higher variance, as indicated by having five or more agents, shows some agents are being less efficient than others. This is due to multiple agents attempting the scan the same sensor. Once one agent scanned a sensor, the other agent spent unnecessary energy on it. This can occur multiple times though out the model problem.

allelizable and scale linearly with increased processing power, for example, on the device it is computed upon. This allows this framework to become a digital twin that runs in tandem with actual physical drones mapping a field. A digital twin that utilizes this framework could be used as a design tool for outputting real-time suggestions to the user based on changes to the system, such as the loss of a drone or movement of farm equipment which may result in parts of the field being inaccessible for scanning sensors at a particular point in time.

The drone flight path mapping shown here does not account for geographic features or weather conditions. Further extensions of this framework include adding variations in terrain height and additional outside forces such as wind drag synced with weather data to obtain a more accurate framework for digital twin capabilities. Additionally, agricultural applications of drone flight path mapping are not limited only to reading sensors. Recently, drones in precision agriculture have taken a more physical role, such as aerial application of fluids, solids, and biological control agents. In 2015, the Federal Aviation Administration approved the first crop-dusting drone

capable of spraying pesticides with tanks weighing more than 55 pounds. This approval allowed the rapid deployment of drones to spray soil amendments and seeds to precise areas indicated by the soil embedded sensors, reducing the amount of irrigation runoff and seeds dispensed in unwanted areas. However, the most significant problems arise from multiple spray drifts caused by wind, which can carry spray material away from intended regions. These changes to how we manage land can significantly improve agricultural yield while decreasing water consumption, carbon emissions, and chemical runoff.

5.6 Concluding Remarks

In this chapter, we investigated the optimal distribution of soil nitrate sensors in various agricultural fields informed by well-accepted geostatistical models. This investigation pointed toward the need for hundreds of sensors in a field, which to be economically viable, would require the sensor nodes to be low-cost and maintenance-free. We then integrated the nitrate sensors with conventional electronics to develop a hybrid electronic sensor node that transmits data over WiFi and characterized the device's response in varying soil types, nitrate concentration, and moisture levels. We then adapted this nitrate sensor node into a naturally-degradable, passive RFID nitrate sensor node. Finally, we demonstrated a paradigm where swarms of UAV drones remotely sample these sensors to provide feedback to a precision farming irrigation system.

Other management systems could also benefit from these sensor technologies, for example, by mounting RFID readers onto central-pivot irrigation arms or unmanned ground vehicle (UGV) drones. Increasing the density of sensors in a field would provide increased spatial resolution, enabling farmers to apply higher control on their irrigation and fertigation decisions.

While nitrate is perhaps the most important parameter of interest after water for precision farming, there are many other signals in the soil that farmers care about. Other nitrogen sources, phosphorous, potassium, magnesium, salinity, and microbial health are just naming a few. The design of the nitrate sensor nodes provided in this chapter can easily be expanded to sense such signals and are particularly easy to adapt to other chemical analytes as only the ion-selective membrane would need to be changed. In the following chapter, we investigate using a nitrogen sensor array to sense the signals of multiple nitrogen sources and increase selectivity.

Chapter 6

Multianalyte Nitrogen Sensor Array

... from fused beads of iron and copper crystals,
the little chemical "garden" in a jar
trembles and stands again,
pale blue, blue-green, and brick.
– Elizabeth Bishop

6.1   The Problem with Interference

A potentiometric sensor measures the open-circuit potential between an ISE and a RE. The potential measured can be calculated by summing the boundary potentials across the electrodes, yielding:

$$E = E_{ISE,i}^0 + \frac{RT}{z_i F} \ln a_{i,membrane} + \frac{RT}{z_i F} \ln \frac{1}{a_{i,solution}} - E_{RE} \qquad (6.1)$$

where E is the measured potential, E^0 is the measured potential of a 1M solution of the primary analyte i at 25°C , R is the ideal gas constant, T is the temperature, z_i is the valency charge of the primary analyte i, F is Faraday's constant, and a_i is the activity of the primary analyte i.

We note that the ionophore binds with the primary ion in the membrane phase, holding the activity, $a_{i,membrane}$, constant. Likewise, ideal RE potential is constant

in varying solutions, meaning the E_{RE} is also constant. We can combine all of the constant potential terms into a single term, $E^{0,*}$, and rewrite the equation as:

$$E = E^{0*} + \frac{RT}{z_i F} \ln a_{i,solution} \tag{6.2}$$

where:

$$E^{0*} = E^0_{ISE,i} + \frac{RT}{z_i F} \ln a_{i,membrane} - E_{RE} \tag{6.3}$$

Equation 6.3 describes the response of an ideal potentiometric ISE sensor to the primary analyte. However, what happens when the sensor is placed in a solution including two or more analytes?

One model for describing non-primary (i.e., interfering) analytes' effect on a potentiometric ISE sensor is the Nicolsky-Eisenman model[286]. This model describes the potential, E generated by a potentiometric ISE sensor in the presence of interfering species as:

$$E = E^{*,0} + \frac{RT}{zF} \ln(a_i + \sum_N k_{ij} a_j^{\left(\frac{z_i}{z_j}\right)}) \tag{6.4}$$

where N is the total number of charged species in the solution, subscript j denotes an interfering analyte, and k_{ij} is the interference coefficient. This model assumes Nernstian behavior for all ions, and interfering species' responses are weighted by their respective interference coefficient, k_{ij}. k_{ij} should be less than 1, and the nearer to zero, the less sensitive the ISE is to that interfering species.

Let's consider two examples to understand the implications of this in the context of measuring chemical concentrations in soil. First, we will see the potential changes for a change in primary analyte concentration. In the second example, we will see how the potential changes for a change in an interfering analyte concentration.

Let us first consider an ideal nitrate sensor in a beaker containing 100 mL of 10 mM $NaNO_3$. What would the change in potential be if we were to add another 10 mL of 100 mM $NaNO_3$? First, we calculate the new concentration of a solution:

$$
\begin{aligned}
C_2 &= \frac{C_1 V_1 + C_{addition} V_{addition}}{V_1 + V_{addition}} \\
&= \frac{0.01 \cdot 0.1 + 0.1 \cdot 0.001}{0.1 + 0.001} \\
&= 18 mM
\end{aligned}
$$

Using this new concentration, we can calculate the change in potential as $\Delta E = E_2 - E_1$. Substituting in Equation 6.3 and using yields:

$$E_1 = E^{0*} + \frac{RT}{z_i F} \ln a_{i,1}$$

$$E_2 = E^{0*} + \frac{RT}{z_i F} \ln a_{i,2}$$

$$\Delta E = \frac{RT}{z_i F} \ln \frac{a_{i,2}}{a_{i,1}}$$

$$\Delta E = -59 \log_{10}(1.8)$$

$$\Delta E = -15mV$$

In this example, we can expect a change of -15 mV in our sensor reading when adding 10 mL of 100 mM $NaNO_3$ to 100 mL of 10 mM $NaNO_3$. It is important to consider that 10 mM $NaNO_3$ is a reasonable value for nitrate concentration in soil and 100 mM $NaNO_3$ is a reasonable concentration for a fertilizer.

Now let us consider the case where an interfering analyte is added to the solution. In this case, we will add a mixed solution of $NaNO_2$ (NO_2^- being the interfering ion) and $NaNO_3$ to keep the primary analyte concentration constant. Beginning again with a 100 mL beaker of 10 mM $NaNO_3$ solution, how would the potential change if we were to add 100 mL of 100 mM $NaNO_2$ + 10 mM $NaNO_3$ solution? Once again, we calculate the new concentration of $NaNO_2$ in the solution:

$$C_2 = \frac{C_1 V_1 + C_{addition} V_{addition}}{V_1 + V_{addition}}$$

$$= \frac{0 \cdot 0.1 + 0.1 \cdot 0.1}{0.1 + 0.1}$$

$$= 50mM$$

Using this new concentration, we can calculate the change in potential as $\Delta E = E_2 - E_1$. However, because we are now including an interfering species, we will substitute Equation 6.4 using, $k_{ij} = 0.063$, which is the interference coefficient for nitrite for our ion-selective membrane formula:

$$E_1 = E^{0*} + \frac{RT}{z_i F} \ln\left(a_{i,1} + k_{ij} a_{j,1}^{\frac{z_i}{z_j}}\right) = E^{0*} + \frac{RT}{z_i F} \ln a_{i,1}$$

$$E_2 = E^{0*} + \frac{RT}{z_i F} \ln\left(a_{i,2} + k_{ij} a_{j,2}^{\frac{z_i}{z_j}}\right)$$

$$\Delta E = \frac{RT}{z_i F} \ln\left(\frac{a_{i,2} + k_{ij} a_{j,2}^{\frac{z_i}{z_j}}}{a_{i,1}}\right)$$

$$\Delta E = -59 \log_{10}\left(1 + \frac{0.063(0.05)^1}{0.01}\right)$$

$$\Delta E = -16 mV$$

Once again, these are reasonable values for these analytes in soil and fertilizer. In this example, we expect a change of -16 mV in the sensor's reading when changing the $NaNO_2$ concentration from zero to 50 mM. Compared to the previous example, this is about the same as expected for an 8 mM change in $NaNO_3$ concentration. Herein lies the heart of the interference problem: *One sensor cannot tell the difference between a small concentration change of primary ion and a large concentration change of an interfering ion.*

6.2   Sensor Arrays

One way of accounting for the interference problem is to implement an array of sensors that are selective to different ions. Consider the previous example, what would happen if we had a nitrate *and* a nitrite sensor? The nitrate sensor would still output a -16 mV change in potential, but the nitrite sensor would output a much larger change in potential. Qualitatively, one could deduce that a change in NO_2^- concentration caused the change in potential.

Sensor arrays can also quantitatively determine the concentrations of mixed analyte solutions, such as those found in soil. Explicitly, for an array of N unique potentiometric ion-selective electrode sensors, we can vectorize the Nikolsky-Eisenman model to:

$$\{E\}_{Nx1} = \{S\}_{Nx1} \ln \{Q\}_{Nx1} \tag{6.5}$$

where:
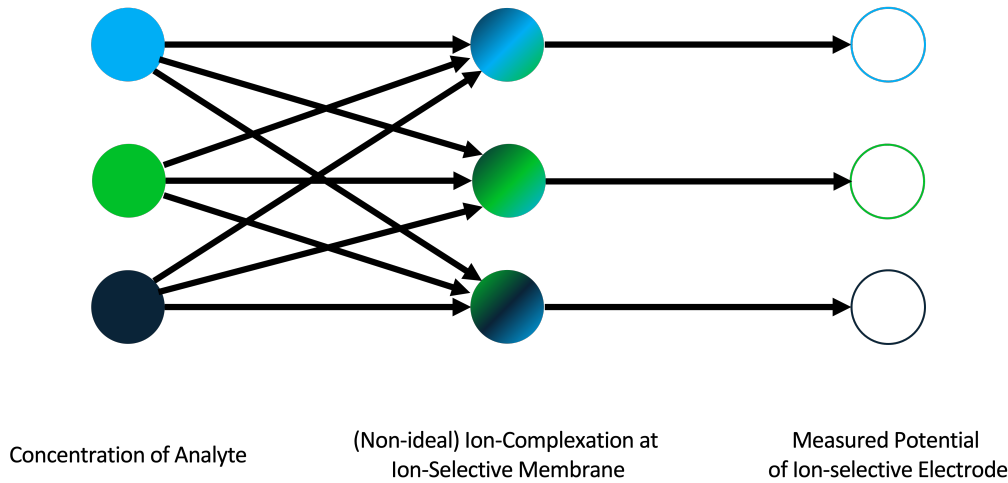
Figure 6.1: Schematic representation of the Nikolsky-Eisenman model. The ions interact with all three ion-selective electrodes, as indicated by the left-most column of arrows. The strength of the interaction between an analyte and the ion-selective membrane is represented graphically by the arrows, and mathematically as the interference coefficient k_{ij}. The sum of all interactions with the three analytes at an ion-selective membrane is transduced into a potential measured against the reference electrode potential.

$$\{S\}_{Nx1} = \left\{ \frac{RT}{z_i F} \right\} \tag{6.6}$$

and:

$$\{Q\}_{Nx1} = \left\{ \begin{array}{c} k_{ii}a_i^{\frac{z_i}{z_i}} + k_{ij}a_j^{\frac{z_i}{z_j}} + \cdots + k_{in}a_n^{\frac{z_i}{z_n}} \\ \cdots \\ k_{ni}a_i^{\frac{z_n}{z_i}} + k_{nj}a_j^{\frac{z_n}{z_j}} + \cdots + k_{nn}a_n^{\frac{z_n}{z_n}} \end{array} \right\} \tag{6.7}$$

When the interference coefficients are known (for example by empirical testing), then Equation 6.5 becomes a system of N equations with N unknowns, $a_i, a_j, \ldots, a_N$. Solving this system of equations analytically becomes increasingly difficult as N increases, though it can be executed computationally. This model is represented visually in Figure 6.1 for a three-sensor array.

One can also expand this to solve for a change in potential or concentration:

$$\{\Delta E\}_{Nx1} = \{S\}_{Nx1} \ln \{\Delta Q\}_{Nx1} \tag{6.8}$$

where:

$$\{\Delta Q\}_{Nx1} = \left\{ \begin{array}{c} \dfrac{k_{ii}a_{i,2}^{\frac{z_i}{z_i}} + k_{ij}a_{j,2}^{\frac{z_i}{z_j}} + \cdots + k_{in}a_{n,2}^{\frac{z_i}{z_n}}}{k_{ii}a_{i,1}^{\frac{z_i}{z_i}} + k_{ij}a_{j,1}^{\frac{z_i}{z_j}} + \cdots + k_{in}a_{n,1}^{\frac{z_i}{z_n}}} \\[2ex] \cdots \\[2ex] \dfrac{k_{ni}a_{i,2}^{\frac{z_n}{z_i}} + k_{nj}a_{j,2}^{\frac{z_n}{z_j}} + \cdots + k_{nn}a_{n,2}^{\frac{z_n}{z_n}}}{k_{ni}a_{i,1}^{\frac{z_n}{z_i}} + k_{nj}a_{j,1}^{\frac{z_n}{z_j}} + \cdots + k_{nn}a_{n,1}^{\frac{z_n}{z_n}}} \end{array} \right\} \tag{6.9}$$

To demonstrate this, we are developing a nitrogen sensor array that makes simultaneous measurements of NO_3^-, NO_2^-, and NH_4^+. This is done by sampling data from nitrate, nitrite, and ammonium ion-selective electrodes, and solving the system of equations shown in Equation 6.5.

Fabrication

The three potentiometric ISE sensors were printed onto a single substrate, and the orientation is shown in Figure 6.2A. Each ISE was paired with a unique RE in this design, though in theory, one could use a single RE.

Creative Material's 126-33 extremely conductive silver ink was screen printed on 100μm thick polyethylene terephthalate (PET) and cured in an oven at 120 °C for two hours. Afterward, Ag/AgCl reference electrodes with 3.5 mm diameter circles were blade coated over half of the electrodes using Engineered Materials Systems, Inc. CI-4001 ink and cured in an oven at 120°C for two hours. Next, carbon transducer layers with 3.5 mm diameter circles were blade coated atop the remaining electrodes using Creative Material's 114-34A/B-187 carbon ink (Creative Materials, Ayer, MA) and cured in an oven at 80°C for four hours.

The sensor arrays were then encapsulated with 75 μm thick laser-cut Teflon tape with circular windows of 5 mm diameter for the active area. The window in the encapsulant was larger than the electrode to allow space for the membrane to seal to the substrate, preventing bubbles or delamination of the membrane.

Nitrate selective ISMs were fabricated by mixing 5.2 wt% Nitrate Ionophore VI, 47.1 wt% dibutyl phthalate, 0.6 wt% tetraoctylammonium chloride, and 47.1 wt% PVC. A total of 0.2 g of this mixture was dissolved in 3.14 mL of THF, and 3x aliquots of 16 μL of the membrane solution were drop-cast on the printed carbon electrode surface, allowing the layers to dry in a fume hood for 15 minutes in between.
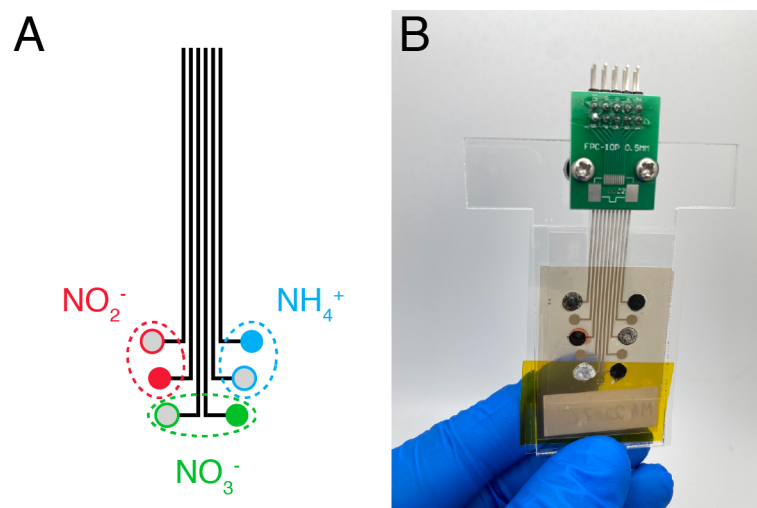
Figure 6.2: Multianalyte nitrogen sensor array. A) Schematic depicting the layout of the three potentiometric ISE sensors. The solid-color circles denote the ion-selective electrode, while the outlined circles indicate the reference electrode. B) Image of the nitrogen sensor array connected to the FPC connector.

Nitrite selective ISMs were fabricated by mixing 1.0 wt% Nitrite Ionophore I, 65.7 wt% 2-nitro-phenyl octyl ether (NPOE), 0.3 wt% potassium tetrakis[3,5-bis(trifluoro-methyl)phenyl], and 33.0 wt% PVC. A total of 0.3 g of this mixture was dissolved in 3.3 mL of THF, and 3x aliquots of 16 μL of the membrane solution were drop-cast on the printed carbon electrode surface, allowing the layers to dry in a fume hood for 15 minutes in between.

Ammonium selective ISMs were fabricated by mixing 0.2 wt% Ammonium Ionophore I, 68.3 wt% 2-nitro-phenyl octyl ether (NPOE), and 31.5 wt% PVC. A total of 0.5 g of this mixture was dissolved in 5.4 mL of THF, and 3x aliquots of 16 μL of the membrane solution were drop-cast on the printed carbon electrode surface, allowing the layers to dry in a fume hood for 15 minutes in between.

The REs employed a CNT transducer layer between the Ag/AgCl electrode and the membrane. This transducer was composed of 0.01 g of CNT (iP-Single Walled Carbon Nanotubes from Carbon Solutions, Inc) and 0.05 g of F127 (poly(ethylene glycol)-block-poly(propylene glycol)-block-poly(ethylene glycol) diacrylate) dissolved in 10 mL of THF, which were sonified for 1 hour in an ice bath using a Branson Digital Sonifier probe. 11 μL of the resulting transducer cocktail was deposited onto the printed REs surface.
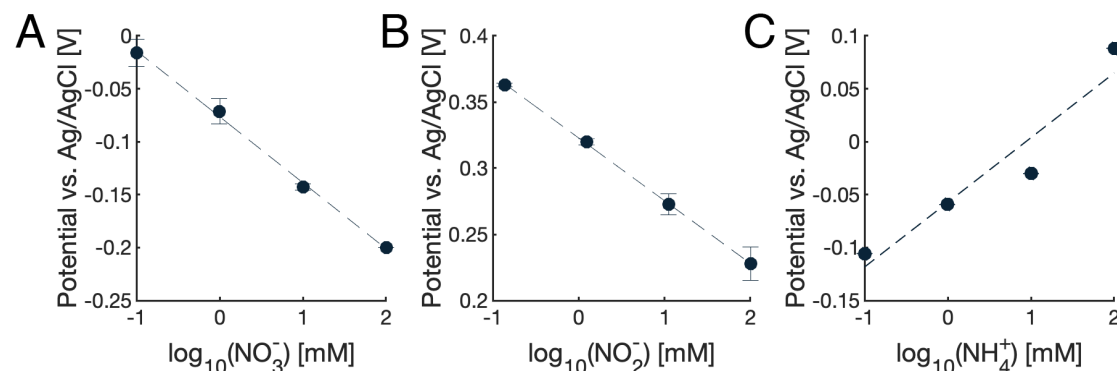
Figure 6.3: A) Nitrate sensor sensitivity to nitrate. B) Nitrite sensor sensitivity to nitrite. Ammonium sensor sensitivity to ammonium.

The salt membrane was made by dissolving 1.58 g of Butvar B-98 (poly(vinyl butyral) (PVB), 1.00 g of NaCl, and 1.00 g of either $NaNO_3$, $NaNO_2$, or NH_4Cl in 20 mL of methanol. The mixtures were sonified for 30 minutes in an ice bath, and 3x aliquots of 16 μL of the resulting salt membrane cocktail were deposited on top of the CNT transducers. Unless otherwise noted, all chemicals used in ISE and salt membranes were obtained from Millipore Sigma.

The sensor array was then connected to a flat flexible cable (FFC) connector and mounted onto a laser-cut acrylic mount for easy handling. Figure 6.2B shows an image of the fabricated analyte array.

Preliminary Results

The three sensors were tested in nitrate, nitrite, and ammonium solutions of varying concentration, and the sensitivities of each sensor to their primary analyte is plotted in Figure 6.3. The nitrate, nitrite, and ammonium sensors demonstrated near-Nernstian sensitivities of -61 mV/dec, -49 mV/dec, and 61 mV/dec, to their primary ions, respectively. The ammonium sensor has a positive slope because the valency charge of the ammonium ion is +1, while the nitrate and nitrite valency charges are -1.

6.3 Future Work

Interference Studies

The next task in characterizing the multianalyte nitrogen sensor arrays is to characterize the sensitivity of each sensor to its interfering ions. In other words, what is the sensitivity of the nitrate sensor to NO_2^- concentration? Or NH_4^+? Once all of these measurements are taken, the interference coefficients k_{ij} can be solved explicitly, and the accuracy of the Nikolsky-Eisenman model can be tested empirically by measuring the potential of the sensor array in mixed analyte solutions and solving Equation 6.5.

Artificial Neural Network Model

The work presented so far uses the Nikolsky-Eisenman model to describe the complex mechanics of ion-selective electrodes. However, this model does not account for higher order effects. One way of accounting for these effects is to train an artificial neural network (ANN) using empirical data collected from the sensor arrays. ANNs were described in Section 3.6. The concept of pairing neural networks with arrays of ion-selective electrodes is not new[138;287], and ANNs are a logical model choice because they are essentially an expansion of the Nikolsky-Eisenman model. Figure 6.1, which shows a schematic of the Nikolsky-Eisenman model, is juxtaposed to an ANN with a single hidden layer, such as the one shown in Figure 3.7, where the k_{ij} terms replace the w_i, b_i terms of the ANN. Adding additional hidden layers to the ANN allows the higher order effects to be captured.

Additional Sensor Inputs

We will also investigate adding additional sensor input into the sensor array. Commercial farmers will get samples of their soil tested by laboratories to benchmark their soils for many properties, such as nitrogen, phosphorous, potassium, magnesium, calcium, pH, and electrical conductivity, to name just a few. The only limitations to the number of inputs into an ANN are those enforced by feasibility, such as the space that will fit on a sensor array, or the number of ADC channels on the controller. Adding more sensors not only has the added benefit of new capabilities but accounting for these potentially interfering species also increases the accuracy of all other sensors in the array. There also isn't any reason other types of sensors could not be

included, for example, a temperature sensor to account for the subtle temperature differences that occur in soil on a diurnal cycle. The addition of moisture sensors would also allow us to know whether or not to make potentiometric measurements, as we found that erroneous measurements are made when the soil VWC is less than 10-30% depending on the soil type in Section 5.3.

6.4 Concluding Remarks

There are myriad opportunities in the area of multianalyte sensing. For example, the nitrogen sensor arrays could be used to study and quantify the rates of the multitude of nitrogen transformations that occur within the soil nitrogen cycle. Due to the modular nature of these sensor arrays, they can also be adapted to specific crops; for example, if the health of a particular crop is more affected by a particular analyte, then a sensor for that analyte could be appended to the array to account for that analyte. The sensor arrays could also be expanded for other industries, such as a wearable sensor array to detect chemicals in sweat [168].

Conclusion

We investigated the optimal distribution of soil nitrate sensors in various agricultural fields informed by well-accepted geostatistical models. This investigation pointed toward the need for hundreds of sensors in a field, which to be economically viable, would require the sensor nodes to be low-cost and maintenance-free.

We designed and fabricated fully printed potentiometric nitrate sensors comprised of a printed nitrate ISE and printed RE. When paired with a glass RE, the printed nitrate ISEs showed a near-Nernstian sensitivity of -54.1 mV/dec $\pm$ 2.1 mV/dec. A printed RE with low sensitivity to nitrate was developed using a membrane composed of PVB, NaCl, and $NaNO_3$. Fully printed nitrate sensors demonstrated a sensitivity of -48.0$\pm$ 3.3 mv/dec in solution and -47 mV/decade in soil. The printed sensors were selective to nitrate and did not have significant sensitivity to sulfate, chloride, phosphate, nitrite, ammonium, potassium, or magnesium at concentrations found in soil, though calcium does interfere with the sensors' behavior. The sensors were as stable as many other potentiometric ISE sensors in the literature.

We then integrated the nitrate sensors with conventional electronics to develop a hybrid electronic sensor node that transmitted data over WiFi and characterized the device's response in varying soil types, nitrate concentration, and moisture levels. We then adapted this nitrate sensor node into a naturally-degradable, passive RFID nitrate sensor node. Finally, we demonstrated a paradigm where swarms of UAV drones remotely sample these sensors to provide feedback to a precision farming irrigation system. Other management systems could also benefit from these sensor technologies, for example, by mounting RFID readers onto central-pivot irrigation arms or unmanned ground vehicle (UGV) drones. Increasing the density of sensors in a field would provide increased spatial resolution, enabling farmers to apply higher control on their irrigation and fertigation decisions.

While nitrate is perhaps the most important parameter of interest after water for precision farming, there are many other signals in the soil. Other nitrogen sources, phosphorous, potassium, magnesium, salinity, and microbial health are just naming a few. The design of the nitrate sensor nodes provided in this chapter can easily be

expanded to sense such signals and are particularly easy to adapt to other chemical analytes as only the ion-selective membrane would need to be changed. We fabricated nitrogen sensor arrays that measured nitrate, nitrite, and ammonium in aqueous solutions. There are myriad opportunities in the area of multianalyte sensing. For example, the nitrogen sensor arrays could be used to study and quantify the rates of the multitude of nitrogen transformations that occur within the soil nitrogen cycle. Due to the modular nature of these sensor arrays, they can also be adapted to specific crops; for example, if the health of a particular crop is more affected by a particular analyte, then a sensor for that analyte could be appended to the array to account for that analyte.

Acknowledgements

The drone photography of the farm field shown in Figure 5.2D is from the publicly available data set from senseFly. This and similar datasets can be accessed at: https://www.sensefly.com/education/datasets/

Bibliography

[1] "Soil test interpretations and fertilizer recommendations,"

[2] K. Good, "Fertilizer prices rise, but pace slows,"

[3] W. G. Crumpton, T. M. Isenhart, and P. D. Mitchell, "Nitrate and organic n analyses with second-derivative spectroscopy," *Limnology and Oceanography*, vol. 37, no. 4, pp. 907–913, 1992.

[4] A. Sempere, J. Oliver, and C. Ramos, "Simple determination of nitrate in soils by second-derivative spectroscopy," *Journal of Soil Science*, vol. 44, no. 4, pp. 633–639, 1993.

[5] I. Raij Hoffman, T. Harter, and I. Kisekka, "Evaluating nitrogen leaching in processing tomatoes for enhanced productivity and sustainability," ASA, CSSA, SSSA International Annual Meeting, 2021.

[6] J. Choosang, A. Numnuam, P. Thavarungkul, P. Kanatharana, T. Radu, S. Ullah, and A. Radu, "Simultaneous Detection of Ammonium and Nitrate in Environmental Samples Using on Ion-Selective Electrode and Comparison with Portable Colorimetric Assays," *Sensors*, vol. 18, p. 3555, 10 2018.

[7] J. Gallardo, S. Alegert, and M. Del Valle, "A flow-injection electronic tongue based on potentiometric sensors for the determination of nitrate in the presence of chloride," *Sensors and Actuators, B: Chemical*, vol. 101, pp. 72–80, 6 2004.

[8] E. H. Hansen, A. K. Ghose, and J. Růžička, "Flow injection analysis of environmental samples for nitrate using an ion-selective electrode," *The Analyst*, vol. 102, pp. 705–713, 1 1977.

[9] B. Schazmann, D. Morris, C. Slater, S. Beirne, C. Fay, R. Reuveny, N. Moyna, and D. Diamond, "A wearable electrochemical sensor for the real-time measurement of sweat sodium concentration," *Analytical Methods*, vol. 2, p. 342, 4 2010.

[10] Y. Li, Q. Yang, M. Chen, M. Wang, and M. Zhang, "An ISE-based On-Site Soil Nitrate Nitrogen Detection System," *Sensors*, vol. 19, p. 4669, 10 2019.

[11] V. A. T. Dam and M. A. G. Zevenbergen, "Low Cost Nitrate Sensor for Agricultural Applications," in *2019 20th International Conference on Solid-State Sensors, Actuators and Microsystems and Eurosensors XXXIII, TRANSDUCERS 2019 and EUROSENSORS XXXIII*, pp. 1285–1288, Institute of Electrical and Electronics Engineers Inc., 6 2019.

[12] J. Artigas, A. Beltran, C. Jiménez, A. Baldi, R. Mas, C. Domínguez, and J. Alonso, "Application of ion sensitive field effect transistor based sensors to soil analysis," *Computers and Electronics in Agriculture*, 2001.

[13] M. A. Ali, X. Wang, Y. Chen, Y. Jiao, N. K. Mahal, S. Moru, M. J. Castellano, J. C. Schnable, P. S. Schnable, and L. Dong, "Continuous monitoring of soil nitrate using a miniature sensor with poly (3-octyl-thiophene) and molybdenum disulfide nanocomposite," *ACS applied materials & interfaces*, vol. 11, no. 32, pp. 29195–29206, 2019.

[14] A. M. Gaikwad, A. C. Arias, and D. A. Steingart, "Recent Progress on Printed Flexible Batteries: Mechanical Challenges, Printing Technologies, and Future Prospects,"

[15] R. A. Street, T. N. Ng, D. E. Schwartz, G. L. Whiting, J. P. Lu, R. D. Bringans, and J. Veres, "From printed transistors to printed smart systems," *Proceedings of the IEEE*, vol. 103, pp. 607–618, 4 2015.

[16] F. C. Krebs, "Fabrication and processing of polymer solar cells: A review of printing and coating techniques," 2008.

[17] H. Jiang, W. Yu, J. F. Waimin, N. Glassmaker, N. Raghunathan, X. Jiang, B. Ziaie, and R. Rahimi, "Inkjet-printed solid-state potentiometric nitrate ion selective electrodes for agricultural application," in *2019 IEEE SENSORS*, pp. 1–4, IEEE, 2019.

[18] T. Wujec, C. Bass, E. Beck, W. Bostwick, D. Brooker, D. E. Brown, J. Carbeck, G. Dobush, C. Garling, and T. e. a. Kellner, *The future of making.*

[19] B. Jovanovic, "Internet of things statistics for 2022 - taking things apart," 2022.

[20] R. Gutierrez-Osuna, "Intelligent sensor systems," 2001.

[21] I. Sinclair, *Sensors and transducers.* Elsevier, 2000.

[22] J. Fraden and J. Fraden, *Handbook of modern sensors: physics, designs, and applications*, vol. 3. Springer, 2004.

[23] N. R. Council *et al.*, "Chemical sensors," *Expanding the vision of sensor materials. National Academies Press, Washington, DC*, pp. 73–88, 1995.

[24] Y. Hishiyama, Y. Kaburagi, and M. Inagaki, "Chapter 9 - magnetoresistance," in *Materials Science and Engineering of Carbon* (M. Inagaki and F. Kang, eds.), pp. 173–204, Butterworth-Heinemann, 2016.

[25] H.-S. Yim, C. E. Kibbey, S.-C. Ma, D. M. Kliza, D. Liu, S.-B. Park, C. E. Torre, and M. E. Meyerhoff, "Polymer membrane-based ion-, gas-and bio-selective potentiometric sensors," *Biosensors and Bioelectronics*, vol. 8, no. 1, pp. 1–38, 1993.

[26] M. C. Gurau, S.-M. Lim, E. T. Castellana, F. Albertorio, S. Kataoka, and P. S. Cremer, "On the mechanism of the hofmeister effect," *Journal of the American Chemical Society*, vol. 126, no. 34, pp. 10522–10523, 2004.

[27] N. Lakshminarayanaiah, *Membrane electrodes.* Elsevier, 2012.

[28] P. Bühlmann and L. D. Chen, "Ion-selective electrodes with ionophore-doped sensing membranes," *Supramolecular Chemistry: From Molecules to Nanomaterials*, vol. 5, p. 2539, 2012.

[29] D. O'Sullivan and T. Igoe, *Physical computing: sensing and controlling the physical world with computers.* Course Technology Press, 2004.

[30] L. Altman, "Single-chip microprocessors open up a new world of applications," *Electronics*, vol. 47, no. 8, pp. 81–87, 1974.

[31] R. Pallas-Areny and J. G. Webster, *Sensors and signal conditioning.* John Wiley & Sons, 2012.

[32] S. D. Senturia, *Microsystem design.* Springer Science & Business Media, 2007.

[33] J. Taylor, *Introduction to error analysis, the study of uncertainties in physical measurements.* 1997.

[34] D. Johnson, "Ibm introduces the world's first 2-nm node chip," 2021.

[35] R. C. Jaeger and T. N. Blalock, *Microelectronic circuit design.* McGraw-Hill New York, 1997.

[36] M. Watanabe and S. Kramer, "450 mm silicon: An opportunity and wafer scaling," *The Electrochemical Society Interface*, vol. 15, no. 4, p. 28, 2006.

[37] A. C. Arias, J. D. MacKenzie, I. McCulloch, J. Rivnay, and A. Salleo, "Materials and applications for large area electronics: solution-based approaches," *Chemical reviews*, vol. 110, no. 1, pp. 3–24, 2010.

[38] S. Khan, L. Lorenzelli, and R. S. Dahiya, "Technologies for printing sensors and electronics over large flexible substrates: A review," *IEEE Sensors Journal*, vol. 15, no. 6, pp. 3164–3185, 2014.

[39] A. Nathan, A. Ahnood, M. T. Cole, S. Lee, Y. Suzuki, P. Hiralal, F. Bonaccorso, T. Hasan, L. Garcia-Gancedo, A. Dyadyusha, *et al.*, "Flexible electronics: the next ubiquitous platform," *Proceedings of the IEEE*, vol. 100, no. Special Centennial Issue, pp. 1486–1517, 2012.

[40] R. F. Pease and S. Y. Chou, "Lithography and other patterning techniques for future electronics," *Proceedings of the IEEE*, vol. 96, no. 2, pp. 248–270, 2008.

[41] R. R. Søndergaard, M. Hösel, and F. C. Krebs, "Roll-to-roll fabrication of large area functional organic materials," *Journal of Polymer Science Part B: Polymer Physics*, vol. 51, no. 1, pp. 16–34, 2013.

[42] A. Pierre, M. Sadeghi, M. M. Payne, A. Facchetti, J. E. Anthony, and A. C. Arias, "All-Printed Flexible Organic Transistors Enabled by Surface Tension-Guided Blade Coating," *Advanced Materials*, vol. 26, pp. 5722–5727, 8 2014.

[43] M. Sadeghi, P. Delparastan, A. Pierre, and A. C. Arias, "Printed Flexible Organic Transistors with Tunable Aspect Ratios," *Advanced Electronic Materials*, vol. 6, p. 1901207, 2 2020.

[44] Y. Khan, A. Thielens, S. Muin, J. Ting, C. Baumbauer, and A. C. Arias, "A new frontier of printed electronics: Flexible hybrid electronics," *Advanced Materials*, vol. 32, no. 15, p. 1905279, 2020.

[45] J. R. Corea, A. M. Flynn, B. Lechêne, G. Scott, G. D. Reed, P. J. Shin, M. Lustig, and A. C. Arias, "Screen-printed flexible mri receive coils," *Nature communications*, vol. 7, no. 1, pp. 1–7, 2016.

[46] S. L. Swisher, M. C. Lin, A. Liao, E. J. Leeflang, Y. Khan, F. J. Pavinatto, K. Mann, A. Naujokas, D. Young, S. Roy, *et al.*, "Impedance sensing device enables early detection of pressure ulcers in vivo," *Nature communications*, vol. 6, no. 1, pp. 1–10, 2015.

[47] A. M. Zamarayeva, A. E. Ostfeld, M. Wang, J. K. Duey, I. Deckman, B. P. Lechêne, G. Davies, D. A. Steingart, and A. C. Arias, "Flexible and stretchable power sources for wearable electronics," *Science Advances*, vol. 3, no. 6, p. e1602051, 2017.

[48] Y. Khan, A. E. Ostfeld, C. M. Lochner, A. Pierre, and A. C. Arias, "Monitoring of vital signs with flexible and wearable medical devices," *Advanced Materials*, vol. 28, no. 22, pp. 4373–4395, 2016.

[49] S. Takamatsu, T. Lonjaret, E. Ismailova, A. Masuda, T. Itoh, and G. G. Malliaras, "Wearable keyboard using conducting polymer electrodes on textiles," *Advanced Materials*, vol. 28, no. 22, pp. 4485–4488, 2016.

[50] S. Choi, H. Lee, R. Ghaffari, T. Hyeon, and D.-H. Kim, "Recent advances in flexible and stretchable bio-electronic devices integrated with nanomaterials," *Advanced materials*, vol. 28, no. 22, pp. 4203–4218, 2016.

[51] M. Drack, I. Graz, T. Sekitani, T. Someya, M. Kaltenbrunner, and S. Bauer, "An imperceptible plastic electronic wrap," *Advanced materials*, vol. 27, no. 1, pp. 34–40, 2015.

[52] B. P. Lechêne, M. Cowell, A. Pierre, J. W. Evans, P. K. Wright, and A. C. Arias, "Organic solar cells and fully printed super-capacitors optimized for indoor light energy harvesting," *Nano Energy*, vol. 26, pp. 631–640, 2016.

[53] J. Jan, J. Zhu, J. Ting, and A. C. Arias, "Flexible blade-coated optoelectronic devices: Dual functionality via simultaneous deposition," *Advanced Functional Materials*, p. 2112343, 2022.

[54] Y. Khan, M. Garg, Q. Gui, M. Schadt, A. Gaikwad, D. Han, N. A. Yamamoto, P. Hart, R. Welte, W. Wilson, S. Czarnecki, M. Poliks, Z. Jin, K. Ghose, F. Egitto, J. Turner, and A. C. Arias, "Flexible Hybrid Electronics: Direct Interfacing of Soft and Hard Electronics for Wearable Health Monitoring," *Advanced Functional Materials*, 2016.

[55] F. C. Krebs, "Fabrication and processing of polymer solar cells: A review of printing and coating techniques," *Solar energy materials and solar cells*, vol. 93, no. 4, pp. 394–412, 2009.

[56] D. S. Kim, A. Khan, K. Rahman, S. Khan, H. C. Kim, and K. H. Choi, "Drop-on-demand direct printing of colloidal copper nanoparticles by electro-hydrodynamic atomization," *Materials and Manufacturing Processes*, vol. 26, no. 9, pp. 1196–1201, 2011.

[57] V. Subramanian, J. B. Chang, A. de la Fuente Vornbrock, D. C. Huang, L. Jagannathan, F. Liao, B. Mattis, S. Molesa, D. R. Redinger, D. Soltman, *et al.*, "Printed electronics for low-cost electronic systems: Technology status and application development," in *ESSCIRC 2008-34th European Solid-State Circuits Conference*, pp. 17–24, IEEE, 2008.

[58] J. Perelaer, P. J. Smith, D. Mager, D. Soltman, S. K. Volkman, V. Subramanian, J. G. Korvink, and U. S. Schubert, "Printed electronics: the challenges involved in printing devices, interconnects, and contacts based on inorganic materials," *Journal of Materials Chemistry*, vol. 20, no. 39, pp. 8446–8453, 2010.

[59] S. Nambiar and J. T. Yeow, "Conductive polymer-based sensors for biomedical applications," *Biosensors and Bioelectronics*, vol. 26, no. 5, pp. 1825–1832, 2011.

[60] M.-C. Choi, Y. Kim, and C.-S. Ha, "Polymers for flexible displays: From material selection to device applications," *Progress in Polymer Science*, vol. 33, no. 6, pp. 581–630, 2008.

[61] B. K. Tehrani, C. Mariotti, B. S. Cook, L. Roselli, and M. M. Tentzeris, "Development, characterization, and processing of thin and thick inkjet-printed dielectric films," *Organic Electronics*, vol. 29, pp. 135–141, 2016.

[62] B. S. Cook, J. R. Cooper, and M. M. Tentzeris, "Multi-layer rf capacitors on flexible substrates utilizing inkjet printed dielectric polymers," *IEEE Microwave and Wireless Components Letters*, vol. 23, no. 7, pp. 353–355, 2013.

[63] J. Lin and Z. Cui, "Printing processes and equipments," *Printed Electronics*, pp. 106–144, 2016.

[64] S. J. Leigh, R. J. Bradley, C. P. Purssell, D. R. Billson, and D. A. Hutchins, "A simple, low-cost conductive composite material for 3d printing of electronic sensors," *PloS one*, vol. 7, no. 11, p. e49365, 2012.

[65] G. Postiglione, G. Natale, G. Griffini, M. Levi, and S. Turri, "Conductive 3d microstructures by direct 3d printing of polymer/carbon nanotube nanocomposites via liquid deposition modeling," *Composites Part A: Applied Science and Manufacturing*, vol. 76, pp. 110–114, 2015.

[66] M. R. Khosravani and T. Reinicke, "3d-printed sensors: Current progress and future challenges," *Sensors and Actuators A: Physical*, vol. 305, p. 111916, 2020.

[67] C. C. Ho, D. Steingart, J. Evans, and P. Wright, "Tailoring electrochemical capacitor energy storage using direct write dispenser printing," *ECS Transactions*, vol. 16, no. 1, p. 35, 2008.

[68] P. K. Wright, D. A. Dornfeld, A. Chen, C. C. Ho, and J. W. Evans, "Dispenser printing for prototyping microscale devices," *Transactions of NAMRI/SME*, vol. 38, 2010.

[69] C. C. Ho, J. W. Evans, and P. K. Wright, "Direct write dispenser printing of a zinc microbattery with an ionic liquid gel electrolyte," *Journal of Micromechanics and Microengineering*, vol. 20, no. 10, p. 104009, 2010.

[70] E. Luoma, M. Välimäki, T. Rokkonen, H. Sääskilahti, J. Ollila, J. Rekilä, and K. Immonen, "Oriented and annealed poly (lactic acid) films and their performance in flexible printed and hybrid electronics," *Journal of Plastic Film & Sheeting*, vol. 37, no. 4, pp. 429–462, 2021.

[71] P. Goodrich, "Unpublished lab experiments," 2018.

[72] J. W. Phair and A. F. Kaiser, "Determination and assessment of the rheological properties of pastes for screen printing ceramics," *Annual Transactions of the Nordic Rheology Society*, vol. 17, no. 5, 2009.

[73] J. Ting, "Unpublished lab experiments," 2018.

[74] A. Grimoldi, "Deposition and patterning techniques for organic materials," *Organic Electronics: Principles, devices and applications*, 2015.

[75] R. Fernando, L.-L. Xing, and J. Glass, "Rheology parameters controlling spray atomization and roll misting behavior of waterborne coatings," *Progress in Organic Coatings*, vol. 40, no. 1, pp. 35–38, 2000.

[76] J. Boetker, J. J. Water, J. Aho, L. Arnfast, A. Bohr, and J. Rantanen, "Modifying release characteristics from 3d printed drug-eluting products," *European Journal of Pharmaceutical Sciences*, vol. 90, pp. 47–52, 2016. EuPAT 7 Special Issue - Inventing Tomorrow's Development and Manufacturing.

[77] I. Gunduz, M. McClain, P. Cattani, G.-C. Chiu, J. Rhoads, and S. Son, "3d printing of extremely viscous materials using ultrasonic vibrations," *Additive Manufacturing*, vol. 22, pp. 98–103, 2018.

[78] P. Cunningham, M. Cord, and S. J. Delany, "Supervised learning," in *Machine learning techniques for multimedia*, pp. 21–49, Springer, 2008.

[79] Z. Ghahramani, "Unsupervised learning," in *Summer school on machine learning*, pp. 72–112, Springer, 2003.

[80] R. S. Sutton and A. G. Barto, *Reinforcement learning: An introduction*. MIT press, 2018.

[81] D. A. Patterson and J. L. Hennessy, *Computer organization and design ARM edition: the hardware software interface*. Morgan kaufmann, 2016.

[82] J. R. Sampson, *Adaptation in natural and artificial systems (John H. Holland)*. Society for Industrial and Applied Mathematics, 1976.

[83] D. E. Goldberg and J. H. Holland, "Genetic algorithms and machine learning," 1988.

[84] L. Davis, "Handbook of genetic algorithms," 1991.

[85] D. E. Goldberg and K. Deb, "Special issue on genetic algorithms," *Computer Methods in Applied Mechanics and Engineering*, vol. 186, no. 2-4, pp. 121–124, 2000.

[86] T. Zohdi, P. Monteiro, and V. Lamour, "Extraction of elastic moduli from granular compacts," *International journal of fracture*, vol. 115, no. 3, pp. 49–54, 2002.

[87] T. Zohdi, "Dynamic thermomechanical modeling and simulation of the design of rapid free-form 3d printing processes with evolutionary machine learning," *Computer Methods in Applied Mechanics and Engineering*, vol. 331, pp. 343–362, 2018.

[88] T. Zohdi, "The game of drones: rapid agent-based machine-learning models for multi-uav path planning," *Computational Mechanics*, vol. 65, pp. 217–228, 2019.

[89] T. Zohdi, "Genetic design of solids possessing a random–particulate microstructure," *Philosophical Transactions of the Royal Society of London. Series A: Mathematical, Physical and Engineering Sciences*, vol. 361, no. 1806, pp. 1021–1043, 2003.

[90] T. Zohdi, "A digital-twin and machine-learning framework for the design of multiobjective agrophotovoltaic solar farms," *Computational Mechanics*, vol. 68, no. 2, pp. 357–370, 2021.

[91] T. Zohdi, "A digital-twin and machine-learning framework for ventilation system optimization for capturing infectious disease respiratory emissions," *Archives of Computational Methods in Engineering*, vol. 28, no. 6, pp. 4317–4329, 2021.

[92] T. Zohdi, "A digital-twin and machine-learning framework for precise heat and energy management of data-centers," *Computational Mechanics*, pp. 1–16, 2022.

[93] S. Jadon, "Introduction to different activation functions for deep learning," *Medium, Augmenting Humanity*, vol. 16, p. 140, 2018.

[94] D. Hebbs, "The organization of behavior," *Wiely and Sons, New York, NY, USA*, 1949.

[95] Q. V. Le, M. Ranzato, R. Monga, M. Devin, K. Chen, G. S. Corrado, J. Dean, and A. Y. Ng, "Building high-level features using large scale unsupervised learning," 2011.

[96] K. Chowdhary, "Natural language processing," *Fundamentals of artificial intelligence*, pp. 603–649, 2020.

[97] X. Le, I. Lancashire, G. Hirst, and R. Jokel, "Longitudinal detection of dementia through lexical and syntactic changes in writing: a case study of three british novelists," *Literary and linguistic computing*, vol. 26, no. 4, pp. 435–461, 2011.

[98] M. M. Silva and F. Lidon, "Food preservatives–an overview on applications and side effects," *Emirates Journal of Food and Agriculture*, pp. 366–373, 2016.

[99] J. Abrams, "Beneficial actions of nitrates in cardiovascular disease," *The American journal of cardiology*, vol. 77, no. 13, pp. C31–C37, 1996.

[100] E. G. Mahadevan, *Ammonium nitrate explosives for civil applications: slurries, emulsions and ammonium nitrate fuel oils*. John Wiley & Sons, 2013.

[101] N. M. Crawford, "Nitrate: nutrient and signal for plant growth.," *The plant cell*, vol. 7, no. 7, p. 859, 1995.

[102] J. Dechorgnat, C. T. Nguyen, P. Armengaud, M. Jossier, E. Diatloff, S. Filleur, and F. Daniel-Vedele, "From the soil to the seeds: the long journey of nitrate in plants," *Journal of experimental botany*, vol. 62, no. 4, pp. 1349–1359, 2011.

[103] K. Messier, D. Wheeler, A. Flory, R. Jones, B. Patel, D.and Nolan, and M. Ward, "Modeling groundwater nitrate exposure in private wells of North Caroline for the Agricultural Health Study," *Sci Total Environ*, 2019.

[104] M. Ward, "Defining the problem (workshop session #1)," *Reducing the Health Impacts of the Nitrogen Problem*, Jan 2021.

[105] S. Van Breda, K. Mathijs, G. Kuhnle, B. van der Veer, R. Sinha, M. Ward, and T. de Kok, "Impact of high drinking water nitrate levels on the endogenous formation of apparent N-nitroso compounds in combination with meat intake in healthy volunteers," *Environ Health*, 2019.

[106] C. J. Gobler, A. Burson, F. Koch, Y. Tang, and M. R. Mulholland, "The role of nitrogenous nutrients in the occurrence of harmful algal blooms caused by cochlodinium polykrikoides in new york estuaries (usa)," *Harmful Algae*, vol. 17, pp. 64–74, 2012.

[107] F. Gilcreas, "Standard methods for the examination of water and waste water.," *American Journal of Public Health and the Nations Health*, vol. 56, no. 3, pp. 387–388, 1966.

[108] R. Kissner and W. H. Koppenol, "Qualitative and quantitative determination of nitrite and nitrate with ion chromatography," *Methods in enzymology*, vol. 396, pp. 61–68, 2005.

[109] M. Badea, A. Amine, G. Palleschi, D. Moscone, G. Volpe, and A. Curulli, "New electrochemical sensors for detection of nitrites and nitrates," *Journal of Electroanalytical Chemistry*, vol. 509, no. 1, pp. 66–72, 2001.

[110] M. E. Alahi, L. Xie, A. I. Zia, S. Mukhopadhyay, and L. Burkitt, "Practical nitrate sensor based on electrochemical impedance measurement," in *2016 IEEE International Instrumentation and Measurement Technology Conference Proceedings*, pp. 1–6, IEEE, 2016.

[111] G. Pandey, R. Kumar, and R. J. Weber, "Real time detection of soil moisture and nitrates using on-board in-situ impedance spectroscopy," in *2013 IEEE International Conference on Systems, Man, and Cybernetics*, pp. 1081–1086, IEEE, 2013.

[112] N. C. Brady, R. R. Weil, and R. R. Weil, *The nature and properties of soils*, vol. 13. Prentice Hall Upper Saddle River, NJ, 2008.

[113] W. Alland, *The Mole people.* Mystery Science Theater 3000, 1956.

[114] M. M. Zareh, "Plasticizers and their role in membrane selective electrodes," *Recent Advances in Plasticizers*, pp. 113–124, 2012.

[115] G. J. Moody, R. B. Oke, and J. D. Thomas, "A calcium-sensitive electrode based on a liquid ion exchanger in a poly(vinyl chloride) matrix," *The Analyst*, 1970.

[116] R. D. Armstrong and G. Horvai, "Properties of PVC based membranes used in ion-selective electrodes," in *Electrochimica Acta*, vol. 35, pp. 1–7, Pergamon, 1 1990.

[117] Y. Wang, H. Xu, X. Yang, Z. Luo, J. Zhang, and G. Li, "All-solid-state blood calcium sensors based on screen-printed poly(3,4-ethylenedioxythiophene) as the solid contact," *Sensors and Actuators, B: Chemical*, 2012.

[118] M. Gutiérrez, V. M. Moo, S. Alegret, L. Leija, P. R. Hernández, R. Muñoz, and M. Del Valle, "Electronic tongue for the determination of alkaline ions using a screen-printed potentiometric sensor array," *Microchimica Acta*, vol. 163, pp. 81–88, 9 2008.

[119] J. R. Sempionatto, A. Martin, L. García-Carmona, A. Barfidokht, J. F. Kurniawan, J. R. Moreto, G. Tang, A. Shin, X. Liu, A. Escarpa, and J. Wang, "Skin-worn Soft Microfluidic Potentiometric Detection System," *Electroanalysis*, 2019.

[120] N. Ruecha, O. Chailapakul, K. Suzuki, and D. Citterio, "Fully Inkjet-Printed Paper-Based Potentiometric Ion-Sensing Devices," *Analytical Chemistry*, vol. 89, pp. 10608–10616, 10 2017.

[121] V. A. Dam, M. A. Zevenbergen, and R. Van Schaijk, "Flexible Ion Sensors for Bodily Fluids," in *Procedia Engineering*, 2016.

[122] S. Osaki, T. Kintoki, T. Moriuchi-Kawakami, K. Kitamura, and S.-i. Wakida, "Investigation of Polyurethane Matrix Membranes for Salivary Nitrate ISFETs to Prevent the Drift," *Sensors*, vol. 19, p. 2713, 6 2019.

[123] G. Eisenman, S. Krasne, and S. Ciani, "The kinetic and equilibrium components of selective ionic permeability mediated by nactinand valinomycin-type carriers having systematically varied degrees of methylation fn1," *Annals of the New York Academy of Sciences*, vol. 264, no. 1, pp. 34–60, 1975.

[124] P. Caroni, P. Gazzotti, P. Vuilleumier, W. Simon, and E. Carafoli, "Ca2+ transport mediated by a synthetic neutral ca2+-ionophore in biological membranes," *Biochimica et Biophysica Acta (BBA)-Biomembranes*, vol. 470, no. 3, pp. 437–445, 1977.

[125] X. Liu, Y. Yao, Y. Shao, J. Wu, Y. Ying, and J. Ping, "Phase-dependent ion-to-electron transducing efficiency of ws2 nanosheets for an all-solid-state potentiometric calcium sensor," *Microchimica Acta*, vol. 187, no. 9, pp. 1–9, 2020.

[126] H. Himmel and M. Siess, "Positive inotropic and chronotropic effects of the calcium ionophore a23187 (calimycin) on guinea-pig atria," *Basic research in cardiology*, vol. 83, no. 2, pp. 167–175, 1988.

[127] M. Asadnia, M. Myers, G. A. Umana-Membreno, T. M. Sanders, U. K. Mishra, B. D. Nener, M. V. Baker, and G. Parish, "Ca2+ detection utilising algan/gan transistors with ion-selective polymer membranes," *Analytica chimica acta*, vol. 987, pp. 105–110, 2017.

[128] H. Hisamoto, K. Watanabe, E. Nakagawa, D. Siswanta, Y. Shichi, and K. Suzuki, "Flow-through type calcium ion selective optodes based on novel neutral ionophores and a lipophilic anionic dye," *Analytica chimica acta*, vol. 299, no. 2, pp. 179–187, 1994.

[129] A. Hauke, S. Oertel, L. Knoke, V. Fein, C. Maier, F. Brinkmann, and M. P. Jank, "Screen-printed sensor for low-cost chloride analysis in sweat for rapid diagnosis and monitoring of cystic fibrosis," *Biosensors*, vol. 10, no. 9, p. 123, 2020.

[130] A. Bratov, N. Abramova, and C. Domınguez, "Investigation of chloride sensitive isfets with different membrane compositions suitable for medical applications," *Analytica chimica acta*, vol. 514, no. 1, pp. 99–106, 2004.

[131] E. Ruggeri, *Analysis of equine zygote development after intracytoplasmic sperm injection.* PhD thesis, Colorado State University, 2016.

[132] J. Li and W. Qin, "A freestanding all-solid-state polymeric membrane cu2+-selective electrode based on three-dimensional graphene sponge," *Analytica Chimica Acta*, vol. 1068, pp. 11–17, 2019.

[133] M. Piek, K. Fendrych, J. Smajdor, R. Piech, and B. Paczosa-Bator, "High selective potentiometric sensor for determination of nanomolar con-centration of cu (ii) using a polymeric electrode modified by a graphene/7, 7, 8, 8-tetracyanoquinodimethane nanoparticles," *Talanta*, vol. 170, pp. 41–48, 2017.

[134] S.-i. Wakida, N. Sato, and K. Saito, "Copper (ii)-selective electrodes based on a novel charged carrier and preliminary application of field-effect transistor type checker," *Sensors and Actuators B: Chemical*, vol. 130, no. 1, pp. 187–192, 2008.

[135] M. O'Dowd, M. Martin, A. Wheble, M. Gillmer, and P. Rolfe, "Ion-selective sensors for assessment of the fetus," *Journal of Biomedical Engineering*, vol. 10, no. 2, pp. 165–170, 1988.

[136] P. Chao, D. Ammann, U. Oesch, W. Simon, and F. Lang, "Extra-and intra-cellular hydrogen ion-selective microelectrode based on neutral carriers with extended ph response range in acid media," *Pflügers Archiv*, vol. 411, no. 2, pp. 216–219, 1988.

[137] X.-J. Liu, B. Peng, F. Liu, and Y. Qin, "Potentiometric liquid membrane ph sensors based on calix [4]-aza-crowns," *Sensors and Actuators B: Chemical*, vol. 125, no. 2, pp. 656–663, 2007.

[138] D. Wilson, J. M. Gutiérrez, S. Alegret, and M. Del Valle, "Simultaneous determination of zn (ii), cu (ii), cd (ii) and pb (ii) in soil samples employing an array of potentiometric sensors and an artificial neural network model," *Electroanalysis*, vol. 24, no. 12, pp. 2249–2256, 2012.

[139] H. A. Arida, A. Al-Haddad, and M. J. Schöning, "New solid-state organic membrane based leadselective micro-electrode," *WIT Transactions on Modelling and Simulation*, vol. 51, pp. 547–557, 2011.

[140] E. Witkowska Nery, J. A. Guimarães, and L. T. Kubota, "Paper-based electronic tongue," *Electroanalysis*, vol. 27, no. 10, pp. 2357–2362, 2015.

[141] Z. Hu, T. Buehrer, M. Mueller, B. Rusterholz, M. Rouilly, and W. Simon, "Intracellular magnesium ion-selective microelectrode based on a neutral carrier," *Analytical chemistry*, vol. 61, no. 6, pp. 574–576, 1989.

[142] S. Gasser, N. Bareza, R. Gasser, D. Pruthi, E. Scheer, U. Spichiger-Keller, and E. Toferer, "Free intracellular magnesium remains uninfluenced by changes of extracellular magnesium in cardiac guinea pig papillary muscle," *Journal of Clinical and Basic Cardiology*, vol. 8, no. 1, pp. 29–32, 2006.

[143] W. Zhang, L. Jenny, and U. E. Spichiger, "A comparison of neutral mg2+-selective ionophores in solvent polymeric membranes: complex stoichiometry and lipophilicity," *Analytical sciences*, vol. 16, no. 1, pp. 11–18, 2000.

[144] M. S. Fonari, Y. A. Simonov, L. Croitoru, S. S. Basok, E. V. Ganin, and J. Lipkowski, "The 1: 2 and 1: 1 molecular complexes of n, n-dibenzyl-4, 13-diaza-18-crown-6 with 4-nitrobenzenesulfonamide and dithiooxamide," *Journal of molecular structure*, vol. 794, no. 1-3, pp. 110–114, 2006.

[145] A. O. Olanrewaju, B. P. Sullivan, J. Y. Zhang, A. T. Bender, D. Sevenler, T. J. Lo, M. Fernandez-Suarez, P. K. Drain, and J. D. Posner, "Enzymatic assay for rapid measurement of antiretroviral drug levels," *ACS sensors*, vol. 5, no. 4, pp. 952–959, 2020.

[146] R. Stepánek, B. Kräutler, P. Schulthess, B. Lindemann, D. Ammann, and W. Simon, "Aquocyanocobalt (iii)-hepta (2-phenylethyl)-cobyrinate as a cationic carrier for nitrite-selective liquid-membrane electrodes," *Analytica chimica acta*, vol. 182, pp. 83–90, 1986.

[147] L. A. Pioda, W. Simon, H.-R. Bosshard, and H. C. Curtius, "Determination of potassium ion concentration in serum using a highly selective liquid-membrane electrode," *Clinica Chimica Acta*, vol. 29, no. 2, pp. 289–293, 1970.

[148] S. S. Smaga, C. Xu, B. J. Summers, K. M. Digianantonio, J. R. Perilla, and Y. Xiong, "Mxb restricts hiv-1 by targeting the tri-hexamer interface of the viral capsid," *Structure*, vol. 27, no. 8, pp. 1234–1245, 2019.

[149] J. Gallardo, S. Alegret, and M. Del Valle, "Application of a potentiometric electronic tongue as a classification tool in food analysis," *Talanta*, vol. 66, no. 5, pp. 1303–1309, 2005.

[150] M. Jayakannan, O. Babourina, and Z. Rengel, "Improved measurements of na+ fluxes in plants using calixarene-based microelectrodes," *Journal of plant physiology*, vol. 168, no. 10, pp. 1045–1051, 2011.

[151] M. E. Poplawski, R. B. Brown, K. L. Rho, S. Y. Yun, H. J. Lee, G. S. Cha, and K.-J. Paeng, "One-component room temperature vulcanizing-type silicone rubber-based sodium-selective membrane electrodes," *Analytica chimica acta*, vol. 355, no. 2-3, pp. 249–257, 1997.

[152] K. Suzuki, K. Sato, H. Hisamoto, D. Siswanta, K. Hayashi, N. Kasahara, K. Watanabe, N. Yamamoto, and H. Sasakura, "Design and synthesis of sodium ion-selective ionophores based on 16-crown-5 derivatives for an ion-selective electrode," *Analytical chemistry*, vol. 68, no. 1, pp. 208–215, 1996.

[153] Y. Shibutani, S. Mino, S. S. Long, T. Moriuchi-Kawakami, K. Yakabe, and T. Shono, "Chiral bis (12-crown-4)-based electrodes for sodium ion," *Chemistry letters*, vol. 26, no. 1, pp. 49–50, 1997.

[154] P. Ciosek, Z. Brzózka, W. Wróblewski, E. Martinelli, C. Di Natale, and A. D'amico, "Direct and two-stage data analysis procedures based on pca, pls-da and ann for ise-based electronic tongue—effect of supervised feature extraction," *Talanta*, vol. 67, no. 3, pp. 590–596, 2005.

[155] C. C. Eylem, M. Taştekin, and A. Kenar, "Simultaneous determination of copper and zinc in brass samples by pcr and pls1 methods using a multiple ion-selective electrode array," *Talanta*, vol. 183, pp. 184–191, 2018.

[156] A. K. Singh, S. Mehtab, U. P. Singh, and V. Aggarwal, "Tripodal chelating ligand-based sensor for selective determination of zn (ii) in biological and environmental samples," *Analytical and bioanalytical chemistry*, vol. 388, no. 8, pp. 1867–1876, 2007.

[157] G. A. Crespo, S. Macho, J. Bobacka, and F. X. Rius, "Transduction mechanism of carbon nanotubes in solid-contact ion-selective electrodes," *Analytical chemistry*, vol. 81, no. 2, pp. 676–681, 2009.

[158] J. Hu, A. Stein, and P. Bühlmann, "Rational design of all-solid-state ion-selective electrodes and reference electrodes," *TrAC Trends in Analytical Chemistry*, vol. 76, pp. 102–114, 2016.

[159] P. T. Gilbert, "The use of silver-silver chloride reference electrodes in dilute solutions," tech. rep., 1947.

[160] B. K. Troudt, C. R. Rousseau, X. I. Dong, E. L. Anderson, and P. Buhlmann, "Recent progress in the development of improved reference electrodes for electrochemistry," *Analytical Sciences*, p. 21SAR11, 2021.

[161] F. Scholz and T. Kakiuchi, "Salt bridges and diaphragms," in *Handbook of reference electrodes*, pp. 49–76, Springer, 2013.

[162] "Soil Test Interpretation Guide — OSU Extension Catalog — Oregon State University."

[163] C. R. Rousseau and P. Buhlmann, "Calibration-free potentiometric sensing with solid-contact ion-selective electrodes," *Trends in Analytical Chemistry*, 2021.

[164] D. Wu, L. Deng, X. Mei, K. S. Teh, W. Cai, Q. Tan, Y. Zhao, L. Wang, L. Zhao, G. Luo, D. Sun, and L. Lin, "Direct-write graphene resistors on aromatic polyimide for transparent heating glass," *Sensors and Actuators A: Physical*, vol. 267, pp. 327 – 333, 2017.

[165] L. X. Duy, Z. Peng, Y. Li, J. Zhang, Y. Ji, and J. M. Tour, "Laser-induced graphene fibers," *Carbon*, vol. 126, pp. 472 – 479, 2018.

[166] S. Luo, P. T. Hoang, and T. Liu, "Direct laser writing for creating porous graphitic structures and their use for flexible and highly sensitive sensor and sensor arrays," *Carbon*, vol. 96, pp. 522 – 531, 2016.

[167] Y. Chyan, R. Ye, Y. Li, S. P. Singh, C. J. Arnusch, and J. M. Tour, "Laser-induced graphene by multiple lasing: Toward electronics on cloth, paper, and food," *ACS Nano*, vol. 12, no. 3, pp. 2176–2183, 2018.

[168] A. M. Zamarayeva, N. A. D. Yamamoto, A. Toor, M. E. Payne, C. Woods, V. I. Pister, Y. Khan, J. W. Evans, and A. C. Arias, "Optimization of printed sensors to monitor sodium, ammonium, and lactate in sweat," *APL Materials*, vol. 8, no. 10, p. 100905, 2020.

[169] R. W. Cattrall, *Chemical sensors*. Oxford University Press, 1997.

[170] Y. Umeaza, P. Buhlmann, K. Umezama, K. Tohda, and S. Amemiya, "Potentiometric selectivity coefficients of ion selective electrodes," *Pure Applied Chem*, vol. 72, pp. 1851–2082, 2000.

[171] Y. Fan, Y. Huang, W. Linthicum, F. Liu, A. O. Beringhs, Y. Dang, Z. Xu, S.-Y. Chang, J. Ling, B. D. Huey, *et al.*, "Toward long-term accurate and continuous monitoring of nitrate in wastewater using poly (tetrafluoroethylene)(ptfe)–solid-state ion-selective electrodes (s-ises)," *ACS sensors*, vol. 5, no. 10, pp. 3182–3193, 2020.

[172] N. T. Garland, E. S. McLamore, N. D. Cavallaro, D. Mendivelso-Perez, E. A. Smith, D. Jing, and J. C. Claussen, "Flexible laser-induced graphene for nitrogen sensing in soil," *ACS applied materials & interfaces*, vol. 10, no. 45, pp. 39124–39133, 2018.

[173] W. Tang, J. Ping, K. Fan, Y. Wang, X. Luo, Y. Ying, J. Wu, and Q. Zhou, "All-solid-state nitrate-selective electrode and its application in drinking water," *Electrochimica acta*, vol. 81, pp. 186–190, 2012.

[174] L. Zhang, Z. Wei, and P. Liu, "An all-solid-state no3- ion-selective electrode with gold nanoparticles solid contact layer and molecularly imprinted polymer membrane," *PLOS ONE*, vol. 15, pp. 1–14, 10 2020.

[175] M. Chen, M. Zhang, X. Wang, Q. Yang, M. Wang, G. Liu, and L. Yao, "An all-solid-state nitrate ion-selective electrode with nanohybrids composite films for in-situ soil nutrient monitoring," *Sensors*, vol. 20, no. 8, 2020.

[176] M. Piek, R. Piech, and B. Paczosa-Bator, "All-solid-state nitrate selective electrode with graphene/tetrathiafulvalene nanocomposite as high redox and double layer capacitance solid contact," *Electrochimica Acta*, vol. 210, pp. 407–414, 2016.

[177] K. Pietrzak and C. Wardak, "Comparative study of nitrate all solid state ion-selective electrode based on multiwalled carbon nanotubes-ionic liquid nanocomposite," *Sensors and Actuators B: Chemical*, vol. 348, p. 130720, 2021.

[178] T. A. Bendikov, J. Kim, and T. C. Harmon, "Development and environmental application of a nitrate selective microsensor based on doped polypyrrole films," *Sensors and Actuators B: Chemical*, vol. 106, no. 2, pp. 512–517, 2005.

[179] C. Wardak, "Solid contact nitrate ion-selective electrode based on ionic liquid with stable and reproducible potential," *Electroanalysis*, vol. 26, no. 4, pp. 864–872, 2014.

[180] Y. Ishige, S. Klink, and W. Schuhmann, "Intercalation compounds as inner reference electrodes for reproducible and robust solid-contact ion-selective electrodes," *Angewandte Chemie International Edition*, vol. 55, no. 15, pp. 4831–4835, 2016.

[181] M. Fibbioli, W. E. Morf, M. Badertscher, N. F. de Rooij, and E. Pretsch, "Potential drifts of solid-contacted ion-selective electrodes due to zero-current ion fluxes through the sensor membrane," *Electroanalysis: An International Journal Devoted to Fundamental and Practical Aspects of Electroanalysis*, vol. 12, no. 16, pp. 1286–1292, 2000.

[182] R. De Marco, J.-P. Veder, G. Clarke, A. Nelson, K. Prince, E. Pretsch, and E. Bakker, "Evidence of a water layer in solid-contact polymeric ion sensors," *Physical Chemistry Chemical Physics*, vol. 10, no. 1, pp. 73–76, 2008.

[183] J.-P. Veder, R. De Marco, G. Clarke, R. Chester, A. Nelson, K. Prince, E. Pretsch, and E. Bakker, "Elimination of undesirable water layers in solid-contact polymeric ion-selective electrodes," *Analytical chemistry*, vol. 80, no. 17, pp. 6731–6740, 2008.

[184] S. Bodor, J. M. Zook, E. Lindner, K. Tóth, and R. E. Gyurcsányi, "Electrochemical methods for the determination of the diffusion coefficient of ionophores and ionophore–ion complexes in plasticized pvc membranes," *Analyst*, vol. 133, no. 5, pp. 635–642, 2008.

[185] E. Lindner and R. E. Gyurcsányi, "Quality control criteria for solid-contact, solvent polymeric membrane ion-selective electrodes," *Journal of Solid State Electrochemistry*, vol. 13, no. 1, pp. 51–68, 2009.

[186] E. Grygolowicz-Pawlak, K. Plachecka, Z. Brzozka, and E. Malinowska, "Further studies on the role of redox-active monolayer as intermediate phase of solid-state sensors," *Sensors and Actuators B: Chemical*, vol. 123, no. 1, pp. 480–487, 2007.

[187] C.-Z. Lai, M. A. Fierke, A. Stein, and P. Bühlmann, "Ion-selective electrodes with three-dimensionally ordered macroporous carbon as the solid contact," *Analytical chemistry*, vol. 79, no. 12, pp. 4621–4626, 2007.

[188] M. Chen, M. Zhang, X. Wang, Q. Yang, M. Wang, G. Liu, and L. Yao, "An all-solid-state nitrate ion-selective electrode with nanohybrids composite films for in-situ soil nutrient monitoring," *Sensors*, vol. 20, no. 8, p. 2270, 2020.

[189] J. Bobacka, "Potential stability of all-solid-state ion-selective electrodes using conducting polymers as ion-to-electron transducers," *Analytical chemistry*, vol. 71, no. 21, pp. 4932–4937, 1999.

[190] M. Diacono, P. Rubino, and F. Montemurro, "Precision nitrogen management of wheat. a review," *Agronomy for Sustainable Development*, vol. 33, no. 1, pp. 219–241, 2013.

[191] P. C. Robert, "Precision agriculture: a challenge for crop nutrition management," in *Progress in Plant Nutrition: Plenary Lectures of the XIV International Plant Nutrition Colloquium*, pp. 143–149, Springer, 2002.

[192] T. Ahrens, D. Lobell, J. Ortiz-Monasterio, Y. Li, and P. Matson, "Narrowing the agronomic yield gap with improved nitrogen use efficiency: a modeling approach," *Ecological Applications*, vol. 20, no. 1, pp. 91–100, 2010.

[193] M. Robertson, P. Carberry, and L. Brennan, "The economic benefits of precision agriculture: case studies from australian grain farms," *Crop Pasture Sci*, vol. 60, p. 2012, 2007.

[194] S. Sela, P. Woodbury, and H. Van Es, "Dynamic model-based n management reduces surplus nitrogen and improves the environmental performance of corn production," *Environmental Research Letters*, vol. 13, no. 5, p. 054010, 2018.

[195] C. A. Dieter, *Water availability and use science program: Estimated use of water in the United States in 2015*. Geological Survey, 2018.

[196] C. Dalin, N. Hanasaki, H. Qiu, D. L. Mauzerall, and I. Rodriguez-Iturbe, "Water resources transfers through chinese interprovincial and foreign food trade," *Proceedings of the National Academy of Sciences*, vol. 111, no. 27, pp. 9774–9779, 2014.

[197] C. B. Hedley and I. J. Yule, "Soil water status mapping and two variable-rate irrigation scenarios," *Precision Agriculture*, vol. 10, no. 4, pp. 342–355, 2009.

[198] D. Comis, "Growing crops and saving water in the west," *Agricultural Research*, vol. 59, no. 7, pp. 12–14, 2011.

[199] R. G. Evans and B. A. King, "Site-specific sprinkler irrigation in a water limited future," in *5th National Decennial Irrigation Conference Proceedings, 5-8 December 2010, Phoenix Convention Center, Phoenix, Arizona USA*, p. 1, American Society of Agricultural and Biological Engineers, 2010.

[200] C. W. Gellings and K. E. Parmenter, "Energy efficiency in fertilizer production and use," *Efficient Use and Conservation of Energy; Gellings, CW, Ed.; Encyclopedia of Life Support Systems*, pp. 123–136, 2016.

[201] Z. R. Helsel, "Energy and alternatives for fertilizer and pesticide use," *Energy in farm production*, vol. 6, pp. 177–201, 1992.

[202] M. S. Mudahar and T. P. Hignett, "Energy efficiency in nitrogen fertilizer production," *Energy in agriculture*, vol. 4, pp. 159–177, 1985.

[203] H. Ritchie and M. Roser, "co_2 and greenhouse gas emissions," *Our World in Data*, 2020. https://ourworldindata.org/co2-and-other-greenhouse-gas-emissions.

[204] K. G. Cassman, A. Dobermann, and D. T. Walters, "Agroecosystems, nitrogen-use efficiency, and nitrogen management," *AMBIO: A Journal of the Human Environment*, vol. 31, no. 2, pp. 132–140, 2002.

[205] J. K. Ladha, H. Pathak, T. J. Krupnik, J. Six, and C. van Kessel, "Efficiency of fertilizer nitrogen in cereal production: retrospects and prospects," *Advances in agronomy*, vol. 87, pp. 85–156, 2005.

[206] M. Gupta and R. Khosla, "Precision nitrogen management and global nitrogen use efficiency," in *Proceedings of the 11th International Conference on Precision Agriculture*, Indianapolis, Ind, USA, 2012.

[207] R. F. Muñoz-Huerta, R. G. Guevara-Gonzalez, L. M. Contreras-Medina, I. Torres-Pacheco, J. Prado-Olivarez, and R. V. Ocampo-Velazquez, "A review of methods for sensing the nitrogen status in plants: advantages, disadvantages and recent advances," *sensors*, vol. 13, no. 8, pp. 10823–10843, 2013.

[208] P. C. Robert, R. H. Rust, and W. E. Larson, "Proceedings of site-specific management for agricultural systems: second international conference, march 27-30, 1994 thunderbird hotel, 2201 east 78th st., minneapolis, mn: conducted by the department of soil science and minnesota extension service, university of minnesota," in *2nd International Conference on Site-Specific Management for Agricultural Systems., Minneapolis, Minn.(USA), 1994*, American Society of Agronomy, 1995.

[209] S. L. SU, D. Singh, and M. S. Baghini, "A critical review of soil moisture measurement," *Measurement*, vol. 54, pp. 92–105, 2014.

[210] P. A. Raats and M. T. Van Genuchten, "Milestones in soil physics," *Soil science*, vol. 171, no. 6, pp. S21–S28, 2006.

[211] M. Govender, P. Govender, I. Weiersbye, E. Witkowski, and F. Ahmed, "Review of commonly used remote sensing and ground-based technologies to measure plant water stress," *Water Sa*, vol. 35, no. 5, 2009.

[212] D. El-Shikha, P. Waller, D. Hunsaker, T. Clarke, and E. Barnes, "Ground-based remote sensing for assessing water and nitrogen status of broccoli," *Agricultural water management*, vol. 92, no. 3, pp. 183–193, 2007.

[213] G. P. Robertson, K. M. Klingensmith, M. J. Klug, E. A. Paul, J. R. Crum, and B. G. Ellis, "Soil resources, microbial activity, and primary production across an agricultural ecosystem," *Ecological Applications*, vol. 7, no. 1, pp. 158–170, 1997.

[214] H. Shahandeh, A. Wright, F. Hons, and R. Lascano, "Spatial and temporal variation of soil nitrogen parameters related to soil texture and corn yield," *Agronomy Journal*, vol. 97, no. 3, pp. 772–782, 2005.

[215] P. Anthony, G. Malzer, M. Zhang, and S. Sparrow, "Soil nitrogen and phosphorus behavior in a long-term fertilization experiment," *Agronomy journal*, vol. 104, no. 5, pp. 1223–1237, 2012.

[216] M. Bachmaier and M. Backes, "Variogram or semivariogram? understanding the variances in a variogram," *Precision Agriculture*, vol. 9, no. 3, pp. 173–175, 2008.

[217] R. Kerry, M. Oliver, and Z. Frogbrook, "Sampling in precision agriculture," in *Geostatistical applications for precision agriculture*, pp. 35–63, Springer, 2010.

[218] L. Longchamps, R. Khosla, R. Reich, and D. Gui, "Spatial and temporal variability of soil water content in leveled fields," *Soil Science Society of America Journal*, vol. 79, no. 5, pp. 1446–1454, 2015.

[219] A. W. Western, G. Blöschl, and R. B. Grayson, "Geostatistical characterisation of soil moisture patterns in the tarrawarra catchment," *Journal of Hydrology*, vol. 205, no. 1-2, pp. 20–37, 1998.

[220] G. P. Robertson, J. R. Crum, and B. G. Ellis, "The spatial variability of soil resources following long-term disturbance," *Oecologia*, vol. 96, no. 4, pp. 451–456, 1993.

[221] L. Nyberg, "Spatial variability of soil water content in the covered catchment at gårdsjön, sweden," *Hydrological Processes*, vol. 10, no. 1, pp. 89–103, 1996.

[222] W. Lehmann, *Anwendung geostatistischer Verfahren auf die Bodenfeuchte in ländlichen Einzugsgebieten.* Institut für Hydrologie und Wasserwirtschaft Universität, 1995.

[223] L. Longchamps and R. Khosla, "Precision maize cultivation techniques," in *Achieving sustainable cultivation of maize Volume 2*, pp. 127–157, Burleigh Dodds Science Publishing, 2017.

[224] D. R. Kanter, A. R. Bell, and S. S. McDermid, "Precision agriculture for smallholder nitrogen management," *One Earth*, vol. 1, no. 3, pp. 281–284, 2019.

[225] Y. Zhou, G. Song, and M. Wang, "Wireless sensor network data fusion algorithm based on neural network in the area of agriculture," *Sensors & Transducers*, vol. 16, p. 128, 2012.

[226] T. Popović, N. Latinović, A. Pešić, Ž. Zečević, B. Krstajić, and S. Djukanović, "Architecting an iot-enabled platform for precision agriculture and ecological monitoring: A case study," *Computers and electronics in agriculture*, vol. 140, pp. 255–265, 2017.

[227] U. Shafi, R. Mumtaz, J. García-Nieto, S. A. Hassan, S. A. R. Zaidi, and N. Iqbal, "Precision agriculture techniques and practices: From considerations to applications," *Sensors*, vol. 19, no. 17, p. 3796, 2019.

[228] R. G. Evans, "Center pivot irrigation," *Agricultural Systems Research Unit, North Plain Agricultural Research laboratory. USDN-Agricultural Research Service*, vol. 1500, 2001.

[229] R. G. Evans, J. LaRue, K. C. Stone, and B. A. King, "Adoption of site-specific variable rate sprinkler irrigation systems," *Irrigation science*, vol. 31, no. 4, pp. 871–887, 2013.

[230] T. H. Lo, D. M. Heeren, L. Mateos, J. D. Luck, D. L. Martin, K. A. Miller, J. B. Barker, and T. M. Shaver, "Field characterization of field capacity and root zone available water capacity for variable rate irrigation," *Applied Engineering in Agriculture*, vol. 33, no. 4, pp. 559–572, 2017.

[231] R. Finger, S. M. Swinton, N. El Benni, and A. Walter, "Precision farming at the nexus of agricultural production and the environment," 2019.

[232] D. B. Jourdan and O. L. de Weck, "Layout optimization for a wireless sensor network using a multi-objective genetic algorithm," in *2004 IEEE 59th Vehicular Technology Conference. VTC 2004-Spring (IEEE Cat. No. 04CH37514)*, vol. 5, pp. 2466–2470, IEEE, 2004.

[233] A. Chlingaryan, S. Sukkarieh, and B. Whelan, "Machine learning approaches for crop yield prediction and nitrogen status estimation in precision agriculture: A review," *Computers and electronics in agriculture*, vol. 151, pp. 61–69, 2018.

[234] A. Chlingaryan, S. Sukkarieh, and B. Whelan, "Machine learning approaches for crop yield prediction and nitrogen status estimation in precision agriculture: A review," *Computers and Electronics in Agriculture*, vol. 151, pp. 61–69, 2018.

[235] V. Akbarzadeh, J.-C. Lévesque, C. Gagné, and M. Parizeau, "Efficient sensor placement optimization using gradient descent and probabilistic coverage," *Sensors*, vol. 14, no. 8, pp. 15525–15552, 2014.

[236] E. Haines, "Point in polygon strategies.," *Graphics Gems*, vol. 4, pp. 24–46, 1994.

[237] G. N. Kumar and M. Bangi, "An extension to winding number and point-in-polygon algorithm," *IFAC-PapersOnLine*, vol. 51, no. 1, pp. 548–553, 2018.

[238] R. TOMBE, "Computer vision for smart farming and sustainable agriculture," in *2020 IST-Africa Conference (IST-Africa)*, pp. 1–8, IEEE, 2020.

[239] D. I. Patrício and R. Rieder, "Computer vision and artificial intelligence in precision agriculture for grain crops: A systematic review," *Computers and electronics in agriculture*, vol. 153, pp. 69–81, 2018.

[240] Y. Akbari, N. Almaadeed, S. Al-maadeed, and O. Elharrouss, "Applications, databases and open computer vision research from drone videos and images: a survey," *Artificial Intelligence Review*, vol. 54, no. 5, pp. 3887–3938, 2021.

[241] M. Hifi and R. M'hallah, "A literature review on circle and sphere packing problems: Models and methodologies," *Advances in Operations Research*, vol. 2009, 2009.

[242] B. Widom, "Random sequential addition of hard spheres to a volume," *The Journal of Chemical Physics*, vol. 44, no. 10, pp. 3888–3894, 1966.

[243] N. Metropolis, A. W. Rosenbluth, M. N. Rosenbluth, A. H. Teller, and E. Teller, "Equation of state calculations by fast computing machines," *The journal of chemical physics*, vol. 21, no. 6, pp. 1087–1092, 1953.

[244] A. R. Kansal, S. Torquato, and F. H. Stillinger, "Diversity of order and densities in jammed hard-particle packings," *Physical Review E*, vol. 66, no. 4, p. 041109, 2002.

[245] A. Donev, S. Torquato, and F. H. Stillinger, "Neighbor list collision-driven molecular dynamics simulation for nonspherical hard particles. i. algorithmic details," *Journal of computational physics*, vol. 202, no. 2, pp. 737–764, 2005.

[246] A. Donev, S. Torquato, and F. H. Stillinger, "Neighbor list collision-driven molecular dynamics simulation for nonspherical hard particles.: Ii. applications to ellipses and ellipsoids," *Journal of computational physics*, vol. 202, no. 2, pp. 765–793, 2005.

[247] H. Steinhaus, *Mathematical snapshots*. Courier Corporation, 1999.

[248] Q. Cao, Z. Cui, X. Chen, R. Khosla, T. H. Dao, and Y. Miao, "Quantifying spatial variability of indigenous nitrogen supply for precision nitrogen management in small scale farming," *Precision Agriculture*, vol. 13, no. 1, pp. 45–61, 2012.

[249] J. M. MacDonald, P. Korb, and R. A. Hoppe, "Farm size and the organization of us crop farming," tech. rep., 2013.

[250] D. Hellerstein and D. Vilorio, "Agricultural resources and environmental indicators, 2019," tech. rep., 2019.

[251] C. L. Baumbauer, P. J. Goodrich, M. E. Payne, T. Anthony, C. Beckstoffer, A. Toor, W. Silver, and A. C. Arias, "Printed potentiometric nitrate sensors for use in soil," *Sensors*, vol. 22, no. 11, p. 4095, 2022.

[252] G. Gridling and B. Weiss, "Introduction to microcontrollers," *Vienna University of Technology Institute of Computer Engineering Embedded Computing Systems Group*, 2007.

[253] I. . 2008, "Plastics–guidelines for the recovery and recycling of plastics waste," 2018.

[254] ASTM, "Standard specification for compostable plastics," ASTM D6400, American Society for Testing and Materials, West Conshohocken, PA, USA, 2009.

[255] EN, "Packaging-requirements for packaging recoverable through composting and biodegradation. test scheme and evaluation criteria for the final acceptance of packaging," EN 13432, European Committee for Standardisation, Brussels, Belgium, 2000.

[256] Degradable plastic ring carriers; definitions. 42 U.S.C. § 6914b. 1988.

[257] N. R. Council *et al.*, "Accelerated aging of materials and structures: the effects of long-term elevated-temperature exposure," 1999.

[258] B. A. Poursat, R. J. van Spanning, P. de Voogt, and J. R. Parsons, "Implications of microbial adaptation for the assessment of environmental persistence of chemicals," *Critical Reviews in Environmental Science and Technology*, vol. 49, no. 23, pp. 2220–2255, 2019.

[259] M. Vert, J. Feijen, A. Albertsson, G. Scott, and E. Chiellini, "Biodegradable polymers and plastics. royal society chemistry," 1992.

[260] A. Göpferich, "Mechanisms of polymer degradation and erosion," *Biomaterials*, vol. 17, no. 2, pp. 103–114, 1996.

[261] R. J. Bartlett and B. R. James, "Redox chemistry of soils," *Adv. Agron*, vol. 50, no. 151208, p. 7, 1993.

[262] Y. K. Lee, J. Kim, Y. Kim, J. W. Kwak, Y. Yoon, and J. A. Rogers, "Room temperature electrochemical sintering of zn microparticles and its use in printable conducting inks for bioresorbable electronics," *Advanced Materials*, vol. 29, no. 38, p. 1702665, 2017.

[263] S. M. Won, J. Koo, K. E. Crawford, A. D. Mickle, Y. Xue, S. Min, L. A. McIlvried, Y. Yan, S. B. Kim, S. M. Lee, *et al.*, "Natural wax for transient electronics," *Advanced Functional Materials*, vol. 28, no. 32, p. 1801819, 2018.

[264] Y. Sui, M. Atreya, S. Dahal, A. Gopalakrishnan, R. Khosla, and G. L. Whiting, "Controlled biodegradation of an additively fabricated capacitive soil moisture sensor," *ACS Sustainable Chemistry & Engineering*, vol. 9, no. 6, pp. 2486–2495, 2021.

[265] R. Li, L. Wang, D. Kong, and L. Yin, "Recent progress on biodegradable materials and transient electronics," *Bioactive materials*, vol. 3, no. 3, pp. 322–333, 2018.

[266] Y. Sui, M. Atreya, S. Dahal, A. Gopalakrishnan, R. Khosla, and G. L. Whiting, "Controlled biodegradation of an additively fabricated capacitive soil moisture sensor," *ACS Sustainable Chemistry & Engineering*, vol. 9, no. 6, pp. 2486–2495, 2021.

[267] S. Dahal, W. Yilma, Y. Sui, M. Atreya, S. Bryan, V. Davis, G. L. Whiting, and R. Khosla, "Degradability of biodegradable soil moisture sensor components and their effect on maize (zea mays l.) growth," *Sensors*, vol. 20, no. 21, p. 6154, 2020.

[268] M. Atreya, K. Dikshit, G. Marinick, J. Nielson, C. Bruns, and G. L. Whiting, "Poly (lactic acid)-based ink for biodegradable printed electronics with conductivity enhanced through solvent aging," *ACS applied materials & interfaces*, vol. 12, no. 20, pp. 23494–23501, 2020.

[269] C. Cambra, J. R. Díaz, and J. Lloret, "Deployment and performance study of an ad hoc network protocol for intelligent video sensing in precision agriculture," in *International Conference on Ad-Hoc Networks and Wireless*, pp. 165–175, Springer, 2014.

[270] N. Shah, U. Desai, I. Das, S. Merchant, S. Yadav, *et al.*, "In-field wireless sensor network(wsn) for estimating evapotranspiration and leaf wetness," *International Agricultural Engineering Journal*, vol. 18, no. 3-4, pp. 43–51, 2009.

[271] A. Tripathy, J. Adinarayana, S. Merchant, U. Desai, S. Ninomiya, M. Hirafuji, and T. Kiura, "Data mining and wireless sensor network for groundnut pest/disease precision protection," in *2013 National Conference on Parallel Computing Technologies (PARCOMPTECH)*, pp. 1–8, IEEE, 2013.

[272] J. Panchard, S. Rao, T. Prabhakar, H. S. Jamadagni, and J.-P. Hubaux, "Common-sense net: Improved water management for resource-poor farmers via sensor networks," in *2006 International Conference on Information and Communication Technologies and Development*, pp. 22–33, IEEE, 2006.

[273] M. E. E. Alahi, A. Nag, S. C. Mukhopadhyay, and L. Burkitt, "A temperature-compensated graphene sensor for nitrate monitoring in real-time application," *Sensors and Actuators A: Physical*, vol. 269, pp. 79–90, 2018.

[274] A. ur Rehman, A. Z. Abbasi, N. Islam, and Z. A. Shaikh, "A review of wireless sensors and networks' applications in agriculture," *Computer Standards Interfaces*, vol. 36, no. 2, pp. 263–270, 2014.

[275] T. Ojha, S. Misra, and N. S. Raghuwanshi, "Wireless sensor networks for agriculture: The state-of-the-art in practice and future challenges," *Computers and electronics in agriculture*, vol. 118, pp. 66–84, 2015.

[276] E. C. Ellis, K. Klein Goldewijk, S. Siebert, D. Lightman, and N. Ramankutty, "Anthropogenic transformation of the biomes, 1700 to 2000," *Global Ecology and Biogeography*, vol. 19, no. 5, pp. 589–606, 2010.

[277] H. Ritchie and M. Roser, "Land use," *Our World in Data*, 2013. https://ourworldindata.org/land-use.

[278] USDA, "The number of u.s. farms continues to decline slowly," *Economic Research Service*, 2022. https://ourworldindata.org/land-use.

[279] J. Ding and R. Chandra, "Towards low cost soil sensing using wi-fi," in *The 25th Annual International Conference on Mobile Computing and Networking*, pp. 1–16, 2019.

[280] T. Syrovỳ, R. Vik, S. Pretl, L. Syrová, J. Čengery, A. Hamáček, L. Kubáč, and L. Menšík, "Fully printed disposable iot soil moisture sensors for precision agriculture," *Chemosensors*, vol. 8, no. 4, p. 125, 2020.

[281] C. Yu, K. Kam, Y. Xu, Z. Cui, D. Steingart, M. Gorlatova, P. Culligan, and I. Kymissis, "Plant spike: A low-cost, low-power beacon for smart city soil health monitoring," *IEEE Internet of Things Journal*, vol. 7, no. 9, pp. 9080–9090, 2020.

[282] L. Y. Sørensen, L. T. Jacobsen, and J. P. Hansen, "Low cost and flexible uav deployment of sensors," *Sensors*, vol. 17, no. 1, p. 154, 2017.

[283] P. Tosato, D. Facinelli, M. Prada, L. Gemma, M. Rossi, and D. Brunelli, "An autonomous swarm of drones for industrial gas sensing applications," in *2019 IEEE 20th International Symposium on" A World of Wireless, Mobile and Multimedia Networks"(WoWMoM)*, pp. 1–6, IEEE, 2019.

[284] M. W. Mueller, M. Hehn, and R. D'Andrea, "A computationally efficient motion primitive for quadrocopter trajectory generation," *IEEE Transactions on Robotics*, vol. 31, no. 6, pp. 1294–1310, 2015.

[285] T. Zohdi, "Electrodynamic machine-learning-enhanced fault-tolerance of robotic free-form printing of complex mixtures," *Computational Mechanics*, vol. 63, no. 5, pp. 913–929, 2019.

[286] B. Nicolsky, "Theory of glass electrodes," *Zh Fis Khim*, vol. 10, no. 495, p. 488, 1937.

[287] L. Nuñez, X. Cetó, M. Pividori, M. V. B. Zanoni, and M. Del Valle, "Development and application of an electronic tongue for detection and monitoring of nitrate, nitrite and ammonium levels in waters," *Microchemical Journal*, vol. 110, pp. 273–279, 2013.

Appendix A

Glossary

A.1 Abbreviations

ADC = analog-to-digital converter
Ag/AgCl = Silver-silver chloride
ANN = artificial neural network
AI = artificial intelligence
BLE = bluetooth low-energy
CNT = carbon nanotube(s)
EIS = electrochemical impedance spectroscopy
FFC = flat flexible cable
GA = genetic algorithm
IC = integrated circuit
ISE = ion-selective electrode
ISM = ion-selective membrane
LoRaWAN = long rang, wide area network
ML = machine learning
MLA = machine learning algorithm
NMP = n-methyl-2-pyrrolidone
NPOE = 2-nitro-phenyl octyl ether
PCB = printed circuit board
PCL = poly(caprolactone)
PEN = poly(ethylene naphthalate)
PET = poly(ethylene terephthalate)
PLA = poly(lactic acid)
PVA = poly(vinyl acetate)

PVB = poly(vinyl butyral)
PVC = poly(vinyl chloride)
RE = reference electrode
RFID = radio frequency identification
SGR = sequential gap reduction
SNR = signal-to-noise ratio
THF = tetrahydrofuran
UAV = unmanned aerial vehicle
VWC = volumetric water content
WSN = wireless sensor network

A.2 Definitions

Accuracy = How close a measurement is to the ground-truth value. Can be reported as an absolute, i.e. $\pm C$, or as a relative value, i.e. $\pm P\%$.

Active Sensor = A sensor that requires an excitation signal to perform its measurement. In other words, power needs to be supplied to the sensor in order to make a measurement.

Actuator = A device that can switch voltages, currents, or mechanical states.

Amplifier = A signal conditioning device that adds a gain factor to a sensors output signal. These are used to make the sensor signal fit in the range of conventional electronics.

Analog Sensor = A sensor that produces a continuous output signal

Analyte = A substance whose chemical constituents are being measured. Synonymous with measurand when the quantity being measured generates a chemical signal.

Annealing = Heat-treatment of a material to relieve internal stress.

Attenuation = A decrease in the amplitude of a signal as it passes through any part of the sensor system.

Bandwidth = A range of frequencies in which a sensor or sensor system can operate in a specified error range.

Bode Plot = Commonly used plot to show the relationship between sensitivity error and phase shift as a function of the frequency of a periodic input signal.

Breakdown = Material failure due to an electrical overload.

Calibration = The act of subjecting a sensor to some number of known inputs and recording the outputs to find the sensor's transfer function.

Cross Sensitivity = See 'Selectivity'.

Curing = Heat-treatment of a material to increase the rate of a chemical reaction, such as the cross-linking of a thermoset polymer.

Dead Band = Insensitivity of a sensor in a specific range of input signals.

Digital Sensor = A sensor that produces a discrete digital output signal that is a digital representation of the quantity being measured.

Discrepancy = Difference between two measurements of the same quantity.

Discrimination = See 'Resolution'.

Distortion = Innaccuracy in an amplified or reproduced signal, such as frequency shift, phase delay, or amplitude modulation.

Dynamic Error = Error caused by rapid changes in the measured signal over time. Sometimes described by a bode plot.

Drift = Low-frequency change of a sensor's output signal with time, often associated with the aging of materials, components, or references for the sensor signal.

Eddy Current = Electrical current induced in a conducting material by a variation of magnetic flux.

Efficiency = Ratio of the useful energy output to the total energy input.

Electrode = A conductive element used to emit, collect, or control the movement of electrons or ions in an electric field.

Electrolytic Solution = A solution containing a finite concentration of dissociated ions and capable of conducting electricity.

Endless Loop = See 'Infinite Loop'.

Error = The difference between a measured value and the true value. While the true value is rarely known, this serves as a reference definition and is a common estimation. See 'Uncertainty'.

Excitation Signal = The electric signal from an external power source that is input into a sensor to power it . Only needed for active sensors.

Fertigation = The application of fertilizers or nutrients into a farming system via the irrigation network.

Full Scale Input = See 'Full Scale Range'.

Full Scale Range = Maximum and minimum values that a sensor can measure.

Full Scale Output = The difference between the electrical output signals obtained for the maximum and minimum input values.

Gain = The ratio of amplitude of an output signal to the input signal. Key metric for amplifiers.

Gauge Factor = Applies only to strain gauges. Ratio between the relative change in the strain gauge's resistance and the strain gauge's state of strain, ie (R/R) / (L/L). This is synonymous with responsivity.

Ground = The zero reference potential in a system. Often short for 'earth ground', which is the potential of the earth.

Grounding = Creating an electrical pathway to the ground of an electric system. See 'Ground'.

Hysterisis = When the output value of the sensor depends on the 'history' of what the sensor experiences. Often tested by cycling the sensor under the same conditions and observing whether or not there is any drift in the output signal.

Infinite Loop = See 'Endless Loop'.

Input Signal = The quantity that the sensor observes.

Interference = Any non-primary signal that causes systematic error in the sensor's output signal.

Instability = The tendency to behave in an unpredictable, changeable, or erratic manner.

Interfering Input/Measurand/Signal/Species = See 'Interference'.

Lag = The time delay for a system to completely respond to a change in the input signal.

Leakage = Unintentional loss of an electric signal through undesired pathways, such as an insulator.

Lifetime = The length of time a sensor can be used before its performance changes.

Limit of Detection = The smallest measurable input. Can be reported in units of the input signal or the output signal. Not to be confused with threshold - the limit of detection is the smallest

Linearity = The degree to which a sensor's sensitivity has a constant slope. See 'Nonlinearity'.

Linear Range = The range of inputs in which a sensor has a linear response.

Measurand = The quantity that is being measured.

Nonlinearity = Maximum deviation of a real transfer function from the approximated straight line that is obtained from a linear regression of the real transfer function.

<u>Noise</u> = Random deviation of a sensors output signal that varies with time. There can be many different sources of noise, most commonly: Brownian noise, which is proportional to the inverse of the frequency squared; Johnson-Nyquist noise, which is the thermal agitation of steady state electric signals; and transient noise, which is a random impulse followed by exponentially decaying low frequency oscillations.

<u>Offset</u> = The output signal when the measurand is zero.

<u>Output Impedance</u> = The impedance of a sensor measured across the interfacing channels. Important value used to design sensor interface circuits and connect to sensor systems.

<u>Output Signal</u> = The signal that a sensor outputs. For most sensors, the output signal is measured in an electrical quantity such as [V] or [A], but it could also be other types. For example, a thermometer's output signal is measured in $[\text{cm}_{Hg}]$.

<u>Packaging</u> = The housing for a sensor, for example a plastic container.

<u>Passive Sensor</u> = A sensor that does not require an excitation signal to perform it's measurement. In other words, the sensor generates the output signal in response to the external stimulus that it is measuring. An example of a passive sensors is a thermocouple, which generates a voltage when exposed to heat.

<u>Precision</u> = A description of random errors; the degree to which repeated measurements under unchanged conditions produce the same results. The precision is related to the variance of a set of measurements. Note: a sensor with high precision does not necessarily have high accuracy).

<u>Primary Input/Measurand/Signal/Species</u> = The physical quantity that a sensor is designed to detect.

<u>Repeatability</u> = The precision of a set of measurements taken over a short time period.

<u>Reproducibility</u> = The precision of a set of measurements taken after a long time period, or by different operators, or with different instruments, or at different locations.

<u>Reliability</u> = The ratio between the number of times a sensor operates properly and the total number of times the sensor was tried.

Resolution = The smallest change that a sensor can detect in the quantity that it is measuring. Also (rarely) referred to as the 'discrimination'.

Resonant Frequency = The frequency at which the sensor has maximum output.

Response Time = The time that it takes for a sensor output signal to converge to the correct value after a change in the input signal.

Responsivity = The ratio of the normalized change in output signal to the change in the input signal. For example, a resistive-type temperature sensor would measure responsiveness in $[(d/)/K]$.

Sampling Frequency = the frequency that the connected electronics take measurements from the sensor.

Saturation Point = Upper limit of the linear range.

Selectivity = See specificity. Sometimes reported in an array format where multiple sensors are sensing multiple signals from a single input. For chemical sensors, selectivity is the measure to which the sensor measures a single chemical species.

Sensitivity = Ratio between the output signal and the measured property. For example, a linear sensor that measures temperature and outputs voltage would have sensitivity reported as $[V/K]$. An ideal sensor has a large and constant sensitivity.

Sensing Element = The part of a transducer that is in contact with the medium that is being measured and changes in response to changes in the medium.

Sensor = A device that detects and measures a physical quantity and communicates that measured value to another device or person.

Sensor Node = A device that detects and measures a physical quantity and communicates that measured value to other nodes in a sensor network.

Sintering = Heat-treatment of a material to cause diffusion of nano- and micro- scale materials.

Span = See 'Full Scale Range'.

Specificity = Measure of to what degree the sensor measures a target quantity alone.

Stability = The tendency to behave in an predictable, unchangeable, or expected manner.

Steady-state = A state where all variables of a system are unchanging with time.

Step-response = The response of a system to an instantaneous change in the input signal.

Threshold = The minimum input necessary for a sensor to register a detectable change. The minimum value of the full scale range.

Time Constant = The time it takes for an output signal to reach 63% of it's steady-state value.

Transducer = Collective term for both sensors and actuators. Any device that converts one form of energy into another kind, such as a microphone, loudspeaker, photodiode, or thermistor.

Transfer Function = Also known as the linear region of a calibration curve. The equation that defines the sensor output signal as a function of the input signal. For a linear sensor, the transfer function is formatted as y = mx+b, where y is the output signal, m is the sensitivity, x is the input signal, and b is the offset.

Transient Response = The response of a sensor to a step-change in the measurand.

Uncertainty = Numerical estimate of the possible range of error in a measurement.

Wireless Sensor Network = Networks of spatially dispersed sensor nodes that monitor physical conditions of the environment and forward the collected data to a central location.